2015-08-21

Double Double Electromagnetically Induced Transparency

Alotaibi, Hessa

UNIVERSITY OF CALGARY

Double Double Electromagnetically Induced Transparency

by

Hessa M. M. Alotaibi

A THESIS

SUBMITTED TO THE FACULTY OF GRADUATE STUDIES

IN PARTIAL FULFILLMENT OF THE REQUIREMENTS FOR THE

DEGREE OF DOCTOR OF PHILOSOPHY

GRADUATE PROGRAM IN PHYSICS AND ASTRONOMY

CALGARY, ALBERTA

August, 2015

Abstract

This study demonstrates that tripod (⫛) atom-field electronic structure can yield rich electromagnetically induced transparency phenomena, even at room temperature. In particular, we introduce double double electromagnetically induced transparency (DDEIT), wherein signal and probe fields each have two transparency windows. Their group velocities can be matched in either the first or second pair of transparency windows. Moreover, signal and probe fields can each experience coherent Raman gain in the second transparency window. Our investigation has demonstrated that the self-phase modulation (SPM) and cross-phase modulation (XPM) vanish at the center of two transparency windows for resonant coupling field. However, the values of the XPM and SPM in the region of the second EIT window are improved by a factor of 1000 compared to their values in the region of the first EIT window under the same conditions, and have non-zero values at the center of the second EIT window for nonresonant coupling field.

Additionally, we derive an analytical solution for the wave equation describing the propagation of the probe field whose amplitude-envelope function is described by the fundamental mode Laguerre-Gaussian function. Our solution exhibits that the group velocity of the probe field reduces as the field propagates through the medium. The group velocity reduction is a consequence of spatially-varying susceptibility. The variation of the susceptibility is established by employing signal field whose amplitude-envelope functions is also described by the fundamental mode Laguerre-Gaussian function.

For Doppler-broadened media, we devise a scheme to control and reduce the probe-field group velocity at the center of the second transparency window. We derive numerical and approximate analytical solutions for the width of electromagnetically induced transparency (EIT) windows and for the group velocities of the probe field at the two distinct transparency windows, and we show that the group velocities of the probe field can be lowered

by judiciously choosing the physical parameters of the system. Our modeling enables us to identify three signal-field strength regimes quantified by the Rabi frequency, for slowing the probe field. Our scheme exploits the fact that the second transparency window is sensitive to a temperature-controlled signal-field nonlinearity, whereas the first transparency window is insensitive to this nonlinearity.

Acknowledgements

First, I would like to express my appreciation and thanks to my supervisor, Professor Barry Sanders. I respect and treasure the time you devoted to me, and all the ideas you shared with me, in order to make my PhD experience productive and stimulating. Thank you for encouraging my research and allowing me to develop as a research scientist. I would also like to thank Professor Alex Lvovsky and Professor Christoph Simon, for serving as my supervisory committee members even when this was difficult. Thank you for your valuable comments and suggestions.

Table of Contents

List of Figures and Illustrations

List of Symbols, Abbreviations and Nomenclature

Symbol	Definition
$\pitchfork$	Tripod
$\hat{H}_0$	Free-atom Hamiltonian
$\hat{H}_{\mathrm{dr}}$	Atom-field interaction Hamiltonian
$\hat{V}$	Interaction-picture Hamiltonian
$\hat{H}'$	Rotating-frame Hamiltonian
ρ	Density operator
$\rho_{\imath\jmath}$	Density-operator element
ϱ	Rotating-frame density operator
$\varrho_{\imath\jmath}$	Rotating-frame density-operator element
$\hat{U}$	Unitary transformation operator
$\boldsymbol{d}$	Dipole moment operator
$\boldsymbol{d}_{\imath\jmath}$	Dipole moment element
$\varLambda$	Hamiltonian eigenvalue
$\omega_{\imath\jmath}$	Transition frequency between state $\lvert\imath\rangle$ and $\lvert\jmath\rangle$.
ω_l	Applied-field frequency of mode l
$\hat{\sigma}_{\imath\jmath}$	Projection operator
$\hat{\varepsilon}$	Eelectric field direction vector
Ω	Rabi frequency
δ_l	Detuning frequency of the applied field of mode l
δ_{xy}	Two-photon detuning frequency
$\gamma_{\jmath\imath}$	Decay rate of state $\lvert\jmath\rangle \to \lvert\imath\rangle$
$\gamma_{\phi\imath}$	Dephasing of state $\lvert\imath\rangle$
$\lvert\imath\rangle \leftrightarrow \lvert\jmath\rangle$	Two-way transition

$\vert\imath\rangle \rightarrow \vert\jmath\rangle$	One-way transition
$\gamma_\jmath$	Coherence decay rate
$\mathscr{P}$	Atomic probability.
$\boldsymbol{E}$	Electric-field vector
$\boldsymbol{\xi}$	Electric-field Amplitude envelop function
$\boldsymbol{D}$	Electric-field induction
$\boldsymbol{B}$	Magnetic-field induction
$\boldsymbol{H}$	Magnetic-field vector
$\boldsymbol{P}$	Electric-dipole polarization vector
$\boldsymbol{p}$	Electric-dipole polarization envelop function
$\boldsymbol{k}$	Wave vector
k	Wave number
λ	Wavelength
ρ_{ch}	Electric charge density
$\boldsymbol{J}$	Current density
ϵ_0	Free-space Permittivity
μ_0	Free-space permeability
$\boldsymbol{\chi}$	Optical susceptibility tensor
$\bar{\boldsymbol{\chi}}$	Doppler-broadening optical susceptibility tensor
$\boldsymbol{\epsilon}$	Dielectric tensor
c	Speed of light in vacuum
$\mathscr{V}$	Volume
N	Number of atom
$\mathcal{N}$	Atom density
n	Index of refraction
α	Absorption coefficient

I	Electric field intensity
v_{g}	Group velocity
v_p	Phase velocity
ϕ	Propagation-wave phase
$w(z)$	Gaussian-beam radius function
w_0	Gaussian-beam waist
$R(z)$	Gaussian-radius curvature function
Θ	Gouy-phase shift
b	Gaussian-beam confocal length
z_{R}	Rayleigh range
$f(v)$	Gaussian Maxwell-Boltzmann distribution
$L(v)$	Lorentzian line-shape function
$\boldsymbol{v}$	Atom velocity
r_{p}	Pumping rate
$h_{\max}$	Maximum of the transparency window
$h_{\min}$	Minimum of the transparency window
$h_{D_{\max}}$	Maximum of Doppler-broadening transparency window
$h_{D_{\min}}$	Minimum of Doppler-broadening transparency window
$\varkappa$	Half-maximum transparency window.
$\bar{\varkappa}$	Half-maximum of Doppler-broadening transparency window
HWHM	Half width at half maximum
W_{L}	HWHM of the Lorentzian profile
W_{G}	HWHM of the Gaussian Maxwell-Boltzmann function
$\daleth$	HWHM of the EIT window
$\bar{\daleth}$	HWHM of the Doppler-broadening EIT window
τ	Pulse duration

EIT	Electromagnetically induced transparency
DEIT	Double electromagnetically induced transparency
DDEIT	Double double electromagnetically induced transparency
AWI	Amplification without inversion
LWI	Lasing without inversion
XPM	Cross-phase modulation
SPM	Self-phase modulation
SRS	Stimulated Raman scattering
SERS	Stimulated electronic Raman scattering

Chapter 1

Introduction

1.1 Background and Literature Review

This chapter comprises of two parts. The first presents the background and literature review on electromagnetically induced transparency (EIT), including its history, definition, basic concepts, importance, and applications. It also discusses the necessity of double-EIT (DEIT) for some optical applications. Publication dates were relied upon in writing about the historical order of EIT prediction. The second part of this chapter introduces the subject of the research, including challenges and motivations, the problem statement, objectives, and the research contribution.

1.1.1 History of EIT

The propagation of an electric pulse in an absorptive medium without attenuation has been observed through a process known as self-induced transparency [1]. In this, the energy of a 2π pulse is absorbed by the ensemble of two-level atoms during the first half of the 2π pulse. Then, during the second half of the pulse, the energy is redelivered to the optical field. Finally, the ensemble is returned to its state of equilibrium. In this way, the 2π pulse is able to propagate in an unattenuated manner, through the absorbing medium [2]. The possibility of making a medium transparent by quantum resonance was first pointed out by Manykin and Afanas'ev [3] by studying the suppression of two-photon absorption. Making the medium transparent results from reducing the probability of several quantum transitions in each atom of a given medium, and the consequence of the corresponding phase relations between the waves [3]. This was called "bleaching" the medium. The bleaching of a two-photon absorbing medium, through the interference of two coherent channels of the excitation of a two-photon transition, was verified experimentally 20 years later [4].

The first experimental prediction of the transmission of an electric pulse through the medium of three-level atoms was performed by Kocharovskaya and Khanin [5] and was called coherent bleaching of a three-level medium. Using an electronic structure similar to that presented in Fig. 1.1(a), the authors demonstrated that a train of ultra-short optical pulses interacting with a three-level atom can effectively excite coherence in the lower-frequency transition, when splitting between the lower levels $|1\rangle$ and $|2\rangle$ is a multiple of the pulse repetition frequency, and the intensity of the laser radiation is sufficiently high. Consequently, the medium becomes transparent to the laser field. The bleaching of a medium required a coherent population trapping (CPT) condition [6]. That is the two photon detuning must vanish ($\delta_{\mathrm{p}} - \delta_{\mathrm{c}} = 0$) (see Fig. 1.1(a)). This result was predicted through the examination of the same atom-level structure Fig. 1.1(a), but in the case of continuous excitation. Additionally, they detected and presented the properties of the transparency window, and found the minimum light intensity at which bleaching of the medium is possible.

The process of transmission of electromagnetic waves through an absorptive medium without attenuation based on atomic coherence and quantum interference has been known as EIT since a 1990 study by Harris et al. [7]. This demonstrated the possibility of creating a nonlinear medium with resonantly enhanced nonlinear optical susceptibility, and revealed an improvement in conversion efficiency and parametric gain, combined with induced transparency. It also detected the effect of the Doppler broadening and coherence dephasing on the transparency window.

The work of Harris et al. prompted interest in EIT. It inspired examination of various atomic configurations under different physical conditions, to discover different optical property improvements and applications based on EIT. Electromagnetically induced transparency has been successfully demonstrated in various experiments, using different nonlinear media [8–23]. It has found applications in the field of fiber optics [22, 24], superconductor circuit [25–27], semiconductor material [28], Bose-Einstein condensates [29], and optomechanics [30], It has also found applications for diverse purposes, such as storage and slow light [18, 20, 23], lasing without inversion [12–17], frequency wave mixing, frequency conversion, and parametric gain nonlinear process [7, 31, 32], large Kerr nonlinearity [10, 11, 33], and optical clock[34, 35].

The goal here is not to present a comprehensive review of all research related to EIT, but to summarize the definitions and some important results used in this study. First, the basic idea of EIT is briefly reviewed, and the EIT phenomena explained using three quantum concepts. Then, two important applications of EIT are presented: slow light and lasing without inversion. The last subsection discusses DEITs ability to enhance the nonlinear interaction between the propagating electromagnetic waves.

1.1.2 Definition of EIT and its Basic Physical Concepts

Electromagnetically induced transparency exploits interfering electronic transitions in a medium to eliminate absorption [36] and dramatically modify dispersion [37, 38] over a narrow frequency band. Usually, the resonant excitation would lead to strong absorption. However, if the atoms are prepared by EIT, the absorption is essentially switched off, and the usual correlation of high refractive index with high absorption can be broken [39]. This leads to the creation of media with unique optical properties. The sufficient system of realizing transparency or enhancing transmission consists of two applied fields and a three-level atom system. The frequencies of the applied fields must differ from a Raman non-allowed transition of the medium [40]. The system in Fig. 1.1(a) shows an example to which the concept of EIT applies. The levels $|1\rangle$ and $|3\rangle$ are coupled by the probe field, whose absorption should be minimized. The interaction strength is defined by the Rabi frequency Ω_{p}. The upper level $|3\rangle$ is coupled to $|2\rangle$ by coupling field with Rabi frequency Ω_{c}. The transition $|1\rangle \leftrightarrow |2\rangle$ is Raman forbidden transition.

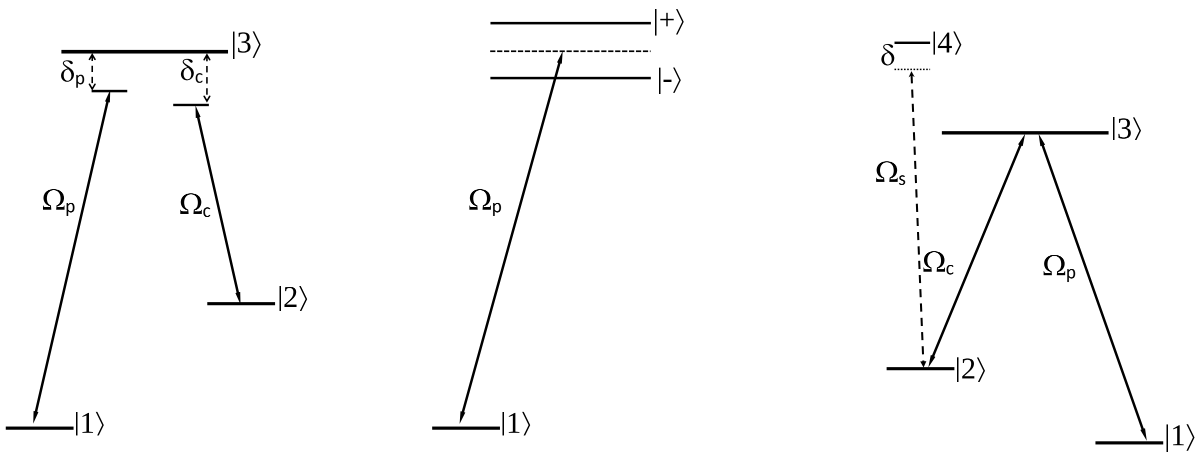

(a) (b) (c)

Figure 1.1: (a) Three-level Λ electronic structure with high-energy state $|3\rangle$ and lower-energy levels $|1\rangle$, $|2\rangle$. Transitions are driven by probe (p) and coupling (c) fields, with frequencies ω_{x} and detunings δ_{x} with x$\in \{p, c\}$. (b) Same atom in dressed state generated by strong-c field, levels $|2\rangle$ and $|3\rangle$ are hybridized into $|\pm\rangle$. (c) Four-level N-scheme structure constructed by attaching a fourth level to the Λ configuration coupled by weak-signal field.

The mechanisms of EIT can be explained using three quantum physical concepts [36, 39, 40]: dark-state analysis, quantum interference and probability amplitudes, or dressed-state analysis.

1.1.2.1 Quantum Interference and Probability Amplitudes

In EIT, the interference occurs between alternative transition pathways, driven by the applied fields within the internal states of the quantum system. Interference effects arise because in quantum mechanics the probability amplitudes which may be positive or negative in sign, must be summed and squared to obtain the total transition probability between the relevant quantum states [36, 40]. Interference between amplitude may lead to either enhancement or complete cancellation in the total transition probability. For the atom-field scheme shown in Figure 1.1(a), the probability amplitudes of state $|3\rangle$ is driven by two terms of equal magnitude and opposite sign. One driving term is proportional to the probability amplitude of state $|1\rangle$. The other term is oppositely phased and proportional to the probability amplitude of state $|2\rangle$. These driving terms have the same frequency and balance, so that the probability amplitude of state $|3\rangle$ is zero [36, 41]. Thus, the transition to state $|3\rangle$ vanishes and the system is driven to EIT.

1.1.2.2 Dark-State Analysis

Another approach to understand EIT is based on the concept of dark-state analysis [39, 40]. For exact two photon resonance at $\delta_{\mathrm{pc}} = \delta_{\mathrm{p}} - \delta_{\mathrm{c}} = 0$, one of the three eigenstates of the total Hamiltonian that describe the optical system in Fig. 1.1(a) turn out to be an antisymmetric coherent superposition of the two lower bare states

$$|D\rangle = \frac{\Omega_{\mathrm{c}}\,|1\rangle - \Omega_{\mathrm{p}}\,|2\rangle}{\sqrt{|\Omega_{\mathrm{p}}|^2 + |\Omega_{\mathrm{c}}|^2}}. \tag{1.1}$$

It is important to note that no component of the bare state $|3\rangle$ appears in these superpositions. The superposition state $|D\rangle$ is not coupled to state $|3\rangle$ because the total dipole moment for the transition from state $|D\rangle$ to the bare state $|3\rangle$ could equal zero [40]. If the magnitudes of the applied fields are appropriately balanced, the negative sign in the superposition of $|1\rangle$ and $|2\rangle$ causes the transition moment $\langle D|\boldsymbol{d}\,|3\rangle$ to vanish, with $\boldsymbol{d}$ the dipole transition moment operator. If the atoms are formed in this state, there is no possibility of excitation to $|3\rangle$, hence no absorption. The state $|D\rangle$ is called a dark state, because it acquires the entire population of the system through optical pumping. Thus, spontaneous emission from state $|3\rangle$ populate state $|D\rangle$, but absorption losses from state $|D\rangle$ back to state $|3\rangle$ are not possible.

1.1.2.3 Dressed-State Analysis

On the other hand, if $\Omega_{\mathrm{p}} \ll \Omega_{\mathrm{c}}$, the subsystem of state $|2\rangle$ and $|3\rangle$ can be described in terms of the dressed state, with the weakly coupled state $|1\rangle$ attached to the subsystem as shown in Fig. 1.1(b). For a strong resonant coupling at the single-photon resonance $\delta_{\mathrm{c}} = 0$ the dressed states of the subsystem are [39, 40]

$$|+\rangle = \frac{|2\rangle + |3\rangle}{\sqrt{2}}\,, |-\rangle = \frac{|2\rangle - |3\rangle}{\sqrt{2}}. \tag{1.2}$$

The transition amplitude at ω_p frequency from the ground state $|1\rangle$ to the dressed states will be the sum of the contribution to the dressed states $|+\rangle$ and $|-\rangle$

$$\begin{aligned}\langle 1|\boldsymbol{d}\,|+\rangle + \langle 1|\boldsymbol{d}\,|-\rangle &\sim \frac{\langle 1|\boldsymbol{d}\,|2\rangle + \langle 1|\boldsymbol{d}\,|3\rangle}{\sqrt{2}} + \frac{\langle 1|\boldsymbol{d}\,|2\rangle - \langle 1|\boldsymbol{d}\,|3\rangle}{\sqrt{2}} \\ &\sim \frac{\boldsymbol{d}_{12} + \boldsymbol{d}_{13}}{\sqrt{2}} + \frac{\boldsymbol{d}_{12} - \boldsymbol{d}_{13}}{\sqrt{2}}.\end{aligned} \tag{1.3}$$

However, the transition of between states $|1\rangle$ and $|2\rangle$ is dipole forbidden, that is $d_{12} = 0$. Then the transition amplitude reduce to zero, which implies vanishing the absorption and the system is driven to EIT.

The implementation of EIT is subject to a number of parameter, for example the choice of the atomic energy-level configuration must satisfy the condition that is, dipole allowed transition $|1\rangle \leftrightarrow |3\rangle$ and $|2\rangle \leftrightarrow |3\rangle$ while the transition $|1\rangle \leftrightarrow |2\rangle$ is dipole forbidden. Decay to other energy levels outside of the specified optical system must be considered which leads to an open system. Collision in the medium must be minimized, to reduce the dephasing of the coherence [36, 39]. The coupling field must be strong enough to overcome the inhomogeneous broadening at high temperature implementation [42]. The line width of the applied laser must also be limited, to reduce the coherence dephasing [43–45].

1.1.3 Electromagnetically Induced Transparency Applications.

Electromagnetically induced transparency affects many applications such as storage and slow light [18, 20, 23], lasing without inversion [12–17], frequency wave mixing, frequency conversion, and parametric gain nonlinear process [7, 31, 32], large Kerr nonlinearity [10, 11, 33], and optical clock [34, 35]. Here, the basic ideas behind two of these applications is discussed: slow light and lasing without inversion. These will be discussed during examination of the $\pitchfork$ configuration.

1.1.3.1 Lasing Without Inversion (LWI)

Under the condition in which EIT occurs and absorption vanishes, the gain can present without the requirement of population inversion in bare states or even in the dressed states. Any small population in the upper states established by incoherent pumping is enough to produce a gain [46–50]. The concept is expanded to employ EIT to obtain lasing without inversion, and much theoretical work has been undertaken on this issue [12–17]. Electromagnetically induced transparency might lead to the construction of short wavelength lasers [48], restricted by population inversion.

1.1.3.2 Slow Light

The EIT technique promotes a high transmission of light through an opaque medium, in addition to enhances the dispersion of the light through medium. The dispersion at the center of EIT window has a similar value, as in the case of high absorption when EIT is not the case. However, in the region of the EIT window, the medium show normal dispersion. The value of the dispersion in this region depends on the shape of the curve, which is controlled by the strong-coupling field. When the coupling-field intensity is small, the dispersion profile can be very steep and the group velocity becomes anomalously low. This offers the possibility of slowing down the speed of light by EIT [18, 20–23, 30]. Slow light has essential application in the field of classical and quantum optics. In optical communication and quantum information processing, slow light enhances light-matter interaction times, thereby leading to an increase in nonlinear interactions [11, 19, 20, 51]. It also enables storage of the quantum state of light for a sufficiently long time, to enable quantum memory [52]. In the field of classical optics, slow light may lead to new types of delay lines [53], and ultra-sensitive Sagnac interferometers [54].

1.1.4 Double Electromagnetically Induced Transparency

Electromagnetically induce transparency is not only used to improve the linear optical process, but also employed to modify the nonlinear optical response of a medium. It has been used to improve frequency wave mixing, frequency conversion, and parametric gain nonlinear processes [7, 31, 32] by greatly reducing the phase-matching requirements. This leads to frequency mixing with greatly enhanced efficiencies. It also used to increase the nonlinear interaction to generate large, Kerr-type nonlinearity [8–10, 51], which is requisite to obtain large cross-phase modulation (XPM) [51] and large self-phase modulation(SPM) [55, 56]. For these purposes the optical system has been upgraded to include more quantum states and more applied fields than that presented in Fig. 1.1(a).

Using EIT, Schmidt and Imamoğlu [51] show that it is theoretically possible to achieve Kerr nonlinearity several orders of magnitude greater than the conventional Kerr nonlinearity produced by three level scheme under similar condition. Their theory was applied on configuration, as shown in Fig. 1.1(c), where they add a fourth level attached to the Λ system by a weak signal field. Experimentally, a phase shift of 7.5° has been measured at low light intensity in the four-level N-type scheme, with a cold atom [9]. The interaction between the probe and the signal fields is limited by temporal walk-off, which result of different group velocities of the probe and signal pulses. The probe pulse propagates with slow group velocity due to EIT, while the signal-field group velocity is close to speed of light in vacuum.

The temporal walk-off dilemma has been treated by creating two simultaneous transparency windows: one for a signal and the other for a probe field. The proposed schemes based on this idea are called DEIT [57–61]. Figure 1.2 shows different proposed schemes, used to generate DEIT. Double EIT enhances XPM shift by forcing the two weak fields to interact for a sufficiently long time, by matching their group velocities. Several Experiments based on DEIT-XPM enhancement have been reported. For example, in cold atom a phase shift of 5° between the two weak fields in a four-level ⋔-atomic configuration has been achieved [33]. In hot atom, a 12° XPM phase shift has been observed using an inverted-Y system at 60° C temperature [10]. Another experiment demonstrate low-light XPM with double-slow light pulses, based on EIT with a cold atom [11].

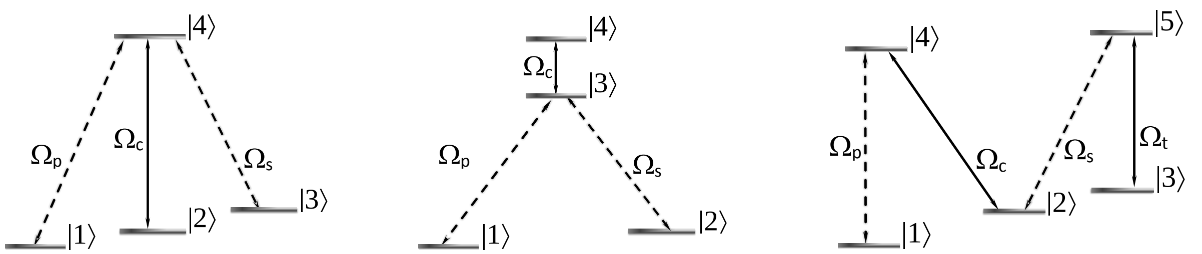

(a) (b) (c)

Figure 1.2: Schematic diagrams of the multi-levels atomic system proposed to implement DEIT. Transitions are driven by weak probe (p) and signal (s) fields, and strong coupling (c) and tuner (t) fields with Rabi frequencies Ω_{x} with x$\in \{p, c, s, t\}$. (a) Four-level ⋔-electronic structure. (b) Four-level inverted Y-scheme structure. (c) Five-level M-scheme configuration.

Double EIT is valuable for coherent control and enabling long-lived nonlinear interactions between weak fields, which could enable deterministic all-optical two-qubit gates for quantum computing [57–61] and all-optical fiber switch [24].

Although, the three-levels atom explains EIT, four levels are required for DEIT, such as the ⋔ atom-field configuration [57] in Fig. 1.2(a). The four-level ⋔-atomic configuration interacting with three electromagnetic fields that were adopted in this research have been studied before. For example, Paspalakis and Knight [62] slowed and control the group velocity of a weak field by varying the Rabi frequencies of the coupling-laser fields. They also showed that the system can exhibit double-transparency windows and, in general, the group velocity of the probe-laser field can obtain, at most, two different values at transparency. The work of Rebic et al. [57] presents the feasibility of implementing a quantum-phase gate using the ⋔ system. They discussed the degree of symmetry between two transparency windows, so that the probe and the signal-group velocities can be made equal. They also discussed the possibility of achieving large cross Kerr nonlinearities between the two weak fields. They suggested operating the system in the region of the EIT window, but not at the equal-detuning frequency, where Kerr-nonlinearity vanishes. They were able to obtain large XPM, but at the expense of increasing the absorption of the weak fields. Tripod-electronic configuration is used to realize simultaneous group-velocity reduction, and storage of the probe and signal fields in the first window [61].

This study presents a $\pitchfork$ configuration with rich EIT phenomena, which has not been presented before. This is what we call DDEIT, whereby both the signal and the probe fields can have two EIT windows, given the right parameter choices. This new, second EIT window for each of the signal and probe fields exhibits a coherent Raman gain, which is also a new prediction. In this approach, we adopt the same conditions as [57] in studying the $\pitchfork$ configuration. However, in the analysis, the effect of the signal field on the linear susceptibility of the probe, and vice versa, are included. By using DDEIT, the group velocities of each of the signals and probes can simultaneously be matched in the first transparency window, and for a different value of group velocity, also in the second window. Further, it is assumed that there are equal, stationary population distributions in states $|1\rangle$ and $|3\rangle$, i.e., $\rho_{11} \approx \rho_{33} \approx \frac{1}{2}$ causes either the signal or the probe field to experience a coherent gain (amplification) in the second transparency window. This could not be seen by [62] due to their assumption that the system is prepared and remains at the ground state. Unlike the case of EIT with amplification (EITA) for a three-level Δ atom [26], in which the gain is due to sum-frequency generation and need phase matching condition to achieve gain, here the gain is due to stimulated Raman scattering (SRS) and the phase-matching condition are automatically satisfied.

1.2 Challenge and motivation

The $\pitchfork$ atom-field structure carries many characteristics that may be of significant interest in the field of nonlinear optics. One of these characteristics, DEIT, was discussed in the previous section [33, 57, 61, 62]: a signal and a probe would each have an EIT window, and both could be decelerated at the same time and interact via XPM. However, there are many other important properties owned by this atom-field configuration that are hidden and have not been addressed previously, so require further study. Therefore, this research examines the $\pitchfork$ atom-field structure in new region, in which the detuning of the probe and signal fields are equal, but differ from the coupling-field detuning. In this region, a new transparency window appears in both the probe and signal-absorption profiles. These have not been studied previously, and could carry an important characteristic, capable of improving optical properties in either the linear or nonlinear domains. The presence of the transparency window in the absorption profile of both the probe and signal fields motivates the employment of the new window as an alternative point of operation, which could lead to a more efficient atom response. That is, the new window could be implemented for group-velocity matching between the signal and probe-propagating waves, and could be used for larger XPM shift than the first window. Therefore, theoretical analysis is undertaken of the linear and nonlinear optical properties over the narrow frequency band of the transparency window. These include:

(i) Examination of the linear absorption and group velocity for different driving-field intensities and coherence dephasings, at low temperatures, and finding the condition to match the group velocities of probe and signal fields.

(ii) Investigation of the optical properties of the $\pitchfork$ atom-field configuration under various temperatures, where the inhomogeneous Doppler broadening affects behavior. The investigation includes determination of the width of the new transparency window, and the group velocity at the center of that window, in addition to study of their evolution for various temperatures.

(iii) Detection of the variation of Kerr nonlinearity in response to the variation of the coupling-field detuning, and determining how this could modify the SPM and XPM.

(iv) Investigation of the spatial variation of the group velocity and phase shift, when the probe and signal fields are propagating-Gaussian beams.

The $\pitchfork$ configuration is complicated, and finding general analytical solutions describing the absorption and dispersion appears to be impossible. Therefore, theoretically analyzing the above points based on an analytical solution is challenging, and requires reliance on assumptions to simplify the problem. Ultimately, an approximate analytical solution is reached, often valid in the narrow frequency band of the second transparency window.

1.3 Problem statement

Low group velocity and high XPM are requisites for many applications in quantum and nonlinear optics. Slow light enhances light-matter interaction times, leading to an increase in nonlinear interactions [11, 19, 20, 51] and possibly in new types of delay lines [53], as well as ultra-sensitive Sagnac interferometers [54]. Conversely, high cross-phase modulation could enable deterministic all-optical two-qubit gates [57–61] in quantum computing, and all-optical fiber switch [24] in the fiber-optics field.

Operating an optical system under EIT condition significantly reduces the group velocity, and enhances nonlinear optical properties. However, what has been accomplished until now is lower than what is required for many optical applications. In this thesis, a strategy for operating the $\pitchfork$ atom-field configuration is established, based on the choice of frequency detuning of applied fields. This strategy could contribute toward the improvement of the optical properties, required by many applications. Under this strategy, our $\pitchfork$ atom-field system exhibits enhanced optical properties under some assumptions, for certain conditions. This study proposes to operate the $\pitchfork$ atom-field configuration in new regions of frequency detuning, where the detuning of the probe and signal fields are equal, but differ from the coupling-field detuning. The $\pitchfork$ atom-field configuration is highly symmetrical between the two transparency windows of the signal and probe fields. It can be used to make the signal and probe-field group velocities equal, and to obtain XPM for both fields. The optical system operating in the new region of frequency detuning leads to:

(i) High XPM at the center of each transparency window of signal and probe fields, by controlling the coupling-field detuning.

(ii) Nonlinear interaction between the probe and signal fields at high temperatures, maintains the width of the second window constant. This result permits a further reduction of the intensity of the signal field without losing the EIT transparency window. Further, it gets a lower probe-field group velocity at the second window than at the first window.

(iii) A reduction in the group velocity of both probe and signal fields, as they propagate through the medium by altering its dielectric. This can be done using both fields as a fundamental Gaussian beam. How fast the group velocity reduction can be is controlled by varying the beam waist of the Gaussian fields.

1.4 Objectives

The main objective here is to theoretically analyze the $\pitchfork$ atom-field structure in the new region, wherein the detuning of the probe and signal fields are equal but differ from the coupling-field detuning. It examines the linear and nonlinear-optical properties of the medium in response to probe and signal fields in low and high temperatures, and uncovers the existence of new phenomena and improvement in optical properties. This theoretical study also focuses on finding techniques to lower the group velocity of the propagating weak fields, and increasing the nonlinear interaction between them to achieve large XPM by involving several sub-objectives. These are:

(i) Determining the limit of the coupling-field detuning values, at which the Kerr nonlinearity of both probe and signal fields achieve high values through analyzing the dispersion of analytical solutions in the region of the new window.

(ii) Employing the Gaussian field instead of the infinite plane waves, to alter the dielectric of the nonlinear medium as the beam propagates through the medium. The medium dielectric varies as the propagation distance of the field changes. The field-medium interaction becomes equivalent to treating the medium as inhomogeneous. This technique of creating inhomogeneity could modify and enhance linear and nonlinear interactions. To realize the effects of using Gaussian signal beam on the a Gaussian probe beam-output function, the wave equation is solved, and the modulated-output probe-field wave function is found. The probe-field output wave function carries all information about how the amplitude and phase of the wave function evolve during the propagation, through the nonlinear-optical medium.

(iii) Proposing a mechanism to slow the probe field in the second transparency window of Doppler-broadened DDEIT. For this slowing to be achieved, we need to balance two competing requirements. One is to slow the probe pulse in Doppler-broadened EIT and reduce the driving field intensity, as the group velocity is proportional to the driving-field intensity. Conversely, the driving-field intensity must be sufficiently large to circumvent inhomogeneous broadening [63–67]. An analytical expression is derived that enables the finding of a parameter regime, whereby these competing requirements can be satisfied simultaneously. Our analytical technique is based on approximating the

Maxwell-Boltzmann velocity distribution for atoms, through Lorentzian distributions over the narrow but relevant domain of small atomic velocities [65].

1.5 Contribution

This thesis introduces some important, previously unpredicted features of the $\pitchfork$ atom-field configuration. These include:

Double double-electromagnetically induced:

The DDEIT phenomenon discussed here has a property in which both the signal and probe fields have two EIT windows, given the right parameter choices. That is, both fields can pass through the medium without absorption, and with a lower group velocity than the speed of light, at two different EIT transparency windows. There is DEIT for the signal and probe for the first EIT windows, and DEIT for the second EIT windows of the signal and probe. For identical probe and signal-Rabi frequencies, the optical properties of both fields at the first and second window are identical. Therefore, their group velocities can be matched in either the first or second pairs of transparency windows. The presence of this window can be explained in terms of the coherence between atomic levels in both the bare and semi-classical dressed bases. Through this DDEIT phenomenon, one could send bichromatic signals and probe fields through the medium, with the lower-frequency chromatic component of the signal and probe fields traveling with one simultaneously matched group velocity, and the upper-frequency chromatic component also traveling through the medium at a different but simultaneously matched-group velocity. The wide importance of EIT in, for example, slow light in atomic vapors [61], optical fibers [22], and Bose-Einstein condensates [29] as well as in solid-state systems such as optonanomechanics [30] and superconducting artificial atoms [68], indicates the broad applicability of our DDEIT properties.

Raman gain under EIT condition:

The gain is achieved with the following usual Raman-gain conditions are not required in our system: The pump does not need to be much stronger than the Stokes field; the population inversion at the operating transition $|1\rangle \leftrightarrow |3\rangle$ is not required; and the detuning from intermediate level $|4\rangle$ dose not to be large, except that $\delta_{\mathrm{p}} = \delta_{\mathrm{s}}$ which could be zero. This condition is not required for the system discussed here, because at steady state the system is trapped to a dark state, which is a superposition of the Raman-scattering states, leaving $|4\rangle$ unoccupied. The only condition required to amplify the probe field is $\varrho_{33} |\Omega_{\mathrm{s}}|^2 > \varrho_{11} |\Omega_{\mathrm{p}}|^2$ and to amplify the signal field is $\varrho_{11} |\Omega_{\mathrm{p}}|^2 > \varrho_{33} |\Omega_{\mathrm{s}}|^2$. The overall gain occurs in the second window due to nonlinear process, whereby the higher order terms of probe and signal fields become significant, and can not be ignored. Amplification can not be detected in the probe and signal field outputs simultaneously, because the gain appears in the probe field is accompanied by absorption of the signal field, and vice versa.

Enhancement of the nonlinear index of refraction:

At the second EIT window, where $\delta_{\mathrm{p}} = \delta_{\mathrm{s}} \neq \delta_{\mathrm{c}}$, enhancement in the SPM and XPM of nonlinear index of refraction by a factor of 1000 was achieved in the region of the new transparency window. This contrasts with its value in the first EIT for the same parameters, and under the same conditions. At the center of the EIT window, the SPM and the XPM of both the probe and signal fields vanish. However, it was found that if the signal field is not in resonance either with the $|3\rangle \leftrightarrow |-\rangle$ or with $|3\rangle \leftrightarrow |+\rangle$ transitions, both SPM and XPM of the probe field are displaced from zero, and reach their maximum value when $\delta_{\mathrm{c}} = \frac{\delta_{\mathrm{s}}}{2}$. Similarly, for the signal field, to get a non-zero value for the SPM and XPM of the signal field, the probe field must not be in resonance either with the $|3\rangle \leftrightarrow |-\rangle$ or with the$|3\rangle \leftrightarrow |+\rangle$ transitions.

Gaussian-beam effect on optical properties:

In this study, the lowest-order Laguerre Gaussian beam was used, to replace the infinite-plane probe and signal fields in the optical susceptibility, and to describe the induced polarization of the probe-field transition. Then the wave equation was solved, so that it described the propagation of the Gaussian probe field through the $\pitchfork$ atom-field configuration, and was able to find the modulated-output probe-field wave function. The solution shows the changes that occur in the amplitude and the phase of the wave during its propagation within the media.

The use of the Gaussian beam for the probe and signal fields makes the optical susceptibility spatially dependent, and varies as the beams propagate through the medium. The variation of the optical susceptibility modify the group velocity of the probe field, but not the nonlinear phase shift. An additional term appears in the denominator of the group velocity of the probe field, and leads to a further reduction in the group velocity, as long as $z > 0$ (where z is the propagation distance). The reduction of the group velocity of the probe field is controlled by the signal-field beam waist.

Group-velocity reduction:

The optical system is examined at various temperatures under Doppler-broadening effect, but is limited to the condition that the probe field is weak compared to the signal field. The second EIT window promises for more reduction in group velocity. The presence of a nonlinear interaction between the probe and signal fields in optical susceptibility has an impact in enabling temperature-controlled modification of the optical response. At the second window the nonlinear interaction signifies the ability to reduce the narrowing of width as the Doppler width increases and permits observing the second window for low-intensity signal field and leads to a further reduction in the group velocity at the second EIT window.

The signal-field boundary values are identified as $\Omega_{\mathrm{s_l}}$ and $\Omega_{\mathrm{s_h}}$. These two values assist in specifying the regime of the signal-field strength values that could result in slower probe-field group velocity than for the first window. The low-strength regime is the best for realizing low group velocity, but the EIT window could be difficult to resolve. The middle-strength regime is more robust in that the second EIT window is expected to be resolvable and the group velocity is expected to be low. The high-strength regime is less interesting as the group velocity is relatively high.

Chapter 2

Tripod Atom-Field Configuration

2.1 Introduction

In this chapter, we analyze our atom-field system, which is composed of four-level atom driven by three detuned electromagnetic fields. The applied fields couple the four level atoms, such that the atom-field system constructs a $\pitchfork$ configuration. We reprise the Hamiltonian equation for our $\pitchfork$ atom-field system in Sec. 2.2. Then, in Sec. 2.3, we present the dynamic in an open system, where the spontaneous and dephasing are considered by determining the equation of motion of the density-matrix elements. We analyze the population of the $\pitchfork$ atom-field system for various driving-field strengths and different detunings of the probe field, and obtain a general expression for atomic populations in steady state for three cases of probe-field detuning in terms of deriving fields Rabi frequencies in Sec. 2.4. Our investigations of the atomic population behavior are based on the dressed-state analysis and on the numerical calculations of atomic population as a function of time. In Sec. 2.5, we discuss the steady-state solution of the density-matrix element. First, we examine the numerical solution for general applied fields, then derive an analytical solution based on a constant population assumption and constrained by the applied-fields strength values. A brief discussion of the semi-classical dressed picture, which connects the $\pitchfork$ electronic structure to a double-Λ electronic structure, to explain how each signal and probe fields experience DEIT windows are introduced in Sec. 2.5.3. Finally, we summarize our results in Sec. 2.6.

2.2 Atom-Field Hamiltonian

The Hamiltonian system that describes the coupling of four non-degenerate states by three coherent radiation fields shown in Fig. 2.1(a) is

$$\hat{H}(t) = \hat{H}_0 + \hat{H}_{\mathrm{dr}}(t), \tag{2.2.1}$$

where $\hat{H}_0$ is the unperturbed part that represents the free-atom Hamiltonian, and $\hat{H}_{\mathrm{dr}}(t)$ is the part of the Hamiltonian representing the interaction of the atom with the incident fields. States $|1\rangle, |2\rangle, |3\rangle$ and $|4\rangle$ are the eigenstates of the unperturbed part of $\hat{H}(t)$, with eigenvalues $\hbar\omega_1$, $\hbar\omega_2$, $\hbar\omega_3$ and $\hbar\omega_4$ respectively. Using the completeness relation

$$\sum_{\imath} |\imath\rangle\langle\imath| = 1, \tag{2.2.2}$$

$\hat{H}_0$ can be written as

$$\begin{aligned}
\hat{H}_0 =& \sum_{\imath} |\imath\rangle\langle\imath|\hat{H}_0|\imath\rangle\langle\imath| \qquad (2.2.3)\\
=&|1\rangle\langle 1|H_0|1\rangle\langle 1| + |2\rangle\langle 2|H_0|2\rangle\langle 2| + |3\rangle\langle 3|H_0|3\rangle\langle 3| + |4\rangle\langle 4|H_0|4\rangle\langle 4|\\
=&\hbar\omega_1|1\rangle\langle 1| + \hbar\omega_2|2\rangle\langle 2| + \hbar\omega_3|3\rangle\langle 3| + \hbar\omega_4|4\rangle\langle 4|\\
=&\sum_{\imath=1}^{4} \hbar\omega_{\imath}|\imath\rangle\langle\imath|,
\end{aligned}$$

with $\hat{H}_0|\imath\rangle = \hbar\omega_{\imath}|\imath\rangle$.

The part of the Hamiltonian $\hat{H}_{\mathrm{dr}}(t)$ that represents the interaction of the atom with the radiation field $\boldsymbol{E}(z,t)$ polarized in ε-direction perpendicular to the propagation z-direction can be written as

$$\hat{H}_{\mathrm{dr}}(t) = -\boldsymbol{d}\cdot\boldsymbol{E}(z,t), \tag{2.2.4}$$

where $\boldsymbol{d}$ is the dipole moment, and the electric field is represented by

$$\boldsymbol{E}(z,t) = \sum_{l} \boldsymbol{E}_l(z,t) = \sum_{l} \frac{\boldsymbol{\xi}_{f_l}(z,t)e^{\mathrm{i}(\omega_l t + k_l z)} + \boldsymbol{\xi}^*_{f_l}(z,t)e^{-\mathrm{i}(\omega_l t + k_l z)}}{2}, \tag{2.2.5}$$

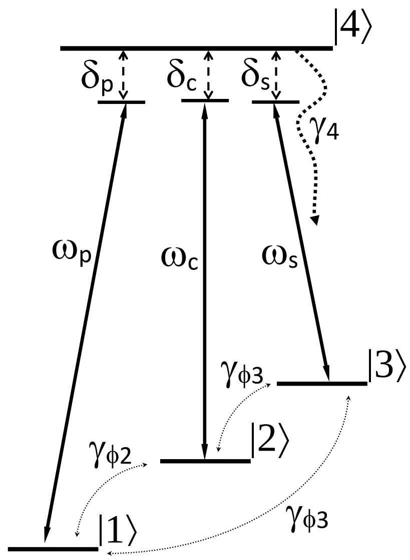

(a)

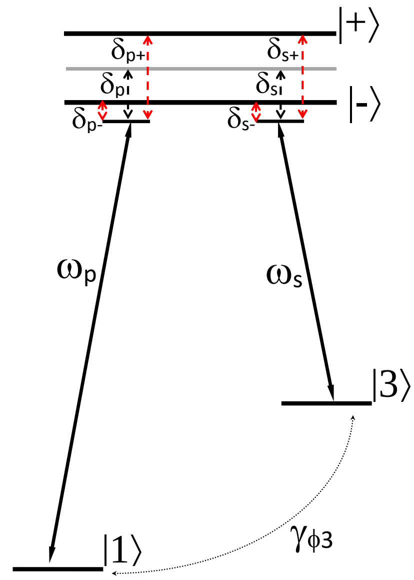

(b)

Figure 2.1: (a) Four-level ⫛-electronic structure with high-energy state $|4\rangle$ and lower-energy levels $|1\rangle$, $|2\rangle$ and $|3\rangle$ in order of increasing energy. Transitions are driven by probe (p), coupling (c) and signal (s) fields, with frequencies ω_{x} and detunings δ_{x} with x$\in \{p, c, s\}$. Decay rates for levels $|i\rangle$ are γ_i for $i \in \{2, 3, 4\}$ and dephasing rates are $\gamma_{\phi i}$ for $i \in \{2, 3\}$. (b) Same atom in the semi-classical dressed state for a strong-c field, which corresponds to a double-Λ level structure. Levels $|2\rangle$ and $|4\rangle$ are hybridized into $|\pm\rangle$.

with $l \in$ {c, p, s} represents the field mode, $\boldsymbol{\xi}_{f_l}(z, t)$ is the slowly modulated amplitude envelope function of the field, and $\boldsymbol{\xi}^*_{f_l}(z, t)$ is its complex conjugate, and k_l is the wave number, defined as $k_l = \frac{2\pi}{\lambda_l}$.

The summation in (2.2.5) considers the positive frequency only. The field modes are: a coupling field of angular frequency ω_{c} interacting with pair of states $|2\rangle \leftrightarrow |4\rangle$, a probe field of angular frequency ω_{p} coupling the transition $|1\rangle \leftrightarrow |4\rangle$, and a signal field of angular frequency ω_{s} coupling the transition $|3\rangle \leftrightarrow |4\rangle$, as shown in Fig. 2.1(a). The terms $e^{\pm \mathrm{i}kz}$

which appear in Eq. (2.2.5) as a Maclaurin series can be written as

$$e^{\pm \mathrm{i}kz} = 1 \pm \mathrm{i}kz - \frac{1}{2}k^2 z^2 \pm \cdots , \tag{2.2.6}$$

where z is on the order of atomic dimension a_0. As $k_l z \approx \frac{a_0}{\lambda_l}$, we can obtain a good approximation for $\boldsymbol{E}(z,t)$ by retaining only the first term (i.e. $e^{\mathrm{i}kz} \approx 1$). This is called the dipole approximation [69], in which an applied field of a wavelength that highly exceeds the size of the atom is treated as spatial independence.

Using the completeness relation (2.2.2), $\hat{H}_{\mathrm{dr}}(t)$ can be written as

$$\begin{aligned}
\hat{H}_{\mathrm{dr}}(t) =& -\left(|1\rangle\langle 1| + |2\rangle\langle 2| + |3\rangle\langle 3| + |4\rangle\langle 4|\right) \boldsymbol{d} \left(|1\rangle\langle 1| + |2\rangle\langle 2| + |3\rangle\langle 3| + |4\rangle\langle 4|\right) \cdot \boldsymbol{E}(z,t) \\
=& -\left(|1\rangle\langle 1|\boldsymbol{d}|4\rangle\langle 4| \cdot \boldsymbol{E}_{\mathrm{p}}(t) + |2\rangle\langle 2|\boldsymbol{d}|4\rangle\langle 4| \cdot \boldsymbol{E}_{\mathrm{c}}(t) + |3\rangle\langle 3|\boldsymbol{d}|4\rangle\langle 4| \cdot \boldsymbol{E}_{\mathrm{s}}(t)\right. \\
&\left. + |4\rangle\langle 4|\boldsymbol{d}|1\rangle\langle 1| \cdot \boldsymbol{E}_{\mathrm{p}}(t) + |4\rangle\langle 4|\boldsymbol{d}|2\rangle\langle 2| \cdot \boldsymbol{E}_{\mathrm{c}}(t) + |4\rangle\langle 4|\boldsymbol{d}|3\rangle\langle 3| \cdot \boldsymbol{E}_{\mathrm{s}}(t)\right).
\end{aligned} \tag{2.2.7}$$

The frequency components of the coupling, probe and signal fields are tuned close to resonance with respect to the one-photon transition. Therefore, the three nearly resonant electric fields are expected to only produce transitions between $|2\rangle \to |4\rangle$, $|1\rangle \to |4\rangle$ and $|3\rangle \to |4\rangle$ respectively. Thus, we can disregard off-resonance terms, and Eq. (2.2.7) is reduced to

$$\begin{aligned}
\hat{H}_{\mathrm{dr}}(t) =& -\left(\boldsymbol{d}_{14} \cdot \hat{\varepsilon}_{\mathrm{p}} \hat{\sigma}_{14} + \boldsymbol{d}_{41} \cdot \hat{\varepsilon}_{\mathrm{p}} \hat{\sigma}_{41}\right) \frac{\xi_{\mathrm{p}_f}(z,t) e^{\mathrm{i}\omega_{\mathrm{p}} t} + \xi^*_{\mathrm{p}_f}(z,t) e^{-\mathrm{i}\omega_{\mathrm{p}} t}}{2} \\
& -\left(\boldsymbol{d}_{24} \cdot \hat{\varepsilon}_{\mathrm{c}} \hat{\sigma}_{24} + \boldsymbol{d}_{42} \cdot \hat{\varepsilon}_{\mathrm{c}} \hat{\sigma}_{42}\right) \frac{\xi_{\mathrm{c}_f}(z,t) e^{\mathrm{i}\omega_{\mathrm{c}} t} + \xi^*_{\mathrm{c}_f}(z,t) e^{-i\omega_{\mathrm{c}} t}}{2}, \\
& -\left(\boldsymbol{d}_{34} \cdot \hat{\varepsilon}_{\mathrm{s}} \hat{\sigma}_{34} + \boldsymbol{d}_{43} \cdot \hat{\varepsilon}_{\mathrm{s}} \sigma_{43}\right) \frac{\xi_{\mathrm{s}_f}(z,t) e^{\mathrm{i}\omega_{\mathrm{s}} t} + \xi^*_{\mathrm{s}_f}(z,t) e^{-i\omega_{\mathrm{s}} t}}{2},
\end{aligned} \tag{2.2.8}$$

where $\hat{\varepsilon}_l$ for $l \in \{c, p, s\}$ are the direction vectors of field of mode l, $\hat{\sigma}_{\imath\jmath} = |\imath\rangle\langle\jmath|$ is the projection operator, and $\boldsymbol{d}_{\imath\jmath} = \boldsymbol{d}^*_{\jmath\imath} = \langle\imath|\boldsymbol{d}|\jmath\rangle$ are the dipole matrix elements of the $|\imath\rangle \leftrightarrow |\jmath\rangle$ transition for $\imath \neq \jmath$. We assume the transitions $|1\rangle \leftrightarrow |2\rangle$, $|1\rangle \leftrightarrow |3\rangle$ and $|2\rangle \leftrightarrow |3\rangle$ are dipole-forbidden. Thus

$$\boldsymbol{d}_{12} = \boldsymbol{d}_{23} = \boldsymbol{d}_{13} = 0. \tag{2.2.9}$$

The terms $\hat{\sigma}_{\imath\jmath} e^{\mathrm{i}\omega_l t}$ for $\imath > \jmath$ and $\hat{\sigma}_{\imath\jmath} e^{-\mathrm{i}\omega_l t}$, where $\imath < \jmath$ varies rapidly, the average over a time larger than $\frac{1}{\omega_{\imath\jmath}}$ is zero. Therefore, these terms can be neglected, which is called the rotating wave approximation. It is a good approximation, and amounts to keeping energy-conservative term (i.e., transition from a low energy state to a higher energy state is combined with the absorption of photons, and transition from a high energy state to a lower energy state is combined with the emission of photons). Then $\hat{H}_{\mathrm{dr}}(t)$ reduces to

$$\begin{aligned}\hat{H}_{\mathrm{dr}}(t) = &-\frac{1}{2}\left(\boldsymbol{d}_{14}\cdot\hat{\varepsilon}_{\mathrm{p}}\xi_{\mathrm{p}_f}(z,t)e^{\mathrm{i}\omega_{\mathrm{p}}t}\hat{\sigma}_{14}+\boldsymbol{d}_{41}\cdot\hat{\varepsilon}_{\mathrm{p}}\xi^*_{\mathrm{p}_f}(z,t)e^{-\mathrm{i}\omega_{\mathrm{p}}t}\hat{\sigma}_{41}\right)\\ &-\frac{1}{2}\left(\boldsymbol{d}_{24}\cdot\hat{\varepsilon}_{\mathrm{c}}\xi_{\mathrm{c}_f}(z,t)e^{\mathrm{i}\omega_{\mathrm{c}}t}\hat{\sigma}_{24}+\boldsymbol{d}_{42}\cdot\hat{\varepsilon}_{\mathrm{c}}\xi^*_{\mathrm{c}_f}(z,t)e^{-\mathrm{i}\omega_{\mathrm{c}}t}\hat{\sigma}_{42}\right)\\ &-\frac{1}{2}\left(\boldsymbol{d}_{34}\cdot\hat{\varepsilon}_{\mathrm{s}}\xi_{\mathrm{s}_f}(z,t)e^{\mathrm{i}\omega_{\mathrm{s}}t}\hat{\sigma}_{34}+\boldsymbol{d}_{43}\cdot\hat{\varepsilon}_{\mathrm{s}}\xi^*_{\mathrm{s}_f}(z,t)e^{-\mathrm{i}\omega_{\mathrm{s}}t}\hat{\sigma}_{43}\right).\end{aligned} \tag{2.2.10}$$

Defining the strength of the resonant interaction between the applied fields and the four-level atom by

$$\begin{aligned}\Omega_{\mathrm{p}}(z,t) &= -\frac{\boldsymbol{d}_{14}\cdot\hat{\varepsilon}_{\mathrm{p}}\xi_{\mathrm{p}_f}(z,t)}{\hbar}, & \Omega^*_{\mathrm{p}}(z,t) &= -\frac{\boldsymbol{d}_{41}\cdot\hat{\varepsilon}_{\mathrm{p}}\xi^*_{\mathrm{p}_f}(z,t)}{\hbar},\\ \Omega_{\mathrm{c}}(z,t) &= -\frac{\boldsymbol{d}_{24}\cdot\hat{\varepsilon}_{\mathrm{c}_f}\xi_{\mathrm{c}}(z,t)}{\hbar}, & \Omega^*_{\mathrm{c}}(z,t) &= -\frac{\boldsymbol{d}_{42}\cdot\hat{\varepsilon}_{\mathrm{c}}\xi^*_{\mathrm{c}_f}(z,t)}{\hbar},\\ \Omega_{\mathrm{s}}(z,t) &= -\frac{\boldsymbol{d}_{34}\cdot\hat{\varepsilon}_{\mathrm{s}}\xi_{\mathrm{s}_f}(z,t)}{\hbar}, & \Omega^*_{\mathrm{s}}(z,t) &= -\frac{\boldsymbol{d}_{43}\cdot\hat{\varepsilon}_{\mathrm{s}}\xi^*_{\mathrm{s}_f}(z,t)}{\hbar},\end{aligned} \tag{2.2.11}$$

which are known as the on-resonance Rabi frequency flopping frequencies or, more often, simply as the Rabi frequencies. Then, we can write Eq. (2.2.10) as

$$\hat{H}_{\mathrm{dr}}(t) = \frac{\hbar}{2}(\Omega_{\mathrm{p}}(z,t)e^{\mathrm{i}\omega_{\mathrm{p}}t}\sigma_{14}+\Omega_{\mathrm{c}}(z,t)e^{\mathrm{i}\omega_{\mathrm{c}}t}\sigma_{24}+\Omega_{\mathrm{s}}(z,t)e^{\mathrm{i}\omega_{\mathrm{s}}t}\sigma_{34}+\mathrm{H.c.}), \tag{2.2.12}$$

and the atom-field Hamiltonian Eq. (2.2.1) as

$$\hat{H}(t) = \sum_{\imath=1}^{4}\hbar\omega_\imath|\imath\rangle\langle\imath| + \frac{\hbar}{2}(\Omega_{\mathrm{p}}(z,t)e^{\mathrm{i}\omega_{\mathrm{p}}t}\sigma_{14}+\Omega_{\mathrm{c}}(z,t)e^{\mathrm{i}\omega_{\mathrm{c}}t}\sigma_{24}+\Omega_{\mathrm{s}}(z,t)e^{\mathrm{i}\omega_{\mathrm{s}}t}\sigma_{34}+\mathrm{H.c.}), \tag{2.2.13}$$

with H.c. denoting the Hermitian conjugate.

2.2.1 Interaction-Picture and Time-Independent Rotating Frame

To study the evolution of a quantum system, we start with the system in a well-defined state at initial time t_0, and trace its evolution up to time t, using the Schrödinger equation [70]

$$\mathrm{i}\hbar\frac{\partial|\psi\rangle}{\partial t} = \hat{H}|\psi\rangle, \tag{2.2.14}$$

following one of three general pictures and many combinations thereof. In every case, we get the same result. Therefore, in order to decide which picture is going to be used, we must define the problem and the output we need. The picture that most easily leads to the required output is the preferable one.

The first is called the Schrödinger picture, which puts all the time dependence in the state vector, and the evolution is determined by integrating the Shrödinger equation (2.2.14) with the state vector, defined by

$$|\psi_{\mathrm{ch}}(t)\rangle = \sum_{n} C_{\imath}(t)\,|\imath\rangle\,, \tag{2.2.15}$$

where the expansion coefficient $C_n(t)$ carries the time dependent of the total Hamiltonian, and is required to calculate the expectation value for any quantum observable .

The second is the Heisenberg picture, which puts all the time dependence in the operators, leaving the state vector stationary in time [70]. The evolution of the system is determined by integrating the equation of motion for the observable operator. This is useful when we want to know a few observables of the system. The Heisenberg picture allows us to focus on these observables and get the required answer without solving the entire problem.

The interaction picture is the third way to trace the evolution of a quantum system. It is an intermediary picture, between the Schrödinger and Heisenberg pictures. It is particularly useful for cases where the Hamiltonian can be written in the form of Eq. (2.2.1); that is, as a sum of two terms, one describing the free part $\hat{H}_0$ which is time independent, and the other describing the interaction part $\hat{H}_{\mathrm{dr}}(t)$ which is time dependent. In the interaction picture, the Hamiltonian is defined as the transformation of the interaction term by the free part of the Hamiltonian. This picture puts only the interaction energy time dependence into the state vector [70]

$$|\psi_{\mathrm{I}}(t)\rangle = \sum_{n} c_{\imath}(t)\,|\imath\rangle\,, \tag{2.2.16}$$

where $c_n(t)$ carries only the time dependent, due the interaction energy.

In the interaction picture, with respect to the free-atom Hamiltonian Eq. (2.2.3), the atom-field system Hamiltonian has the form

$$\hat{V}(t) = \hat{U}^{\dagger}(t)\hat{H}_{\mathrm{dr}}(t)\hat{U}(t), \tag{2.2.17}$$

with $\hat{U}(t)$ as the unitary transformation operator, defined as

$$\begin{aligned}\hat{U}(t) =& e^{\frac{-\mathrm{i}\hat{H}_0 t}{\hbar}} \\ =& \sum_{i=1}^{4} e^{-\mathrm{i}\omega_i t}|i\rangle\langle i|,\end{aligned} \tag{2.2.18}$$

where we use the fact that the eigenstates of H_0 are orthonormal (i.e.; $\langle\imath|\jmath\rangle = 0$ for $\imath \neq \jmath$, and $\langle\imath|\imath\rangle = 1$ to get the second line of (2.2.18). By substituting Eq. (2.2.12) and Eq. (2.2.18) into Eq. 2.2.17 we get

$$\hat{V}(t) = \frac{\hbar}{2}\Big(\Omega_{\mathrm{p}}\mathrm{e}^{-\mathrm{i}\delta_{\mathrm{p}}t}\hat{\sigma}_{14} + \Omega_{\mathrm{c}}\mathrm{e}^{-\mathrm{i}\delta_{\mathrm{c}}t}\hat{\sigma}_{24} + \Omega_{\mathrm{s}}\mathrm{e}^{-\mathrm{i}\delta_{\mathrm{s}}t}\hat{\sigma}_{34} + \mathrm{H.c.}\Big), \tag{2.2.19}$$

with δ_{p} as the detuning of the probe field from $|1\rangle \leftrightarrow |4\rangle$ transition, δ_{c} as the detuning of the coupling field from $|2\rangle \leftrightarrow |4\rangle$ transition, and δ_{s} as the detuning of the signal field from $|3\rangle \leftrightarrow |4\rangle$ transition, mathematically represented by:

$$\delta_{\mathrm{p}} :=\omega_{41} - \omega_{\mathrm{p}}, \tag{2.2.20}$$

$$\delta_{\mathrm{c}} :=\omega_{42} - \omega_{\mathrm{c}}, \tag{2.2.21}$$

$$\delta_{\mathrm{s}} :=\omega_{43} - \omega_{\mathrm{s}}, \tag{2.2.22}$$

respectively.

The atom-field system Hamiltonian described by Eq. (2.2.19) involves terms oscillating at different optical frequencies. Thus, our next step is to find a Hermitian operator to transform the Hamiltonian to a rotating frame, in order to eliminate the time dependence [71]. The transformation we apply is constructed to remove all time dependence from the interaction Hamiltonian. This new basis is known as the rotating-frame basis, and is related to the old basis by

$$|\psi'\rangle = \hat{U}'(t)|\psi\rangle, \tag{2.2.23}$$

with $\hat{U}'(t)$ given by

$$\hat{U}'(t) = e^{\frac{-\mathrm{i}\hat{A}t}{\hbar}}, \tag{2.2.24}$$

where A is a self-adjoint operator. The corresponding transformed Hamiltonian $\hat{H}'$ for the transformed wavefunction $|\psi'\rangle$ can be found using the following steps.

We Start from the fact that our transformed basis evolves according to the Schrödinger picture,

$$\mathrm{i}\hbar\frac{\partial|\psi'\rangle}{\partial t} = \hat{H}'|\psi'\rangle. \tag{2.2.25}$$

Substituting Eq. (2.2.23) into (2.2.25), we get

$$\begin{aligned} \mathrm{i}\hbar\frac{\partial(\hat{U}'(t)|\psi\rangle)}{\partial t} &= \hat{H}'|\psi'\rangle, \\ \mathrm{i}\hbar\left(\hat{U}'(t)\frac{\partial|\psi\rangle}{\partial t} + \frac{\partial\hat{U}'(t)}{\partial t}|\psi\rangle\right) &= \hat{H}'|\psi'\rangle. \end{aligned} \tag{2.2.26}$$

By substituting Eq. (2.2.24) into (2.2.26), and using

$$\mathrm{i}\hbar\frac{\partial|\psi\rangle}{\partial t} = \hat{V}|\psi\rangle, \tag{2.2.27}$$

the following is obtained:

$$\begin{aligned} &\hat{U}'(t)\hat{V}(t)|\psi\rangle + \hat{A}\hat{U}'|\psi\rangle = \hat{H}'|\psi'\rangle, \\ &\hat{U}'(t)\hat{V}(t)\hat{U}'^{\dagger}(t)\hat{U}'(t)|\psi\rangle + \hat{A}\hat{U}'\hat{U}'^{\dagger}(t)\hat{U}'(t)|\psi\rangle = \hat{H}'|\psi'\rangle, \\ &\hat{U}'(t)\hat{V}(t)\hat{U}'^{\dagger}(t)|\psi'\rangle + \hat{A}|\psi'\rangle = \hat{H}'|\psi'\rangle, \end{aligned} \tag{2.2.28}$$

where $\hat{U}'^{\dagger}(t)\hat{U}'(t) = 1$ is used to get the last line in (2.2.28). This step gives us the transformed Hamiltonian $\hat{H}'$

$$\hat{H}' = \hat{U}'(t)\hat{V}(t)\hat{U}'^{\dagger}(t) + \hat{A}. \tag{2.2.29}$$

In the case of our atom-field system, the operator $\hat{A}$ used to eliminate the time dependence is defined by

$$\hat{A} = 3\delta_{\mathrm{p}}\sigma_{11} + (2\delta_{\mathrm{p}} + \delta_{\mathrm{c}})\sigma_{22} + (2\delta_{\mathrm{p}} + \delta_{\mathrm{s}})\sigma_{33} + 2\delta_{\mathrm{p}}\sigma_{44}, \tag{2.2.30}$$

and the unitary transformation operator is defined by

$$\hat{U}'(t) = e^{\frac{-3i\delta_{\mathrm{p}}t}{\hbar}}\sigma_{11} + e^{\frac{-i(2\delta_{\mathrm{p}}+\delta_{\mathrm{c}})t}{\hbar}}\sigma_{22} + e^{\frac{-i(2\delta_{\mathrm{p}}+\delta_{\mathrm{s}})t}{\hbar}}\sigma_{33} + e^{\frac{-2i\delta_{\mathrm{p}}t}{\hbar}}\sigma_{44}. \tag{2.2.31}$$

The resulting Hamiltonian after transformation is given by [72]

$$\hat{H}' = \hat{H}'_0 + \frac{\hbar}{2}\Big(\Omega_{\mathrm{p}}\hat{\sigma}_{14} + \Omega_{\mathrm{c}}\hat{\sigma}_{24} + \Omega_{\mathrm{s}}\hat{\sigma}_{34} + \mathrm{H.c.}\Big), \tag{2.2.32}$$

for

$$\hat{H}'_0 := \delta_{\mathrm{pc}}\hat{\sigma}_{22} + \delta_{\mathrm{ps}}\hat{\sigma}_{33} + \delta_{\mathrm{p}}\hat{\sigma}_{44}, \tag{2.2.33}$$

and

$$\delta_{\mathrm{xy}} := \delta_{\mathrm{x}} - \delta_{\mathrm{y}}. \tag{2.2.34}$$

We added $3\delta_{\mathrm{p}}(\sigma_{11} + \sigma_{22} + \sigma_{33} + \sigma_{44})$ to the transformed Hamiltonian $\hat{H}'$, which shifts the eigenvalue by $3\delta_{\mathrm{p}}$. This has no physical effect, as the physically relevant terms are the differences between energy levels. This form of Hamiltonian is the same as the one determined by [57].

2.3 Open-System Dynamics and Density-Matrix Elements

All the information about any quantum system can be extracted from the state vector $|\Psi\rangle$ by calculating the expectation value $\boldsymbol{O}$

$$\langle\boldsymbol{O}\rangle = \langle\Psi|\boldsymbol{O}|\Psi\rangle. \tag{2.3.1}$$

In some cases we may not know the state of the system $|\Psi\rangle$, but know the probability $\mathscr{P}_\Psi$ of the system being in the state $|\Psi\rangle$. In these cases, we need to take in addition to the quantum mechanical average, the ensemble average over many identical systems that have been similarly prepared. So, instead of Eq. (2.3.1) we now have[73]

$$\langle\langle\boldsymbol{O}\rangle\rangle_{\mathrm{ensemble}} = \sum_{\Psi}\mathscr{P}_\Psi\langle\Psi|\boldsymbol{O}\,|\Psi\rangle \tag{2.3.2}$$

which can be written as

$$
\begin{aligned}
\langle\langle \boldsymbol{O} \rangle\rangle_{\text{ensemble}} &= \sum_{\phi}\sum_{\Psi} \mathscr{P}_{\Psi} \langle \Psi | \boldsymbol{O} \, |\phi\rangle \, \langle \phi \, |\Psi\rangle \\
&= \sum_{\phi}\sum_{\Psi} \mathscr{P}_{\Psi} \langle \phi \, |\Psi\rangle \, \langle \Psi | \boldsymbol{O} \, |\phi\rangle \\
&= \sum_{\phi} \langle \phi | \rho \boldsymbol{O} \, |\phi\rangle \\
&= \mathrm{Tr}(\boldsymbol{O}\rho),
\end{aligned} \tag{2.3.3}
$$

where (2.2.2) is used in the second line of (2.3.2), and the density operator ρ is defined by

$$
\rho = \sum_{\Psi} \mathscr{P}_{\Psi} \, |\Psi\rangle \, \langle \Psi|. \tag{2.3.4}
$$

Thus, to extract any information about a system in which we do not know $|\Psi\rangle$, the density operator gives a more general description than can be provided by the state vector. It contains all possible information about the system, and any physical system can be described by ρ. It is also useful to apply the density operator to describe quantum systems with various types of damping that cannot be directly incorporated into the equation of motion for the probability amplitude.

In the presence of damping, the atomic dynamics and state time evolution described by the density operator are governed by a master equation for the atomic density operator. The resulting Lindblad master equation is [72]

$$
\begin{aligned}
\dot{\varrho} = &-\frac{\mathrm{i}}{\hbar}[\varrho, \hat{H}'] + \sum_{\imath<\jmath}^{4} \frac{\gamma_{\jmath\imath}}{2}(\sigma_{\imath\jmath}\varrho\sigma_{\jmath\imath} - \sigma_{\jmath\jmath}\varrho - \varrho\sigma_{\jmath\jmath}) \\
&+ \sum_{\jmath=2}^{4} \frac{\gamma_{\phi j}}{2}(\sigma_{\jmath\jmath}\varrho\sigma_{\jmath\jmath} - \sigma_{\jmath\jmath}\varrho - \varrho\sigma_{\jmath\jmath}),
\end{aligned} \tag{2.3.5}
$$

with ϱ the density matrix in the rotated frame. The Lindblad master equation includes both spontaneous emissions and dephasing, where $\gamma_{\jmath\imath}$ is the decay rate of state $|\jmath\rangle \to |\imath\rangle$, and $\gamma_{\phi\imath}$ is the dephasing of state $|\imath\rangle$. By substituting Eq. (2.2.32) into Eq. (2.3.5) we get ten optical Bloch equations. Six more optical Bloch equations are obtained from complex conjugates of the six off-diagonal density matrix expressions shown below:

$$
\begin{aligned}
\dot{\varrho}_{12}(t) &= \left(-\frac{1}{2}\gamma_2 + \mathrm{i}\delta_{\mathrm{pc}}\right)\varrho_{12}(t) - \frac{\mathrm{i}}{2}\left[-\Omega_{\mathrm{c}}^{*}\varrho_{14}(t) + \Omega_{\mathrm{p}}\varrho_{24}(t)\right],\\
\dot{\varrho}_{13}(t) &= \left(-\frac{1}{2}\gamma_3 + \mathrm{i}\delta_{\mathrm{ps}}\right)\varrho_{13}(t) - \frac{\mathrm{i}}{2}\left[-\Omega_{\mathrm{s}}^{*}\varrho_{14}(t) + \Omega_{\mathrm{p}}\varrho_{43}(t)\right],\\
\dot{\varrho}_{14}(t) &= \left(-\frac{1}{2}\gamma_4 + \mathrm{i}\delta_{\mathrm{p}}\right)\varrho_{14}(t) + \frac{\mathrm{i}}{2}\left[\Omega_{\mathrm{c}}\varrho_{12} + \Omega_{\mathrm{s}}\varrho_{13} + \Omega_{\mathrm{p}}\left(\varrho_{11}(t) - \varrho_{44}(t)\right)\right],\\
\dot{\varrho}_{23}(t) &= \left(-\frac{1}{2}\Gamma_{32} - \mathrm{i}\delta_{\mathrm{sc}}\right)\varrho_{23}(t) - \frac{\mathrm{i}}{2}\left[\Omega_{\mathrm{c}}\varrho_{43}(t) - \Omega_{\mathrm{s}}^{*}\varrho_{24}(t)\right],\\
\dot{\varrho}_{24}(t) &= \left(-\frac{1}{2}\Gamma_{42} + \mathrm{i}\delta_{\mathrm{c}}\right)\varrho_{24}(t) - \frac{\mathrm{i}}{2}\left[-\Omega_{\mathrm{p}}\varrho_{21}(t) + \Omega_{\mathrm{c}}\left(\varrho_{44}(t) - \varrho_{22}(t)\right) - \Omega_{\mathrm{s}}\varrho_{23}\right],\\
\dot{\varrho}_{43}(t) &= \left(-\frac{1}{2}\Gamma_{43} - \mathrm{i}\delta_{\mathrm{s}}\right)\varrho_{43}(t) + \frac{\mathrm{i}}{2}\left[-\Omega_{\mathrm{c}}^{*}\varrho_{23}(t) + \Omega_{\mathrm{s}}^{*}(\varrho_{44}(t) - \varrho_{33}(t)) - \Omega_{\mathrm{p}}^{*}\varrho_{13}(t)\right],
\end{aligned}
\tag{2.3.6}
$$

and four equations represent the equations of motion for the population:

$$
\begin{aligned}
\dot{\varrho}_{11}(t) =&\gamma_{21}\varrho_{22}(t) + \gamma_{31}\varrho_{33}(t) + \gamma_{41}\varrho_{44}(t) - \frac{\mathrm{i}}{2}\left[\Omega_{\mathrm{p}}\varrho_{41}(t) - \Omega_{\mathrm{p}}^{*}\varrho_{14}(t)\right],\\
\dot{\varrho}_{22}(t) =&-\gamma_{21}\varrho_{22}(t) + \gamma_{32}\varrho_{33}(t) + \gamma_{42}\varrho_{44}(t) - \frac{\mathrm{i}}{2}\left[-\Omega_{\mathrm{c}}^{*}\varrho_{24}(t) + \Omega_{\mathrm{c}}\varrho_{42}(t)\right],\\
\dot{\varrho}_{33}(t) =&-\gamma_{31}\varrho_{33}(t) - \gamma_{32}\varrho_{33}(t) + \gamma_{43}\varrho_{44}(t) - \frac{\mathrm{i}}{2}\left[-\Omega_{\mathrm{s}}^{*}\varrho_{34}(t) + \Omega_{\mathrm{s}}\varrho_{43}(t)\right],\\
\dot{\varrho}_{44}(t) =&-\gamma_{4}\varrho_{44}(t) - \frac{\mathrm{i}}{2}[\Omega_{\mathrm{c}}\varrho_{24}(t) - \Omega_{\mathrm{c}}^{*}\varrho_{42}(t) + \Omega_{\mathrm{s}}\varrho_{34}(t) - \Omega_{\mathrm{s}}^{*}\varrho_{43}(t) + \Omega_{\mathrm{p}}\varrho_{14}(t) - \Omega_{\mathrm{p}}^{*}\varrho_{41}(t)].
\end{aligned}
\tag{2.3.7}
$$

The decay rates in Eqs. (2.3.6) and (2.3.7) are

$$
\gamma_{\jmath} := \sum_{\imath<\jmath}(\gamma_{\jmath\imath} + \gamma_{\phi\jmath}).
\tag{2.3.8}
$$

As the dephasing rate between the forbidden transitions is not zero, $\gamma_2 = \gamma_{\phi 2}$ and $\gamma_3 = \gamma_{\phi 3}$. We now have the requisite equations of motion for the density-matrix elements to solve the dynamics.

The diagonal elements represent the probability of atoms being in base state $|\imath\rangle$, for a quantum system in a mixture or pure vector state. For this reason, $\varrho_{\imath\imath}$ is called the population of the state $|\imath\rangle$. The off-diagonal elements express the interference between states $|\imath\rangle$ and $|\jmath\rangle$ when the state $|\psi'\rangle$ is in coherent linear superposition of these states. See Appendix B for details about the meaning of the diagonal and off-diagonal elements of the density matrix.

To summarize, we derived the equations of motion of the density-matrix elements for the $\pitchfork$ atom-field system in the presence of decaying and dephasing. We reviewed several fundamental points that will help us study, understand and interpret the optical properties of the $\pitchfork$ atom-field system. The density operator contains all possible information about the quantum system, and provides a more general description than the state vector. The diagonal elements of the density matrix describe the population of the quantum state, while the off-diagonal elements describe the coherence and are used to calculate the induced polarization of an applied field.

2.4 Dressed-State Analysis and Atomic Population

In this section, we use the diagonal elements of the density matrix obtained in the previous section 2.3 to study the population of each atomic state. However, general analytical expression of the atomic population using Eqs. (2.3.6) and (2.3.7) is not feasible, due to the difficulty of decoupling the equations of motion of coherence from those of the population. Therefore, we analyze the dynamics of the atomic population using the interpretation from the dressed-state analysis and the numerical calculation of the atomic population described by the diagonal elements of the density matrix.

General expressions for the eigenstates of the Hamiltonian Eq. (2.2.32) are complex. To simplify, we choose to find the eigenstates for the three following tractable cases:

2.4.1 Probe-Field Detuning Equal to the Coupling-Field Detuning

The first case is $\delta_{\mathrm{pc}} = 0$, or, equivalently, $\delta_{\mathrm{p}} = \delta_{\mathrm{c}}$. We allow δ_{s} to assume any different value. In this case, one of the eigenvalues $\mathit{\Lambda}_1 = 0$ corresponds to eigenstate

$$|\psi_{\mathrm{D}}\rangle = -\frac{\Omega_{\mathrm{c}}^*}{\sqrt{|\Omega_{\mathrm{c}}|^2 + |\Omega_{\mathrm{p}}|^2}}\,|1\rangle + \frac{\Omega_{\mathrm{p}}^*}{\sqrt{|\Omega_{\mathrm{c}}|^2 + |\Omega_{\mathrm{p}}|^2}}\,|2\rangle\,. \tag{2.4.1}$$

This eigenstate is a dark state, as it does not contain a contribution from state $|4\rangle$ and is not coupled to state $|4\rangle$. This is evident from studying the total dipole moment $\boldsymbol{d}_{4\mathrm{D}}$

for a transition from state $|\psi_{\mathrm{D}}\rangle$ to the bare state $|4\rangle$. If the magnitudes of the coupling field and probe field are appropriately balanced, the negative sign in the superposition of $|1\rangle$ and $|2\rangle$ (2.4.1), which form the state $|\psi_{\mathrm{D}}\rangle$, cause the transition moment $\langle\psi_{\mathrm{D}}|\boldsymbol{d}_{4\mathrm{D}}|4\rangle$ to vanish. If the atoms are formed in this state, there is no possibility of excitation to $|4\rangle$, hence no absorption.

For the case of the coupling field being much stronger than the probe field, ($\Omega_{\mathrm{c}} \gg \Omega_{\mathrm{p}}$), state $|1\rangle$ is almost equivalent to $|\psi_{\mathrm{D}}\rangle$. Thus, atoms decaying to state $|1\rangle$ are trapped in this state, and remain so throughout the interaction. The atomic probability of being in state $|1\rangle$ is

$$\mathscr{P}_1 = |\langle 1\,|\psi_{\mathrm{D}}\rangle|^2 = \frac{|\Omega_{\mathrm{c}}|^2}{|\Omega_{\mathrm{c}}|^2 + |\Omega_{\mathrm{p}}|^2}, \tag{2.4.2}$$

and being in state $|2\rangle$ is

$$\mathscr{P}_2 = |\langle 2\,|\psi_{\mathrm{D}}\rangle|^2 = \frac{|\Omega_{\mathrm{p}}|^2}{|\Omega_{\mathrm{c}}|^2 + |\Omega_{\mathrm{p}}|^2}. \tag{2.4.3}$$

We numerically solve the master equation and plot atomic populations in Fig. 2.2. After a time of order of the radiative lifetime, the atoms should be trapped in the dark state $|\psi_{\mathrm{D}}\rangle$, which we verify by comparing the populations in Fig. 2.2 with the calculated dark-state populations. The disappearance of the probe-field absorption $\mathrm{Im}\varrho_{14}$ supports the claim that the atom has decayed into a dark state. Furthermore, state $|4\rangle$ does not become populated.

For Fig. 2.2(a) the dark state is equivalent to state $|1\rangle$, whereas, for Fig. 2.2(b) it is a superposition of states $|1\rangle$ and $|2\rangle$. The atoms are pumped into the state by the combined actions of the coupling, signal and the probe fields, and spontaneous emissions. At steady state, the distribution of atoms largely depends on the magnitude of the driving fields, following the rule of Eqs. (2.4.2) and (2.4.3).

The other three eigenstates are

$$|\psi_\imath\rangle = \frac{\Omega_{\mathrm{p}}\,|1\rangle + \Omega_{\mathrm{c}}\,|2\rangle + \frac{\Lambda_\imath\Omega_{\mathrm{s}}}{\Lambda_\imath - \delta_{\mathrm{ps}}}\,|3\rangle + 2\Lambda_\imath|4\rangle}{\sqrt{|\Omega_{\mathrm{p}}|^2 + |\Omega_{\mathrm{c}}|^2 + \frac{|\Omega_{\mathrm{s}}|^2|\Lambda_\imath|^2}{|\Lambda_\imath - \delta_{\mathrm{ps}}|^2} + 4|\Lambda_\imath|^2}}, \tag{2.4.4}$$

with eigenvalues $\Lambda_\imath$ ($\imath \in 2,3,4$), where each $\{\Lambda_\imath\}$ is a root of the eigenvalue equation.

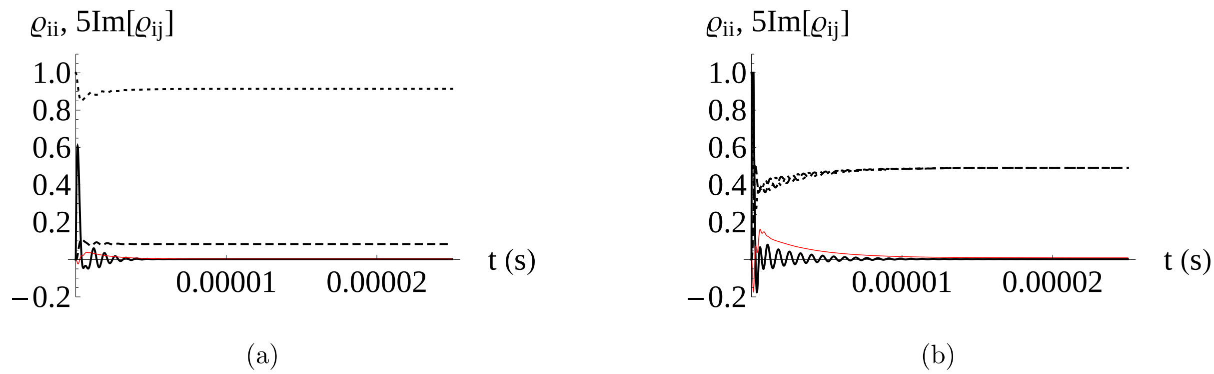

Figure 2.2: The populations of state $|1\rangle$ and $|2\rangle$ are represented by ϱ_{11} (dotted line) and ϱ_{22} (dashed line) respectively as a function of time t, and the absorption of the probe and signal fields, represented by 5Im$[\varrho_{ij}]$(black-solid line) and (red-solid line) respectively, evaluated numerically by solving the master equation. (a) Coupling field is stronger than the probe field with $\Omega_{\rm c} = \gamma_4$ and $\Omega_{\rm p} = 0.3\gamma_4$. (b) Coupling and probe fields have the same strength with $\Omega_{\rm c} = \Omega_{\rm p} = \gamma_4$. The system is initially prepared with $\varrho_{11}^{(0)} = 1$ and $\varrho_{22}^{(0)} = \varrho_{33}^{(0)} = \varrho_{44}^{(0)} = 0$. The chosen parameters are $\gamma_4 = 18$ MHz, $\gamma_3 = 10$ kHz, $\gamma_2 = 40$ kHz, $\Omega_{\rm s} = 0.3\gamma_4$, $\delta_{\rm s} = 0.5\Omega_{\rm c}$ and $\delta_{\rm p} = \delta_{\rm c} = 0$.

$$
\begin{aligned}
4\Lambda^3 - 4\Lambda^2(\delta_{\rm ps} + \delta_{\rm p}) + \Lambda(4\delta_{\rm ps}\delta_{\rm p} - |\Omega_{\rm c}|^2 - |\Omega_{\rm p}|^2 - |\Omega_{\rm s}|^2) \\
+ \delta_{\rm ps}(|\Omega_{\rm c}|^2 + |\Omega_{\rm p}|^2) = 0.
\end{aligned}
\tag{2.4.5}
$$

Although the atoms are not prepared in the dark state, detuning plays an important role in their distribution. Thus, when $\delta_{\rm pc} = 0$, and after a period of the same order as atom relaxation time, the atoms are trapped in the dark state, and their distribution in the bare state $|1\rangle$ and $|2\rangle$ depends on the magnitude of $\Omega_{\rm c}$ and $\Omega_{\rm p}$.

2.4.2 Probe-Field Detuning Equal to the Signal-Field Detuning

We now study the case in which the probe and signal fields are at two-photon resonance with a $|1\rangle \leftrightarrow |3\rangle$ transition (i.e. $\delta_{\rm ps} = 0$). We allow the coupling-field detuning $\delta_{\rm c}$ to assume any value. In this case the Hamiltonian (2.2.32) has an eigenvalue $\varLambda' = 0$ with eigenstate

$$|\psi'_{\rm D}\rangle = \frac{-\Omega_{\rm s}^*}{\sqrt{|\Omega_{\rm s}|^2 + |\Omega_{\rm p}|^2}}\,|1\rangle + \frac{\Omega_{\rm p}^*}{\sqrt{|\Omega_{\rm s}|^2 + |\Omega_{\rm p}|^2}}\,|3\rangle\,, \tag{2.4.6}$$

and eignvalues $\varLambda'_\imath$ ($\imath \in 1,2,3$) with eigenstates

$$|\psi'_\imath\rangle = \frac{\Omega_{\rm p}\,|1\rangle + \frac{\varLambda'_\imath\Omega_{\rm c}}{\varLambda'_\imath-\delta_{\rm pc}}\,|2\rangle + \Omega_{\rm s}\,|3\rangle + 2\varLambda'_\imath|4\rangle}{\sqrt{\frac{|\Omega_{\rm c}|^2\varLambda'^2_\imath}{(\varLambda'_\imath-\delta_{\rm pc})^2} + |\Omega_{\rm p}|^2 + |\Omega_{\rm s}|^2 + 4\varLambda'^2_\imath}}, \tag{2.4.7}$$

where each $\varLambda'_\imath$ is a root of the eigenvalue equation

$$\begin{aligned} 4\varLambda'^3 - &4\varLambda'^2(\delta_{\rm pc}+\delta_{\rm p}) + \varLambda'(4\delta_{\rm pc}\delta_{\rm p} - |\Omega_{\rm c}|^2 - |\Omega_{\rm p}|^2 - |\Omega_{\rm s}|^2) \\ &+ \delta_{\rm pc}(|\Omega_{\rm s}|^2 + |\Omega_{\rm p}|^2) = 0. \end{aligned} \tag{2.4.8}$$

The eigenstate $|\psi'_{\rm D}\rangle$ is also a dark state, as it does not contain a contribution from state $|4\rangle$ and is not coupled to state $|4\rangle$.

Atomic populations for states $|1\rangle$ and $|3\rangle$ are calculated numerically, and shown in Fig. 2.3. At steady state, the atoms are trapped in the dark state $|\psi'_{\rm D}\rangle$ as long as the coupling field is greater than or equal to the probe and the signal fields. We claim that the atom is trapped in the dark state, because if it were in one of the bright states of Eq. (2.4.7), the following phenomena would arise.

(i) We would expect to see some population in states $|2\rangle$ and $|4\rangle$, whereas in Figs. 2.3(a) and (b), the populations of states $|1\rangle$ and $|3\rangle$ total almost one, making the combined population of states $|2\rangle$ and $|4\rangle$ nearly zero.

(ii) For the case that $\Omega_{\rm c} \gg \Omega_{\rm s} > \Omega_{\rm p}$, as shown in Fig. 2.3(c), if the system is in a bright state the population in state $|3\rangle$ will exceed the population in state $|1\rangle$ (i.e. $\varrho_{33} > \varrho_{11}$). However, the opposite is true; most of the population has been transferred to $|1\rangle$.

(iii) the absorption would not disappear for a bright state, but in Figs. 2.3(a),(b),(c) absorption vanishes; hence the atoms are trapped in the dark state $|\psi'_{\rm D}\rangle$.

At steady state, the populations in $|1\rangle$ and $|3\rangle$ are governed by the signal and probe-field Rabi frequencies, according to

$$\mathscr{P}_1' = |\langle 1|\psi_{\mathrm{D}}'\rangle|^2 = \frac{|\Omega_{\mathrm{s}}|^2}{|\Omega_{\mathrm{s}}|^2 + |\Omega_{\mathrm{p}}|^2}, \tag{2.4.9}$$

and

$$\mathscr{P}_3' = |\langle 3|\psi_{\mathrm{D}}'\rangle|^2 = \frac{|\Omega_{\mathrm{p}}|^2}{|\Omega_{\mathrm{s}}|^2 + |\Omega_{\mathrm{p}}|^2}, \tag{2.4.10}$$

respectively.

2.4.3 The Three Fields of Equal Detuning

The last case pertains to the three detunings that are equal [57], ($\delta_{\mathrm{p}} = \delta_{\mathrm{c}} = \delta_{\mathrm{s}}$), which results in zero two-photon resonance. Two of the eigenstates are degenerate eigenstates, with eigenvalues $\tilde{\Lambda}_1 = \tilde{\Lambda}_2 = 0$:

$$\begin{aligned}
|\tilde{\psi}_{\mathrm{D1}}\rangle =& \frac{-\Omega_{\mathrm{s}}^*}{\sqrt{|\Omega_{\mathrm{s}}|^2 + |\Omega_{\mathrm{p}}|^2}} |1\rangle + \frac{\Omega_{\mathrm{p}}^*}{\sqrt{|\Omega_{\mathrm{s}}|^2 + |\Omega_{\mathrm{p}}|^2}} |3\rangle , \\
|\tilde{\psi}_{\mathrm{D2}}\rangle =& \frac{\Omega_{\mathrm{c}}\Omega_{\mathrm{p}} |1\rangle - (\Omega_p^2 + \Omega_s^2) |2\rangle + \Omega_{\mathrm{c}}\Omega_{\mathrm{s}} |3\rangle}{\sqrt{\left(|\Omega_{\mathrm{c}}|^2 + |\Omega_{\mathrm{p}}|^2 + |\Omega_{\mathrm{s}}|^2\right)\left(|\Omega_{\mathrm{p}}|^2 + |\Omega_{\mathrm{s}}|^2\right)}}.
\end{aligned} \tag{2.4.11}$$

These two states are dark, as neither contains contribution from state $|4\rangle$, or involves transitions to state $|4\rangle$. However, the remaining eigenstates retain a component of all the bare atomic states:

$$|\tilde{\psi}^{\pm}\rangle = \frac{\Omega_{\mathrm{p}} |1\rangle + \Omega_{\mathrm{c}} |2\rangle + \Omega_{\mathrm{s}} |3\rangle \pm 2\tilde{\Lambda}^{\pm}|4\rangle}{\sqrt{|\Omega_{\mathrm{c}}|^2 + |\Omega_{\mathrm{p}}|^2 + |\Omega_{\mathrm{s}}|^2 + 4(\tilde{\Lambda}^{\pm})^2}}, \tag{2.4.12}$$

with

$$\tilde{\Lambda}^{\pm} = \frac{1}{2}\left(\delta_{\mathrm{p}} \pm \sqrt{\delta_{\mathrm{p}}^2 + \Omega_{\mathrm{p}}^2 + \Omega_{\mathrm{c}}^2 + \Omega_{\mathrm{s}}^2}\right), \tag{2.4.13}$$

the corresponding eigenvalues.

The steady-state atomic populations for the case

$$\delta_{\mathrm{p}} = \delta_{\mathrm{s}} = \delta_{\mathrm{c}} = 0, \tag{2.4.14}$$

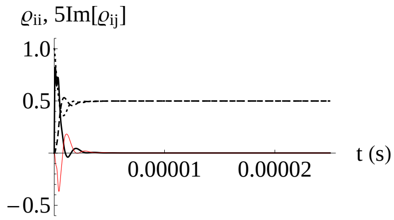

(a)

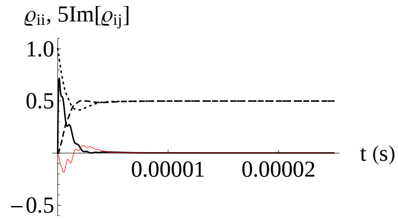

(b)

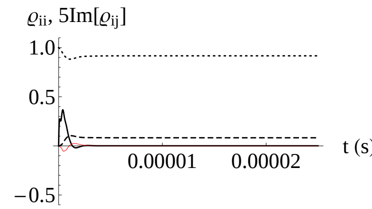

(c)

Figure 2.3: Populations of level $|1\rangle$ and $|3\rangle$ are represented by ϱ_{11} (dotted line) and ϱ_{33} (dashed line) respectively, as a function of time t. The absorption of the probe and signal fields, represented by $5\text{Im}[\varrho_{ij}]$ (black-solid line) and (red-solid line) respectively, is evaluated numerically by solving the master equation. (a) Signal and probe-field strengths are of equal magnitude less than coupling field, with $\Omega_\text{s} = \Omega_\text{p} = 0.5\gamma_4$, while $\Omega_\text{c} = \gamma_4$. (b) Coupling, signal and probe-field strengths are of equal magnitude $\Omega_\text{c} = \Omega_\text{s} = \Omega_\text{p} = 0.35\gamma_4$. (c) Signal-field strength is stronger than the probe field, with $\Omega_\text{c} = \gamma_4$, $\Omega_\text{s} = 0.5\gamma_4$, and $\Omega_\text{p} = 0.15\gamma_4$. Other parameters are $\gamma_4 = 18$ MHz, $\gamma_3 = 10$ kHz, $\gamma_2 = 40\,\text{kHz}$, $\delta_\text{s} = \delta_\text{p} = 0.5\Omega_\text{c}$, and $\delta_\text{c} = 0$. Initial populations are $\varrho_{11}^{(0)} = 1$ and $\varrho_{22}^{(0)} = \varrho_{33}^{(0)} = \varrho_{44}^{(0)} = 0$.

are shown Fig. 2.4. In all cases, the atomic population is distributed between state $|1\rangle$, $|2\rangle$ and $|3\rangle$, and excludes $|4\rangle$. This exclusion suggests that, for cases (a), (b) and (c), atoms are trapped in the dark state $|\tilde{\psi}_\text{D2}\rangle$, but we now see that this could be true for case (a) but not for cases (b) and (c).

In Fig. 2.4(b), we have $\Omega_\text{p}, \Omega_\text{c} \gg \Omega_\text{s}$, which means that if the system is in dark state $|\tilde{\psi}_\text{D2}\rangle$ the population in $|1\rangle$ must be higher. However, we actually found that the population of state $|3\rangle$ was higher, and it exhibited the opposite behavior to that shown in Fig. 2.4(c). Thus, the system corresponding to Figs. 2.4(b) and 2.4(c) could be trapped in $|\tilde{\psi}_\text{D1}\rangle$. However, the low population in state $|2\rangle$ prevents us from coming to this conclusion as well. From this argument, we concluded that the system is not in a pure dark state, but relaxes into a mixture of two dark states (2.4.11), which is also a dark state given by

$$\tilde{\varrho}_\text{D} = \mathscr{P}_\text{D1} |\tilde{\psi}_\text{D1}\rangle \langle\tilde{\psi}_\text{D1}| + \mathscr{P}_\text{D2} |\tilde{\psi}_\text{D2}\rangle \langle\tilde{\psi}_\text{D2}| \,, \tag{2.4.15}$$

where $\mathscr{P}_{\mathrm{D1}}$ is the probability of being in state $|\tilde{\psi}_{\mathrm{D1}}\rangle$ and $\mathscr{P}_{\mathrm{D2}}$ is the probability of being in state $|\tilde{\psi}_{\mathrm{D2}}\rangle$, such that

$$\mathscr{P}_{\mathrm{D1}} + \mathscr{P}_{\mathrm{D2}} = 1. \tag{2.4.16}$$

The probability for state $|1\rangle$ being populated is

$$\begin{aligned}\tilde{\mathscr{P}}_1 &= \langle 1\,|\tilde{\varrho}_{\mathrm{D}}|\,1\rangle \\ &= \frac{1}{|\Omega_{\mathrm{p}}|^2 + |\Omega_{\mathrm{s}}|^2}\left(\mathscr{P}_{\mathrm{D1}}\,|\Omega_{\mathrm{s}}|^2 + \frac{\mathscr{P}_{\mathrm{D2}}\,|\Omega_{\mathrm{p}}|^2\,|\Omega_{\mathrm{c}}|^2}{|\Omega_{\mathrm{c}}|^2 + |\Omega_{\mathrm{p}}|^2 + |\Omega_{\mathrm{s}}|^2}\right),\end{aligned} \tag{2.4.17}$$

for state $|2\rangle$ being populated is

$$\begin{aligned}\tilde{\mathscr{P}}_2 &= \langle 2\,|\tilde{\varrho}_{\mathrm{D}}|\,2\rangle \\ &= \frac{\mathscr{P}_{\mathrm{D2}}\left|\Omega_{\mathrm{p}}^2 + \Omega_{\mathrm{s}}^2\right|^2}{\left(|\Omega_{\mathrm{c}}|^2 + |\Omega_{\mathrm{p}}|^2 + |\Omega_{\mathrm{s}}|^2\right)\left(|\Omega_{\mathrm{p}}|^2 + |\Omega_{\mathrm{s}}|^2\right)},\end{aligned} \tag{2.4.18}$$

and for state $|3\rangle$ being populated is

$$\begin{aligned}\tilde{\mathscr{P}}_3 &= \langle 3\,|\tilde{\varrho}_{\mathrm{D}}|\,3\rangle \\ &= \frac{1}{|\Omega_{\mathrm{p}}|^2 + |\Omega_{\mathrm{s}}|^2}\left(\mathscr{P}_{\mathrm{D1}}\,|\Omega_{\mathrm{p}}|^2 + \frac{\mathscr{P}_{\mathrm{D2}}\,|\Omega_{\mathrm{s}}|^2\,|\Omega_{\mathrm{c}}|^2}{|\Omega_{\mathrm{c}}|^2 + |\Omega_{\mathrm{p}}|^2 + |\Omega_{\mathrm{s}}|^2}\right).\end{aligned} \tag{2.4.19}$$

The relation between $\tilde{\mathscr{P}}_1$, $\tilde{\mathscr{P}}_2$ and $\tilde{\mathscr{P}}_3$ is

$$\tilde{\mathscr{P}}_1 + \tilde{\mathscr{P}}_2 + \tilde{\mathscr{P}}_3 = 1, \tag{2.4.20}$$

from $\mathrm{Tr}\,\tilde{\varrho}_{\mathrm{D}} = 1$.

We use numerical calculations of the population in state $|2\rangle$ and Eq. (2.4.18) to determine the value of $\mathscr{P}_{\mathrm{D2}}$. Once $\mathscr{P}_{\mathrm{D2}}$ is known, $\mathscr{P}_{\mathrm{D1}}$ is calculated from Eq. (2.4.16). The agreement between the numerical values of ϱ_{11} and ϱ_{33}, and the calculated values of $\tilde{\mathscr{P}}_1$ and $\tilde{\mathscr{P}}_3$ using Eqs. (2.4.18) and (2.4.19) respectively, verifies that the system is in a mixture of the two dark states (2.4.11).

We see that for certain two-photon detunings, the system is eventually trapped in a dark state, even if the atom has not been prepared initially (at $t = 0$) in a dark state. The atom is driven into the dark state by the combined action of coupling, signal, and probe fields and spontaneous emissions.

For stationary atoms, the steady-state atomic population depends on probe-field detuning due to the dark-state dependence on probe-field detuning. Thus, changing the probe-field detuning modifies the steady-state population in each energy state if the probe field is comparable in strength to the signal field, even if both are quite weak when compared to the coupling-field strengths shown in Fig. 2.5(a). However, the dependence of the atomic population on probe-field detuning decreases as the probe-field strength becomes weaker than the signal-field strength. This feature is apparent when comparing Fig. 2.5(a) with Fig. 2.5(b). Almost the entire population is evidently trapped in the dark state $|\psi_{\rm D}\rangle$ when $\delta_{\rm pc} = 0$, and in dark state $|\psi'_{\rm D}\rangle$ when $\delta_{\rm ps} = 0$. This corresponds to state $|1\rangle$ when $\Omega_{\rm s} \gg \Omega_{\rm p}$.

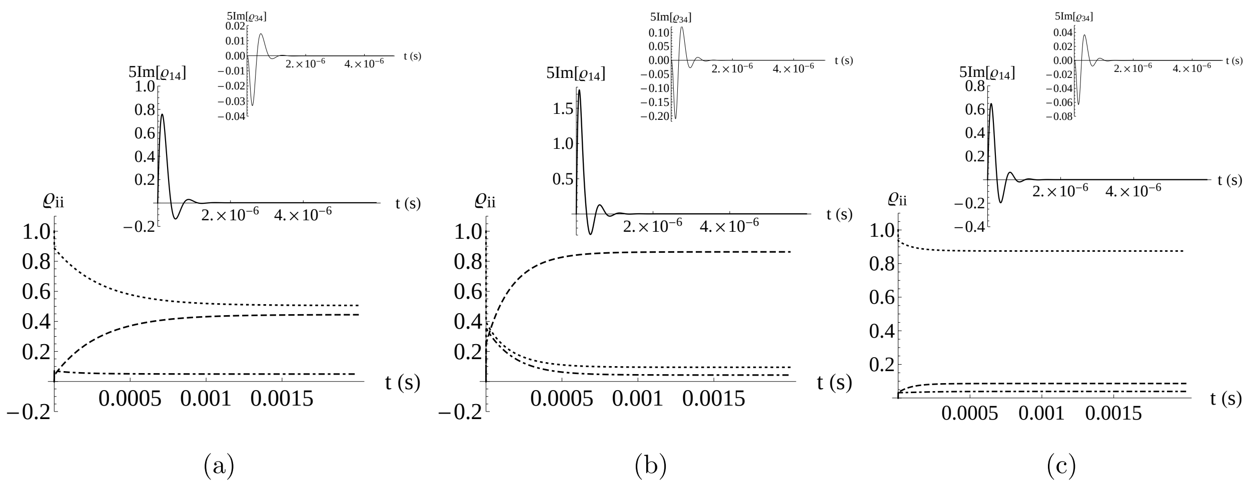

Figure 2.4: Populations of levels $|1\rangle$, $|2\rangle$ and $|3\rangle$ represented by ϱ_{11} (dotted line), ϱ_{22} (dotted-dashed line), and ϱ_{33} (dashed line) respectively, as a function of time t evaluated numerically by solving the master equation. The conditions are (a) $\Omega_{\rm s} = \Omega_{\rm p} = 0.3\gamma_4$ and $\Omega_{\rm c} = \gamma_4$, (b) $\Omega_{\rm p}, \Omega_{\rm c} \gg \Omega_{\rm s}$ with $\Omega_{\rm c} = \Omega_{\rm p} = \gamma_4$ and $\Omega_{\rm s} = 0.3\gamma_4$, and (c) $\Omega_{\rm s}, \Omega_{\rm c} \gg \Omega_{\rm p}$ with $\Omega_{\rm c} = \Omega_{\rm s} = 1\gamma_4$ and $\Omega_{\rm p} = 0.3\gamma_4$. The initial population is $\varrho_{11}^{(0)} = 1$ and $\varrho_{22}^{(0)} = \varrho_{33}^{(0)} = \varrho_{44}^{(0)} = 0$. Other parameters are $\gamma_4 = 18$ MHz, $\gamma_3 = 10$ kHz, $\gamma_2 = 40$ kHz and $\delta_{\rm p} = \delta_{\rm s} = \delta_{\rm c} = 0$. Insets (a), (b) and (c) are the absorptions of probe and signal fields represented by $5{\rm Im}\varrho_{14}$ and $5{\rm Im}\varrho_{34}$ respectively.

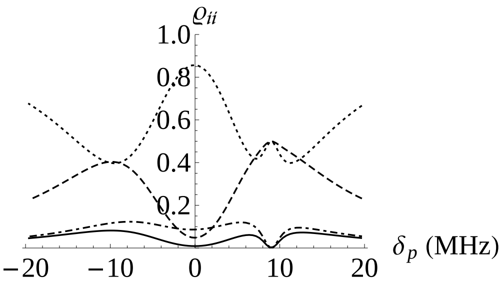

(a)

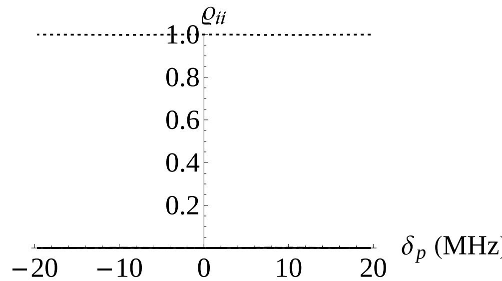

(b)

Figure 2.5: Numerically evaluated steady-state populations at zero temperature ϱ_{11} (dotted line), ϱ_{22} (dotted-dashed line), ϱ_{33} (dashed line), and ϱ_{44} (solid line) versus probe-field detuning δ_{p}. Parameter choices are (a) $\Omega_{\mathrm{s}} = \Omega_{\mathrm{p}} = 0.3\gamma_4$, and (b) $\Omega_{\mathrm{s}} \gg \Omega_{\mathrm{p}}$. $\Omega_{\mathrm{s}} = 0.3\gamma_4$ and $\Omega_{\mathrm{p}} = 0.01\gamma_4$. Other parameters are $\gamma_4 = 18$ MHz, $\gamma_3 = 10$ kHz, $\gamma_2 = 40$ kHz, $\Omega_{\mathrm{c}} = \gamma_4$, $\delta_{\mathrm{s}} = 0.5\Omega_{\mathrm{c}}$, and $\delta_{\mathrm{c}} = 0$.

2.5 Steady-State Solution for the Density-Matrix Element

In the previous section 2.4, we saw that the population and coherence elements ϱ_{14} and ϱ_{34} of the density matrix tend to have constant values after a period comparable to the atom relaxation time. The behavior of the density-matrix elements allows us to equate Eqs. (2.3.6) and (2.3.7) to zero, and to study the variation of the coherence and population elements of the density matrix as functions of the applied fields frequency detunings.

In this section, we study the coherence elements ϱ_{14} and ϱ_{34} as functions of the probe field and signal-frequency detunings respectively, when they reach the steady-state condition. We start with a numerical-analysis solution, calculated without approximations or assumptions, followed by an analytical analysis determined with some assumptions and approximated conditions.

2.5.1 Numerical Steady-State Solution

The density-matrix elements ϱ_{14} and ϱ_{34} are related to the polarization and optical susceptibility (3.3.6), (3.3.13) and (3.3.14); hence, they carry all the optical properties of the medium, in response to probe and signal fields respectively. We start section 2.5 by studying ϱ_{14} and ϱ_{34} when they reach the steady state, by solving Eqs. (2.3.6) and (2.3.7) numerically. The advantages of the numerical solution are that it gives a general solution, and exact behavior.

In Figure 2.6, we plot the real and imaginary parts of ϱ_{14} versus the probe-field detuning and ϱ_{34} versus signal-field detuning, for $\gamma_4 \gg \gamma_2, \gamma_3$ defined by (2.3.8) and $|\Omega_c|^2 \gg |\Omega_p|^2, |\Omega_s|^2$. As stated earlier, the real and the imaginary parts of the coherence ϱ_{ij} are related to dispersion and absorption respectively. We found that at zero two-photon detuning $\delta_{pc} = 0$ and $\delta_{ps} = 0$, both the real and imaginary parts are almost zero (i.e., the absorption is near zero where the index of refraction is one). The medium is driven to electromagnetically induced transparency (EIT). The physical origin of EIT can be understood in term of the dark states discussed in the previous section 2.4. The atoms are pumped into the dark state by the combined action of the strong coupling and weak probe and signal fields and spontaneous emissions. The EIT is induced in an atom in the radiative lifetime, since this is the time for an excited atom to decay to an uncoupled dark state.

It also clear from Fig. 2.6 that, for identical probe and signal-Rabi frequencies, ϱ_{14} and ϱ_{34} have identical behavior. Both fields can pass through the medium without absorption, and with a lower group velocity than the speed of light, at two different EIT transparency windows. This system creates DEIT windows for the double fields; thus we call it DDEIT. The first DEIT window occurs when $\delta_{pc} = 0$, and both signal and probe fields have identical optical properties. The second DEIT window occurs when $\delta_{ps} = 0$, and both signal and probe fields have identical optical properties at this window. The plots of the imaginary part of ϱ_{14} and ϱ_{34} in Fig. 2.6 show that the first DEIT has higher window width than the second DEIT window. The Figure also shows that the slopes of the real parts of ϱ_{14} and ϱ_{34} at the region of the second EIT window apparently exceed the slope at the region of the first window for the given parameters.

Our next step, is to change some parameters, such as the Rabi frequencies, decay rate and dephasing, and see how this influences the DDEIT system. We considered the probe-field case first, and then the signal-field case, which is similar.

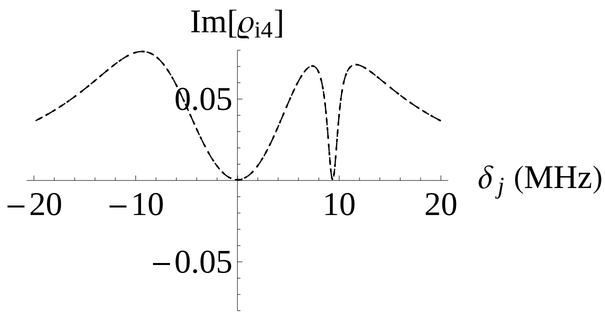

(a)

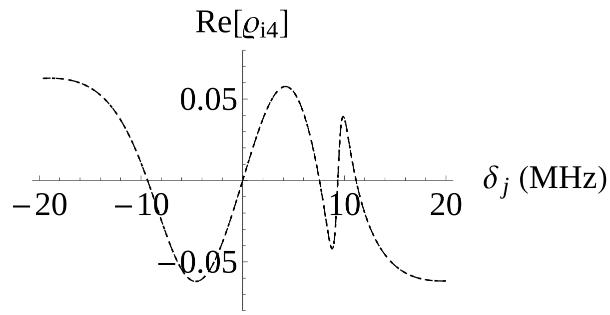

(b)

Figure 2.6: Numerically evaluated steady-state coherences ϱ_{14} (dashed line) versus probe-field detuning δ_p and ϱ_{34} (dotted line) versus signal-field detuning δ_s. Parameter choices are $\Omega_\mathrm{s} = 0.2\gamma_4$ and $\Omega_\mathrm{p} = 0.2\gamma_4$. Other parameters are $\gamma_4 = 18$ MHz, $\gamma_3 = 10$ kHz, $\gamma_2 = 40$ kHz, $\Omega_\mathrm{c} = \gamma_4$, and $\delta_\mathrm{c} = 0$.

2.5.1.1 Parameters Affect the Density-Matrix Element ϱ_{14}

The effect of the signal-field Rabi frequency on the probe-field optical profile can be observed in Fig. 2.7. The signal field mainly affects the second EIT (i.e., when $\delta_\mathrm{ps} = 0$), but it has negligible effect on the first EIT window. Increasing the signal-field Rabi frequency value increases the width of second EIT and decreases the slope of dispersion in the region of the second window, as shown in Figs. 2.7(a) and (b) respectively.

For a lower value of γ_3, the absorption of the probe field is almost zero, but increases the value of γ_3, will increase the absorption of the probe field when $\delta_\mathrm{ps} = 0$, as shown in Figs. 2.7(a) and (c) respectively. The decay and dephasing rate from level $|3\rangle$ do not influence the transparency of the first window.

The effect of the coupling field on the medium response to the probe field is shown in Fig. 2.8. The coupling-field strength controls the width of the first EIT transparency window, as well as the dispersion inclination. Higher values of the coupling-Rabi frequency result in increased width of the EIT window, and in a lower dispersion slope at the region of the first window when $\delta_{\mathrm{pc}} = 0$ as shown in Figs. 2.8(a) and (b) respectively. The coupling field does not influence the absorption or dispersion at the second EIT window.

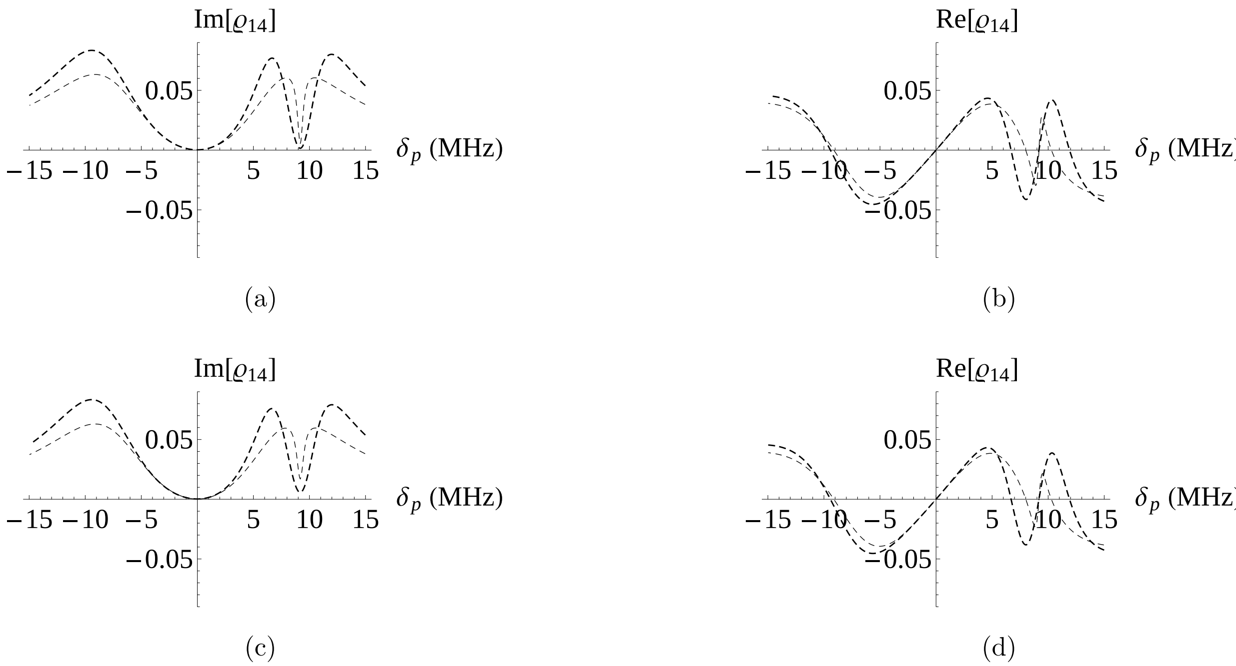

Figure 2.7: Numerically evaluated steady-state coherences ϱ_{14} versus probe-field detuning δ_{p}, for two different values of signal-field Rabi frequencies; $\Omega_{\mathrm{s}} = 0.1\gamma_4$ (dashed line) and $\Omega_{\mathrm{s}} = 0.6\gamma_4$ (bold-dashed line). (a),(b) $\gamma_3 = 50$ kHz. (c),(d) $\gamma_3 = 200$ kHz. Other parameters are $\gamma_4 = 18$ MHz, $\gamma_2 = 40$ kHz, $\Omega_{\mathrm{c}} = \gamma_4$, $\Omega_{\mathrm{p}} = 0.1\gamma_4$ and $\delta_{\mathrm{c}} = 0$.

The dephasing and decay rate from level $|2\rangle$ affect the absorption at the first window. For a lower value of γ_2 the absorption of the probe field is zero, while a higher value of γ_2 leads to a higher absorption of the probe field at $\delta_{\mathrm{pc}} = 0$, as shown in Figs. 2.8(a) and (c) respectively. The decay and dephasing rates from level $|2\rangle$ do not influence the transparency of the second window.

There is a limited value of γ_2 and γ_3 associated with the coupling and signal-field Rabi frequencies respectively, for which the absorption is still close to zero at the first and second-EIT transparency windows. However, the numerical solution does not help to determine this value, or show how the coherence decay rates γ_2 and γ_3 are related to Ω_c and Ω_s respectively, to achieve minimum absorption. We expect the relation between γ_3 and Ω_s, and that between γ_2 and Ω_c, are similar to those obtained for Λ scheme [39]. If we consider our system as double-Λ schemes, the first (Λ_1) is constructed by $|1\rangle$, $|2\rangle$ and $|4\rangle$, and the second (Λ_2) is defined by $|1\rangle$, $|3\rangle$ and $|4\rangle$. Then, the relation is expected to be

$$|\Omega_c|^2 \gg \gamma_2\gamma_4, \tag{2.5.1}$$

for Λ_1, and

$$|\Omega_s|^2 \gg \gamma_3\gamma_4, \tag{2.5.2}$$

for Λ_2. The only way to test the validity of our numerical-analysis conclusion that leads to these two relations, is to compare the product of $\gamma_2\gamma_4$ to $|\Omega_c|^2$ for the values presented in Figs. 2.8(a) and (c), and then do the same for the second window by comparing the product of $\gamma_3\gamma_4$ to $|\Omega_s|^2$ for the value introduced in Figs. 2.7(a) and (c). In case (a) of both figures, the relations (2.5.2) and (2.5.1) are satisfied and the absorption value is close to zero. However, for case (c) of both figures, the absorption increases when the relations (2.5.2) and (2.5.1) are not satisfied. Although we able to examine the validity of (2.5.2) and (2.5.1) for the cases shown in the Figs. 2.7 and 2.8, it does not mean that this is valid for all cases. We need to derive these relations analytically to prove their validity in all cases.

In conclusion, the signal field and the coherence decay of level $|3\rangle$ are the critical parameters that affect the absorption and dispersion of the probe field at the second EIT window, while the coupling field and coherence decay of state $|2\rangle$ represent the parameters that influence the absorption and dispersion at the first EIT transparency window. The relations (2.5.2) and (2.5.1) are important to achieve minimum absorption and observe the EIT window for the probe field, if we prove their validity, in general.

2.5.1.2 Parameters Affect Density-Matrix Element ϱ_{34}

Similar to the probe-field cases studied in the previous subsection and shown in Figs. 2.7 and 2.8, we now examine the signal-field propagation in the atomic medium. In Figs. 2.9 and 2.10

we plot the imaginary and real parts of ϱ_{34}, which describe the absorption and dispersion of the signal field by the medium. We used different parameters for each figure, to test their effects on the two transparency windows of the signal field.

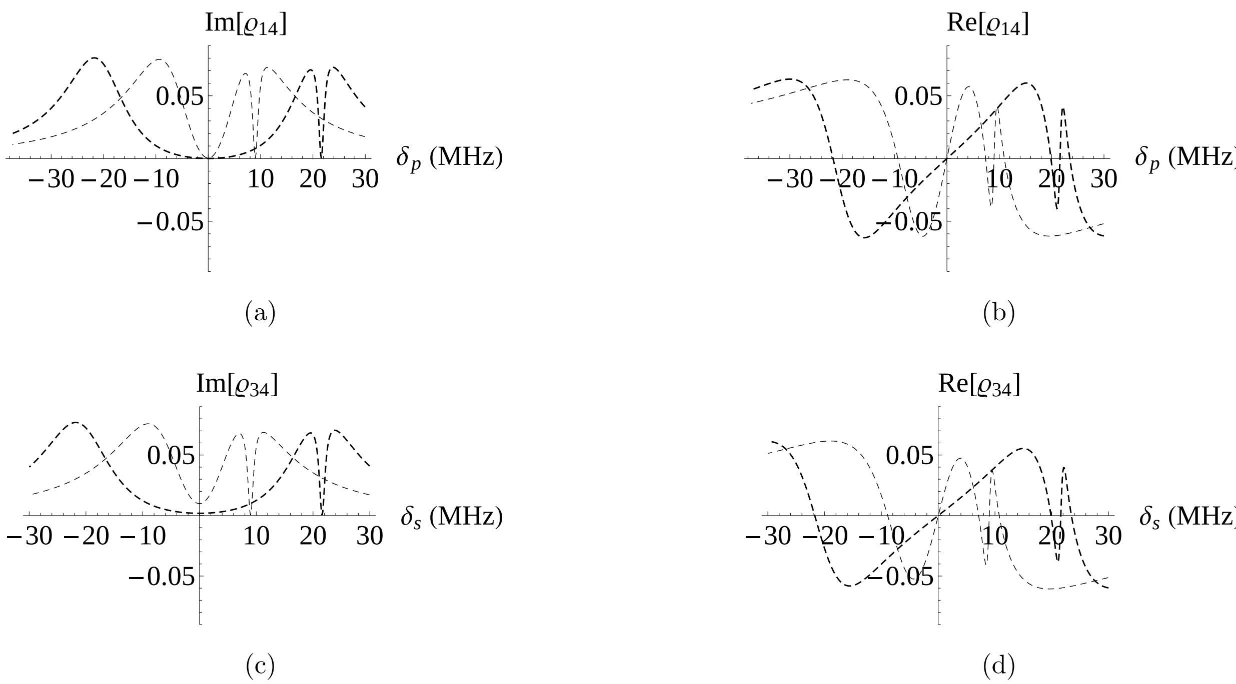

Figure 2.8: Numerically evaluated steady-state coherences ϱ_{14} versus probe-field detuning $\delta_{\rm p}$ for two different values of coupling-field Rabi frequencies; $\Omega_{\rm c} = \gamma_4$ (dashed line) and $\Omega_{\rm c} = 2.4\gamma_4$ (bold-dashed line). (a),(b) $\gamma_2 = 40$ kHz. (c),(d) $\gamma_2 = 1$ MHz. Other parameters are $\gamma_4 = 18$ MHz, $\gamma_3 = 5$ kHz, $\Omega_{\rm s} = 0.2\gamma_4$, $\Omega_{\rm p} = 0.2\gamma_4$, $\delta_{\rm s} = 0.5\Omega_{\rm c}$ and $\delta_{\rm c} = 0$.

Similar to the probe-field case, the coupling-field strength affects the width of the first EIT transparency window, as well as the dispersion inclination of the signal field. A higher value of the coupling-Rabi frequency leads to a wider EIT window, and to a lower dispersion slope in the region of the first window when $\delta_{\rm pc} = 0$, as shown in Figs. 2.10(a) and (b) respectively. The coupling field does not influence the absorption or the dispersion at the second EIT window.

The dephasing and decay rate from level $|2\rangle$ affect the absorption at the first window, increasing the value of γ_2, increases the absorption of the signal field and vice versa (see

Fig. 2.10(a) and (c)). The decay and dephasing rate from level $|2\rangle$ do not influence the transparency of the second window.

The relation connects the probe-field Rabi frequency to the coherence decay γ_3, that governs the absorption of the signal field at the second window is similar to (2.5.2), but modified to

$$|\Omega_{\rm p}|^2 \gg \gamma_3\gamma_4, \tag{2.5.3}$$

while the relation governs the signal-field absorption at the first EIT window, remains the same as (2.5.1).

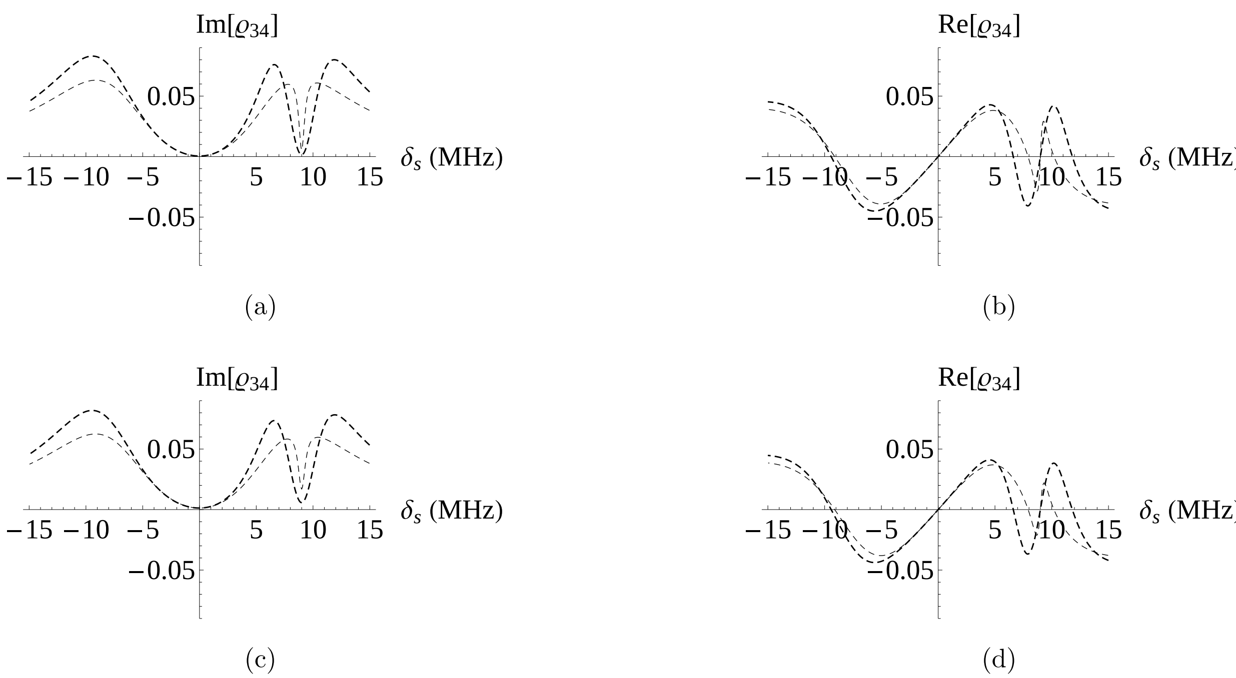

Figure 2.9: Numerically evaluated steady-state coherences ϱ_{34} versus signal-field detuning $\delta_{\rm s}$ for two different values of probe-field Rabi frequencies. Parameter choices are $\Omega_{\rm p} = 0.1\gamma_4$ (dashed line) and $\Omega_{\rm p} = 0.6\gamma_4$ (bold-dashed line). (a),(b) $\gamma_3 = 50$ kHz. (c),(d) $\gamma_3 = 200$ kHz. Other parameters are $\gamma_4 = 18$ MHz, $\gamma_2 = 40$ kHz, $\Omega_{\rm c} = \gamma_4$, $\Omega_{\rm s} = 0.1\gamma_4$, and $\delta_{\rm c} = 0$.

We can summarize this subsection in two points: First, The probe field and the coherence decay of level $|3\rangle$ are the critical parameters that effect the absorption and dispersion of the signal field at the second EIT window, and the coupling field and coherence decay of state $|2\rangle$ are key parameters that influence the absorption and dispersion at the first EIT window. Second, the relations (2.5.3) and (2.5.1) are important to achieve minimum absorption and observe the EIT windows for the signal field.

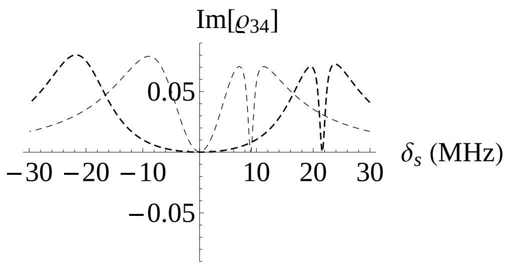

(a)

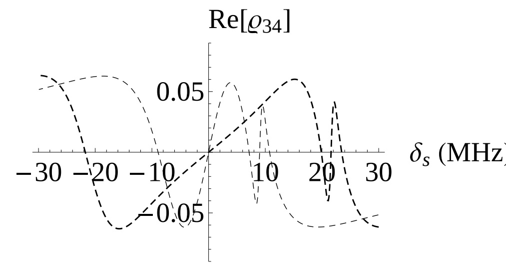

(b)

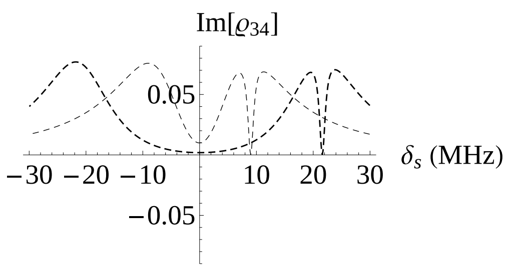

(c)

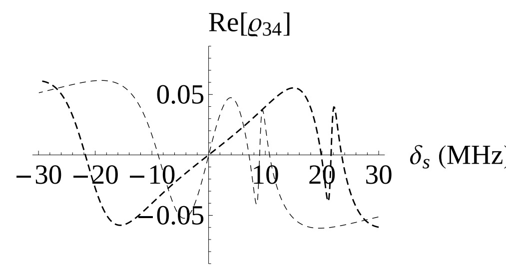

(d)

Figure 2.10: Numerically evaluated steady-state coherences ϱ_{34} versus signal-field detuning δ_{s} for two different values of coupling-field Rabi frequencies; $\Omega_{\mathrm{c}} = \gamma_4$ (dashed line) and $\Omega_{\mathrm{c}} = 2.4\gamma_4$ (bold-dashed line). (a),(b) $\gamma_2 = 40$ kHz. (c),(d) $\gamma_2 = 1$ MHz. Other parameters are $\gamma_4 = 18$ MHz, $\gamma_3 = 5$ kHz, $\Omega_{\mathrm{s}} = 0.2\gamma_4$, $\Omega_{\mathrm{p}} = 0.2\gamma_4$, and $\delta_{\mathrm{c}} = 0$.

2.5.2 Analytical Steady-State Solution

A general analytical solution for ϱ_{14} and ϱ_{34} is impossible without assumptions or approximated conditions. Therefore, in our system we impose the equal-population condition

$$\varrho_{11} \approx \varrho_{33} \approx 0.5. \tag{2.5.4}$$

Condition (2.5.4) makes the equations somewhat solvable analytically, as the equations of motion for population (2.3.7) are effectively decoupled from the equations of motion for coherence (2.3.6). We also assume that

$$\Omega_{\mathrm{c}} > \Omega_{\mathrm{p}}, \Omega_{\mathrm{s}}, \tag{2.5.5}$$

which implies

$$|\Omega_{\mathrm{c}}|^2 \gg |\Omega_{\mathrm{p}}|^2, |\Omega_{\mathrm{s}}|^2, \tag{2.5.6}$$

which is always valid for all chosen values of Ω_{c}, Ω_{p} and Ω_{s}. This assumption makes it possible to decouple ϱ_{24} from other coherences, by eliminating the $\Omega_{\mathrm{s}}^*\varrho_{24}$ and $\Omega_{\mathrm{p}}\varrho_{24}$ terms from $\dot{\varrho}_{23}(t)$ and $\dot{\varrho}_{12}(t)$ equations in (2.3.6) respectively, because their influence is weak compared to other terms.

Then, the off-diagonal steady-state density-matrix element ϱ_{14} can be calculated

$$\varrho_{14} = \Omega_{\mathrm{p}} \frac{\mathrm{i}\left(\varrho_{11} - \varrho_{44}\right) + \frac{\Omega_{\mathrm{s}}}{\gamma_3 - 2\mathrm{i}\delta_{\mathrm{ps}}}\varrho_{43}}{\gamma_4 - 2\mathrm{i}\delta_{\mathrm{p}} + \frac{|\Omega_{\mathrm{c}}|^2}{\gamma_2 - 2\mathrm{i}\delta_{\mathrm{pc}}} + \frac{|\Omega_{\mathrm{s}}|^2}{\gamma_3 - 2\mathrm{i}\delta_{\mathrm{ps}}}}, \tag{2.5.7}$$

where

$$\varrho_{43} = \Omega_{\mathrm{s}}^* \frac{-\mathrm{i}\left(\varrho_{33} - \varrho_{44}\right) + \frac{\Omega_{\mathrm{p}}^*}{\gamma_3 - 2\mathrm{i}\delta_{\mathrm{ps}}}\varrho_{14}}{\Gamma_{43} + 2\mathrm{i}\delta_{\mathrm{s}} + \frac{|\Omega_{\mathrm{c}}|^2}{\Gamma_{32} + 2\mathrm{i}\delta_{\mathrm{sc}}}}, \tag{2.5.8}$$

is the optical response to the signal field for the $|4\rangle \to |3\rangle$ transition direction and

$$\Gamma_{kl} = \gamma_k + \gamma_l. \tag{2.5.9}$$

We substitute Eq. (2.5.8) into Eq. (2.5.7) to obtain

$$\varrho_{14} = \mathrm{i}\Omega_{\mathrm{p}} \frac{\left(\varrho_{11} - \varrho_{44}\right)\left(\Gamma_{43} + 2\mathrm{i}\delta_{\mathrm{s}} + \frac{|\Omega_{\mathrm{c}}|^2}{\Gamma_{32} + 2\mathrm{i}\delta_{\mathrm{sc}}}\right) + \left(\varrho_{11} - \varrho_{44}\right)\frac{|\Omega_{\mathrm{p}}|^2}{\gamma_3 - 2\mathrm{i}\delta_{\mathrm{ps}}} + \left(\varrho_{44} - \varrho_{33}\right)\frac{|\Omega_{\mathrm{s}}|^2}{\gamma_3 - 2\mathrm{i}\delta_{\mathrm{ps}}}}{\left(\Gamma_{43} + 2\mathrm{i}\delta_{\mathrm{s}} + \frac{|\Omega_{\mathrm{c}}|^2}{\Gamma_{32} + 2\mathrm{i}\delta_{\mathrm{sc}}}\right)\left(\gamma_4 - 2\mathrm{i}\delta_{\mathrm{p}} + \frac{|\Omega_{\mathrm{c}}|^2}{\gamma_2 - 2\mathrm{i}\delta_{\mathrm{pc}}} + \frac{|\Omega_{\mathrm{s}}|^2}{\gamma_3 - 2\mathrm{i}\delta_{\mathrm{ps}}}\right) + \frac{|\Omega_{\mathrm{p}}|^2}{\gamma_3 - 2\mathrm{i}\delta_{\mathrm{ps}}}\left(\gamma_4 - 2\mathrm{i}\delta_{\mathrm{p}} + \frac{|\Omega_{\mathrm{c}}|^2}{\gamma_2 - 2\mathrm{i}\delta_{\mathrm{pc}}}\right)}. \tag{2.5.10}$$

Equation (2.5.10) generalizes the previous expression for the response function [57], which focuses on the special case of equal detuning between all fields and ignores signal-field and nonlinear probe-field terms.

Our assumption of constant population surprised us with the presence of negative absorption; in other words, a gain in the absorption profile of the probe field, as shown in

Fig. 2.11(a). The amplification of the probe field was absent in the numerical solution. To explain the gain presence and its source, we need to understand each term in the analytical solution (2.5.10).

The analytical solution (2.5.10) consists of three terms. The imaginary part of the first term is positive, which is represented by the dashed line in Fig. 2.11 and due to the optical linear process of the probe field, since the nonlinear term $|\Omega_{\mathrm{p}}|^2$ in the denominator does not have an influential effect in the first term, and can be ignored. This is evident from Eq. (2.5.7), where this term is represented by the first, and excludes any nonlinear terms in the probe-field Rabi frequency. The first term reflects the expected absorption, which results of having more population in level $|1\rangle$ than level $|4\rangle$, and is responsible for the presence of the EIT windows, as shown in Fig. 2.11.

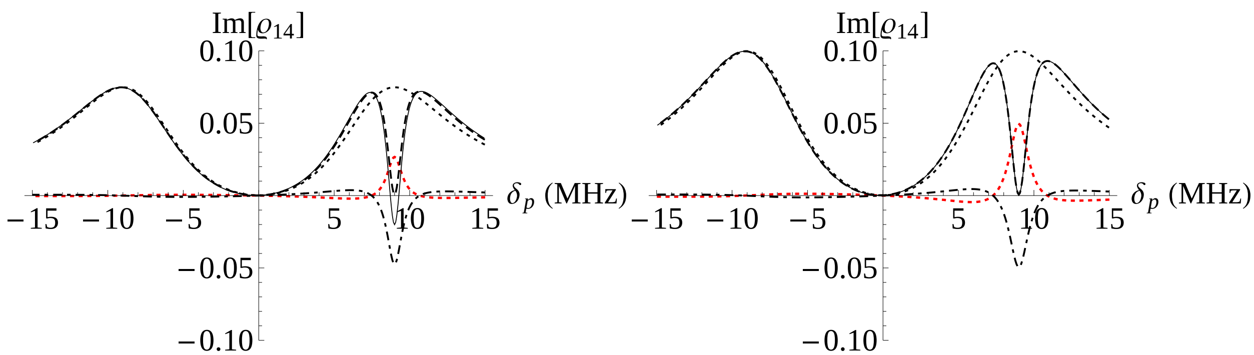

(a) (b)

Figure 2.11: Im[ϱ_{14}] versus probe-field detuning δ_{p}. (a) $\Omega_{\mathrm{s}} = 0.2\gamma_4$, $\Omega_{\mathrm{p}} = 0.15\gamma_4$. (b) $\Omega_{\mathrm{s}} = \Omega_{\mathrm{p}} = 0.2\gamma_4$. Parameter choices are $\gamma_4 = 18$ MHz, $\gamma_3 = 10$ kHz, $\gamma_2 = 40$ kHz, $\Omega_c = \gamma_4$, $\delta_{\mathrm{s}} = 9$ MHz, and $\delta_{\mathrm{c}} = 0$ with all terms of Eq. (2.5.10) included (solid line), $\varrho_{43} \equiv 0$ imposed (dashed line), gain term (dotted-dashed line), nonlinear absorption term (dotted red line) and for $\Omega_{\mathrm{s}} \equiv 0$ (dotted line).

With existence of the analytical solution (2.5.10), the presence of EIT windows in the imaginary profile of the first term can be explained using quantum interference. The EIT window at $\delta_{\mathrm{p}} = \delta_{\mathrm{c}}$ is due to the destructive interference between the indirect channels for the excitation $|1\rangle \rightarrow |4\rangle$ (which involves the multi-photon transition channels of the coupling field between level $|2\rangle$ and $|4\rangle$ described by $|\Omega_{\rm c}|^2$ in the denominator [74]), and the direct transition of the probe field between $|1\rangle$ and $|4\rangle$. On other hand, the vanishing of absorption at $\delta_{\rm p} = \delta_{\rm s}$ is due to the destructive interference between the indirect channels, which involves the multi-photon transitions of the signal field between level $|3\rangle$ and $|4\rangle$ described by $|\Omega_s|^2$ in the denominator [74], and the direct transition of the probe field between $|1\rangle$ and $|4\rangle$.

The second term is proportional to $|\Omega_{\rm p}|^2$. It is due to the nonlinear process in the probe field. The imaginary part of this term reflects the higher order of absorption in the probe field, which results of having more population in level $|1\rangle$ than level $|4\rangle$. The third term of Eq. (2.5.10) is proportional to $|\Omega_{\rm s}|^2$, and contributes to the gain if the population in state $|3\rangle$ is higher than the population in $|4\rangle$. The second and third terms have an influential effect when $\delta_{\rm s} = \delta_{\rm p}$, and thus cannot be ignored. The validity of ignoring these terms is evident in Fig. 2.11, near $\delta_{\rm p} = \delta_{\rm c} = 0$, but not far away from the region where the signal and higher-order probe-field effects are key to interference. Their effect is described by the dotted-red line and dotted-dashed- black line of Fig. 2.11 respectively.

To explain the parameter choices in Fig. 2.11, we refer to Fig. 2.1. Specifically, we consider ^{87}Rb and assign $|1\rangle$, $|2\rangle$ and $|3\rangle$ to the $5S_{1/2}$ level with $F = 1, m_F = 0$, $F = 2$ and $m_F = \{-2, 0\}$ respectively. Level $|4\rangle$ corresponds to level $5P_{1/2}$ with $F = 2$ and $m_F = -1$. The decay rates [61] and field strengths are given in the captions of figures.

The last two terms arise due to signal-driven coherence via $|1\rangle \leftrightarrow |3\rangle$ coherence: $\dot{\varrho}_{13} = (-\frac{1}{2}\gamma_3 + i\delta_{\rm ps})\varrho_{13} - \frac{i}{2}(-\varrho_{14}\Omega_{\rm s}^* + \varrho_{43}\Omega_{\rm p})$, which shows that the coherence is responsible for coupling the signal and probe-driven transitions. This $|1\rangle \leftrightarrow |3\rangle$ coherence is crucial to establish the requisite interfering channels, in order for the gain to outweigh the effects of absorption [14, 50].

For perfect EIT, i.e. vanishing linear absorption at $\delta_{\rm p} = \delta_{\rm s}$, the gain which is represented by the imaginary part of the third term is negative in our system, and exceeds the nonlinear absorption represented by the second term by satisfying the following relations

$$\varrho_{33} \left|\Omega_{\rm s}\right|^2 > \varrho_{11} \left|\Omega_{\rm p}\right|^2 , \tag{2.5.11}$$

where ϱ_{44} is excluded from the above equation because the population in $|4\rangle$ vanishes at steady state. Since there is no decay from $|3\rangle$ to $|2\rangle$, any population pumped by the coupling field to $|4\rangle$ will then decay to $|1\rangle$ and $|3\rangle$ (see Sec. 2.4 for more detail about atom population).

Reaching this point, explains why a net gain is observed when we assume constant population in our analytical solution, and is not observed in the case of a numerical solution. For equal $\Omega_{\rm p}$ and $\Omega_{\rm s}$ the population $\varrho_{11} = \varrho_{33} = 0.5$ (see Fig. 2.3(a)). In this case, the second and third terms cancel each other out, because they are equal and opposite in sign, as shown in Fig. 2.11(b). Hence, no net gain is observed using either numerical calculation as in Fig. 2.7(a), or using analytical calculation as in Fig. 2.11(b).

For the case $\Omega_{\rm s} > \Omega_{\rm p}$, the population changes such that $\varrho_{11} > \varrho_{33}$, as shown in Fig. 2.3(c). Since the change in the populations of ϱ_{11} and ϱ_{33} due to the variation of $\Omega_{\rm s}$ occurs in such a way that condition (2.5.11) always fails in real situations, we do not observe gain in the numerical calculations, as seen in Fig. 2.7(a). However, the assumption of constant population while varying the driving field makes (2.5.11) valid when $\Omega_{\rm s} > \Omega_{\rm p}$, which is the case for the analytical solution in Fig. 2.11(a).

In both numerical and analytical analyses, the physical mechanism responsible for the gain is present, but we require condition (2.5.11) to observe it. If we maintained ϱ_{11} and ϱ_{33} constant, we would observe gain in our system. One suggestion to achieve condition (2.5.4), is to apply incoherent excitation from ground state $|1\rangle$ to the excited state $|4\rangle$ with a constant pumping rate $r_{\rm p}$.

The equations of motion of the density-matrix element with incoherent pumping are similar to those without incoherent pumping Eqs. (2.3.6) and (2.3.7), differing only in the replacement

$$\gamma_4 \rightarrow \gamma_4 + 2r_{\rm p},\ \gamma_3 \rightarrow \gamma_3 + r_{\rm p}, \tag{2.5.12}$$

and

$$\gamma_2 \rightarrow \gamma_2 + r_{\rm p},\ \Gamma_{34} \rightarrow \Gamma_{34} + r_{\rm p}. \tag{2.5.13}$$

The incoherent pumping adds more dephasing, but does not change the form of the equations of motion for coherence. As shown in Fig. 2.12, the gain is achieved by applying incoherent pumping. The incoherent pumping modifies the population in states $|1\rangle$ and $|3\rangle$ such that $\varrho_{33} > \varrho_{11}$. We discuss incoherent pumping in more detail in Chapter 6.

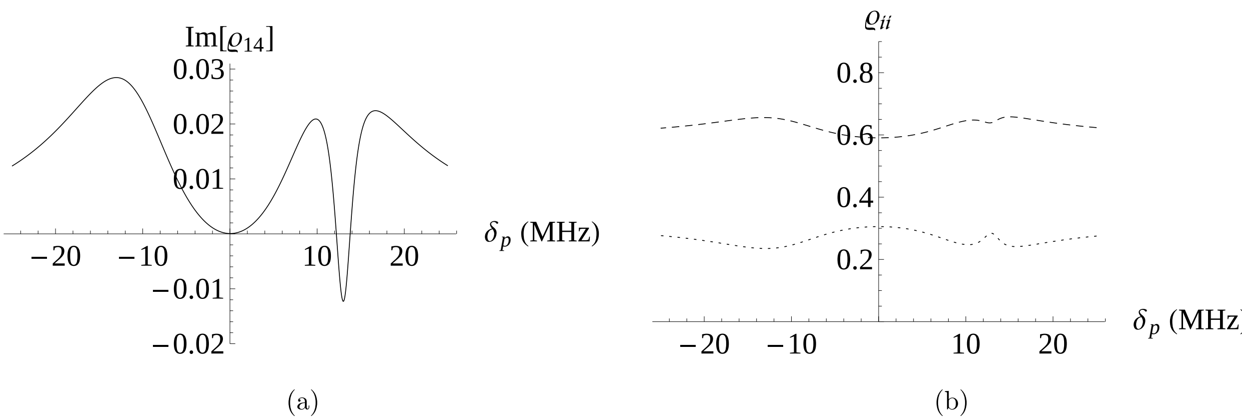

Figure 2.12: Numerically steady-state density matrix elements (a) Im[ϱ_{14}] and (b) ϱ_{11} (dotted line) and ϱ_{33} (dashed line) versus probe detuning $\delta_{\rm p}$, using constant pumping rate $r_{\rm p} = 1$ MHz. Other parameters are $\Omega_{\rm s} = 0.2\gamma_4$, $\Omega_{\rm p} = 0.15\gamma_4$, $\gamma_4 = 24$MHz, $\gamma_3 = 10$ kHz, $\gamma_2 = 40$ kHz, $\Omega_c = \gamma_4$, $\delta_{\rm s} = 13$ MHz and $\delta_{\rm c} = 0$.

The density master approach shows that coherence between the bare levels $|1\rangle$ and $|3\rangle$ is crucial for any overall gain. However, it does not describe the precise mechanisms which provide the gain in the system. The gain in the second window, when $\delta_{\rm s} = \delta_{\rm p}$, could be the result of one of two physical processes:

The first process is amplification without inversion (AWI), which is defined as amplification of a probe-laser field in a system that exhibits no population inversion on the probe transition in a bare or dressed state. Two conditions are required for this mechanism to occur [14, 15, 46]. The first condition is destructive quantum interference to prevent any absorption of the probe field due to the transition from $|1\rangle$ to $|4\rangle$, which is satisfied by the first term of Eq. (2.5.10). The second condition, amplification is taken from the medium via depletion of the upper operating level, which then requires incoherent pumping to populate the upper level. This condition is described by the term $(\varrho_{44} - \varrho_{33})$ of Eq. (2.5.10). Thus, the system will always exhibit gain as long as $(\varrho_{44} < \varrho_{33})$; however, this raises a question: What happens if there are no atoms occupy state $|4\rangle$, i.e., if $\varrho_{44} = 0$? does the $\pitchfork$ atom-field exhibit gain when $\delta_{\mathrm{s}} = \delta_{\mathrm{p}}$? The answer, according to Eq. (2.5.10), is yes. Thus, the gain exists at the second window, even if there is no atom in the upper state $|4\rangle$. Therefore, this scheme does not qualify as AWI.

The second process that could be responsible for the presence of gain in our system is Raman scattering, which occurs among the electronic states and works without population inversion at the operating transition $|1\rangle \rightarrow |4\rangle$ (i.e. occurs even with $\varrho_{44} = 0$), but needs population inversion between two lower levels which define the direction of frequency conversion. State $|4\rangle$ plays the role of intermediate state in Raman scattering, and states $|1\rangle$ and $|3\rangle$ represent the initial state and the final state of the electronic-Raman transition respectively.

To observe Raman gain in general, population inversion must occur between state $|1\rangle$ and $|3\rangle$. For example, to achieve gain in the probe field (anti-Stokes), the population in state $|3\rangle$, which represents the initial state of Raman transition, must be greater than the population in state $|1\rangle$, which represents the final state of Raman transition; thus $\varrho_{33} > \varrho_{11}$. Hence, the number of scattered signal photons required to stimulate the emission of probe photons is greater than the number of absorbed probe photons. Thus, the stimulated emission of the probe photon will be greater than the absorbed probe photon, and as a result the probe field is amplified. To amplify the signal field (stokes) ϱ_{11} must be greater than ϱ_{33}. In this case, scattering of the probe field induces emission in the signal field. The gain in our system is due to Raman scattering, but instead of the requirement of $\varrho_{11} > \varrho_{33}$, condition (2.5.11) is required to amplify the probe field.

The analytical optical response of the signal field is described by

$$\varrho_{34} = \mathrm{i}\Omega_\mathrm{s}\frac{(\varrho_{33}-\varrho_{44})\left(\gamma_4+2\mathrm{i}\delta_\mathrm{p}+\frac{|\Omega_\mathrm{c}|^2}{\gamma_2+2\mathrm{i}\delta_\mathrm{pc}}\right)+(\varrho_{33}-\varrho_{44})\frac{|\Omega_\mathrm{s}|^2}{\gamma_3+2\mathrm{i}\delta_\mathrm{ps}}+(\varrho_{44}-\varrho_{11})\frac{|\Omega_\mathrm{p}|^2}{\gamma_3+2\mathrm{i}\delta_\mathrm{ps}}}{\left(\Gamma_{43}-2\mathrm{i}\delta_\mathrm{s}+\frac{|\Omega_\mathrm{c}|^2}{\Gamma_{32}-2\mathrm{i}\delta_\mathrm{sc}}+\frac{|\Omega_\mathrm{p}|^2}{\gamma_3+2\mathrm{i}\delta_\mathrm{ps}}\right)\left(\gamma_4+2\mathrm{i}\delta_\mathrm{p}+\frac{|\Omega_\mathrm{c}|^2}{\gamma_2+2\mathrm{i}\delta_\mathrm{pc}}\right)+\frac{|\Omega_\mathrm{s}|^2}{\gamma_3+2\mathrm{i}\delta_\mathrm{ps}}\left(\Gamma_{43}-2\mathrm{i}\delta_\mathrm{s}+\frac{|\Omega_\mathrm{c}|^2}{\Gamma_{32}-2\mathrm{i}\delta_\mathrm{sc}}\right)}. \tag{2.5.14}$$

The corresponding absorption curve for the signal field is plotted in Fig. 2.13. Similar to the probe-field case, we observe two EIT windows in the signal-field absorption plot, and gain in the second window.

The analytical solution of ϱ_{34} also consists of three terms. The imaginary part of the first term is positive. It is described by the dashed line in Fig. 2.13, and is due to the optical linear process of the signal field, since the nonlinear term $|\Omega_\mathrm{s}|^2$ in the denominator doesn't have any influential effect in the first term, and thus can be ignored. The first term reflects the expected absorption, which results of having more population in $|3\rangle$ than level $|4\rangle$, and is responsible for the existence of the EIT transparency windows, as shown in Fig. 2.13. The EIT transparency window at $\delta_\mathrm{s} = \delta_\mathrm{c}$ is due to the destructive interference between the indirect channels for the excitation $|3\rangle \to |4\rangle$, which involves multi-photon transition channels of the coupling field between levels $|2\rangle$ and $|4\rangle$, as described by the $|\Omega_\mathrm{c}|^2$ term in the denominator [74], and the direct transition of the signal field between $|3\rangle$ and $|4\rangle$. The EIT transparency window at $\delta_\mathrm{p} = \delta_\mathrm{s}$ is due to the destructive interference between the indirect channels that involve multi-photon transitions of the probe field between levels $|1\rangle$ and $|4\rangle$, described by $|\Omega_\mathrm{p}|^2$ term in the denominator [74], and the direct transition of the signal field between $|3\rangle$ and $|4\rangle$.

The second term is proportional to $|\Omega_\mathrm{s}|^2$. Its imaginary part represents the nonlinear absorption in the signal field, which results of having more population in level $|3\rangle$ than level $|4\rangle$. The third term in Eq. 2.5.14 is proportional to $|\Omega_\mathrm{p}|^2$, and contributes to the gain as long as the population in state $|1\rangle$ is higher than the population in $|4\rangle$. Terms two and three cannot be ignored when $\delta_\mathrm{s} = \delta_\mathrm{p}$. The validity of ignoring these two terms is evident in Fig. 2.13 near $\delta_\mathrm{p} = \delta_\mathrm{c} = 0$, but not far from the region where the probe and higher-order signal field effects play a crucial role in the interference. The effects are described by the dotted-dashed black line and the dotted-red line in Fig. 2.13 respectively.

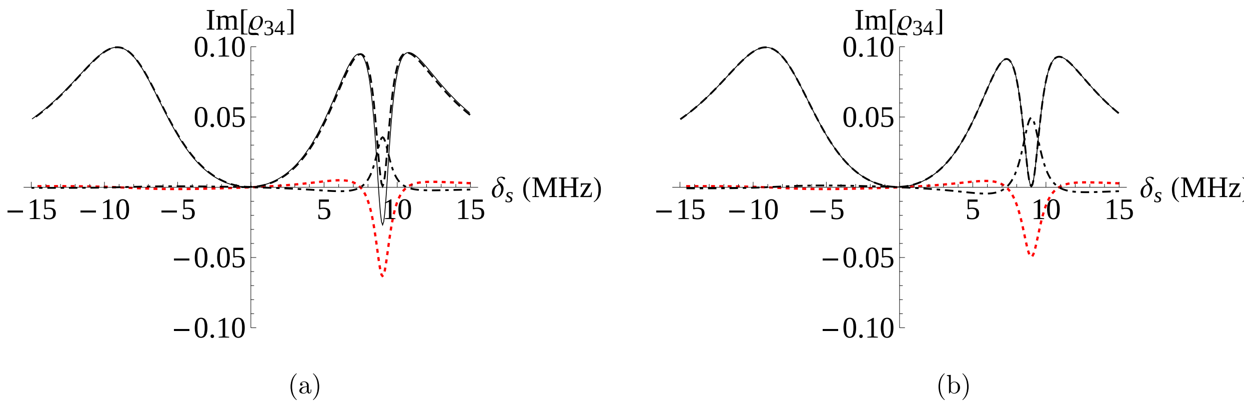

Figure 2.13: Im[ϱ_{34}] versus signal-field detuning δ_s. (a) $\Omega_\mathrm{s} = 0.15\gamma_4$ and $\Omega_\mathrm{p} = 0.2\gamma_4$. (b) $\Omega_\mathrm{s} = \Omega_\mathrm{p} = 0.2\gamma_4$ for $\gamma_4 = 18$ MHz, $\gamma_3 = 10$ kHz, $\gamma_2 = 40$ kHz, $\Omega_c = \gamma_4$, $\delta_\mathrm{s} = 9$ MHz and $\delta_\mathrm{c} = 0$, with all terms of Eq. (2.5.14) included (solid line), $\varrho_{41} \equiv 0$ imposed (dashed line), the gain term (dotted red line) and the nonlinear absorption term (dotted-dashed line).

The amplification can be understood as a Raman gain by ignoring level $|2\rangle$, and considering only the Λ system that corresponds to the three levels $|1\rangle$, $|3\rangle$ and $|4\rangle$. Under the two-photon resonance condition, the probe pumps and the signal behave as a Stokes field [75–77]. However, for perfect EIT at $\delta_\mathrm{p} = \delta_\mathrm{s}$, Raman gain can be observed in the signal profile without population inversion between the states of the Raman transition. But, it still needs to overcome the nonlinear absorption in the system by satisfying following condition

$$\varrho_{11}|\Omega_\mathrm{p}|^2 > \varrho_{33}|\Omega_\mathrm{s}|^2 \tag{2.5.15}$$

to amplify the signal field (Stokes).

EIT effects introduce new physics, specifically the following normal Raman-gain conditions that are not required in our system: The pump does not need to be much stronger than the Stokes field, population inversion of the lower levels is not required (but still requires validation of (2.5.11) and (2.5.15), and detuning from the upper level can be minor.

Equations (2.5.10) and (2.5.14) show the dependence on population differences $\varrho_{11} - \varrho_{44}$ and $\varrho_{33} - \varrho_{44}$, which reduces to the usual Raman population condition $\varrho_{33} - \varrho_{11}$ in the limit $|\Omega_\mathrm{s}| = |\Omega_\mathrm{p}|$. From (2.5.11) and (2.5.15), amplifying one field means increasing the absorption of the other. When $\varrho_{11}|\Omega_p|^2 = \varrho_{33}|\Omega_s|^2$ the gain term will cancel the nonlinear absorption in both Eq. (2.5.10) and Eq. (2.5.14), and only the linear response survives for both the probe and signal fields, as shown in Figs. 2.11(b) and 2.13(b).

2.5.3 Semi-Classical Dressed-State Analysis

In this section, we further investigate using semi-classical dressed picture [39, 78, 79]. Although the semi-classical dressed equations may not provide analytical simplification, they do help obtain interpretations of the ongoing physical processes, which could be helpful in understanding the atom-field interactions. This differs from the conventional dressed atom picture, in which the field is assumed to be classical, while in the conventional dressed atom picture the electromagnetic field is quantized.

We assume the bare states $|2\rangle$ and $|4\rangle$ are strongly coupled by Ω_c, whereas Ω_p and Ω_s provide weak coupling between $|1\rangle$ and $|4\rangle$, and $|3\rangle$ and $|4\rangle$ respectively. The semi-classical dressed basis is obtained by applying a unitary transformation on the bare basis state vector

$$|D\rangle = \hat{U}_\mathrm{T}\,|\psi\rangle\,, \tag{2.5.16}$$

where $|D\rangle$ is the dressed state with basis vectors $|+\rangle$, $|-\rangle$, $|D_1\rangle$, and $|D_3\rangle$, $|\psi\rangle$ is the bare state with basis vectors $|1\rangle$, $|2\rangle$, $|3\rangle$, and $|4\rangle$, and $\hat{U}_\mathrm{T}$ is the unitary transformation matrix defined by

$$\hat{U}_\mathrm{T} = \begin{pmatrix} 1 & 0 & 0 & 0 \\ 0 & \vartheta & 0 & \vartheta\varsigma \\ 0 & 0 & 1 & 0 \\ 0 & -\vartheta\varsigma & 0 & \vartheta \end{pmatrix} \tag{2.5.17}$$

The dressed state $|+\rangle$ is symmetric coherent superposition of the two bare states $|2\rangle$ and $|4\rangle$, and the dressed state $|-\rangle$ is antisymmetric coherent superposition of the two bare states $|2\rangle$

and $|4\rangle$, while the dresses states $|D_1\rangle$ and $|D_3\rangle$ are the same as $|1\rangle$ and $|3\rangle$ respectively in the bare picture. That is

$$|+\rangle = \vartheta\varsigma\,|4\rangle + \vartheta\,|2\rangle\,, \tag{2.5.18}$$

$$|-\rangle = \vartheta\,|4\rangle - \vartheta\varsigma\,|2\rangle\,, \tag{2.5.19}$$

$$|D_1\rangle = |1\rangle\,, \tag{2.5.20}$$

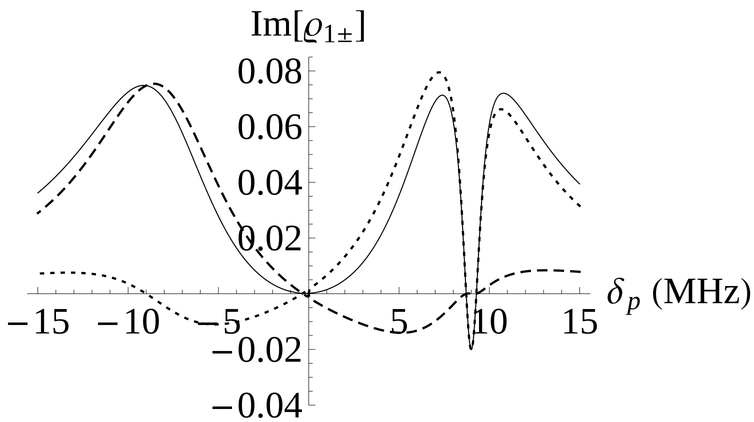

Figure 2.14: Plot of $\mathrm{Im}(\varrho_{1\pm})$ versus probe detuning δ_p for the same parameters as in Fig. 2.13(a) with ϱ_{1+} (dashed line), ϱ_{1-} (dotted line) and $\varrho_{1+}+\varrho_{1-}$ (solid line).

and

$$|D_3\rangle = |3\rangle\,, \tag{2.5.21}$$

where $\varsigma := \frac{R+\delta_\mathrm{c}}{\Omega_\mathrm{c}}$, with $R := \sqrt{|\Omega_\mathrm{c}|^2+\delta_\mathrm{c}^2}$ and $\vartheta := \frac{1}{\sqrt{1+|\varsigma|^2}}$. For simplification, we assume the Rabi frequency to be real. The dressed state $|+\rangle$ has an eigenvalue shift from state $|4\rangle$ by $\omega_+ = \frac{\delta_\mathrm{c}+R}{2}$, and $|-\rangle$ has an eigenvalue shift by $\omega_- = \frac{\delta_\mathrm{c}-R}{2}$. For $\delta_\mathrm{c}=0$, $\omega_+ = \frac{\Omega_\mathrm{c}}{2}$ and $\omega_- = -\frac{\Omega_\mathrm{c}}{2}$. The ⋔ atom-field configuration in the semi-classical dressed state for a strong coupling field are shown in Fig. 2.1(b).

Mathematically, the semi-classical dressed density matrix is obtained by the unitary transformation [78, 79]

$$\varrho \mapsto \hat{U}_\mathrm{T}\varrho\hat{U}_\mathrm{T}^\dagger. \tag{2.5.22}$$

In this semi-classical dressed basis

$$\varrho_{1-} = \left(\vartheta\varsigma + \frac{i\vartheta\Omega_{\rm c}}{\gamma_2 - 2i\delta_{\rm pc}}\right)\varrho_{14}, \tag{2.5.23}$$

and

$$\varrho_{1+} = \left(\vartheta - \frac{i\vartheta\varsigma\Omega_{\rm c}}{\gamma_2 - 2i\delta_{\rm pc}}\right)\varrho_{14}, \tag{2.5.24}$$

as plotted in Fig. 2.14. Equations (2.5.23) and (2.5.24) are useful because the undressed state ϱ_{14} corresponds to the interfering channel described by $\varrho_{1\pm}$. Using Figs. 2.11, 2.14, and 2.1(b) we have clear interpretation of the ongoing physical processes.

First, consider the case of $\Omega_{\rm s} \equiv 0$, which decouples $|3\rangle$ from the dynamics and restores ordinary Λ-atom EIT. The semi-classical dressed picture of Fig. 2.1(b) clarifies the dynamics where we introduce two dressed states $|\pm\rangle$. The $\Omega_{\rm s} \equiv 0$ line in Fig. 2.11 shows two EIT absorption peaks at $\delta_{\rm p\pm}$, corresponding to $|1\rangle \leftrightarrow |\pm\rangle$ transitions respectively.

For $\Omega_{\rm s} \neq 0$, Fig. 2.11 shows that the second absorption peak at $\delta_{\rm p+}$ is split by a transparency window with negative absorption (i.e. gain). This splitting of the second peak is due to the formation of a double-Λ electronic structure [80], as shown in Fig. 2.1(b). Specifically, level $|+\rangle$ gives the absorption peak at $\delta_{\rm p-}$, but the peak at $\delta_{\rm p+}$ is split by competing transitions $|1\rangle \leftrightarrow |-\rangle$ and $|3\rangle \leftrightarrow |-\rangle$.

This explanation of competing transitions clarifies the splitting of the $\delta_{\rm p}^{+}$ peak, but not the presence of gain in the second EIT window ($\delta_{\rm p} = \delta_{\rm s}$). In Fig. 2.14, gain in ϱ_{1+} is apparent over a wide domain of $\delta_{\rm p}$, but is cancelled everywhere in the sum $\varrho_{1+} + \varrho_{1-}$ except the narrow second EIT window. This gain is due to off-resonant driving to one of the upper levels, and $\mathrm{Im}\varrho_{1\pm}$ contributing to $\mathrm{Im}\varrho_{14}$. The gain for the $|1\rangle \leftrightarrow |+\rangle$ is overcome by the loss due to driving the $|1\rangle \leftrightarrow |-\rangle$ transition at or near resonance. This loss negates the gain for the probe transition, except in the narrow window, as shown in Fig. 2.14.

2.6 Summary

To summarize, we have shown that the steady-state atomic population for a $\pitchfork$ atom-field system depends on probe-field detuning, due to the dark-state reliance of probe-field detuning. Thus, changing the probe-field detuning modifies the steady-state population in each energy state if the probe field has comparable strength to the signal field, even if both are relatively weak compared to the coupling-field strength. However, the dependence of atomic population on probe-field detuning decreases as the probe-field strength become weaker than the signal-field strength.

We have also shown that $\pitchfork$ atom-field electronic structure in a four-levels atom can produce significant outcomes; in particular, DDEIT with gain for constant-population assumptions.

EIT effects introduce new physics, specifically the following normal Raman-gain conditions that are not required for our system: The pump does not need to be much stronger than the Stokes field, population inversion of the lower levels is not required, though it requires validation of (2.5.11) and (2.5.15), and detuning from the upper level can be minor.

We used a semi-classical dressed picture to connect the $\pitchfork$ electronic structure to a double-Λ electronic structure, to explain how each signal and probe fields interacts with DEIT windows. This representation simplifies the master equation, and provides an intuitive understanding of $\pitchfork$ atom-field coherent phenomena, particularly those that would otherwise seem complicated and dispersed.

In the well-studied case of DEIT, a signal and a probe would each have an EIT window, and both could be decelerated at the same time and interact via XPM. In our case, DDEIT exhibits DEIT for both the first and second EIT windows of the signal and the probe.

Chapter 3

Linear and Nonlinear-Optical Susceptibility of Tripod Atom-Field Configuration

3.1 Introduction

In the previous chapter, the density matrix element was used to characterize the absorption and dispersion of an applied field within the medium. However, the origin of the relation connecting the density matrix element to the optical properties, in response to a material system of an applied field, is discussed here. In this chapter, the derivation of the wave equation from Maxwell's equation, in which the polarization acts as a source term, will be addressed first. With the help of the quantum mechanical rule discussed in (2.3.2), an expression for the mean value of the polarization or an ensemble of four-level atoms of $\pitchfork$ structure is found, in terms of density matrix elements. The relation is used to extract all information about linear and nonlinear optical properties of the $\pitchfork$ atom-field system in response to the applied field, as well as to offer a full description of the optical system. At this stage, cases of low temperature are focused on, and the Doppler broadening effect is ignored, as this will be discussed in Chapter 6.

Concerning the linear optical response, the required conditions were derived, to attain minimum absorption of the probe and signal fields at the EIT windows and to determine the parameters affecting the width of transparency windows and group velocities in the region of the EIT windows. Further, at the end of the linear optical susceptibility investigation, the conditions required to match the group velocities of the probe and signal fields at the region of the second EIT window were discovered.

For the nonlinear optical response of the $\pitchfork$ atom-field configuration, the phase- matching conditions are satisfied automatically. The propagation-probe and signal waves are subject to two types of nonlinear-phase shift. One is due to the action of the propagation wave, which produces SPM, and the second is due to the action of other waves, which produce XPM. A technique to enhance the nonlinear-phase shift by controlling the propagation wave detuning was offered. Additionally, the existence of Raman gain under EIT conditions was revealed, displaying new conditions in which Raman gains can occur.

3.2 Propagation of Electromagnetic Wave in Nonlinear Medium

To examine light propagation through the medium, Maxwell's equations are used as a starting point for macroscopic variables in differential forms. The divergence relations are [2, 81]

$$\begin{aligned} \nabla \cdot \boldsymbol{D} &= \rho_{\text{ch}}, \\ \nabla \cdot \boldsymbol{B} &= 0, \end{aligned} \tag{3.2.1}$$

and the curl relations are [2, 81]

$$\begin{aligned} \nabla \times \boldsymbol{E} &= -\frac{\partial \boldsymbol{B}}{\partial t}, \\ \nabla \times \boldsymbol{H} &= \frac{\partial \boldsymbol{D}}{\partial t} + \boldsymbol{J}, \end{aligned} \tag{3.2.2}$$

where ρ_{ch} and $\boldsymbol{J}$ are the electric charge and current densities, respectively. In this thesis, material is dealt with that has no free charges, and in which there is no current flow. Therefore, ρ_{ch} and $\boldsymbol{J}$ will always be zero. Nonmagnetic media is the focus here, for which the following can be written

$$\boldsymbol{B} = \mu_0 \boldsymbol{H}, \tag{3.2.3}$$

where $\boldsymbol{B}$ is the magnetic-induction vector, $\boldsymbol{H}$ is the magnetic field and μ_0 is free-space permeability. The electric induction $\boldsymbol{D}$ is related to the electric field and induced-dipole polarization $\boldsymbol{P}$ through the constitutive relation [2, 81]

$$\boldsymbol{D} = \epsilon_0 \boldsymbol{E} + \boldsymbol{P}, \tag{3.2.4}$$

with ϵ_0 being free-space permittivity of . The higher order multi-pole polarizations are neglected because they are very weak in comparison. In vacuum, $\boldsymbol{P}$ is zero. When light propagate in the medium, however, the electric field causes distortion in atomic structure, creating local dipole moments, and thereby induced a polarization depends on $\boldsymbol{E}$. The dependence of $\boldsymbol{P}$ on the time history, spatial inhomogeneities, and field intensity leads to interesting and nontrivial behavior in the propagation of light. When the medium is isotropic (meaning that the polarization is parallel to the applied electric field, and that each component of $\boldsymbol{P}$ is linearly proportional to each component of $\boldsymbol{E}$) and responds instantaneously to the electric field, $\boldsymbol{P}$ is simply [81]

$$\boldsymbol{P} = \epsilon_0 \boldsymbol{\chi}(\omega) \boldsymbol{E}, \tag{3.2.5}$$

where the electric susceptibility $\boldsymbol{\chi}(\omega)$ in this case is scalar. Appendix C.1 further discusses the relationship between the applied electric field and the induced electric polarization.

To derive the vector wave propagation equation of an electric field, $\nabla \times$ is operated on the first equation of (3.2.2), and operate $\mu_0 \frac{\partial}{\partial t}$ on the second. Next, we use Eq. (3.2.3) to substitute $\boldsymbol{H}$ by $\boldsymbol{B}$. By subtracting the two equations, the following is obtained [2]

$$\nabla \times \nabla \times \boldsymbol{E} = -\frac{1}{c^2} \frac{\partial^2 \boldsymbol{E}}{\partial t^2} - \mu_0 \frac{\partial^2 \boldsymbol{P}}{\partial t^2}. \tag{3.2.6}$$

This is the most general form of the wave equation in nonlinear optics. It can be simplified using the calculus identity

$$\nabla \times \nabla \times \boldsymbol{F} = \nabla(\nabla \cdot \boldsymbol{F}) - \nabla^2 \boldsymbol{F}. \tag{3.2.7}$$

Then, (3.2.6) becomes

$$\nabla(\nabla \cdot \boldsymbol{E}) - \nabla^2 \boldsymbol{E} = -\frac{1}{c^2} \frac{\partial^2 \boldsymbol{E}}{\partial t^2} - \mu_0 \frac{\partial^2 \boldsymbol{P}}{\partial t^2}. \tag{3.2.8}$$

The first term in the left-hand side vanishes in linear optics of isotropic media because $\nabla \cdot \boldsymbol{D} = 0$, which implies that $\nabla \cdot \boldsymbol{E} = 0$. However, in nonlinear optics this term is generally nonvanishing, due to the general relation (3.2.4). However, vanishes if $\boldsymbol{E}$ is transverse, infinite plane wave or can be neglected because it is very small specially when the slowly varying amplitude approximation is valid [81]. This study is concerned with cases in which a slowly varying amplitude approximation is valid. Then, the wave equation (3.2.8) can be taken to have the form

$$\nabla^2 \boldsymbol{E} - \frac{1}{c^2}\frac{\partial^2 \boldsymbol{E}}{\partial t^2} = \mu_0 \frac{\partial^2 \boldsymbol{P}}{\partial t^2}. \tag{3.2.9}$$

Depending on the particular problem, it may be decided to work in the time domain, as in (3.2.9) or instead transform to the frequency domain, by expressing $\boldsymbol{E}(t)$ and $\boldsymbol{P}(t)$ in terms of their Fourier transforms given by (C.1.5) and (C.1.6) of Appendix C, respectively.

$$\nabla^2 \boldsymbol{E}(\omega) + \frac{\omega^2}{c^2}\boldsymbol{E}(\omega) = -\mu_0 \omega^2 \boldsymbol{P}(\omega), \tag{3.2.10}$$

where the following fact is used

$$\frac{\partial^n}{\partial t} F(t) = (\mathrm{i}\omega)^n F(\omega). \tag{3.2.11}$$

3.3 Microscopic Polarization

To obtain the expectation value of the atomic polarization, a macroscopic electric field, $\boldsymbol{E}(z,t)$,), is applied to a small volume $\mathscr{V}$ of the medium. We assume that $\mathscr{V}$ contains N four-level atoms, and denotes the position vector of the $\jmath$ electron by $\boldsymbol{r}_\jmath$. Then, the dipole moment of the charged particles within the small volume $\mathscr{V}$ is [77]

$$\boldsymbol{d} = -e \sum_{\jmath} \boldsymbol{r}_\jmath, \tag{3.3.1}$$

and the expectation value of the atomic polarization in terms of the dipole moment is [77]

$$\boldsymbol{P} = \frac{N\langle \boldsymbol{d} \rangle}{\mathscr{V}}. \tag{3.3.2}$$

The expectation value of the dipole moment is determined by Eq. (2.3.2)

$$\boldsymbol{P} = \frac{N}{\mathscr{V}} \operatorname{Tr}(\boldsymbol{d}\rho). \tag{3.3.3}$$

By evaluating the trace for the four-level system, the following is obtained

$$\boldsymbol{P} = \frac{N}{\mathscr{V}}(\boldsymbol{d}_{21}\rho_{12} + \boldsymbol{d}_{31}\rho_{13} + \boldsymbol{d}_{41}\rho_{14} + \boldsymbol{d}_{32}\rho_{23} + \boldsymbol{d}_{42}\rho_{24} + \boldsymbol{d}_{43}\rho_{34} + \text{c.c.}), \tag{3.3.4}$$

with ρ_{ij} being the density matrix element in the original frame. As the transitions between the states $|1\rangle$, $|2\rangle$ and $|3\rangle$ are dipole forbidden, we use (2.2.9), which reduces (3.3.4) to

$$\boldsymbol{P} = \mathcal{N}(\boldsymbol{d}_{41}\rho_{14} + \boldsymbol{d}_{42}\rho_{24} + \boldsymbol{d}_{43}\rho_{34} + \text{c.c.}), \tag{3.3.5}$$

with $\mathcal{N} = \frac{N}{\mathscr{V}}$ as the atom density. In the following, the notation $|\imath\rangle \to |\jmath\rangle$ indicates a one-way transition, that is, a transition from level $|\imath\rangle$ to level $|\jmath\rangle$. The notation $|\imath\rangle \leftrightarrow |\jmath\rangle$ indicates two-way transitions, that is a transition from level $|\imath\rangle$ to level $|\jmath\rangle$ and from level $|\jmath\rangle$ back to level $|\imath\rangle$.

Each term in Eq. (3.3.5) describes the induced polarization of the $|i\rangle \to |j\rangle$ transition. In the atom-field system, the optical response of the medium to the probe field and the signal field is studied, so the terms that oscillate with ω_{p} and ω_{s} are tracked. As the probe field is coupled $|1\rangle \leftrightarrow |4\rangle$ transition, these terms exist in $\boldsymbol{d}_{41}\rho_{14}$ and its conjugate. The term $\boldsymbol{d}_{41}\rho_{14}$ describes the induced optical polarization by the probe field in the $|1\rangle \to |4\rangle$ transition direction, while its conjugate $\boldsymbol{d}_{14}\rho_{41}$ describes the induced optical polarization by the probe field in the $|4\rangle \to |1\rangle$ transition direction. As with the signal field, the terms that oscillate with ω_{s} exist in $\boldsymbol{d}_{43}\rho_{34}$ and its conjugate. Then, the following can be written as

$$\begin{aligned}
\boldsymbol{p}_{\text{c}}e^{\text{i}\omega_{\text{c}}t} &= \mathcal{N}\boldsymbol{d}_{42}\rho_{24} = \mathcal{N}\boldsymbol{d}_{42}\varrho_{24}e^{\text{i}\omega_{\text{c}}t}, &\quad \boldsymbol{p}^*_{\text{c}}e^{-\text{i}\omega_{\text{c}}t} &= \mathcal{N}\boldsymbol{d}_{24}\rho_{42} = \mathcal{N}\boldsymbol{d}_{24}\varrho_{42}e^{-\text{i}\omega_{\text{c}}t}, \\
\boldsymbol{p}_{\text{p}}e^{\text{i}\omega_{\text{p}}t} &= \mathcal{N}\boldsymbol{d}_{41}\rho_{14} = \mathcal{N}\boldsymbol{d}_{41}\varrho_{14}e^{\text{i}\omega_{\text{p}}t}, &\quad \boldsymbol{p}^*_{\text{p}}e^{-\text{i}\omega_{\text{p}}t} &= \mathcal{N}\boldsymbol{d}_{14}\rho_{41} = \mathcal{N}\boldsymbol{d}_{14}\varrho_{41}e^{-\text{i}\omega_{\text{p}}t}, \\
\boldsymbol{p}_{\text{s}}e^{\text{i}\omega_{\text{s}}t} &= \mathcal{N}\boldsymbol{d}_{43}\rho_{34} = \mathcal{N}\boldsymbol{d}_{43}\varrho_{34}e^{\text{i}\omega_{\text{s}}t}, &\quad \boldsymbol{p}^*_{\text{s}}e^{-\text{i}\omega_{\text{s}}t} &= \mathcal{N}\boldsymbol{d}_{34}\rho_{43} = \mathcal{N}\boldsymbol{d}_{34}\varrho_{43}e^{-\text{i}\omega_{\text{s}}t},
\end{aligned} \tag{3.3.6}$$

Using Appendix C Eqs. (C.1.2) and (C.1.24) in vector notation, optical susceptibility up to the third order of the density matrix element is related by

$$\begin{aligned}
&\epsilon_0\boldsymbol{\chi}^{(1)}(\omega_{\text{p}})\boldsymbol{\xi}_{\text{p}}(t) + \epsilon_0\sum_l K(\omega_{\text{p}};\omega_{\text{c}},\omega_{\text{p}},\omega_{\text{s}})\boldsymbol{\chi}^{(2)}(\omega_{\text{p}};\omega_{\text{c}},\omega_{\text{p}},\omega_{\text{s}})\boldsymbol{\xi}_l(t)\boldsymbol{\xi}_{\text{p}}(t) \\
&+ \epsilon_0\sum_{ab} K(\omega_{\text{p}};\omega_{\text{c}},\omega_{\text{p}},\omega_{\text{s}})\boldsymbol{\chi}^{(3)}(\omega_{\text{p}};\omega_{\text{c}},\omega_{\text{p}},\omega_{\text{s}})\boldsymbol{\xi}_a(t)\boldsymbol{\xi}_b(t)\boldsymbol{\xi}_{\text{p}}(t) = \mathcal{N}\boldsymbol{d}_{41}\varrho_{14},
\end{aligned} \tag{3.3.7}$$

where K is defined in (C.1.15), and l, a and b varies over the different applied electric field modes. The signal field is similar

$$\epsilon_0 \boldsymbol{\chi}^{(1)}(\omega_\mathrm{s})\boldsymbol{\xi}_\mathrm{s}(t) + \epsilon_0 \sum_l K(\omega_\mathrm{s};\omega_\mathrm{c},\omega_\mathrm{p},\omega_\mathrm{s})\boldsymbol{\chi}^{(2)}(\omega_\mathrm{s};\omega_\mathrm{c},\omega_\mathrm{p},\omega_\mathrm{s})\boldsymbol{\xi}_l(t)\boldsymbol{\xi}_\mathrm{s}(t) \tag{3.3.8}$$
$$+ \epsilon_0 \sum_{ab} K(\omega_\mathrm{s};\omega_\mathrm{c},\omega_\mathrm{p},\omega_\mathrm{s})\boldsymbol{\chi}^{(3)}(\omega_\mathrm{s};\omega_\mathrm{c},\omega_\mathrm{p},\omega_\mathrm{s})\boldsymbol{\xi}_a(t)\boldsymbol{\xi}_b(t)\boldsymbol{\xi}_\mathrm{s}(t) = \mathcal{N}\boldsymbol{d}_{43}\varrho_{34}.$$

For centrosymmetric materials which display inversion symmetry, such as gases and liquids, $\boldsymbol{\chi}^{(2)}$ vanishes identically [81]. Then (3.3.7) and (3.3.8) reduces to following respectively

$$\epsilon_0 \boldsymbol{\chi}^{(1)}(\omega_\mathrm{p})\boldsymbol{\xi}_\mathrm{p}(t) + \epsilon_0 \sum_{ab} K(\omega_\mathrm{p};\omega_\mathrm{c},\omega_\mathrm{p},\omega_\mathrm{s})\boldsymbol{\chi}^{(3)}(\omega_\mathrm{p};\omega_\mathrm{c},\omega_\mathrm{p},\omega_\mathrm{s})\boldsymbol{\xi}_a(t)\boldsymbol{\xi}_b(t)\boldsymbol{\xi}_\mathrm{p}(t) = \mathcal{N}\boldsymbol{d}_{41}\varrho_{14}, \tag{3.3.9}$$

and

$$\epsilon_0 \boldsymbol{\chi}^{(1)}(\omega_\mathrm{s})\boldsymbol{\xi}_\mathrm{s}(t) + \epsilon_0 \sum_{ab} K(\omega_\mathrm{s};\omega_\mathrm{c},\omega_\mathrm{p},\omega_\mathrm{s})\boldsymbol{\chi}^{(3)}(\omega_\mathrm{s};\omega_\mathrm{c},\omega_\mathrm{p},\omega_\mathrm{s})\boldsymbol{\xi}_a(t)\boldsymbol{\xi}_b(t)\boldsymbol{\xi}_\mathrm{s}(t) = \mathcal{N}\boldsymbol{d}_{43}\varrho_{34}, \tag{3.3.10}$$

It is convenient to introduce $\boldsymbol{\chi}_\mathrm{p}$ and $\boldsymbol{\chi}_\mathrm{s}$ defined as

$$\boldsymbol{\chi}_\mathrm{p} = \boldsymbol{\chi}^{(1)}(\omega_\mathrm{p}) + \sum_{ab} K(\omega_\mathrm{p};\omega_\mathrm{c},\omega_\mathrm{p},\omega_\mathrm{s})\boldsymbol{\chi}^{(3)}(\omega_\mathrm{p};\omega_\mathrm{c},\omega_\mathrm{p},\omega_\mathrm{s})\boldsymbol{\xi}_a(t)\boldsymbol{\xi}_b(t), \tag{3.3.11}$$

and

$$\boldsymbol{\chi}_\mathrm{s} = \boldsymbol{\chi}^{(1)}(\omega_\mathrm{s}) + \sum_{ab} K(\omega_\mathrm{s};\omega_\mathrm{c},\omega_\mathrm{p},\omega_\mathrm{s})\boldsymbol{\chi}^{(3)}(\omega_\mathrm{s};\omega_\mathrm{c},\omega_\mathrm{p},\omega_\mathrm{s})\boldsymbol{\xi}_a(t)\boldsymbol{\xi}_b(t), \tag{3.3.12}$$

respectively. Then (3.3.9) and (3.3.10) become

$$\epsilon_0 \boldsymbol{\chi}_\mathrm{p}(\omega_\mathrm{p})\boldsymbol{\xi}_\mathrm{p}(t) = \mathcal{N}\boldsymbol{d}_{41}\varrho_{14}, \tag{3.3.13}$$

and

$$\epsilon_0 \boldsymbol{\chi}_\mathrm{s}(\omega_\mathrm{s})\boldsymbol{\xi}_\mathrm{s}(t) = \mathcal{N}\boldsymbol{d}_{43}\varrho_{34}, \tag{3.3.14}$$

respectively. From the two relations above, it can be concluded that the rotated frame density matrix elements ϱ_{14} and ϱ_{34} carry all the optical responses of the medium to the probe and signal fields, respectively. As the imaginary part of optical susceptibility describes the absorption, and the real part describes the dispersion, the density matrix elements ϱ_{14} and ϱ_{34} will give the same description. The imaginary part of ϱ_{14} and ϱ_{34} describe how the probe and signal fields are absorbed and amplified by the medium, while the dispersion of the probe and signal are described by the real parts of ϱ_{14} and ϱ_{34} respectively.

3.4 Linear Optical Susceptibility and Linear Optical Parameters.

First, the solutions of the wave equation in the linear regime are considered. An expression for polarization is obtained from (C.1.8) for the case $m = 1$

$$\boldsymbol{P}(\omega) = \epsilon_0 \boldsymbol{\chi}^{(1)}(\omega)\boldsymbol{E}(\omega). \tag{3.4.1}$$

By inserting (3.4.1) into (3.2.10) the following is obtained

$$\nabla^2 \boldsymbol{E}(\omega) + \frac{\omega^2}{c^2}\left[1 + \boldsymbol{\chi}^{(1)}(\omega)\right]\boldsymbol{E}(\omega) = 0. \tag{3.4.2}$$

The dielectric tensor is defined as

$$\boldsymbol{\epsilon}(\omega) = 1 + \boldsymbol{\chi}^{(1)}(\omega), \tag{3.4.3}$$

then (3.4.2) becomes

$$\nabla^2 \boldsymbol{E}(\omega) + \frac{\omega^2}{c^2}\boldsymbol{\epsilon}(\omega)\boldsymbol{E}(\omega) = 0. \tag{3.4.4}$$

Assuming that the dielectric tensor does not depend on the coordinates, (i.e.; homogeneous media), possible set of solutions are running waves

$$\boldsymbol{E}(r,\omega) = \boldsymbol{\xi}_0 e^{\pm\frac{\mathrm{i}\omega}{c}\sqrt{\boldsymbol{\epsilon}(\omega)}\cdot\boldsymbol{r}}. \tag{3.4.5}$$

For simplicity, it can be assumed that Eq. (3.4.5) describes a planar wave traveling along the z-axis. This depends on the exponential sign in (3.4.5) whether the wave is running into the positive or negative direction. If a wave running in a positive direction is selected, the following is obtained

$$\boldsymbol{E}(\omega) = \boldsymbol{\xi}_0 e^{\frac{\mathrm{i}\omega}{c}\sqrt{\epsilon(\omega)}z}. \tag{3.4.6}$$

$\boldsymbol{\xi}_0$ is the field amplitude at $z = 0$.

If (3.4.6) is examined in more detail, it is found that the dielectric function may be complex, hence it has imaginary and real parts. The square root will also be a complex function. Therefore, the following is produced

$$\sqrt{\epsilon(\omega)} = \mathrm{Re}\left[\sqrt{\epsilon(\omega)}\right] + \mathrm{iIm}\left[\sqrt{\epsilon(\omega)}\right]. \tag{3.4.7}$$

By substituting (3.4.7) into (3.4.6) the following occurs

$$\boldsymbol{E}(\omega) = \boldsymbol{\xi}_0 e^{\frac{\mathrm{i}\omega}{c}\mathrm{Re}\left[\sqrt{\epsilon(\omega)}\right]z - \frac{\omega}{c}\mathrm{Im}\left[\sqrt{\epsilon(\omega)}\right]z}. \tag{3.4.8}$$

Equation (3.4.8) describes a damped wave with a z-dependent amplitude

$$\boldsymbol{E}(\omega) = \boldsymbol{\xi}_0 e^{-\frac{\omega}{c}\mathrm{Im}\left[\sqrt{\epsilon(\omega)}\right]z}. \tag{3.4.9}$$

Further, the phase

$$\phi = \frac{\omega}{c}\mathrm{Re}\left[\sqrt{\epsilon(\omega)}\right]z. \tag{3.4.10}$$

Therefore, the propagation constant is

$$k(\omega) = \frac{\omega}{c}n(\omega), \tag{3.4.11}$$

which has reciprocal length unit, and the refractive index $n(\omega)$

$$n(\omega) = \mathrm{Re}\left[\sqrt{\epsilon(\omega)}\right]. \tag{3.4.12}$$

The intensity of wave is proportional to the square of the field modulus

$$I \propto |\boldsymbol{E}|^2, \tag{3.4.13}$$

the intensity damps inside the medium as

$$I = I_0 e^{-2\frac{\omega}{c}\mathrm{Im}\left[\sqrt{\epsilon(\omega)}\right]z} = I_0 e^{-\alpha z}, \tag{3.4.14}$$

where I_0 is the intensity of the light at the entrance of medium. This exponential decay of light intensity for wave traveling in a lossy medium is well known as Lambert's law of absorption with a frequency-dependent absorption coefficient α defined as

$$\alpha(\omega) = 2\frac{\omega}{c}\mathrm{Im}\left[\sqrt{\epsilon(\omega)}\right]. \tag{3.4.15}$$

The absorption coefficient is given in reciprocal length units. The reciprocal value of the absorption coefficient is sometimes called penetration depth.

Another interesting parameter measure how fast the actual energy travels can be determined from the fundamental relation (3.4.11), and is called group velocity. The group velocity is important when there are number of electric waves with slightly different frequencies travel together, each with different phase velocity

$$v_p = \frac{\omega}{k(\omega)}. \tag{3.4.16}$$

The group velocity then, is the velocity of envelope wave of all the individual different frequencies defined by

$$v_{\mathrm{g}} = \frac{\partial \omega}{\partial k(\omega)}. \tag{3.4.17}$$

Using (3.4.11), the following can be written

$$\frac{\partial k(\omega)}{\partial \omega} = \frac{n(\omega)}{c} + \frac{\omega}{c}\frac{\partial n(\omega)}{\partial \omega}. \tag{3.4.18}$$

Then the group velocity is just the reciprocal of (3.4.18)

$$v_{\mathrm{g}} = \frac{c}{n(\omega) + \omega\frac{\partial n(\omega)}{\partial \omega}}. \tag{3.4.19}$$

Now, all linear optical parameters necessary to describe the light propagation inside an optical medium are in existence. Once the optical susceptibility is known, the optical parameters given by (3.4.11), (3.4.15) and (3.4.19) can be determined.

Before further describing the atom-field system, the optical parameter equations, (3.4.12) and (3.4.15), are simplified, focusing on the case of nonlinear optics, where the imaginary and real parts of the linear optical susceptibility are less than one, which implies that $|\chi(\omega)| < 1$. For

$$\sqrt{\epsilon(\omega)} = \sqrt{1 + \chi^{(1)}(\omega)}, \tag{3.4.20}$$

we can use the Taylor series of $\sqrt{1 + \chi^{(1)}(\omega)}$ about $\chi^{(1)}(\omega) = 0$ that converges for $|\chi(\omega)| \leq 1$

$$\sqrt{1 + \chi^{(1)}(\omega)} = 1 + \frac{\chi^{(1)}(\omega)}{2} - \frac{\left(\chi^{(1)}(\omega)\right)^2}{8} + \frac{\left(\chi^{(1)}(\omega)\right)^3}{16} + \cdots , \tag{3.4.21}$$

Keeping only the first two terms, while neglecting the higher order terms we get

$$\sqrt{1 + \chi^{(1)}(\omega)} \approx 1 + \frac{\chi^{(1)}(\omega)}{2} = 1 + \frac{\mathrm{Re}\left[\chi^{(1)}(\omega)\right]}{2} + \frac{\mathrm{Im}\left[\chi^{(1)}(\omega)\right]}{2}. \tag{3.4.22}$$

Then, the real and the imaginary parts of the optical susceptibility can be written as

$$\mathrm{Re}\left[\sqrt{\epsilon(\omega)}\right] \approx 1 + \frac{\mathrm{Re}\left[\chi^{(1)}(\omega)\right]}{2}, \tag{3.4.23}$$

and

$$\mathrm{Im}\left[\sqrt{\epsilon(\omega)}\right] \approx \frac{\mathrm{Im}\left[\chi^{(1)}(\omega)\right]}{2}. \tag{3.4.24}$$

Consequently, Eq. (3.4.12) becomes

$$n(\omega) \approx 1 + \frac{\mathrm{Re}\left[\chi^{(1)}(\omega)\right]}{2}, \tag{3.4.25}$$

and Eq. (3.4.15) can be written as

$$\alpha(\omega) \approx \frac{\omega}{c}\mathrm{Im}\left[\chi^{(1)}(\omega)\right]. \tag{3.4.26}$$

Using Eq. (3.3.13) with the definition of the Rabi frequency Eq. (2.2.11), the probe-field optical susceptibility can be written as

$$\chi_{\mathrm{p}}(\omega) = \eta_{\mathrm{p}}\frac{\varrho_{14}}{\Omega_{\mathrm{p}}}, \tag{3.4.27}$$

with ϱ_{14} is defined by (2.5.10), and

$$\eta_{\mathrm{p}} = \frac{\mathcal{N}\left|\boldsymbol{d}_{41}\right|^2}{\epsilon_0\hbar}. \tag{3.4.28}$$

As with the probe field, using (3.3.14) and the definition Rabi frequency in (2.2.11), it is possible to write the signal-field optical susceptibility, in term of the density matrix element as

$$\chi_{\mathrm{s}}(\omega) = \eta_{\mathrm{s}}\frac{\varrho_{34}}{\Omega_{\mathrm{s}}}, \tag{3.4.29}$$

with ϱ_{34} is defined by (2.5.14), and

$$\eta_{\mathrm{s}} = \frac{\mathcal{N}\left|\boldsymbol{d}_{43}\right|^2}{\epsilon_0\hbar}. \tag{3.4.30}$$

From (3.4.27), (2.5.10) and (3.3.11) we can define the optical susceptibility of the atom-field system oscillating in the probe-field frequency, up to third order as

$$\chi_{\mathrm{p}}(\omega) = \chi_{\mathrm{p}}^{(1)}(\omega) + \chi_{\mathrm{p}}^{(\mathrm{NL})}(\omega), \tag{3.4.31}$$

where

$$\chi_{\mathrm{p}}^{(\mathrm{NL})}(\omega) = \chi_{\mathrm{p}_1}^{(3)}(\omega)\left|\xi_{\mathrm{p}_f}\right|^2 + \chi_{\mathrm{p}_2}^{(3)}(\omega)\left|\xi_{\mathrm{s}_f}\right|^2. \tag{3.4.32}$$

The first term of Eq. (3.4.31) is the linear optical susceptibility, defined by

$$\chi_{\mathrm{p}}^{(1)}(\omega) = \frac{\mathrm{i}\eta_{\mathrm{p}}(\varrho_{11}-\varrho_{44})}{\gamma_4 - 2\mathrm{i}\delta_{\mathrm{p}} + \frac{|\Omega_{\mathrm{c}}|^2}{\gamma_2 - 2\mathrm{i}\delta_{\mathrm{pc}}} + \frac{|\Omega_{\mathrm{s}}|^2}{\gamma_3 - 2\mathrm{i}\delta_{\mathrm{ps}}}}. \tag{3.4.33}$$

While the second term of Eq. (3.4.31) represents the nonlinear optical susceptibility, which is used to describe the nonlinear process, with

$$\chi_{\mathrm{p}_1}^{(3)}(\omega) = \frac{\mathrm{i}\eta_{\mathrm{p}_1}\left(\varrho_{11}-\varrho_{44}\right)}{(\gamma_3 - 2\mathrm{i}\delta_{\mathrm{ps}})\left(\Gamma_{43} + 2\mathrm{i}\delta_{\mathrm{s}} + \frac{|\Omega_{\mathrm{c}}|^2}{\Gamma_{32}+2\mathrm{i}\delta_{\mathrm{sc}}}\right)} \times \frac{1 - \frac{\gamma_4 - 2\mathrm{i}\delta_{\mathrm{p}} + \frac{|\Omega_{\mathrm{c}}|^2}{\gamma_2 - 2\mathrm{i}\delta_{\mathrm{pc}}}}{\gamma_4 - 2\mathrm{i}\delta_{\mathrm{p}} + \frac{|\Omega_{\mathrm{c}}|^2}{\gamma_2 - 2\mathrm{i}\delta_{\mathrm{pc}}} + \frac{|\Omega_{\mathrm{s}}|^2}{\gamma_3 - 2\mathrm{i}\delta_{\mathrm{ps}}}}}{\gamma_4 - 2\mathrm{i}\delta_{\mathrm{p}} + \frac{|\Omega_{\mathrm{c}}|^2}{\gamma_2 - 2\mathrm{i}\delta_{\mathrm{pc}}} + \frac{|\Omega_{\mathrm{s}}|^2}{\gamma_3 - 2\mathrm{i}\delta_{\mathrm{ps}}}}, \tag{3.4.34}$$

and

$$\chi_{\mathrm{p}_2}^{(3)}(\omega) = \frac{\mathrm{i}\eta_{\mathrm{sp}}\left(\varrho_{44}-\varrho_{33}\right)}{(\gamma_3 - 2\mathrm{i}\delta_{\mathrm{ps}})\left(\Gamma_{43} + 2\mathrm{i}\delta_{\mathrm{s}} + \frac{|\Omega_{\mathrm{c}}|^2}{\Gamma_{32}+2\mathrm{i}\delta_{\mathrm{sc}}}\right)} \times \frac{1}{\gamma_4 - 2\mathrm{i}\delta_{\mathrm{p}} + \frac{|\Omega_{\mathrm{c}}|^2}{\gamma_2 - 2\mathrm{i}\delta_{\mathrm{pc}}} + \frac{|\Omega_{\mathrm{s}}|^2}{\gamma_3 - 2\mathrm{i}\delta_{\mathrm{ps}}}}, \tag{3.4.35}$$

are the third-order nonlinear optical susceptibilities at probe-field frequency, with

$$\eta_{\mathrm{p}_1} = \frac{\mathcal{N}\left|\boldsymbol{d}_{41}\right|^4}{\hbar^3\epsilon_0}, \tag{3.4.36}$$

and

$$\eta_{\mathrm{sp}} = \frac{\mathcal{N}\left|\boldsymbol{d}_{41}\right|^2\left|\boldsymbol{d}_{43}\right|^2}{\hbar^3\epsilon_0}. \tag{3.4.37}$$

Similar to the probe-field case, the linear and third-order nonlinear optical susceptibilities for the signal field can be written using (3.4.29), (2.5.8) and (3.3.12) as

$$\chi_{\mathrm{s}}(\omega) = \chi_{\mathrm{s}}^{(1)}(\omega) + \chi_{\mathrm{s}}^{(\mathrm{NL})}(\omega), \tag{3.4.38}$$

with

$$\chi_{\mathrm{s}}^{(\mathrm{NL})}(\omega) = \chi_{\mathrm{s}_1}^{(3)}(\omega_{\mathrm{s}})\left|\xi_{\mathrm{s}_f}\right|^2 + \chi_{\mathrm{s}_2}^{(3)}(\omega)\left|\xi_{\mathrm{p}_f}\right|^2, \tag{3.4.39}$$

is the nonlinear optical susceptibility. The linear-optical susceptibility at signal-field frequency is defined by

$$\chi_{\mathrm{s}}^{(1)}(\omega) = \frac{\mathrm{i}\eta_{\mathrm{s}}\left(\varrho_{33}-\varrho_{44}\right)}{\Gamma_{43}-2\mathrm{i}\delta_{\mathrm{s}}+\frac{|\Omega_{\mathrm{c}}|^2}{\Gamma_{32}-2\mathrm{i}\delta_{\mathrm{sc}}}+\frac{|\Omega_{\mathrm{p}}|^2}{\gamma_3+2\mathrm{i}\delta_{\mathrm{ps}}}}. \tag{3.4.40}$$

The nonlinear terms of optical susceptibility present in Eq. (3.4.39) are defined by

$$\chi_{\mathrm{s}_1}^{(3)}(\omega) = \frac{\mathrm{i}\eta_{\mathrm{s}_1}\left(\varrho_{33}-\varrho_{44}\right)}{\left(\gamma_3+2\mathrm{i}\delta_{\mathrm{ps}}\right)\left(\gamma_4+2\mathrm{i}\delta_{\mathrm{p}}+\frac{|\Omega_{\mathrm{c}}|^2}{\gamma_2+2\mathrm{i}\delta_{\mathrm{pc}}}\right)} \times \frac{1-\frac{\Gamma_{43}-2\mathrm{i}\delta_{\mathrm{s}}+\frac{|\Omega_{\mathrm{c}}|^2}{\Gamma_{32}-2\mathrm{i}\delta_{\mathrm{sc}}}}{\Gamma_{43}-2\mathrm{i}\delta_{\mathrm{s}}+\frac{|\Omega_{\mathrm{c}}|^2}{\Gamma_{32}-2\mathrm{i}\delta_{\mathrm{sc}}}+\frac{|\Omega_{\mathrm{p}}|^2}{\gamma_3+2\mathrm{i}\delta_{\mathrm{ps}}}}}{\Gamma_{43}-2\mathrm{i}\delta_{\mathrm{s}}+\frac{|\Omega_{\mathrm{c}}|^2}{\Gamma_{32}-2\mathrm{i}\delta_{\mathrm{sc}}}+\frac{|\Omega_{\mathrm{p}}|^2}{\gamma_3+2\mathrm{i}\delta_{\mathrm{ps}}}}, \tag{3.4.41}$$

and

$$\chi_{\mathrm{s}_2}^{(3)}(\omega) = \frac{\mathrm{i}\eta_{\mathrm{sp}}\left(\varrho_{44}-\varrho_{11}\right)}{\left(\gamma_3+2\mathrm{i}\delta_{\mathrm{ps}}\right)\left(\gamma_4+2\mathrm{i}\delta_{\mathrm{p}}+\frac{|\Omega_{\mathrm{c}}|^2}{\gamma_2+2\mathrm{i}\delta_{\mathrm{pc}}}\right)} \times \frac{1}{\Gamma_{43}-2\mathrm{i}\delta_{\mathrm{s}}+\frac{|\Omega_{\mathrm{c}}|^2}{\Gamma_{32}-2\mathrm{i}\delta_{\mathrm{sc}}}+\frac{|\Omega_{\mathrm{p}}|^2}{\gamma_3+2\mathrm{i}\delta_{\mathrm{ps}}}}, \tag{3.4.42}$$

are the third-order nonlinear-optical susceptibilities at signal-field frequency, with

$$\eta_{\mathrm{s}_1} = \frac{\mathcal{N}\left|\boldsymbol{d}_{43}\right|^4}{\hbar^3\epsilon_0}, \tag{3.4.43}$$

This section has restricted its discussion to the linear term of optical susceptibility, represented by (3.4.33) and (3.4.40). Discussion of the nonlinear terms, described by Eqs. (3.4.34), (3.4.35), (3.4.41), and (3.4.42) follows later.

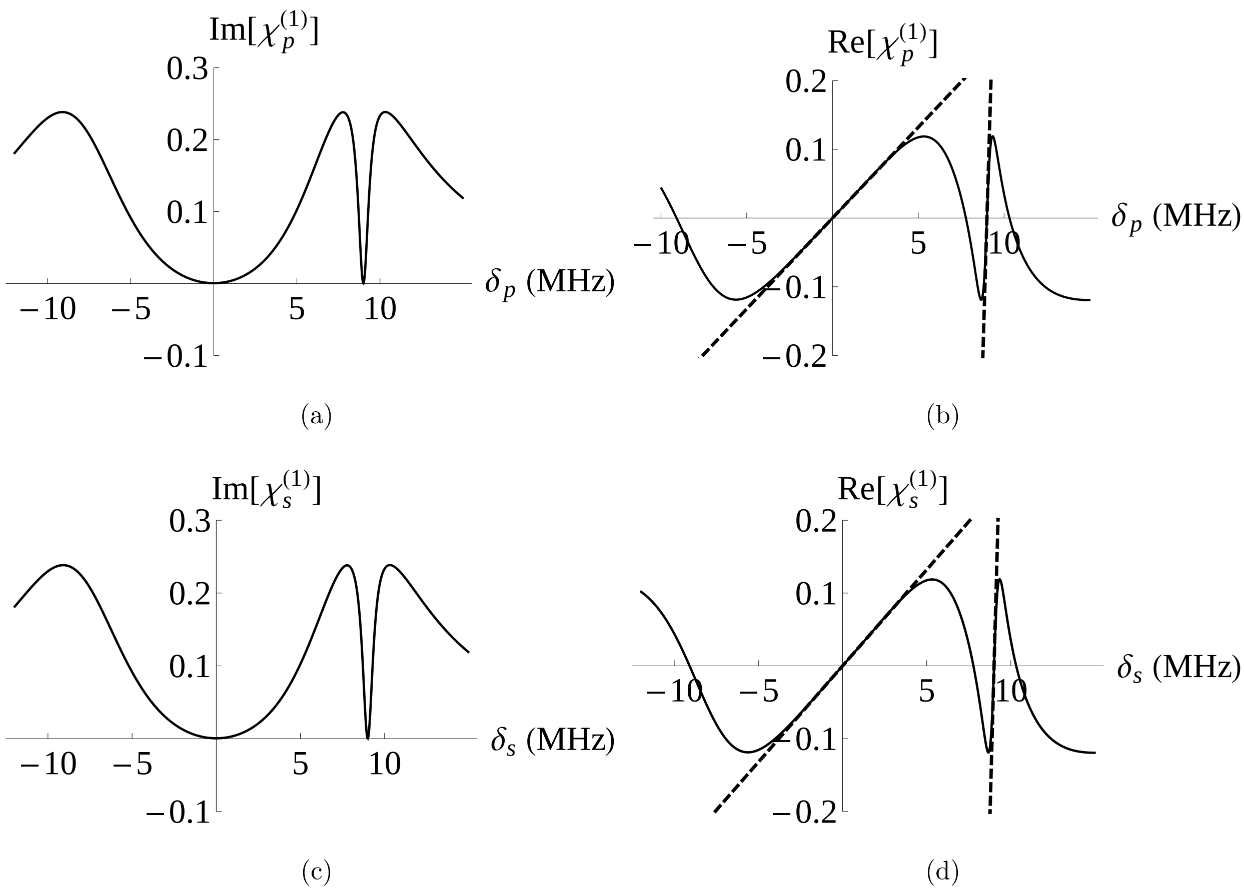

Figure 3.1: $\mathrm{Im}[\chi_l^{(1)}]$ and $\mathrm{Re}[\chi_l^{(1)}]$ as function of the field detuning δ_l, with $l \in \{\mathrm{p},\ \mathrm{s}\}$ and approximate linear equation determined by finding the derivative of dispersion using (6.3.30) (dashed line). (a),(b) $\Omega_\mathrm{s} = 0.2\gamma_4$ and $\delta_\mathrm{s} = 9$ MHz. (c),(d) $\Omega_\mathrm{p} = 0.2\gamma_4$ and $\delta_\mathrm{p} = 9$ MHz. Other parameters are $\gamma_4 = 18$ MHz, $\Omega_\mathrm{c} = \gamma_4$, $\gamma_3 = 1$ kHz, $\gamma_2 = 40$ kHz, $\delta_\mathrm{c} = 0$, $\varrho_{11} = \varrho_{33} = 0.5$, $\mathcal{N} = 1 \times 10^{14}$ cm^{-3}, and using ^{87}Rb atom dipole moments $|\boldsymbol{d}_{14}| = |\boldsymbol{d}_{34}| = 1.269 \times 10^{-29}$ C·m.

The linear optical response is shown in Fig. 3.1. We plot the imaginary and real parts of the linear optical susceptibility for the probe field in Figs 3.1(a) and 3.1(b) respectively, while for the signal-electric field in Fig. 3.1(c) and Fig. 3.1(d) respectively. The real and Imaginary parts of the linear optical susceptibility for both field almost vanishes at $\delta_{\mathrm{p,s}} = \delta_\mathrm{c}$, the center of the first EIT window and at $\delta_\mathrm{p} = \delta_\mathrm{s}$, the center of the second EIT window.

3.4.1 Absorption Constant

According to Eq. (3.4.26), the absorption constant of the probe field, as function of the frequency detuning δ_{p} is defined by

$$\alpha_{\mathrm{p}_1} = \frac{\omega_{41} - \delta_{\mathrm{p}}}{c} \mathrm{Im}\left[\chi_{\mathrm{p}}^{(1)}(\omega_{\mathrm{p}})\right], \tag{3.4.44}$$

with $\chi_{\mathrm{p}}^{(1)}(\delta_{\mathrm{p}})$ is defined by (3.4.33) and ω_{41} is the transition frequency of $|1\rangle \to |4\rangle$ as defined in (2.2.20) and (2.2.22).

The minimum absorption occurs at $\delta_{\mathrm{p}} = \delta_{\mathrm{c}} = 0$ and at $\delta_{\mathrm{p}} = \delta_{\mathrm{s}}$. The equation of the probe field absorption constant at $\delta_{\mathrm{p}} = \delta_{\mathrm{c}} = 0$

$$\alpha_{\mathrm{p}_1} = \frac{\omega_{41}}{c} \mathrm{Im}\left[\chi_{\mathrm{p}}^{(1)}\right]_{\mathrm{min}_{\mathrm{p}_1}}, \tag{3.4.45}$$

with $\mathrm{Im}\left[\chi_{\mathrm{p}}^{(1)}\right]_{\mathrm{min}_{\mathrm{p}_1}}$ determined by setting $\Omega_{\mathrm{s}} = 0$ in Eq. (3.4.33) but $\Omega_{\mathrm{c}} \neq 0$, then evaluating the imaginary part at $\delta_{\mathrm{p}} = \delta_{\mathrm{c}} = 0$. We obtain

$$\mathrm{Im}\left[\chi_{\mathrm{p}}^{(1)}\right]_{\mathrm{min}_{\mathrm{p}_1}} = \frac{\eta_{\mathrm{p}}\left(\varrho_{11} - \varrho_{44}\right)\gamma_2}{\gamma_4\gamma_2 + |\Omega_{\mathrm{c}}|^2} \xrightarrow{\gamma_2 \to 0} 0, \tag{3.4.46}$$

with zero absorption attained for $\gamma_2 = 0$. If $\gamma_2 \neq 0$, then the minimum absorption is reached when

$$|\Omega_{\mathrm{c}}|^2 \gg \gamma_4\gamma_2. \tag{3.4.47}$$

The equation for the absorption of the signal field when $\delta_{\mathrm{s}} = \delta_{\mathrm{c}} = 0$

$$\alpha_{\mathrm{s}_1} = \frac{\omega_{43} - \delta_{\mathrm{s}}}{c} \mathrm{Im}\left[\chi_{\mathrm{p}}^{(1)}(\omega_{\mathrm{s}})\right], \tag{3.4.48}$$

where the minimum signal-field absorption occurs for

$$\alpha_{\mathrm{s}_1} = \frac{\omega_{43}}{c} \mathrm{Im}\left[\chi_{\mathrm{s}}^{(1)}\right]_{\mathrm{min}_{\mathrm{s}_1}}, \tag{3.4.49}$$

with $\mathrm{Im}\left[\chi_{\mathrm{s}}^{(1)}\right]_{\mathrm{min}_{\mathrm{s}_1}}$ determined by setting $\Omega_{\mathrm{p}} = 0$ in Eq. (3.4.40) but $\Omega_{\mathrm{c}} \neq 0$, then evaluating the imaginary part at $\delta_{\mathrm{s}} = \delta_{\mathrm{c}} = 0$. We obtain

$$\mathrm{Im}\left[\chi_{\mathrm{s}}^{(1)}\right]_{\mathrm{min}_{\mathrm{s}_1}} = \frac{\eta_{\mathrm{s}}\left(\varrho_{33} - \varrho_{44}\right)\Gamma_{32}}{\Gamma_{43}\Gamma_{32} + |\Omega_{\mathrm{c}}|^2} \xrightarrow{\Gamma_{32} \to 0} 0, \tag{3.4.50}$$

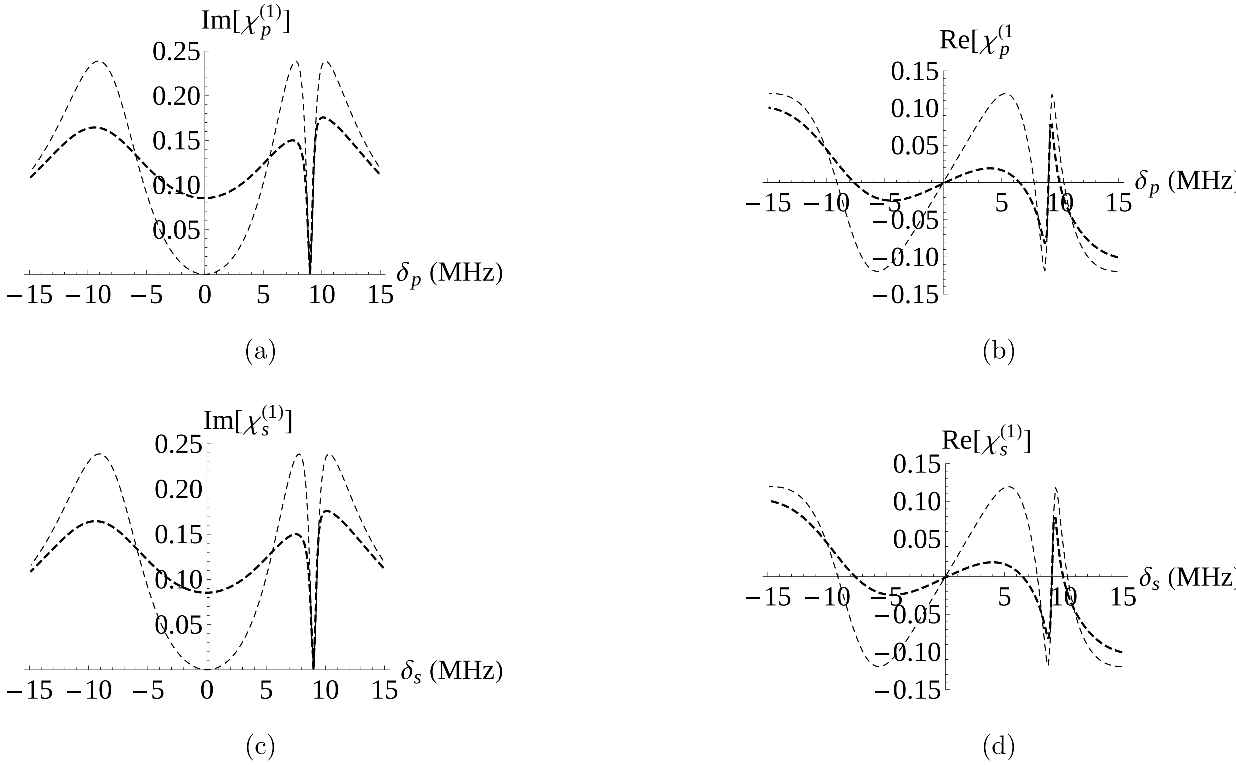

Figure 3.2: $\mathrm{Im}[\chi_l^{(1)}]$ and $\mathrm{Re}[\chi_l^{(1)}]$ as function of the field detuning δ_l, with $l \in \{\mathrm{p},\ \mathrm{s}\}$ for $\gamma_2 = 1$ kHz (dashed line) and $\gamma_2 = 10$ MHz (bold-dashed line). (a),(b) $\Omega_\mathrm{s} = 0.2\gamma_4$ and $\delta_\mathrm{s} = 9$ MHz. (c),(d) $\Omega_\mathrm{p} = 0.2\gamma_4$ and $\delta_\mathrm{p} = 9$ MHz. Other parameters are $\gamma_4 = 18$ MHz, $\Omega_\mathrm{c} = \gamma_4$, $\gamma_3 = 1$ kHz, $\delta_\mathrm{c} = 0$, $\varrho_{11} = \varrho_{33} = 0.5$, $\mathcal{N} = 1 \times 10^{14}$ cm^{-3}, and using ^{87}Rb atom dipole moments $|\boldsymbol{d}_{14}| = |\boldsymbol{d}_{34}| = 1.269 \times 10^{-29}$ C·m.

with zero absorption attained for $\Gamma_{32} = 0$. If $\Gamma_{32} \neq 0$, then the minimum absorption is reached when

$$|\Omega_\mathrm{c}|^2 \gg \Gamma_{43}\Gamma_{32}. \tag{3.4.51}$$

Although, γ_3 affects the absorption of the signal field as is evident from the denominator of (3.4.50), Eqs. (3.4.47) and (3.4.51) are consistent with the expectation in (2.5.1) for $\gamma_4 \gg \gamma_3$. Figure 3.2 shows how the coherence decay including spontaneous decay and dephasing from state $|2\rangle$ affects the absorption of the probe and signal fields at the first EIT window. When the value of γ_2 satisfies conditions (3.4.47) and (3.4.51), the absorption is close to zero. With higher values of γ_2 for which (3.4.47) and (3.4.51) are not correct, the absorption increases.

In order to calculate the minimum absorption for the second transparency window when $\delta_{\mathrm{p}} = \delta_{\mathrm{s}}$, we set $\Omega_{\mathrm{p}} \neq 0$, $\Omega_{\mathrm{s}} \neq 0$ and $\Omega_{\mathrm{c}} \neq 0$ under the approximation that

$$\gamma_4 \gg \frac{|\Omega_{\mathrm{c}}|^2}{2\delta_{\mathrm{sc}}^2}\frac{\gamma_2}{2}, \tag{3.4.52}$$

and evaluate $\mathrm{Im}\left[\chi_{\mathrm{p}}^{(1)}\right]$ and $\mathrm{Im}\left[\chi_{\mathrm{s}}^{(1)}\right]$ from Eq. (3.4.33) and Eq. (3.4.40) to obtain the absorption minimum of probe field

$$\mathrm{Im}\left[\chi_{\mathrm{p}}^{(1)}\right]_{\mathrm{min}_{\mathrm{p}_2}} = \eta_{\mathrm{p}}\frac{\left(\varrho_{11} - \varrho_{44}\right)\gamma_3}{\gamma_4\gamma_3 + |\Omega_{\mathrm{s}}|^2}, \tag{3.4.53}$$

and the absorption minimum of signal field

$$\mathrm{Im}\left[\chi_{\mathrm{s}}^{(1)}\right]_{\mathrm{min}_{\mathrm{s}_2}} = \eta_{\mathrm{s}}\frac{\left(\varrho_{33} - \varrho_{44}\right)\gamma_3}{\Gamma_{43}\gamma_3 + |\Omega_{\mathrm{p}}|^2}, \tag{3.4.54}$$

respectively. If it is necessary to reduce absorption, decay from level $|3\rangle$ must be minimized, i.e., $\gamma_3 \to 0$. For the case $\gamma_3 \neq 0$, the condition

$$|\Omega_{\mathrm{s}}|^2 \gg \gamma_3\gamma_4, \tag{3.4.55}$$

is required to minimize the absorption of the probe field, and the condition

$$|\Omega_{\mathrm{p}}|^2 \gg \gamma_3\Gamma_{43}, \tag{3.4.56}$$

is necessary to minimize the absorption of the signal field. In Fig. 3.3, the linear optical susceptibility of the probe and the signal fields are plotted, using two different values of γ_3. The absorption almost reaches zero, as the value of γ_3 satisfies conditions (3.4.55) and (3.4.56). However, the absorption becomes higher for the value of γ_3 for which the conditions (3.4.55) and (3.4.56) are not valid, as shown in Figs. 3.3(a) and (c). Additionally, the high value of γ_3 increases absorption at the first EIT window for signal field.

Now, it is possible to write the absorption constant of the probe field, when $\delta_{\mathrm{p}} = \delta_{\mathrm{s}}$ using (3.4.48) and(3.4.53) as

$$\alpha_{\mathrm{p}_2} = \frac{\omega_{41} - \delta_{\mathrm{s}}}{c}\eta_{\mathrm{p}}\frac{\left(\varrho_{11} - \varrho_{44}\right)\gamma_3}{\gamma_4\gamma_3 + |\Omega_{\mathrm{s}}|^2}, \tag{3.4.57}$$

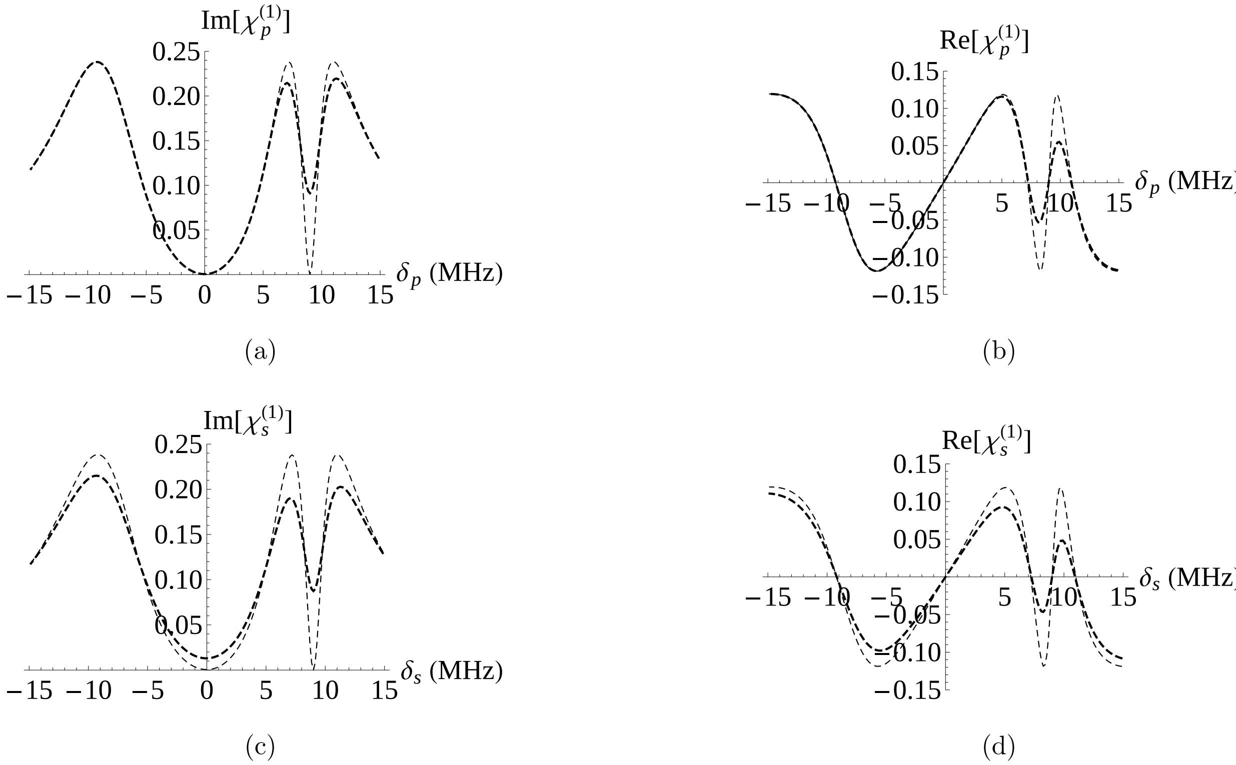

Figure 3.3: $\mathrm{Im}[\chi_l^{(1)}]$ and $\mathrm{Re}[\chi_l^{(1)}]$ as function of the field detuning δ_l, with $l \in \{\mathrm{p},\ \mathrm{s}\}$ for $\gamma_3 = 1$ kHz (dashed line) and $\gamma_3 = 1$ MHz (bold-dashed line). (a),(b) $\Omega_\mathrm{s} = 0.2\gamma_4$ and $\delta_\mathrm{s} = 9$ MHz. (c),(d) $\Omega_\mathrm{p} = 0.2\gamma_4$ and $\delta_\mathrm{p} = 9$ MHz. Other parameters are $\gamma_4 = 18$ MHz, $\Omega_\mathrm{c} = \gamma_4$, $\gamma_2 = 40$ kHz, $\delta_\mathrm{c} = 0$, $\varrho_{11} = \varrho_{33} = 0.5$, $\mathcal{N} = 1 \times 10^{14}$ cm^{-3}, and using ^{87}Rb atom dipole moments $|\boldsymbol{d}_{14}| = |\boldsymbol{d}_{34}| = 1.269 \times 10^{-29}$ C·m.

and the absorption constant of the signal field for same frequency detuning, using (3.4.48) and (3.4.54) as

$$\alpha_{\mathrm{s}_2} = \frac{\omega_{43} - \delta_\mathrm{p}}{c}\eta_\mathrm{s}\frac{(\varrho_{33} - \varrho_{44})\,\gamma_3}{\Gamma_{43}\gamma_3 + |\Omega_\mathrm{p}|^2}, \tag{3.4.58}$$

In conclusion, the coherence decay from level $|2\rangle$ plays an important role in controlling the absorption of the applied probe and signal fields at the first EIT window around the region where $\delta_{\mathrm{p,s}} = \delta_\mathrm{c}$. The coherence decay from level $|3\rangle$ has an influential impact on controlling the absorption of the applied probe and signal fields at the second EIT window, around the region where $\delta_\mathrm{p} = \delta_\mathrm{s}$ and the absorption of the signal field around the region of the first EIT, where $\delta_{\mathrm{s}} = \delta_{\mathrm{c}}$.

3.4.2 Refractive Index and Group Velocity

The index of refraction for the atom-field system, in response to probe-field propagation, is

$$n_{\mathrm{p}}(\omega_{\mathrm{p}}) = 1 + \frac{1}{2}\mathrm{Re}\left[\chi_{\mathrm{p}}^{(1)}(\omega_{\mathrm{p}})\right]. \tag{3.4.59}$$

Then the group velocity of the probe field inside the medium can be calculated using the group-velocity relation defined by (3.4.19)

$$v_{g_{\mathrm{p}}} = \left.\frac{c}{1 + \frac{1}{2}\mathrm{Re}\left[\chi_{\mathrm{p}}^{(1)}(\omega_{\mathrm{p}})\right] + \frac{\omega}{2}\frac{\partial \mathrm{Re}\left[\chi_{\mathrm{p}}^{(1)}(\omega_{\mathrm{p}})\right]}{\partial \omega_{\mathrm{p}}}}\right|_{\omega_0}, \tag{3.4.60}$$

where ω_0 is the frequency of the applied field at the center of the EIT window. The refractive index of an optical medium in response to the signal field can be written as

$$n_{\mathrm{s}}(\omega) = 1 + \frac{1}{2}\mathrm{Re}\left[\chi_{\mathrm{s}}^{(1)}(\omega_{\mathrm{s}})\right], \tag{3.4.61}$$

and the group velocity is

$$v_{g_{\mathrm{s}}} = \left.\frac{c}{1 + \frac{1}{2}\mathrm{Re}\left[\chi_{\mathrm{s}}^{(1)}(\omega_{\mathrm{s}})\right] + \frac{\omega_{\mathrm{s}}}{2}\frac{\partial \mathrm{Re}\left[\chi_{\mathrm{s}}^{(1)}(\omega_{\mathrm{s}})\right]}{\partial \omega_{\mathrm{s}}}}\right|_{\omega_0}. \tag{3.4.62}$$

At the center of each EIT window, the real part is zero or close to zero as shown in Figs.3.1(b) and (d). Therefore, Eqs. (3.4.60) and (3.4.62) can be simplify to

$$v_{g_{\mathrm{p}}} = \left.\frac{c}{1 + \frac{\omega_{\mathrm{p}}}{2}\frac{\partial \mathrm{Re}\left[\chi_{\mathrm{p}}^{(1)}(\omega_{\mathrm{p}})\right]}{\partial \omega_{\mathrm{p}}}}\right|_{\omega_0}, \tag{3.4.63}$$

and

$$v_{g_{\mathrm{s}}} = \left.\frac{c}{1 + \frac{\omega_{\mathrm{s}}}{2}\frac{\partial \mathrm{Re}\left[\chi_{\mathrm{s}}^{(1)}(\omega_{\mathrm{s}})\right]}{\partial \omega_{\mathrm{s}}}}\right|_{\omega_0}, \tag{3.4.64}$$

respectively.

In term of δ_{p} and δ_{s}, Eqs. (3.4.63) and (3.4.64) become

$$v_{\mathrm{g_p}} = \frac{c}{1 + (\omega_{41} - \delta_{\mathrm{cen}}) \left.\frac{\partial \mathrm{Re}[\chi_{\mathrm{p}}^{(1)}]}{\partial \delta_{\mathrm{p}}}\right|_{\delta_{\mathrm{cen}}}}, \tag{3.4.65}$$

and

$$v_{\mathrm{g_s}} = \frac{c}{1 + (\omega_{43} - \delta_{\mathrm{cen}}) \left.\frac{\partial \mathrm{Re}[\chi_{\mathrm{s}}^{(1)}]}{\partial \delta_{\mathrm{s}}}\right|_{\delta_{\mathrm{cen}}}}, \tag{3.4.66}$$

where δ_{cen} is the detuning at the center of each window. For the nonlinear optical medium where the second term of the denominator of Eqs. (3.4.65) and (3.4.66) is much larger than for the first, it is possible to neglect the first term and write the group velocity of the probe and signal fields inside the medium as

$$v_{\mathrm{g_p}} \approx \frac{c}{(\omega_0 - \delta_{\mathrm{cen}}) \left.\frac{\partial \mathrm{Re}[\chi_{\mathrm{p}}^{(1)}]}{\partial \delta_{\mathrm{p}}}\right|_{\delta_{\mathrm{cen}}}} \tag{3.4.67}$$

and

$$v_{\mathrm{g_s}} \approx \frac{c}{(\omega_0 - \delta_{\mathrm{cen}}) \left.\frac{\partial \mathrm{Re}[\chi_{\mathrm{s}}^{(1)}]}{\partial \delta_{\mathrm{s}}}\right|_{\delta_{\mathrm{cen}}}}. \tag{3.4.68}$$

The group velocity is proportionally reciprocal to the derivative of the dispersion, so is proportionally reciprocal of the slope of a straight line tanging the dispersion curve at the point $\delta_l = \delta_{\mathrm{cen}}$. Using the definition of the derivative we obtain

$$\left.\frac{\partial \mathrm{Re}[\chi_l^{(1)}]}{\partial \delta_l}\right|_{\delta_{\mathrm{cen}}} = \lim_{\delta_l \to \delta_{\mathrm{cen}}} \frac{\mathrm{Re}[\chi_l^{(1)}(\delta_l)] - \mathrm{Re}[\chi_l^{(1)}(\delta_l = \delta_{\mathrm{cen}})]}{\delta_l - \delta_{\mathrm{cen}}}, \tag{3.4.69}$$

it is possible to find an approximated analytical expression for the group velocity of the probe and signal fields, at both EIT windows, with $l \in \{\mathrm{p}, \mathrm{s}\}$.

The analytical group velocity of the probe at the first EIT window, for $\gamma_4 \gg \gamma_3$ is

$$v_{g_{\mathrm{p}1}} \approx \frac{c}{\frac{\omega_{14} - \delta_{\mathrm{c}}}{2} \frac{\eta_{\mathrm{p}}(\varrho_{11} - \varrho_{44})\left(|\Omega_{\mathrm{c}}|^2 - \gamma_2^2\right)}{\left(\gamma_2\gamma_4 + |\Omega_{\mathrm{c}}|^2\right)^2}}, \tag{3.4.70}$$

and at the second window, for $\gamma_4 \gg \gamma_2$ is

$$v_{g_{\mathrm{p}2}} \approx \frac{c}{\frac{\omega_{14} - \delta_{\mathrm{s}}}{2} \frac{\eta_{\mathrm{p}}(\varrho_{11} - \varrho_{44})\left(|\Omega_{\mathrm{s}}|^2 - \gamma_3^2\right)}{\left(\gamma_3\gamma_4 + |\Omega_{\mathrm{s}}|^2\right)^2}}. \tag{3.4.71}$$

Similar to the case of absorption, the coherence decay from state $|2\rangle$ has a significant effect on the group velocity of the probe field and could change its value at $\delta_\mathrm{p} = \delta_\mathrm{c}$, if γ_2 value fails to satisfy condition (3.4.47). This can be seen in Fig. 3.2(b), where the incline of dispersion's line changes due to the change of γ_2. However, Ω_c is the primary controlled parameter that can be used to modify the group velocity of the probe field for inequality (3.4.47) being satisfied.

The effect of the coupling on the group velocity of the probe field is shown in Fig. 3.4(a). Increasing the value of Ω_c decreases the dispersion's derivative, which is represented by the slope of the tangent line to the dispersion curve at $\delta_\mathrm{p} = \delta_\mathrm{c}$ point. Consequently, the group velocity of the probe field within the medium increases.

At $\delta_\mathrm{p} = \delta_\mathrm{s}$, the coherence decay of state $|3\rangle$ affects the group velocity of the probe field for unsatisfied (3.4.55). Figure 3.3(b) shows how γ_3 effects the dispersion inclination around the region where $\delta_\mathrm{p} = \delta_\mathrm{s}$. Increasing the vale of γ_3 will increase the group velocity. Conversely, for a satisfied (3.4.55) the only controlled parameter is Ω_s. The effect of Ω_s on the group velocity of the probe field when $\delta_\mathrm{p} = \delta_\mathrm{s}$ is similar to the effect of the Ω_c on the group velocity of the probe field when $\delta_\mathrm{p} = \delta_\mathrm{c}$ as shown in Fig. 3.4(b). Thus increasing Ω_s decreases the group velocity and vice versa.

The analytical expression for the group velocity of the signal at the first EIT window, when $\delta_\mathrm{p} = \delta_\mathrm{c}$ and for $\gamma_4 \gg \gamma_3$ can be written as

$$v_{g_{\mathrm{s}_1}} \approx \frac{c}{\frac{\omega_{34}-\delta_\mathrm{c}}{2}\frac{\eta_\mathrm{s}(\varrho_{33}-\varrho_{44})\left(|\Omega_\mathrm{c}|^2-\Gamma_{32}^2\right)}{\left(\Gamma_{32}\Gamma_{43}+|\Omega_\mathrm{c}|^2\right)^2}} \tag{3.4.72}$$

At the second EIT window, when $\delta_\mathrm{s} = \delta_\mathrm{p}$ and for $\gamma_4 \gg \Gamma_{32}$, the group velocity can be written as

$$v_{g_{\mathrm{s}_2}} \approx \frac{c}{\frac{\omega_{34}-\delta_\mathrm{s}}{2}\frac{\eta_\mathrm{s}(\varrho_{33}-\varrho_{44})\left(|\Omega_\mathrm{p}|^2-\gamma_3^2\right)}{\left(\Gamma_{32}\Gamma_{43}+|\Omega_\mathrm{p}|^2\right)^2}}. \tag{3.4.73}$$

The signal-field case differs from the probe-field case. Not only does the coherence decay from state $|2\rangle$ significantly affect the group velocity of the signal field at $\delta_\mathrm{s} = \delta_\mathrm{c}$, but also the decay from $|3\rangle$ plays an important role in modifying the group velocity of the signal field, when the chosen value of γ_2 and γ_3 unsatisfied condition (3.4.51). The effect of γ_2 and γ_3 is

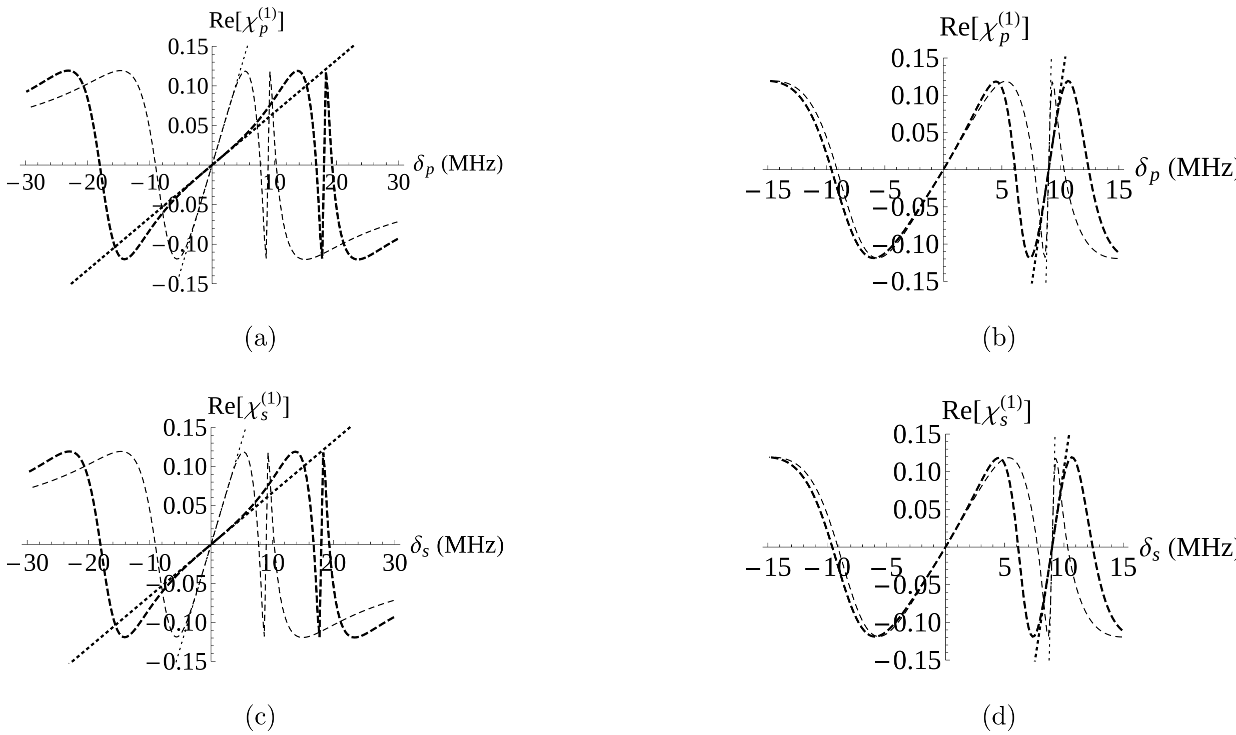

Figure 3.4: $\mathrm{Re}[\chi_l^{(1)}]$ as function of the field detuning δ_l, with $l \in \{\mathrm{p},\ \mathrm{s}\}$. (a) $\Omega_\mathrm{c} = \gamma_4$ (dashed line), $\Omega_\mathrm{c} = 2\gamma_4$ (bold-dashed line), $\delta_\mathrm{s} = 0.5\Omega_\mathrm{c}$, and $\Omega_\mathrm{s} = 0.2\gamma_4$. (b) $\Omega_\mathrm{s} = 0.2\gamma_4$ (dashed line), $\Omega_\mathrm{s} = 0.4\gamma_4$ (bold-dashed line), $\Omega_\mathrm{c} = \gamma_4$, and $\delta_\mathrm{s} = 0.5\Omega_\mathrm{c}$. (c) $\Omega_\mathrm{c} = \gamma_4$ (dashed line), $\Omega_\mathrm{c} = 2\gamma_4$ (bold-dashed line), $\delta_\mathrm{p} = 0.5\Omega_\mathrm{c}$, and $\Omega_\mathrm{p} = 0.2\gamma_4$. (d) $\Omega_\mathrm{p} = 0.2\gamma_4$ (dashed line), $\Omega_\mathrm{p} = 0.4\gamma_4$ (bold-dashed line) $\Omega_\mathrm{c} = \gamma_4$, and $\delta_\mathrm{s} = 0.5\Omega_\mathrm{c}$. The approximate linear equation determined by finding the derivate of dispersion using (3.4.69) is represented by (dotted line). Other parameters are $\gamma_4 = 18$ MHz, $\gamma_2 = 40$ kHz, $\gamma_3 = 1$ kHz, $\delta_\mathrm{c} = 0$, $\varrho_{11} = \varrho_{33} = 0.5$, $\mathcal{N} = 1 \times 10^{14}$ cm^{-3}, and using ^{87}Rb atom dipole moments $|\boldsymbol{d}_{14}| = |\boldsymbol{d}_{34}| = 1.269 \times 10^{-29}$ C·m.

demonstrated in Figs. 3.2(d) and 3.3(d), where the inclination of dispersion line modifies, due to the change of γ_2 and γ_3 respectively. For condition (3.4.51) being satisfied, the coupling-field Rabi frequency is the main parameter that can be used to control the group velocity of the signal field as shown Fig. 3.4(c). Increasing the value of Ω_c decreases the dispersion derivative, represented by the slope of the line tangent to the dispersion curve at $\delta_\mathrm{s} = \delta_\mathrm{c}$ point, as shown in Fig. 3.4(c). Consequently, the group velocity of the signal field inside the medium increases.

When $\delta_\mathrm{p} = \delta_\mathrm{s}$, the coherence decay of state $|3\rangle$ affects the group velocity of the signal field for condition (3.4.56) is not satisfied. Figure 3.3(d) shows how γ_3 influences the dispersion inclination around the region where $\delta_\mathrm{p} = \delta_\mathrm{s}$. Increasing the vale of γ_3 increases the group velocity. For a satisfied (3.4.56), the only controlled parameter is Ω_s. Increasing the value of Ω_s decreases the group velocity and vice versa.

Although the probe-field group velocity reacts similarly to the signal-field group velocity, in response to the decoherence of the lower levels, and to the applied fields in each EIT window of the DDEIT system, several parameters must be taken into account, to match the group velocities. Referring to the analytical expression of the group velocity of the probe field at the first windows (3.4.70), and the analytical expression of group velocity of the signal field (3.4.72), it can be seen that the group velocities can be matched if the following condition is achieved

$$\eta_\mathrm{p}(\omega_{14} - \delta_\mathrm{c})(\varrho_{11} - \varrho_{44}) = \eta_\mathrm{s}(\omega_{34} - \delta_\mathrm{c})(\varrho_{33} - \varrho_{44}), \tag{3.4.74}$$

which can be reduced to

$$\varrho_{11} - \varrho_{44} = \varrho_{33} - \varrho_{44}, \tag{3.4.75}$$

if we specifically consider ^{87}Rb and assign $|1\rangle$, $|2\rangle$ and $|3\rangle$ to the $5S_{1/2}$ level with $F = 1$, $m_F = 0$, $F = 2$ and $m_F = \{-2, 0\}$ respectively. Level $|4\rangle$ corresponds to level $5P_{1/2}$ with $F = 2$ and $m_F = -1$. In this case $\omega_{14} = \omega_{34} = 2\pi \cdot 377.110$ THz, and $|\boldsymbol{d}_{41}| = |\boldsymbol{d}_{43}| = 1.269 \times 10^{-29}$ C·m. Otherwise, all the parameters must be chosen such that the left-hand side of (3.4.74) is equal to the right-hand side. Matching the group velocity of the probe and signal fields at the second EIT window, when $\delta_\mathrm{p} = \delta_\mathrm{s}$, needs an additional requirement, $\Omega_\mathrm{p} = \Omega_\mathrm{s}$.

3.5 Nonlinear-Optical Susceptibility

The solution of the wave equations (3.2.9) or (3.2.10) in the nonlinear regime is now discussed [2]. It is customary to separate the polarization into its linear and nonlinear parts

$$\boldsymbol{P}(\omega) = \epsilon_0 \boldsymbol{\chi}^{(1)}(\omega)\boldsymbol{E}(\omega) + \boldsymbol{P}^{(\mathrm{NL})}(\omega), \tag{3.5.1}$$

with

$$\boldsymbol{P}^{(\mathrm{NL})}(\omega) = \sum_{m=2}^{\infty} \boldsymbol{P}^{(m)}(\omega), \tag{3.5.2}$$

and $\boldsymbol{P}^{(m)}(\omega)$ are given by (C.1.8). Substituting (3.5.1) into the wave equation (3.2.10) we get

$$\nabla^2 \boldsymbol{E}(\omega) + \frac{\omega^2}{c^2}\boldsymbol{E}(\omega) = -\mu_0\omega^2\epsilon_0\boldsymbol{\chi}^{(1)}(\omega)\boldsymbol{E}(\omega) - \mu_0\omega^2\boldsymbol{P}^{(\mathrm{NL})}(\omega). \tag{3.5.3}$$

Let us take the electric field to be linearly polarized in ε-direction perpendicular to the direction of propagation and in the form of

$$\boldsymbol{E}(\boldsymbol{r},\omega) = \boldsymbol{\xi}(\boldsymbol{r},\omega)e^{\pm \mathrm{i}\boldsymbol{k}\cdot\boldsymbol{r}}, \tag{3.5.4}$$

where the envelope function $\boldsymbol{\xi}(\boldsymbol{r},\omega)$ is complex; it incorporates both amplitude and phase information about the wave and, in general, is a function of all three space coordinates. To simplify the analysis, it will be assumed that the $\boldsymbol{\xi}(\boldsymbol{r},\omega)$ are infinite plane wave, which propagate in the z-direction, so that $\boldsymbol{\xi}(\boldsymbol{r},\omega)$ is a function of z only, such that $\pm\mathrm{i}\boldsymbol{k}\cdot\boldsymbol{r} = \pm kz$, with a positive sign for forward-traveling waves in the z-direction and a negative sign for backward wave. Thus (3.5.4) can be written as

$$\boldsymbol{E}(z,\omega) = \boldsymbol{\xi}(z,\omega)e^{\pm \mathrm{i}kz}. \tag{3.5.5}$$

Then we can write (3.5.3) according to the above assumption as

$$\frac{\partial^2 \boldsymbol{E}(z,\omega)}{\partial z^2} + \frac{\omega^2}{c^2}\boldsymbol{E}(z,\omega) = -\mu_0\omega^2\epsilon_0\boldsymbol{\chi}^{(1)}(\omega)\boldsymbol{E}(z,\omega) - \mu_0\omega^2\boldsymbol{P}^{(\mathrm{NL})}(z,\omega). \tag{3.5.6}$$

Similarly, polarization is taken as an infinite plane wave that propagates in z-direction and is polarized in the ε-direction

$$\boldsymbol{P}^{(\mathrm{NL})}(z,\omega) = \boldsymbol{p}^{(\mathrm{NL})}(z,\omega)e^{\pm \mathrm{i}kz}, \tag{3.5.7}$$

with $\boldsymbol{p}^{(\mathrm{NL})}(z,\omega)$ is the polarization-envelope wave function. The possibility of a wavevector mismatch is not allowed, by choosing the wavevector $\boldsymbol{k}$ of the polarization, similar to the electric field [2]. This is because all nonlinear optical processes involved in our optical system satisfy the phase-matching condition automatically, which appears in the optical susceptibility described by (3.4.31) and (3.4.38). By substituting (3.5.5) and (3.5.7) into the wave equation (3.5.6), the following equation is obtained

$$\frac{\partial^2\boldsymbol{\xi}(z,\omega)}{\partial z^2}+2\mathrm{i}k\frac{\partial\boldsymbol{\xi}(z,\omega)}{\partial z}-k^2\boldsymbol{\xi}(z,\omega)+\frac{\omega^2}{c^2}\boldsymbol{\xi}(z,\omega)=-\mu_0\omega^2\epsilon_0\boldsymbol{\chi}^{(1)}(\omega)\boldsymbol{\xi}(z,\omega)-\mu_0\omega^2\boldsymbol{p}^{(\mathrm{NL})}(z,\omega). \tag{3.5.8}$$

The wave envelope $\boldsymbol{\xi}(z,\omega)$ varies with distance through the medium, as a result of both linear and nonlinear processes. If the variations of $\boldsymbol{\xi}(z,\omega)$ both in magnitude and phase are sufficiently slow with distance z, it can be assumed that

$$\left|\frac{\partial^2\boldsymbol{\xi}(z,\omega)}{\partial z^2}\right|\ll\left|k\frac{\partial\boldsymbol{\xi}(z,\omega)}{\partial z}\right|. \tag{3.5.9}$$

This is known as a slowly-varying envelope approximation [2], and suggests that it is possible to neglect the second derivative of $\boldsymbol{\xi}(z,\omega)$, with respect to z in (3.5.8), so that for a forward-traveling wave we have

$$2\mathrm{i}k(\omega)\frac{\partial\boldsymbol{\xi}(z,\omega)}{\partial z}-k^2(\omega)\boldsymbol{\xi}(z,\omega)=-\frac{\omega^2}{c^2}\left[1+\boldsymbol{\chi}^{(1)}(\omega)\right]\boldsymbol{\xi}(z,\omega)-\mu_0\omega^2\boldsymbol{p}^{(\mathrm{NL})}(z,\omega), \tag{3.5.10}$$

where $c=\frac{1}{\sqrt{\mu_0\epsilon_0}}$ is used in the right-hand side of Eq. (3.5.10). Using the definition of the propagation constant k (3.4.11) and the linear absorption constant (3.4.15), we can write the wave equation as

$$\begin{aligned}2\mathrm{i}k(\omega)\frac{\partial\boldsymbol{\xi}(z,\omega)}{\partial z}-k^2(\omega)\boldsymbol{\xi}(z,\omega)&=-k^2(\omega)\boldsymbol{\xi}(z,\omega)-\frac{\mathrm{i}\alpha^2(\omega)}{4}\boldsymbol{\xi}(z,\omega)-\mu_0\omega^2\boldsymbol{p}^{(\mathrm{NL})}(z,\omega),\\ 2\mathrm{i}k(\omega)\frac{\partial\boldsymbol{\xi}(z,\omega)}{\partial z}&=-\frac{\mathrm{i}\alpha^2(\omega)}{4}\boldsymbol{\xi}(z,\omega)-\mu_0\omega^2\boldsymbol{p}^{(\mathrm{NL})}(z,\omega).\end{aligned} \tag{3.5.11}$$

If the definition of the polarization envelope described in Appendix C by (C.1.16) is used, we can write the forward-traveling wave equation as

$$\frac{\partial\boldsymbol{\xi}(z,\omega)}{\partial z}=-\frac{\alpha^2(\omega)}{8k(\omega)}\boldsymbol{\xi}(z,\omega)+\frac{\mathrm{i}\epsilon_0\mu_0\omega^2}{2k(\omega)}\boldsymbol{\chi}^{(\mathrm{NL})}(\omega)\boldsymbol{\xi}(z,\omega), \tag{3.5.12}$$

with

$$\boldsymbol{\chi}^{(\mathrm{NL})}(\omega)=\sum_{m=2}^{\infty}\boldsymbol{\chi}^{(m)}(\omega). \tag{3.5.13}$$

For the probe field mode, Eq. (3.5.12) becomes

$$\frac{\partial\boldsymbol{\xi}_{\mathrm{p}}(z,\omega)}{\partial z}=-\frac{\alpha_{\mathrm{p}}^{2}(\omega)}{8k_{\mathrm{p}}(\omega)}\boldsymbol{\xi}_{\mathrm{p}}(z,\omega)+\frac{\mathrm{i}\omega^{2}}{2c^{2}k_{\mathrm{p}}(\omega)}\chi_{\mathrm{p}}^{(\mathrm{NL})}(\omega)\boldsymbol{\xi}_{\mathrm{p}}(z,\omega), \tag{3.5.14}$$

with $\chi_{\mathrm{p}}^{(\mathrm{NL})}(\omega)$ is defined by (3.4.32), and for signal-field mode, the wave equation (3.5.12) becomes

$$\frac{\partial\boldsymbol{\xi}_{\mathrm{s}}(z,\omega)}{\partial z}=-\frac{\alpha_{\mathrm{s}}^{2}(\omega)}{8k_{\mathrm{s}}(\omega)}\boldsymbol{\xi}_{\mathrm{s}}(z,\omega)+\frac{\mathrm{i}\omega^{2}}{2c^{2}k_{\mathrm{s}}(\omega)}\chi_{\mathrm{s}}^{(\mathrm{NL})}(\omega)\boldsymbol{\xi}_{\mathrm{s}}(z,\omega), \tag{3.5.15}$$

with $\chi_{\mathrm{s}}^{(\mathrm{NL})}(\omega)$ is defined by (3.4.39).

As discussed in section (3.4.1), the linear absorption constant vanishes, or has an extremely small value at the center of each of EIT windows for conditions (3.4.47), (3.4.51), (3.4.55), and (3.4.56) are all satisfied. Evaluating (3.5.14) and (3.5.14) for negligible absorption, the following are obtained:

$$\frac{\partial\boldsymbol{\xi}_{\mathrm{p}}(z,\omega)}{\partial z}=\mathrm{i}\frac{\omega^{2}}{c^{2}}\frac{\chi_{\mathrm{p}}^{(\mathrm{NL})}(\omega)}{2k_{\mathrm{p}}(\omega)}\boldsymbol{\xi}_{\mathrm{p}}(z,\omega), \tag{3.5.16}$$

and

$$\frac{\partial\boldsymbol{\xi}_{\mathrm{s}}(z,\omega)}{\partial z}=\mathrm{i}\frac{\omega^{2}}{c^{2}}\frac{\chi_{\mathrm{s}}^{(\mathrm{NL})}(\omega)}{2k_{\mathrm{s}}(\omega)}\boldsymbol{\xi}_{\mathrm{s}}(z,\omega). \tag{3.5.17}$$

Assuming that the medium is homogeneous (i.e., the medium's dielectric does not depend on the coordinates), then the wave equation solution for the probe field

$$\boldsymbol{\xi}_{\mathrm{p}}(z,\omega)=\boldsymbol{\xi}_{0p}e^{\mathrm{i}\frac{\omega^{2}}{c^{2}}\frac{\chi_{\mathrm{p}}^{(\mathrm{NL})}(\omega)}{2k_{\mathrm{p}}(\omega)}z}, \tag{3.5.18}$$

and for the signal field

$$\boldsymbol{\xi}_{\mathrm{s}}(z,\omega)=\boldsymbol{\xi}_{0s}e^{\mathrm{i}\frac{\omega^{2}}{c^{2}}\frac{\chi_{\mathrm{s}}^{(\mathrm{NL})}(\omega)}{2k_{\mathrm{s}}(\omega)}z}, \tag{3.5.19}$$

where $\boldsymbol{\xi}_{0s}$ and $\boldsymbol{\xi}_{0s}$ are the values of the envelope function at $z=0$. The nonlinear optical susceptibility can be written as

$$\chi_{l}^{(\mathrm{NL})}(\omega)=\mathrm{Re}\left[\chi_{l}^{(\mathrm{NL})}(\omega)\right]+\mathrm{iIm}\left[\chi_{l}^{(\mathrm{NL})}(\omega)\right], \tag{3.5.20}$$

where $l \in \{\mathrm{p,s}\}$, the real part represents the nonlinear dispersive, and the imaginary part describes either the nonlinear absorption or amplification depending on its sign. For positive $\mathrm{Im}\left[\chi_l^{(\mathrm{NL})}(\omega)\right]$, the field is absorbed as it passes through the medium, while for negative $\mathrm{Im}\left[\chi_l^{(\mathrm{NL})}(\omega)\right]$ the field is amplified as it passes through the medium. The nonlinear phase shift by the probe field can be written as

$$\phi_{NL_\mathrm{p}}(\omega) = \frac{\omega}{c}\frac{\mathrm{Re}\left[\chi_\mathrm{p}^{(\mathrm{NL})}(\omega)\right]}{2n_\mathrm{p}(\omega)}z. \tag{3.5.21}$$

The nonlinear absorption constant, or the gain constant of the probe field, can be written as

$$\alpha_{NL_\mathrm{p}}(\omega) = \frac{\omega}{c}\frac{\mathrm{Im}\left[\chi_\mathrm{p}^{(\mathrm{NL})}(\omega)\right]}{n_\mathrm{p}(\omega)}. \tag{3.5.22}$$

Similarly, the signal-field nonlinear-phase shift can be written as

$$\phi_{NL_\mathrm{s}}(\omega) = \frac{\omega}{c}\frac{\mathrm{Re}\left[\chi_\mathrm{s}^{(\mathrm{NL})}(\omega)\right]}{2n_\mathrm{s}(\omega)}z. \tag{3.5.23}$$

The nonlinear absorption constant, or gain constant of the signal field, can be written as

$$\alpha_{NL_\mathrm{s}}(\omega) = \frac{\omega}{c}\frac{\mathrm{Im}\left[\chi_\mathrm{s}^{(\mathrm{NL})}(\omega)\right]}{n_\mathrm{s}(\omega)}, \tag{3.5.24}$$

where (3.4.11) is used to substitute the propagation constant with the index of refraction.

Nonlinear optical phenomena are generated by the wave propagation inside the medium, or due to the interaction of optical waves inside a nonlinear medium. The presence of nonlinear-optical phenomena is known by studying the optical response, represented by the imaginary and real parts of the nonlinear-optical susceptibility. Therefore, in the following two sections, a detailed study of the nonlinear-optical susceptibility terms is provided. This provides complete information about which types of optical phenomena are occurring in our optical system.

3.5.1 Stimulated Raman Scattering

The nonlinear optical susceptibility of the atom-field optical system is represented by Eqs. (3.4.32) and (3.4.39). The second terms in each of the nonlinear-optical susceptibility equations result from the interaction of the probe and signal fields, through the nonlinear medium. Such an interaction can amplify one of the incident applied fields under appropriate condition through SRS, which is represented by the imaginary parts of (3.5.27) and (3.5.28). The nonlinearity of the medium also provides a coupling between the incident waves through a phenomenon referred to as XPM, which is described by the real parts of (3.5.27) and (3.5.28). Cross-phase modulation occurs because the effective refractive index of a wave proportional to the intensity of the other copropagating waves, which is known as the optical-Kerr effect [81].

Raman scattering can be described using quantum mechanics, as the process in which the material system absorbs a photon at ω_x, emits a photon at ω_y and makes a transition to some excited state at $\hbar(\omega_x - \omega_y)$ [75]. When the Raman scattering is stimulated by highly intense incident beam such that the initially scattered waves enhance further scattering of the incident wave, leading to an exponential growth of the total scattered wave, and the scattered light is characterized by narrow linewidth [82], then Raman scattering is known as SRS [82, 83]. For a molecular system, the final state in the process is usually a vibrational or rotational level. Therefore, the process results from the coupling of light wave to vibrational or rotational waves [75, 76, 82, 83]. However, for an atomic system the Raman scattering is due to the coupling of the incident waves to the electronic states. The initial and final states are electronic states and define the Raman transition, so it is known as stimulated electronic Raman scattering (SERS) [84–86]. In SRS, phase matching condition is automatically satisfied [81].

The basic SERS of our field-atom system scheme is illustrated in the electronic-energy level diagram of Fig. 3.5. The probe field excites a Raman transition between the electronic-ground state $|1\rangle$ and the excited $|3\rangle$. In this way, Raman-shifted (Stokes) radiation is produced at the frequency of the signal field

$$\omega_{\mathrm{s}} = \omega_{\mathrm{p}} - \omega_{13}, \tag{3.5.25}$$

where ω_{p} is the probe-field frequency, and $\hbar\omega_{13}$ is the energy of the electronic-Raman transition [85]. Similarly, the signal field excites a Raman transition between the electronic-ground state $|1\rangle$ and the excited $|3\rangle$. In this way, Raman-shifted (anti-Stokes) radiation is produced at the frequency of the probe field

$$\omega_{\rm p} = \omega_{\rm s} + \omega_{13}, \tag{3.5.26}$$

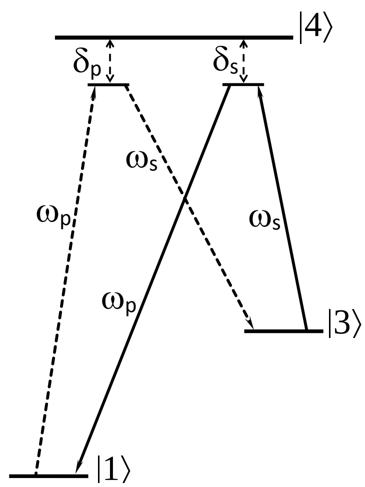

Figure 3.5: Energy-level diagram showing the SERS scheme in our atom-field system. The generation of signal Stokes field frequency is shown by the dashed-line transition path, while the generation of probe anti-Stokes field frequency is shown by solid-line transition path.

In usual Raman scattering, the detuning from intermediate level which in this case is level $|4\rangle$ needs to be so large (far from material resonance) so that no population is created in the intermediate level [77]. However, in the atom-field system used here, no constraints on the detuning from $|4\rangle$ are considered, except that $\delta_{\rm p} = \delta_{\rm s}$ which could take the value of zero. This condition is not required in this system, as we know from Sec. 2.4.2 that the system is trapped at steady state to a dark state, which is superposition of the states defining the Raman transition, leaving $|4\rangle$ unoccupied.

Stimulated electronic Raman scattering appears in our atom-field system through the imaginary parts

$$\chi_{\mathrm{p}_2}^{(3)}(\omega)\left|\xi_{\mathrm{s}_f}\right|^2, \tag{3.5.27}$$

and

$$\chi_{\mathrm{s}_2}^{(3)}(\omega)\left|\xi_{\mathrm{p}_f}\right|^2, \tag{3.5.28}$$

of Eqs. (3.4.32) and (3.4.39) respectively, with $\chi_{\mathrm{p}_2}^{(3)}(\omega)$ defined by (3.4.35) and $\chi_{\mathrm{s}_2}^{(3)}(\omega)$ defined by (3.4.42). Stimulated electronic Raman scattering occurs in the probe-field optical response, as well as in the signal-field optical response. Hence, the process is accompanied with absorption of probe field, as well as absorption of signal field, described by the imaginary of the first term of Eqs. (3.4.32) and (3.4.39) respectively.

$$\chi_{\mathrm{p}_1}^{(3)}(\omega)\left|\xi_{\mathrm{p}_f}\right|^2, \tag{3.5.29}$$

and

$$\chi_{\mathrm{s}_1}^{(3)}(\omega)\left|\xi_{\mathrm{s}_f}\right|^2, \tag{3.5.30}$$

with $\chi_{\mathrm{p}_1}^{(3)}(\omega)$ represented by (3.4.34) and $\chi_{\mathrm{s}_1}^{(3)}(\omega)$ by (3.4.41). The imaginary parts of (3.5.27), (3.5.29), (3.5.28) and (3.5.30) are illustrated in Figs. 3.6(a) and 3.7(a). The stimulated-Raman amplification appears in the figures as the negative profile, while the absorption is the positive profile. The stimulated Raman amplification and the nonlinear absorption reach their maximum when $\delta_{\mathrm{p}} = \delta_{\mathrm{s}}$.

Using Eq. (3.5.21), the probe-field absorption coefficient can be written as

$$\alpha_{NL_{\mathrm{p}}}(\omega) = \frac{\omega}{c}\frac{\mathrm{Im}\left[\chi_{\mathrm{p}_1}^{(3)}(\omega)\left|\xi_{\mathrm{p}_f}\right|^2 + \chi_{\mathrm{p}_2}^{(3)}(\omega)\left|\xi_{\mathrm{s}_f}\right|^2\right]}{2n_{\mathrm{p}}(\omega)}. \tag{3.5.31}$$

According to Eq. (3.5.18), the probe field experiences an exponential growth (amplified) if the second term is dominant, while it experiences an exponential decay if the first is dominant term. The second term exceeds the first if the relation (2.5.11) is satisfied.

Similarly, the signal-field absorption constant can be obtained from Eq. (3.5.23)

$$\alpha_{NL_{\mathrm{s}}}(\omega) = \frac{\omega}{c} \frac{\mathrm{Im}\left[\chi^{(3)}_{\mathrm{s}_1}(\omega)\left|\xi_{\mathrm{s}_f}\right|^2 + \chi^{(3)}_{\mathrm{s}_2}(\omega)\left|\xi_{\mathrm{p}_f}\right|^2\right]}{n_{\mathrm{s}}(\omega)}. \tag{3.5.32}$$

The signal-field amplitude spatial variation is described by Eq. (3.5.19). For negative $\alpha_{NL_{\mathrm{s}}}(\omega)$, the signal field experiences an exponential growth. This occurs if the second term exceeds the first, while positive $\alpha_{NL_{\mathrm{s}}}(\omega)$ implies that the signal field experiences attenuation. As discussed in earlier, the second term exceeds the first when (2.5.15) is valid.

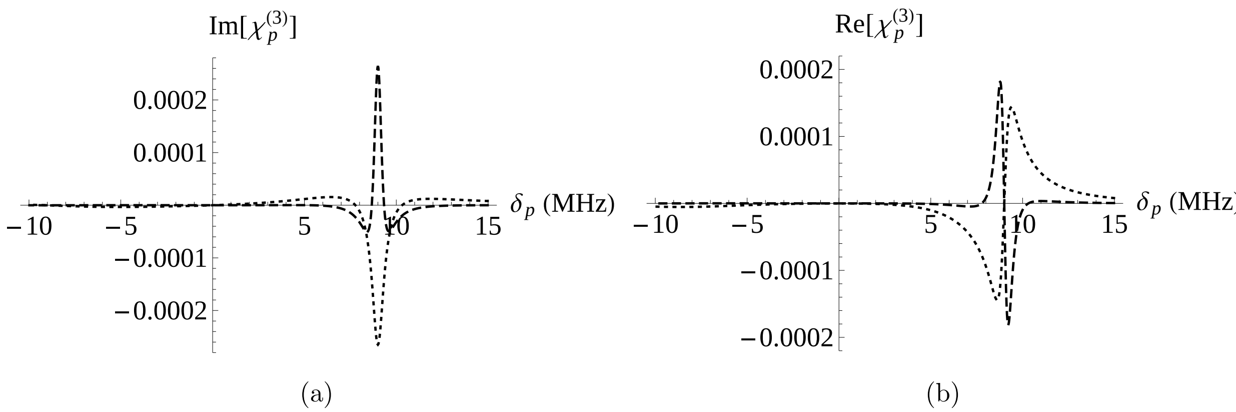

Figure 3.6: Nonlinear-optical susceptibility. (a) $\mathrm{Im}\left[\chi^{(3)}_{\mathrm{p}_1}\right]$ (dashed line) and $\mathrm{Im}\left[\chi^{(3)}_{\mathrm{p}_2}\right]$ (dotted line). (b) $\mathrm{Re}\left[\chi^{(3)}_{\mathrm{p}_1}\right]$ (dashed line) and $\mathrm{Re}\left[\chi^{(3)}_{\mathrm{p}_2}\right]$ (dotted line), as function of the probe-field detuning δ_{p}, using ^{87}Rb dipole moments $|\boldsymbol{d}_{14}| = |\boldsymbol{d}_{34}| = 1.269 \times 10^{-29}$ C·m. Other parameters are $\gamma_4 = 18$ MHz, $\Omega_{\mathrm{c}} = \gamma_4$, $\Omega_{\mathrm{s}} = 0.2\gamma_4$, $\gamma_3 = 10$ kHz, $\gamma_2 = 40$ kHz, $\delta_{\mathrm{s}} = 0.5\Omega_{\mathrm{c}}$, $\delta_{\mathrm{c}} = 0$, $\varrho_{11} = \varrho_{33} = 0.5$, and $\mathcal{N} = 1 \times 10^{14}$ cm^{-3}.

The absorption of the probe field (3.5.29) appears as an amplification in signal field (3.5.28), and the absorption of the signal field (3.5.30) appears as an amplification in the probe field (3.5.27). However, the resultant output depends on the weight of each term. Thus, if the detected probe field is amplified, this implies that the signal field is absorbed. Amplification can not be detected simultaneously in the probe and signal-field outputs.

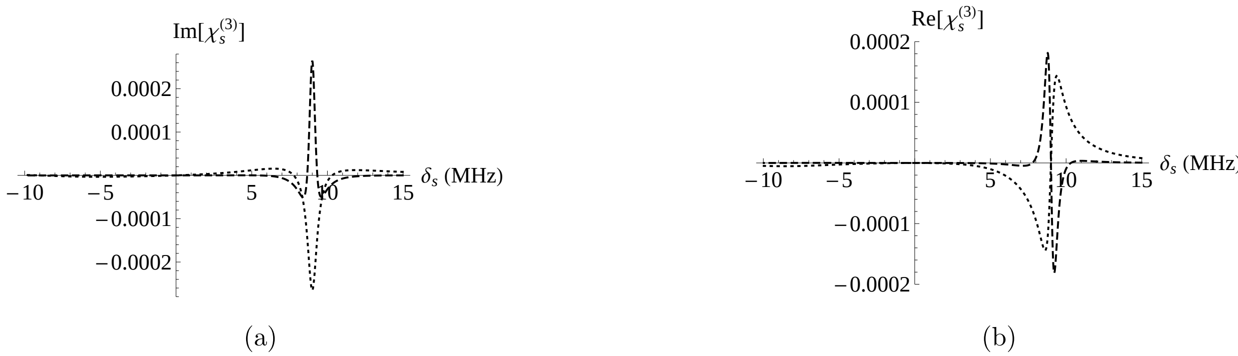

Figure 3.7: Nonlinear-optical susceptibility. (a) $\mathrm{Im}\left[\chi^{(3)}_{\mathrm{s}_1}\right]$ (dashed line) and $\mathrm{Im}\left[\chi^{(3)}_{\mathrm{s}_2}\right]$ (dotted line). (b) $\mathrm{Re}\left[\chi^{(3)}_{\mathrm{s}_1}\right]$ (dashed line) and $\mathrm{Re}\left[\chi^{(3)}_{\mathrm{s}_2}\right]$ (dotted line), as function of the signal-field detuning δ_s, using ^{87}Rb dipole moments $|\boldsymbol{d}_{14}| = |\boldsymbol{d}_{34}| = 1.269 \times 10^{-29}$ C·m. Other parameters are $\gamma_4 = 18$ MHz, $\Omega_\mathrm{c} = \gamma_4$, $\Omega_\mathrm{p} = 0.2\gamma_4$, $\gamma_3 = 10$ kHz, $\gamma_2 = 40$ kHz, $\delta_\mathrm{p} = 0.5\Omega_\mathrm{c}$, $\delta_\mathrm{c} = 0$, $\varrho_{11} = \varrho_{33} = 0.5$, and $\mathcal{N} = 1 \times 10^{14}$ cm^{-3}.

3.5.2 Phase Modulation

The phase of a field propagating through a nonlinear medium can be modulated either by its own intensity, or by the intensity of other field propagating in the same nonlinear medium. The process is known as SPM for phase modulation, due to the variation of its own intensity, and as XPM for phase modulation, due to variations in the other field intensity.

By substituting (3.4.32) into (3.5.33), the nonlinear probe-field phase shift can be examined as it propagates through the medium

$$\phi_{\mathrm{NL}_\mathrm{p}}(\omega) = \frac{\omega}{c} \frac{\mathrm{Re}\left[\chi^{(3)}_{\mathrm{p}_1}(\omega)\left|\xi_{\mathrm{p}_f}\right|^2 + \chi^{(3)}_{\mathrm{p}_2}(\omega)\left|\xi_{\mathrm{s}_f}\right|^2\right]}{2n_\mathrm{p}(\omega)} z. \tag{3.5.33}$$

The phase equation consist of two terms; the first term

$$\phi_{\mathrm{SPM}_\mathrm{p}}(\omega) = \frac{\omega}{\epsilon_0 c^2} \frac{\mathrm{Re}\left[\chi^{(3)}_{\mathrm{p}_1}(\omega)\right] I_\mathrm{p}}{n^2_\mathrm{p}(\omega)} z, \tag{3.5.34}$$

with the probe-field intensity defined by

$$I_\mathrm{p} = \frac{c\epsilon_0 n_\mathrm{p}(\omega)}{2}\left|\xi_{\mathrm{p}_f}\right|^2, \tag{3.5.35}$$

represents the probe field SPM. While the second term

$$\phi_{\mathrm{XPM_p}}(\omega) = \frac{\omega}{\epsilon_0 c^2} \frac{\mathrm{Re}\left[\chi^{(3)}_{\mathrm{p_2}}(\omega)\right] I_{\mathrm{s}}}{n_{\mathrm{p}}(\omega) n_{\mathrm{s}}(\omega)} z, \tag{3.5.36}$$

with the signal-field intensity is defined by

$$I_{\mathrm{s}} = \frac{c\epsilon_0 n_{\mathrm{s}}(\omega)}{2} \left|\xi_{\mathrm{s}_f}\right|^2, \tag{3.5.37}$$

is the XPM of the probe field. Referring to Fig. 3.7, the SPM and the XPM of the probe field vanishes at the center of two transparency windows; i.e.; at $\delta_{\mathrm{p}} = \delta_{\mathrm{c}}$ and $\delta_{\mathrm{p}} = \delta_{\mathrm{s}}$. However, the SPM and the XPM around the region of the second window exceed their values around the region of the first window. The values of SPM and XPM at the region of second window are higher than their values in the region of first window by a factor of 1000.

The detuning of the coupling field plays an important role in modifying the values of SPM and XPM at the center of the second windows, when $\delta_{\mathrm{p}} = \delta_{\mathrm{s}}$. Figure 3.8(a) demonstrates the variation of SPM and XPM as function of the coupling-field detuning. When the coupling field is in resonance with $|2\rangle \leftrightarrow |4\rangle$ transition, the nonlinear dispersion response SPM and XPM vanishes. However, detuning the coupling field to lower or higher energy than $|2\rangle \leftrightarrow |4\rangle$ transition, displaces the value of XPM and SPM from zero, and both reach their maximum values when $\delta_{\mathrm{c}} = \frac{\delta_{\mathrm{s}}}{2}$. The SPM and XPM vanish also, when the coupling-field detuning reach the signal-field detuning $\delta_{\mathrm{c}} = \delta_{\mathrm{s}} = \delta_{\mathrm{p}} = 0$.

It is possible to investigate which term is responsible for the variation of the SPM and XPM in response to the coupling field, by analyzing the real part of $\chi^{(3)}_{\mathrm{p_2}}(\omega)$, when $\delta_{\mathrm{p}} = \delta_{\mathrm{s}}$. From Eq. (3.4.35), the real part of $\chi^{(3)}_{\mathrm{p_2}}(\omega)$ can be written as, when $\delta_{\mathrm{p}} = \delta_{\mathrm{s}}$

$$\begin{aligned}\mathrm{Re}\left[\chi^{(3)}_{\mathrm{p_2}}(\omega)\right] =& \frac{2\eta_{\mathrm{sp}}\left(\varrho_{44} - \varrho_{33}\right)}{\gamma_3\left[\left(\Gamma_{43} + \frac{|\Omega_{\mathrm{c}}|^2\Gamma_{32}}{\Gamma_{32}^2+4\delta_{\mathrm{sc}}^2}\right)^2 + 4\left(\delta_{\mathrm{s}} - \frac{|\Omega_{\mathrm{c}}|^2\delta_{\mathrm{sc}}}{\Gamma_{32}^2+4\delta_{\mathrm{sc}}^2}\right)^2\right]} \\ &\times \frac{\left(\delta_{\mathrm{s}} - \frac{|\Omega_{\mathrm{c}}|^2\delta_{\mathrm{sc}}}{\Gamma_{32}^2+4\delta_{\mathrm{sc}}^2}\right)\left(\gamma_4 + \frac{|\Omega_{\mathrm{c}}|^2\gamma_2}{\gamma_2^2+4\delta_{\mathrm{pc}}^2} + \frac{|\Omega_{\mathrm{s}}|^2}{\gamma_3}\right) + \left(\frac{|\Omega_{\mathrm{c}}|^2\delta_{\mathrm{pc}}}{\gamma_2^2+4\delta_{\mathrm{pc}}^2} - \delta_{\mathrm{p}}\right)\left(\Gamma_{43} + \frac{|\Omega_{\mathrm{c}}|^2\Gamma_{32}}{\Gamma_{32}^2+4\delta_{\mathrm{sc}}^2}\right)}{\left(\gamma_4 + \frac{|\Omega_{\mathrm{c}}|^2\gamma_2}{\gamma_2^2+4\delta_{\mathrm{pc}}^2} + \frac{|\Omega_{\mathrm{s}}|^2}{\gamma_3}\right)^2 + 4\left(\frac{|\Omega_{\mathrm{c}}|^2\delta_{\mathrm{pc}}}{\gamma_2^2+4\delta_{\mathrm{pc}}^2} - \delta_{\mathrm{p}}\right)^2},\end{aligned} \tag{3.5.38}$$

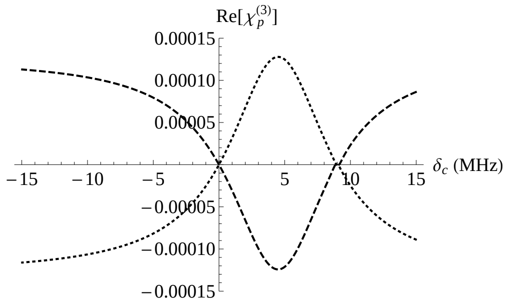

(a)

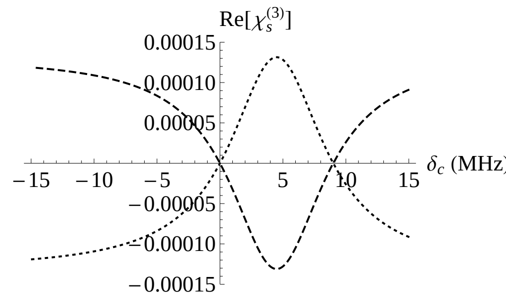

(b)

Figure 3.8: Real part of the nonlinear-optical susceptibility versus coupling-field detuning. (a) $\mathrm{Re}\left[\chi^{(3)}_{\mathrm{p}_1}\right]$ (dashed line) and $\mathrm{Re}\left[\chi^{(3)}_{\mathrm{p}_2}\right]$ (dotted line), for $\delta_\mathrm{s} = 9$ MHz and $\Omega_\mathrm{s} = 0.2\gamma_4$. (b) $\mathrm{Re}\left[\chi^{(3)}_{\mathrm{s}_1}\right]$ (dashed line) and $\mathrm{Re}\left[\chi^{(3)}_{\mathrm{s}_2}\right]$ (dotted line), for $\delta_\mathrm{p} = 9$ MHz and $\Omega_\mathrm{p} = 0.2\gamma_4$. Other parameters are $\gamma_4 = 18$ MHz, $\Omega_\mathrm{c} = \gamma_4$, $\gamma_3 = 10$ kHz, $\gamma_2 = 40$ kHz, $\varrho_{11} = \varrho_{33} = 0.5$, $\mathcal{N} = 1 \times 10^{14}\mathrm{cm}^{-3}$ and using ^{87}Rb dipole moments $|\boldsymbol{d}_{14}| = |\boldsymbol{d}_{34}| = 1.269 \times 10^{-29}$ C·m.

where η_sp is defined by (3.4.37). The terms $\frac{|\Omega_\mathrm{c}|^2\gamma_2}{\gamma_2^2+4\delta_\mathrm{pc}^2}$ and $+\frac{|\Omega_\mathrm{c}|^2\Gamma_{32}}{\Gamma_{32}^2+4\delta_\mathrm{sc}^2}$ are of order of magnitude of γ_2 and Γ_{32}; therefore, they can be neglected compared to γ_4 and Γ_{43}. Then Eq. (3.4.35) becomes

$$\mathrm{Re}\left[\chi^{(3)}_{\mathrm{p}_2}(\omega)\right] \approx \frac{2\eta_\mathrm{sp}\left(\varrho_{44}-\varrho_{33}\right)\left[\left(\delta_\mathrm{s}-\frac{|\Omega_\mathrm{c}|^2\delta_\mathrm{sc}}{\Gamma_{32}^2+4\delta_\mathrm{sc}^2}\right)\left(\gamma_3\gamma_4+|\Omega_\mathrm{s}|^2\right)+\gamma_3\Gamma_{43}\left(\frac{|\Omega_\mathrm{c}|^2\delta_\mathrm{pc}}{\gamma_2^2+4\delta_\mathrm{pc}^2}-\delta_\mathrm{p}\right)\right]}{\left[\Gamma_{43}^2+4\left(\delta_\mathrm{s}-\frac{|\Omega_\mathrm{c}|^2\delta_\mathrm{sc}}{\Gamma_{32}^2+4\delta_\mathrm{sc}^2}\right)^2\right]\left[\left(\gamma_3\gamma_4+|\Omega_\mathrm{s}|^2\right)^2+4\gamma_3^2\left(\frac{|\Omega_\mathrm{c}|^2\delta_\mathrm{pc}}{\gamma_2^2+4\delta_\mathrm{pc}^2}-\delta_\mathrm{p}\right)^2\right]}. \tag{3.5.39}$$

For negligible absorption, when condition (3.4.55) is valid

$$\mathrm{Re}\left[\chi^{(3)}_{\mathrm{p}_2}(\omega)\right] \approx \frac{2\eta_\mathrm{sp}\left(\varrho_{44}-\varrho_{33}\right)\left[\left(\delta_\mathrm{s}-\frac{|\Omega_\mathrm{c}|^2\delta_\mathrm{sc}}{\Gamma_{32}^2+4\delta_\mathrm{sc}^2}\right)|\Omega_\mathrm{s}|^2+\gamma_3\Gamma_{43}\left(\frac{|\Omega_\mathrm{c}|^2\delta_\mathrm{pc}}{\gamma_2^2+4\delta_\mathrm{pc}^2}-\delta_\mathrm{p}\right)\right]}{\left[\Gamma_{43}^2+4\left(\delta_\mathrm{s}-\frac{|\Omega_\mathrm{c}|^2\delta_\mathrm{sc}}{\Gamma_{32}^2+4\delta_\mathrm{sc}^2}\right)^2\right]\left[|\Omega_\mathrm{s}|^4+4\gamma_3^2\left(\frac{|\Omega_\mathrm{c}|^2\delta_\mathrm{pc}}{\gamma_2^2+4\delta_\mathrm{pc}^2}-\delta_\mathrm{p}\right)^2\right]}. \tag{3.5.40}$$

When $\delta_\mathrm{s} = \delta_\mathrm{p}$, the detuning inequality $\delta_\mathrm{sc} = \delta_\mathrm{pc} \gg \gamma_2, \Gamma_{32}$ that holds, which lead to simplification of (3.5.38) yielding

$$\mathrm{Re}\left[\chi^{(3)}_{\mathrm{p}_2}(\omega)\right] \approx \frac{2\eta_\mathrm{sp}\left(\varrho_{44}-\varrho_{33}\right)\left(\delta_\mathrm{s}-\frac{|\Omega_\mathrm{c}|^2}{4\delta_\mathrm{sc}}\right)|\Omega_\mathrm{s}|^2}{\left[\Gamma_{43}^2+4\left(\delta_\mathrm{s}-\frac{|\Omega_\mathrm{c}|^2}{4\delta_\mathrm{sc}}\right)^2\right]\left[|\Omega_\mathrm{s}|^4+4\gamma_3^2\left(\frac{|\Omega_\mathrm{c}|^2}{4\delta_\mathrm{pc}}-\delta_\mathrm{p}\right)^2\right]}. \tag{3.5.41}$$

By neglecting the term $4\gamma_3^2\left(\frac{|\Omega_\mathrm{c}|^2}{4\delta_\mathrm{pc}}-\delta_\mathrm{p}\right)^2$ compared to $|\Omega_\mathrm{s}|^4$, we reach the final approximate equation of $\mathrm{Re}\left[\chi^{(3)}_{\mathrm{p}_2}(\omega)\right]$ as function of coupling-field detuning

$$\mathrm{Re}\left[\chi^{(3)}_{\mathrm{p}_2}(\delta_\mathrm{c})\right]\approx\frac{2\eta_\mathrm{sp}\left(\varrho_{44}-\varrho_{33}\right)\delta_\mathrm{sc}^2\left(\delta_\mathrm{s}-\frac{|\Omega_\mathrm{c}|^2}{4\delta_\mathrm{sc}}\right)}{|\Omega_\mathrm{s}|^2\left[\delta_\mathrm{sc}^2\Gamma_{43}^2+4\left(\delta_\mathrm{sc}\delta_\mathrm{s}-\frac{|\Omega_\mathrm{c}|^2}{4}\right)^2\right]}. \tag{3.5.42}$$

Thus, the XPM vanishes for $\delta_\mathrm{s}=\delta_\mathrm{c}$ and for

$$\delta_\mathrm{s}-\frac{|\Omega_\mathrm{c}|^2}{4\delta_\mathrm{sc}}=0, \tag{3.5.43}$$

which can be written as

$$\delta_\mathrm{s}-\frac{|\Omega_\mathrm{c}|^2}{4\delta_\mathrm{s}}=\delta_\mathrm{c}. \tag{3.5.44}$$

However, at the second EIT window, $\delta_\mathrm{s}\neq\delta_\mathrm{c}$ is always true. Therefore, XPM vanishes only whenever (3.5.43) is correct. In the cases studied, the coupling field has been selected to be in resonance with the $|2\rangle\leftrightarrow|4\rangle$ transition, thus $\delta_\mathrm{c}=0$. Accordingly, the signal field was chosen to be in resonance with the dressed state $|3\rangle\leftrightarrow|-\rangle$, i.e., $\delta_\mathrm{s}=\frac{\Omega_\mathrm{c}}{2}$. This makes the second EIT window, at $\delta_\mathrm{p}=\delta_\mathrm{s}$, located at the center of the absorption peak of $|1\rangle\rightarrow|-\rangle$ transition. This choice of frequency detuning makes

$$\delta_\mathrm{s}-\frac{|\Omega_\mathrm{c}|^2}{4\delta_\mathrm{s}}=0, \tag{3.5.45}$$

or in different form

$$\left(\delta_\mathrm{s}-\frac{|\Omega_\mathrm{c}|}{2}\right)\left(\delta_\mathrm{s}+\frac{|\Omega_\mathrm{c}|}{2}\right)=0. \tag{3.5.46}$$

This means that, to enhance the nonlinear index of refraction of the probe field, the signal field must not be in resonance either with dressed state $|3\rangle\leftrightarrow|-\rangle$ or with the dressed state $|3\rangle\leftrightarrow|+\rangle$. This result can be generalized to the case of SPM, since analyzing $\mathrm{Re}\left[\chi^{(3)}_{\mathrm{p}_1}(\omega)\right]$ leads to the same result as above.

Similar to the probe-field case, the phase shift of the signal field can be written as

$$\phi_{\mathrm{NL}_\mathrm{s}}(\omega)=\frac{\omega}{c}\frac{\mathrm{Re}\left[\chi^{(3)}_{\mathrm{s}_1}(\omega)\left|\xi_{\mathrm{s}_f}\right|^2+\chi^{(3)}_{\mathrm{s}_2}(\omega)\left|\xi_{\mathrm{p}_f}\right|^2\right]}{2n_\mathrm{s}(\omega)}z. \tag{3.5.47}$$

The SPM term is represented by the first term of (3.5.47)

$$\phi_{\mathrm{SPM_s}}(\omega) = \frac{\omega}{\epsilon_0 c^2} \frac{\mathrm{Re}\left[\chi^{(3)}_{\mathrm{s}_1}(\omega)\right] I_{\mathrm{s}}}{n^2_{\mathrm{s}}(\omega)} z, \tag{3.5.48}$$

where the signal-field intensity defined by (3.5.37). The XPM term is described by the second term of (3.5.47)

$$\phi_{\mathrm{XPM_s}}(\omega) = \frac{\omega}{\epsilon_0 c^2} \frac{\mathrm{Re}\left[\chi^{(3)}_{\mathrm{s}_2}(\omega)\right] I_{\mathrm{p}}}{n_{\mathrm{p}}(\omega) n_{\mathrm{s}}(\omega)} z, \tag{3.5.49}$$

where the probe-field intensity defined by (3.5.35). The detuning of the coupling field modifies the values of SPM and XPM in the same way as it does with the probe field (see Fig. 3.8(b)). Increasing or decreasing the energy of the coupling field from the $|2\rangle \leftrightarrow |4\rangle$ transition energy displace the SPM and XPM value from zero. Reaching their maximum when $\delta_{\mathrm{c}} = \frac{\delta_{\mathrm{p}}}{2}$. The values SPM and XPM return to the zero value at equal detunings.

The approximated equation of $\mathrm{Re}\left[\chi^{(3)}_{\mathrm{s}_2}(\omega)\right]$ as function of coupling-field detuning is derived, when $\delta_{\mathrm{s}} = \delta_{\mathrm{s}}$ in similar way to (3.5.42)

$$\mathrm{Re}\left[\chi^{(3)}_{\mathrm{s}_2}(\delta_{\mathrm{c}})\right] \approx \frac{2\eta_{\mathrm{sp}} \left(\varrho_{44} - \varrho_{11}\right) \delta_{\mathrm{pc}} \left(\delta_{\mathrm{p}} - \frac{|\Omega_{\mathrm{c}}|^2}{4\delta_{\mathrm{pc}}}\right)}{|\Omega_{\mathrm{p}}|^2 \left[\delta^2_{\mathrm{pc}} \gamma_4 3^2 + 4\left(\delta_{\mathrm{pc}}\delta_{\mathrm{p}} - \frac{|\Omega_{\mathrm{c}}|^2}{4}\right)^2\right]}. \tag{3.5.50}$$

Thus, the XPM vanishes for $\delta_{\mathrm{p}} = \delta_{\mathrm{c}}$ and for

$$\delta_{\mathrm{p}} - \frac{|\Omega_{\mathrm{c}}|^2}{4\delta_{\mathrm{pc}}} = 0, \tag{3.5.51}$$

which are exactly the same conditions for vanishing SPM and XPM of probe field at $\delta_{\mathrm{p}} = \delta_{\mathrm{s}}$. Therefore, to enhance the nonlinear index of refraction of the signal field, the probe field must not be in resonance either with dressed state $|3\rangle \leftrightarrow |-\rangle$ or with dressed state $|3\rangle \leftrightarrow |+\rangle$. The result can be generalized to the case of SPM, as analyzing $\mathrm{Re}\left[\chi^{(3)}_{\mathrm{s}_1}(\omega)\right]$ leads to the same result.

3.6 Summary

The wave equations for the probe and signal-field modes have been solved. The phase and amplitude of the wave function are controlled by the real and imaginary part of the optical susceptibility respectively. A close study of the linear term of the optical susceptibility shows that the absorption and the group velocity of the probe and signal fields can be reduced at the DDEIT windows, by adjusting the values of γ_4, γ_3, and γ_2 such that the inequalities (3.4.47), (3.4.51), (3.4.55), and (3.4.56) are all satisfied Then, the applied fields can be used for better control of both absorption and the group velocity.

Nonlinear-optical phenomena are generated in the $\pitchfork$ atom-field system, discovered by analyzing the nonlinear optical susceptibility. The imaginary part of the nonlinear-optical susceptibility reveals the existence of two optical phenomena: Raman amplification and nonlinear absorption. The real part reveals the dependence of the index of refraction on the intensity of the applied field through SPM and XPM optical process.

Raman amplification, as a process, exists in both the probe and the signal fields, but cannot be detected in both field outputs simultaneously. The gain of the probe field is accompanied by nonlinear absorption, and the gain of the signal field is accompanied by nonlinear absorption. When the gain of either field exceeds its absorption, the field is amplified. The amplification occurs only if (2.5.11) or (2.5.15) are satisfied.

The SPM and the XPM of the probe and signal fields vanishes at the center of each transparency window. However, their values around the region of the second window exceed their values around the region of the first window. To enhance the nonlinear index of refraction of the probe field, the signal field must not be in resonance either with the $|3\rangle \leftrightarrow |-\rangle$ or with the $|3\rangle \leftrightarrow |+\rangle$ transitions. Similar for the signal field, the nonlinear index of refraction of the signal field can be increased by detuning the probe field off-resonance from the $|3\rangle \leftrightarrow |-\rangle$ and from the $|3\rangle \leftrightarrow |+\rangle$ transitions.

Chapter 4

Tripod Atom-Field Configuration using Gaussian-Probe and Signal Beams

4.1 Introduction

In the previous chapter, linear and nonlinear interactions were dealt with, by assuming that all interacting waves are infinite plane waves. However, in practice, the incident radiation is commonly focused on the nonlinear-optical medium, in order to increase the intensity, and hence to increase the efficiency of the nonlinear-optical interactions excited by focused laser beams. The output modes of most conventional lasers are designed so that the output beam is the lowest-order Hermite-Gaussian, or Laguerre-Gaussian functions.

In this chapter, Gaussian beams replace the infinite-plane probe and signal fields in the optical susceptibility, describing the induced polarization of the probe-field transition. To understand the effects of using the Gaussian signal beam on the Gaussian probe beam output function, the wave equation is solved analytically, and the modulated output probe-field wave function is found. This carries all information on how the amplitude and phase of the wave function evolve during their journey within the nonlinear optical medium.

The signal-Gaussian beam is used to alter the dielectric of the nonlinear medium, as the beam propagates through the medium. The mediums dielectric varies as the propagation distance of the signal field changes. The signal field-medium interaction becomes equivalent to treating the medium as if it is inhomogeneous. The technique of altering the medium's dielectric could modify and enhance the linear and nonlinear interactions.

This chapter is organized as follows: In Sec. 4.2, the derivation of the paraxial equation and the fundamental Laguerre-Gaussian solution of the paraxial wave equation are discussed, which are used as input to the optical system. After the discussion of the replacement of the infinite-plane probe and signal waves with fundamental Gaussian-probe and signal fields in the optical susceptibilities in Sec. 4.3, the optical susceptibility simplified in Sec. 4.4. The solution of the wave equation using Gaussian-signal and probe fields is elaborated in Sec. 4.5. Then the modulation of optical parameters of the output wave function is explored in Sec. 4.6. Finally, Sec. 4.7 provides a summary.

4.2 Paraxial-Wave Equation and Fundamental-Mode Gaussian Beam

To derive the paraxial equation we start with wave equation defined by 3.2.9

$$\nabla^2 \boldsymbol{E} - \frac{1}{c^2}\frac{\partial^2 \boldsymbol{E}}{\partial t^2} = \mu_0 \frac{\partial^2 \boldsymbol{P}}{\partial t^2}. \tag{4.2.1}$$

Next, we represent the electric field and polarization as

$$\boldsymbol{E}(z,r,t) = \boldsymbol{\xi}(z,r)e^{-\mathrm{i}(kz-\omega t)} + \text{c.c.}, \tag{4.2.2}$$

$$\boldsymbol{P}(z,r,t) = \boldsymbol{p}(z,r)e^{-\mathrm{i}(kz-\omega t)} + \text{c.c.}. \tag{4.2.3}$$

Here, $\boldsymbol{E}$ and $\boldsymbol{P}$ are allowed to represent non-plane waves by allowing the complex amplitude $\boldsymbol{\xi}$ and $\boldsymbol{p}$ to be spatially varying quantities. By choosing the wavevector $\boldsymbol{k}$ of the polarization similar to the electric field we do not allow possibility of a wavevector mismatch. As the z-direction is specified as the direction of propagation, it is convenience to express the Laplace operator as

$$\nabla^2 = \frac{\partial^2}{\partial z^2} + \nabla_{\mathrm{T}}^2, \tag{4.2.4}$$

where the transverse Laplacian is give by

$$\nabla_{\mathrm{T}}^2 = \frac{\partial^2}{\partial x^2} + \frac{\partial^2}{\partial y^2}, \tag{4.2.5}$$

in rectangular coordinates, and given by

$$\nabla_{\mathrm{T}}^2 = \frac{1}{r}\frac{\partial}{\partial r}(r\frac{\partial}{\partial r}) + (\frac{1}{r})^2\frac{\partial^2}{\partial \phi^2}, \tag{4.2.6}$$

in cylindrical coordinates. By substituting (4.2.2) and (4.2.3) into (4.2.1) the following is obtained:

$$\nabla_{\mathrm{T}}^2 \boldsymbol{\xi}(z,r) + \frac{\partial^2 \boldsymbol{\xi}(z,r)}{\partial z^2} - 2\mathrm{i}k\frac{\partial \boldsymbol{\xi}(z,r)}{\partial z} - k^2\boldsymbol{\xi}(z,r) + \frac{\omega^2}{c^2}\boldsymbol{\xi}(z,r) = -\mu_0\omega^2 k\boldsymbol{p}(z,r). \tag{4.2.7}$$

The medium is assumed to be isotropic and to respond instantaneously to the electric field; this permits us to use (3.2.5). By separating the polarization into its linear and nonlinear parts as in (3.5.1), we obtain

$$\nabla_{\mathrm{T}}^2 \boldsymbol{\xi}(z,r) + \frac{\partial^2 \boldsymbol{\xi}(z,r)}{\partial z^2} - 2\mathrm{i}k\frac{\partial \boldsymbol{\xi}(z,r)}{\partial z} - k^2\boldsymbol{\xi}(z,r) + \frac{\omega^2}{c^2}\left[1 + \boldsymbol{\chi}^{(1)}(\omega)\right]\boldsymbol{\xi}(z,r) = -\mu_0\omega^2 k\boldsymbol{p}^{(\mathrm{NL})}(z,r). \tag{4.2.8}$$

For a non-dissipative medium, the last two terms on the left hand side of the wave equation cancel each other out. Then the wave equation reduces to

$$\nabla_{\mathrm{T}}^2 \boldsymbol{\xi}(z,r) + \frac{\partial^2 \boldsymbol{\xi}(z,r)}{\partial z^2} - 2\mathrm{i}k\frac{\partial \boldsymbol{\xi}(z,r)}{\partial z} = -\mu_0\omega^2 k\boldsymbol{p}^{(\mathrm{NL})}(z,r). \tag{4.2.9}$$

Using slowly-wave approximation (3.5.9), the wave equation becomes

$$\nabla_{\mathrm{T}}^2 \boldsymbol{\xi}(z,r) - 2\mathrm{i}k\frac{\partial \boldsymbol{\xi}(z,r)}{\partial z} = -\mu_0\omega^2 k\boldsymbol{p}^{(\mathrm{NL})}(z,r). \tag{4.2.10}$$

In the linear regime the wave equation reduces to

$$\nabla_{\mathrm{T}}^2 \boldsymbol{\xi}(z,r) - 2\mathrm{i}k\frac{\partial \boldsymbol{\xi}(z,r)}{\partial z} = 0. \tag{4.2.11}$$

This equation is often known as the paraxial equation. This is solved in such a case by a beam having a transverse intensity distribution that is everywhere a Gaussian and that can be represented in the scalar approximation [87]. This type of solution has been discussed in several text books [88, 89]. Here, we are going to discuss briefly the fundamental Gaussian beam, as many lasers generate beams in the fundamental mode. Additionally, this order of Gaussian beam will be used as an input to the optical system

$$\xi(z,r) = \xi_0\frac{w_0}{w(z)}e^{-r^2\left(\frac{1}{w^2(z)} + \frac{\mathrm{i}k}{2R(z)}\right)}e^{\mathrm{i}\Theta(z)}, \tag{4.2.12}$$

with

$$w^2(z) = w_0^2 \left[1 + \left(\frac{\lambda z}{\pi w_0^2} \right)^2 \right], \tag{4.2.13}$$

representing the beam radius,

$$R(z) = z \left[1 + \left(\frac{\pi w_0^2}{\lambda z} \right)^2 \right], \tag{4.2.14}$$

representing the radius of the curvature, and

$$\Theta(z) = \tan^{-1} \left(\frac{\lambda z}{\pi w_0^2} \right), \tag{4.2.15}$$

which is the called Gouy phase shift, and representing the spatial variation of the wave phase. It is equal to zero at $z = 0$, and reaches π as the wave passes through the focus, relative to an infinite plane wave. The constant w_0 in the above equations denotes the beam radius at $z = 0$, which is called the beam waist radius. At beam waist, the beam radius w attains its minimum value w_0, and the electric field distribution is most concentrated. The radius of beam curvature is infinite there, as the phase front is planar at the beam waist. The term λ is the wavelength of the electric-field wave. The quantity $\frac{\pi w_0^2}{\lambda}$ is called the Rayleigh range z_{R} and defined as the z-distance at which the radius has expanded by a factor of $\sqrt{2}$. The confocal length of the beam is defined in term of the Rayleigh range as

$$b = 2z_{\mathrm{R}}. \tag{4.2.16}$$

For theoretical work it is often convenient to represent the Gaussian beam in more compact form [81] as

$$\xi(r) = \frac{\xi_0}{1 - \mathrm{i}\varsigma(z)} e^{\frac{-r^2}{w_0^2[1-\mathrm{i}\varsigma(z)]}}, \tag{4.2.17}$$

with ς being the dimensionless longitudinal coordinate defined in term of confocal length b as

$$\varsigma(z) = \frac{2z}{b} = \frac{z}{z_{\mathrm{R}}}. \tag{4.2.18}$$

See Appendix D for the details of how Eq. (4.2.17) is equivalent to (4.2.12).

4.3 Atom-Field Optical Susceptibilities using Gaussian Beams

Before writing the optical susceptibility of the atom-field system using the Gaussian fundamental mode beam, let us first represent the probe and the signal-field input-envelope wave functions as Gaussian. The probe-field input envelope function can be written as

$$\xi_{\mathrm{p}_f}(z,r,\omega) = \frac{\xi_{\mathrm{p}_0}}{1-\mathrm{i}\varsigma_{\mathrm{p}}(z,\omega)} e^{\frac{-r^2}{w_{0_\mathrm{p}}^2[1-\mathrm{i}\varsigma_\mathrm{p}(z,\omega)]}}, \tag{4.3.1}$$

where

$$\varsigma_\mathrm{p}(z,\omega) = \frac{z}{z_{R_\mathrm{p}}(\omega)}, \tag{4.3.2}$$

and the Rayleigh range of the probe field is calculated from

$$\begin{aligned} z_{R_\mathrm{p}}(\omega) &= \frac{k_{\mathrm{p}_f}(\omega) w_{0_\mathrm{p}}^2}{2} \\ &= \frac{b_\mathrm{p}(\omega)}{2}, \end{aligned} \tag{4.3.3}$$

with $k_{\mathrm{p}_f}(\omega)$ calculated using Eq. (3.4.11), where the linear index of refraction $n_{\mathrm{p}_f}(\omega)$ is defined by (3.4.59) in absence of the signal field as

$$n_{\mathrm{p}_f}(\omega) = 1 + \frac{\eta_\mathrm{p}\left(\varrho_{11}-\varrho_{44}\right)\left[\frac{|\Omega_\mathrm{c}|^2\delta_\mathrm{pc}}{\gamma_2^2+4\delta_\mathrm{pc}^2} - \delta_\mathrm{p}\right]}{\left(\gamma_4 + \frac{|\Omega_\mathrm{c}|^2\gamma_2}{\gamma_2^2+4\delta_\mathrm{pc}^2}\right)^2 + 4\left(\frac{|\Omega_\mathrm{c}|^2\delta_\mathrm{pc}}{\gamma_2^2+4\delta_\mathrm{pc}^2} - \delta_\mathrm{p}\right)^2}. \tag{4.3.4}$$

Then the modulus square of the probe-field envelope function can be written as

$$\begin{aligned} \left|\xi_{\mathrm{p}_f}(z,r,\omega)\right|^2 &= \frac{\left|\xi_{\mathrm{p}_0}\right|^2 \wp_\mathrm{p}(r)}{1+\varsigma_\mathrm{p}^2(z,\omega)} \\ &= \frac{\left|\xi_{\mathrm{p}_0}\right|^2 \wp_\mathrm{p}(r)}{1+\left(\frac{2z}{b_\mathrm{P}(\omega)}\right)^2}, \end{aligned} \tag{4.3.5}$$

and the modulus square of the probe-field Rabi frequency, defined by (2.2.11) as

$$\begin{aligned} \left|\Omega_{\mathrm{p}_f}(z,r,\omega)\right|^2 &= \frac{\left|\Omega_{\mathrm{p}_0}\right|^2 \wp_\mathrm{p}(r)}{1+\varsigma_\mathrm{p}^2(z,\omega)} \\ &= \frac{\left|\Omega_{\mathrm{p}_0}\right|^2 \wp_\mathrm{p}(r)}{1+\left(\frac{2z}{b_\mathrm{P}(\omega)}\right)^2}, \end{aligned} \tag{4.3.6}$$

with

$$\wp_{\mathrm{p}}(r) = e^{\frac{-2r^2}{w_{0_{\mathrm{p}}}^2}}, \tag{4.3.7}$$

where (4.2.18) is used to write the second line of Eqs. (4.3.5) and (4.3.6).

Similar to the probe field, the signal-field input-envelope wave function can be written as

$$\xi_{\mathrm{s}_f}(z,r,\omega) = \frac{\xi_{\mathrm{s}0}}{1-\mathrm{i}\varsigma_{\mathrm{s}}(z,\omega)} e^{\frac{-r^2}{w_{0_{\mathrm{s}}}^2[1-\mathrm{i}\varsigma_{\mathrm{s}}(z,\omega)]}}, \tag{4.3.8}$$

where

$$\varsigma_{\mathrm{s}}(z,\omega) = \frac{z}{z_{R_{\mathrm{s}}}(\omega)}, \tag{4.3.9}$$

with $z_{R_{\mathrm{s}}}$ being the Rayleigh range of the signal field obtained using

$$\begin{aligned} z_{R_{\mathrm{s}}}(\omega) &= \frac{k_{\mathrm{s}_f}(\omega) w_{0_{\mathrm{s}}}^2}{2} \\ &= \frac{b_{\mathrm{s}}(\omega)}{2}, \end{aligned} \tag{4.3.10}$$

The wave propagation constant $k_{\mathrm{s}_f}(\omega)$ is calculated using (3.4.11), where the signal-field linear index of refraction $n_{\mathrm{s}_f}(\omega)$ is determined using (3.4.61), but in the absence of the probe field as

$$n_{\mathrm{s}_f}(\omega) = 1 + \frac{\eta_{\mathrm{s}}\left(\varrho_{33}-\varrho_{44}\right)\left(\frac{|\Omega_{\mathrm{c}}|^2\delta_{\mathrm{sc}}}{\Gamma_{32}^2+4\delta_{\mathrm{sc}}^2}-\delta_{\mathrm{s}}\right)}{\left(\Gamma_{43}+\frac{|\Omega_{\mathrm{c}}|^2\Gamma_{32}}{\Gamma_{32}^2+4\delta_{\mathrm{sc}}^2}\right)^2+4\left(\frac{|\Omega_{\mathrm{c}}|^2\delta_{\mathrm{sc}}}{\Gamma_{32}^2+4\delta_{\mathrm{sc}}^2}-\delta_{\mathrm{s}}\right)^2}. \tag{4.3.11}$$

Then, the modulus square of the signal-field envelope function can be written as

$$\begin{aligned} \left|\xi_{\mathrm{s}_f}(z,r,\omega)\right|^2 &= \frac{\left|\xi_{\mathrm{s}0}\right|^2 \wp_{\mathrm{s}}(r)}{1+\varsigma_{\mathrm{s}}^2(z,\omega)} \\ &= \frac{\left|\xi_{\mathrm{s}0}\right|^2 \wp_{\mathrm{s}}(r)}{1+\left(\frac{2z}{b_{\mathrm{s}}(\omega)}\right)^2}. \end{aligned} \tag{4.3.12}$$

The modulus square of the signal-field Rabi frequency can be obtained using (2.2.11) and (4.3.12) as

$$\begin{aligned} \left|\Omega_{\mathrm{s}_f}(z,r,\omega)\right|^2 &= \frac{\left|\Omega_{\mathrm{s}0}\right|^2 \wp_{\mathrm{s}}(r)}{1+\varsigma_{\mathrm{s}}^2(z,\omega)} \\ &= \frac{\left|\Omega_{\mathrm{p}_0}\right|^2 \wp_{\mathrm{p}}(r)}{1+\left(\frac{2z}{b_{\mathrm{P}}(\omega)}\right)^2}, \end{aligned} \tag{4.3.13}$$

with

$$\wp_{\mathrm{s}}(r) = e^{\frac{-2r^2}{w_{0\mathrm{s}}^2}}. \tag{4.3.14}$$

Now, we can write the optical susceptibilities of the probe field defined by (3.4.33), (3.4.34), and (3.4.35) and of the signal field defined by (3.4.40), (3.4.41) and (3.4.42) using Gaussian-probe and signal beams. The linear term of the probe field modifies to

$$\chi^{(1)}_{\mathrm{p}_G}(z,\omega) = \frac{\mathrm{i}\eta_{\mathrm{p}}(\varrho_{11}-\varrho_{44})}{\beth_- + \frac{|\Omega_{\mathrm{s}0}|^2\wp_{\mathrm{s}}}{\gamma_{\mathrm{ps}_-}(1+\varsigma_{\mathrm{s}}^2(z))}}, \tag{4.3.15}$$

with

$$\beth_\pm = \gamma_4 \pm 2\mathrm{i}\delta_{\mathrm{p}} + \frac{|\Omega_{\mathrm{c}}|^2}{\gamma_2 \pm 2\mathrm{i}\delta_{\mathrm{pc}}}, \tag{4.3.16}$$

and

$$\gamma_{\mathrm{ps}_\pm} = \gamma_3 \pm 2\mathrm{i}\delta_{\mathrm{ps}}, \tag{4.3.17}$$

and the nonlinear terms modify to

$$\chi^{(3)}_{\mathrm{p}_{G1}}(z,\omega) = \frac{\mathrm{i}\eta_{\mathrm{p}_1}(\varrho_{11}-\varrho_{44})}{\gamma_{\mathrm{ps}_-}\aleph_+} \times \frac{1-\frac{\beth_-}{\beth_- + \frac{|\Omega_{\mathrm{s}0}|^2\wp_{\mathrm{s}}}{\gamma_{\mathrm{ps}_-}(1+\varsigma_{\mathrm{s}}^2(z))}}}{\beth_- + \frac{|\Omega_{\mathrm{s}0}|^2\wp_{\mathrm{s}}}{\gamma_{\mathrm{ps}_-}(1+\varsigma_{\mathrm{s}}^2(z))}}, \tag{4.3.18}$$

and

$$\chi^{(3)}_{\mathrm{p}_{G2}}(z,\omega) = \frac{\mathrm{i}\eta_{sp}\,(\varrho_{44}-\varrho_{33})}{\gamma_{\mathrm{ps}_-}\aleph_+} \times \frac{1}{\beth_- + \frac{|\Omega_{\mathrm{s}0}|^2\wp_{\mathrm{s}}}{\gamma_{\mathrm{ps}_-}(1+\varsigma_{\mathrm{s}}^2(z))}}, \tag{4.3.19}$$

with

$$\aleph_\pm = \Gamma_{43} \pm 2\mathrm{i}\delta_{\mathrm{s}} + \frac{|\Omega_{\mathrm{c}}|^2}{\Gamma_{32} \pm 2\mathrm{i}\delta_{\mathrm{sc}}}. \tag{4.3.20}$$

Similarly, the signal-field linear optical susceptibility using Gaussian beam is

$$\chi^{(1)}_{\mathrm{s}_G}(z,\omega) = \frac{\mathrm{i}\eta_{\mathrm{s}}(\varrho_{33}-\varrho_{44})}{\aleph_- + \frac{|\Omega_{\mathrm{p}0}|^2\wp_{\mathrm{p}}}{\gamma_{\mathrm{ps}_+}\left(1+\varsigma_{\mathrm{p}}^2(z)\right)}}, \tag{4.3.21}$$

while the nonlinear terms are

$$\chi^{(3)}_{\mathrm{s}_{G1}}(z,\omega) = \frac{\mathrm{i}\eta_{\mathrm{s}_1}\,(\varrho_{33}-\varrho_{44})}{\gamma_{\mathrm{ps}_+}\beth_+} \times \frac{1-\frac{\aleph_-}{\aleph_- + \frac{|\Omega_{\mathrm{p}0}|^2\wp_{\mathrm{p}}}{\gamma_{\mathrm{ps}_+}(1+\varsigma_{\mathrm{p}}^2(z))}}}{\aleph_- + \frac{|\Omega_{\mathrm{p}0}|^2\wp_{\mathrm{p}}}{\gamma_{\mathrm{ps}_+}\left(1+\varsigma_{\mathrm{p}}^2(z)\right)}}, \tag{4.3.22}$$

and

$$\chi^{(3)}_{\mathrm{s}_{G2}}(z,\omega)=\frac{\mathrm{i}\eta_{\mathrm{sp}}\left(\varrho_{44}-\varrho_{11}\right)}{\gamma_{\mathrm{ps}_+}\gimel_+}\times\frac{1}{\aleph_-+\frac{|\Omega_{\mathrm{p}0}|^2\wp_{\mathrm{p}}}{\gamma_{\mathrm{ps}_+}\left(1+\varsigma_{\mathrm{p}}^2(z)\right)}}. \tag{4.3.23}$$

The signal field is part of the linear and nonlinear-optical susceptibilities equations of the probe field. The signal field is Gaussian, and its intensity and strength depend on the z-coordinate as appears in (4.3.13). Therefore, the probe-field optical susceptibility varies as the signal field propagates through the medium, and the dielectric of the medium varies with z-distance. Hence, it can be said that the medium becomes effectively inhomogeneous with respect to the probe field. This type of inhomogeneity is not due to medium structure and characteristic, but it is created by the propagation of the signal field through the medium. The same happens to the signal field; the probe field is part of the optical susceptibility of the signal field. Therefore, the signal-field optical susceptibility varies as the probe field propagates through the medium. Thus, the propagation of the probe field creates inhomogeneity effecting the signal field.

4.4 Simplified Atom-Field Optical Susceptibilities in the Region of the Second EIT Window

The optical properties of the $\pitchfork$ atom-field system excited by Gaussian probe and signal beams are discussed now. It is assumed that the coupling field is an infinite-plane wave. This assumption makes the optical properties at the first EIT window, when $\delta_l=\delta_{\mathrm{c}}, l\in\{\mathrm{p},\mathrm{s}\}$, not change from those discussed in Sec. 3.4. The modifications occur only at the second EIT window, when $\delta_{\mathrm{p}}=\delta_{\mathrm{s}}$. In this section, we simplify the optical susceptibility around the region, where $\delta_{\mathrm{p}}=\delta_{\mathrm{s}}$ by expanding the linear and the nonlinear term as a polynomial of the propagation distance z. The simplified form of the optical susceptibility is used to solve the probe-field wave equation in the next section.

In the region where $\delta_\mathrm{p} = \delta_\mathrm{s}$, the term

$$\mathfrak{D} = \frac{1}{\gimel_- + \frac{|\Omega_{\mathrm{s}_0}|^2 \wp_\mathrm{s}}{\gamma_{\mathrm{ps}_-}\left[1+\varsigma_\mathrm{s}^2(z)\right]}}, \tag{4.4.1}$$

that appears in the probe-field susceptibility can be written as

$$\mathfrak{D} = \frac{\gamma_{\mathrm{ps}_-}\left[1+\varsigma_\mathrm{s}^2(z)\right]}{|\Omega_{\mathrm{s}_0}|^2 \wp_\mathrm{s}\left(\frac{\gimel_- \gamma_{\mathrm{ps}_-}\left[1+\varsigma_\mathrm{s}^2(z)\right]}{|\Omega_{\mathrm{s}_0}|^2 \wp_\mathrm{s}} + 1\right)}. \tag{4.4.2}$$

It is assumed that for all values of z where the wave propagating, the term $\frac{\gimel_- \gamma_{\mathrm{ps}_-}\left[1+\varsigma_\mathrm{s}^2(z)\right]}{|\Omega_{\mathrm{s}_0}|^2 \wp_\mathrm{s}}$ in the denominator of (4.4.2) is always less than one around the region, where $\delta_\mathrm{p} = \delta_\mathrm{s}$. Hence, the Maclaurin series

$$\frac{1}{1+x} = 1 - x + x^2 + \cdots\ , \tag{4.4.3}$$

for $|x| < 1$, can be used to write (4.4.2) as

$$\mathfrak{D} = \frac{\gamma_{\mathrm{ps}_-}\left[1+\varsigma_\mathrm{s}^2(z)\right]}{|\Omega_{\mathrm{s}_0}|^2 \wp_\mathrm{s}}\left[1 - \frac{\gimel_- \gamma_{\mathrm{ps}_-}\left[1+\varsigma_\mathrm{s}^2(z)\right]}{|\Omega_{\mathrm{s}_0}|^2 \wp_\mathrm{s}} + \left(\frac{\gimel_- \gamma_{\mathrm{ps}_-}\left[1+\varsigma_\mathrm{s}^2(z)\right]}{|\Omega_{\mathrm{s}_0}|^2 \wp_\mathrm{s}}\right)^2 - \cdots +\right]. \tag{4.4.4}$$

Keeping only the first three terms while neglecting the higher order terms, Eq. (4.4.2) can be approximated as

$$\mathfrak{D} \approx \frac{\gamma_{\mathrm{ps}_-}\left[1+\varsigma_\mathrm{s}^2(z)\right]}{|\Omega_{\mathrm{s}_0}|^2 \wp_\mathrm{s}}\left[1 - \left(\frac{\gamma_{\mathrm{ps}_-}\left[1+\varsigma_\mathrm{s}^2(z)\right]}{|\Omega_{\mathrm{s}_0}|^2 \wp_\mathrm{s}}\right)\gimel_- + \left(\frac{\gamma_{\mathrm{ps}_-}\left[1+\varsigma_\mathrm{s}^2(z)\right]}{|\Omega_{\mathrm{s}_0}|^2 \wp_\mathrm{s}}\right)^2 \gimel_-^2\right]. \tag{4.4.5}$$

Equations (4.4.5) can be simplified farther by expanding the bracket of the third term

$$\mathfrak{D} \approx \frac{\gamma_{\mathrm{ps}_-}\left[1+\varsigma_\mathrm{s}^2(z)\right]}{|\Omega_{\mathrm{s}_0}|^2 \wp_\mathrm{s}}\left[1 - \left(\frac{\gamma_{\mathrm{ps}_-}\left[1+\varsigma_\mathrm{s}^2(z)\right]}{|\Omega_{\mathrm{s}_0}|^2 \wp_\mathrm{s}}\right)\gimel_- + \left(\frac{\gamma_{\mathrm{ps}_-}}{|\Omega_{\mathrm{s}_0}|^2 \wp_\mathrm{s}}\right)^2 \left[1 + 2\varsigma_\mathrm{s}^2(z) + \varsigma_\mathrm{s}^4(z)\right]\gimel_-^2\right]. \tag{4.4.6}$$

By collecting the terms of same power of z together, we can write (4.4.6) in a reduced form as

$$\mathfrak{D} = \frac{\gamma_{\mathrm{ps}_-}\left[1+\varsigma_\mathrm{s}^2(z)\right]}{|\Omega_{\mathrm{s}_0}|^2 \wp_\mathrm{s}}\left[\mathfrak{D}_0 + \mathfrak{D}_2\varsigma_\mathrm{s}^2(z) + \mathfrak{D}_4\varsigma_\mathrm{s}^4(z)\right], \tag{4.4.7}$$

with

$$\begin{aligned}\mathfrak{D}_0 &= 1 - \left(\frac{\gamma_{\mathrm{ps}_-}}{|\Omega_{\mathrm{s}_0}|^2\wp_{\mathrm{s}}}\right)\beth_- + \left(\frac{\gamma_{\mathrm{ps}_-}}{|\Omega_{\mathrm{s}_0}|^2\wp_{\mathrm{s}}}\right)^2\beth_-^2,\\ \mathfrak{D}_2 &= -\frac{\gamma_{\mathrm{ps}_-}}{|\Omega_{\mathrm{s}_0}|^2\wp_{\mathrm{s}}}\beth_-\left[1 - 2\left(\frac{\gamma_{\mathrm{ps}_-}}{|\Omega_{\mathrm{s}_0}|^2\wp_{\mathrm{s}}}\right)\beth_-\right],\\ \mathfrak{D}_4 &= \left(\frac{\gamma_{\mathrm{ps}_-}}{|\Omega_{\mathrm{s}_0}|^2\wp_{\mathrm{s}}}\right)^2\beth_-^2.\end{aligned} \tag{4.4.8}$$

Each term in (4.4.8) is complex, which can be written as

$$\begin{aligned}\mathfrak{D}_0 &= \mathfrak{D}_{0r} + \mathrm{i}\mathfrak{D}_{0i},\\ \mathfrak{D}_2 &= \mathfrak{D}_{2r} + \mathrm{i}\mathfrak{D}_{2i},\\ \mathfrak{D}_4 &= \mathfrak{D}_{4r} + \mathrm{i}\mathfrak{D}_{4i},\end{aligned} \tag{4.4.9}$$

where $\mathfrak{D}_{mr}$ and $\mathfrak{D}_{mi}$ are the real and imaginary parts of $\mathfrak{D}_m$ respectively, with $m \in \{0, 2, 4\}$. Now, the probe-field susceptibilities can be written using the approximation defined by (4.4.7) and (4.4.8) as

$$\chi^{(1)}_{\mathrm{p}_G}(z,\omega) \approx \frac{\mathrm{i}\eta_{\mathrm{p}}(\varrho_{11}-\varrho_{44})\gamma_{\mathrm{ps}_-}\left[1+\varsigma_{\mathrm{s}}^2(z)\right]}{|\Omega_{\mathrm{s}_0}|^2\wp_{\mathrm{s}}}\left[\mathfrak{D}_0 + \mathfrak{D}_2\varsigma_{\mathrm{s}}^2(z) + \mathfrak{D}_4\varsigma_{\mathrm{s}}^4(z)\right], \tag{4.4.10}$$

$$\begin{aligned}\chi^{(3)}_{\mathrm{p}_{G1}}(z,\omega) \approx{}& \frac{\mathrm{i}\eta_{\mathrm{p}_1}(\varrho_{11}-\varrho_{44})\left[1+\varsigma_{\mathrm{s}}^2(z)\right]}{|\Omega_{\mathrm{s}_0}|^2\wp_{\mathrm{s}}\aleph_+}\left[\mathfrak{D}_0 + \mathfrak{D}_2\varsigma_{\mathrm{s}}^2(z) + \mathfrak{D}_4\varsigma_{\mathrm{s}}^4(z)\right]\\ &\times\left(1 - \frac{\gamma_{\mathrm{ps}_-}\left[1+\varsigma_{\mathrm{s}}^2(z)\right]}{|\Omega_{\mathrm{s}_0}|^2\wp_{\mathrm{s}}}\left[\mathfrak{D}_0 + \mathfrak{D}_2\varsigma_{\mathrm{s}}^2(z) + \mathfrak{D}_4\varsigma_{\mathrm{s}}^4(z)\right]\right),\end{aligned} \tag{4.4.11}$$

and

$$\chi^{(3)}_{\mathrm{p}_{G2}}(z,\omega) \approx \frac{\mathrm{i}\eta_{\mathrm{sp}}\left(\varrho_{44}-\varrho_{33}\right)\left[1+\varsigma_{\mathrm{s}}^2(z)\right]}{|\Omega_{\mathrm{s}_0}|^2\wp_{\mathrm{s}}\aleph_+}\left[\mathfrak{D}_0 + \mathfrak{D}_2\varsigma_{\mathrm{s}}^2(z) + \mathfrak{D}_4\varsigma_{\mathrm{s}}^4(z)\right]. \tag{4.4.12}$$

Figure 4.1 shows how the approximated optical susceptibility, using Maclurian series of $\mathfrak{D}$ defined by Eq. (4.4.5), fits the exact optical susceptibilities using the analytical expressions (4.3.15), (4.3.19), and (4.3.18) around the region of the second EIT window.

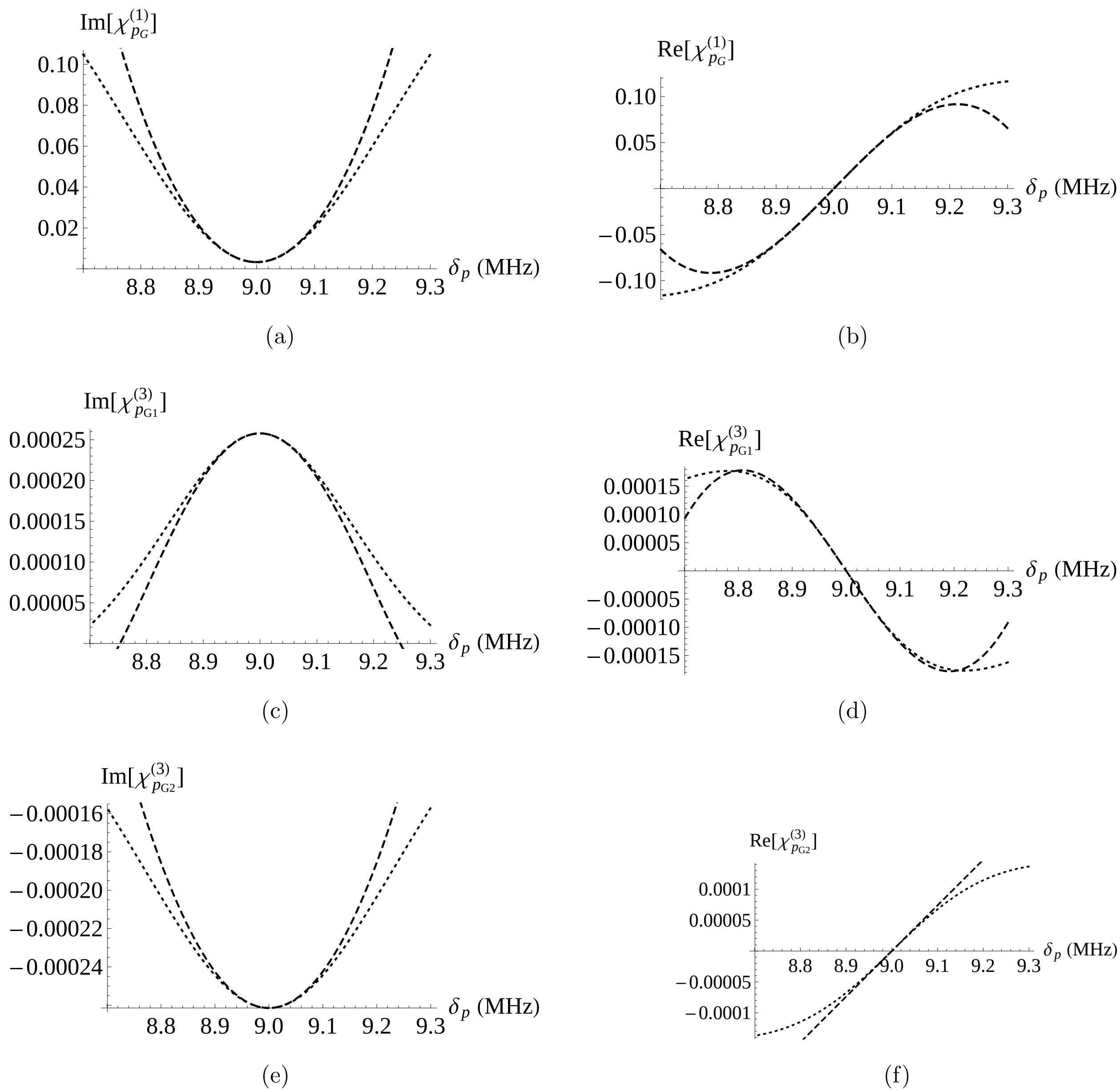

Figure 4.1: Real and imaginary parts of the linear and nonlinear-optical susceptibility for $\pitchfork$ atom-field configuration, approximated using Maclurian series (dashed line) and analytical exact solution (dotted line) around the region where $\delta_{\mathrm{p}} = \delta_{\mathrm{s}} = 9$ MHz versus probe-field detunings δ_{p}, at $z = 0$. Other parameters are $\gamma_4 = 18$ MHz, $\Omega_{\mathrm{c}} = \gamma_4$, $\Omega_{\mathrm{s}} = 0.2\gamma_4$, $\gamma_3 = 10$ kHz, $\gamma_2 = 40$ kHz, $\delta_{\mathrm{c}} = 0$, $\varrho_{11} = \varrho_{33} = 0.5$, $\mathcal{N} = 1 \times 10^{14}$ cm^{-3} and using ^{87}Rb dipole moments $|\boldsymbol{d}_{14}| = |\boldsymbol{d}_{34}| = 1.269 \times 10^{-29}$ C$\cdot$m.

4.5 Solution of the Wave Equation using Gaussian-Probe Beam for ⫛ Atom-Field Optical System

The optical susceptibilities (4.4.10), (4.4.11) and (4.4.12) are polynomial in z. Therefore, to solve the wave equation we have to treat the medium as inhomogeneous. It is assumed that the propagation of Gaussian beams have slow spatial variations of the gain and index of refraction [90]. The variation are sufficiently slow in the vicinity of the beam that the optical susceptibility can be expanded, keeping only the linear and quadratic terms. If this condition is satisfied, the propagating beam remains Gaussian, even though its spot size, phase-front curvature, amplitude, and phase of direction of propagation are significantly altered by the inhomogeneity of the medium. In this section, the details of how the probe-field wave equation can be solved are presented. However, the signal-field wave equation follows the same steps.

To begin, the wave equation defined by (4.2.1) is

$$\nabla^2 \boldsymbol{E}(z,r) - \frac{1}{c^2}\frac{\partial^2 \boldsymbol{E}(z,r)}{\partial t^2} = \mu_0 \frac{\partial^2 \boldsymbol{P}(z,r)}{\partial t^2}. \tag{4.5.1}$$

Next, we use (3.2.5) to substitute the polarization in (4.5.1)

$$\nabla^2 \boldsymbol{E}(z,r) - \frac{1}{c^2}\left[1+\boldsymbol{\chi}(z,\omega)\right]\frac{\partial^2 \boldsymbol{E}(z,r)}{\partial t^2} = 0. \tag{4.5.2}$$

Upon the assumption that $\boldsymbol{\chi}(z,\omega)$ is not altered over the wave length by the inhomogeneity of the medium created by the signal field, the probe field can be written as [90, 91]

$$\boldsymbol{E}_{\mathrm{p}}(z,t) = \boldsymbol{\xi}_{\mathrm{p}}(z,r)e^{-\mathrm{i}\left(\int k_{\mathrm{p}}(z,\omega)dz-\omega t\right)}\hat{\varepsilon}_{\mathrm{p}}, \tag{4.5.3}$$

where $\hat{\varepsilon}_{\mathrm{p}}$ is the field-polarization direction, and $k_{\mathrm{p}}(z,\omega)$ is defined in (3.4.11) as

$$\begin{aligned} k_{\mathrm{p}}(z,\omega) &= \frac{\omega}{c}\sqrt{\mathrm{Re}\left[\chi^{(1)}_{\mathrm{p}_G}(z,\omega)\right]}, \\ k_{\mathrm{p}}(z,\omega) &\approx \frac{\omega}{c}\left(1+\frac{1}{2}\mathrm{Re}\left[\chi^{(1)}_{\mathrm{p}_G}(z,\omega)\right]\right), \end{aligned} \tag{4.5.4}$$

with $\chi^{(1)}_{\mathrm{p}_G}(z,\omega)$ are defined in (4.4.10).

The variation of the propagation constant is only along the z-direction, where r in Eq. (4.3.14) is treated as constant, evaluated at transverse distance $r = 0$. Consequently, the propagation of the probe-field envelope function in the presence of the signal field can be obtained by substituting (4.5.3) into (4.5.2) to obtain

$$\begin{aligned}\nabla^2_{\mathrm{T}}\boldsymbol{\xi}_{\mathrm{p}}(z,r) + \frac{\partial^2\boldsymbol{\xi}_{\mathrm{p}}(z,r)}{\partial z^2} - 2\mathrm{i}k_{\mathrm{p}}\frac{\partial\boldsymbol{\xi}_{\mathrm{p}}(z,r)}{\partial z} - \mathrm{i}\frac{\partial k_{\mathrm{p}}}{\partial z}\boldsymbol{\xi}_{\mathrm{p}}(z,r) - k^2_{\mathrm{p}}\boldsymbol{\xi}_{\mathrm{p}}(z,r) \\ + \frac{\omega^2_{\mathrm{p}}}{c^2}\left[1+\chi_{\mathrm{p}_G}(z,\omega)\right]\boldsymbol{\xi}_{\mathrm{p}}(z,r) = 0,\end{aligned} \tag{4.5.5}$$

with

$$\chi_{\mathrm{p}_G}(z,\omega) = \chi^{(1)}_{\mathrm{p}_G}(z,\omega) + \chi^{(3)}_{\mathrm{p}_{G1}}(z,\omega)\left|\xi_{\mathrm{p}_f}(z,\omega)\right|^2 + \chi^{(3)}_{\mathrm{p}_{G2}}(z,\omega)\left|\xi_{\mathrm{s}_f}(z,\omega)\right|^2, \tag{4.5.6}$$

where $\left|\xi_{\mathrm{p}_f}(z,\omega)\right|^2$ and $\left|\xi_{\mathrm{s}_f}(z,\omega)\right|^2$ are defined in (4.3.5) and (4.3.12) respectively. The probe-field envelope function is assumed to vary so slowly with z, such that is the slowly-varying envelope approximation (3.5.9) are valid and the second derivative in z can be neglected.

$$\nabla^2_{\mathrm{T}}\boldsymbol{\xi}_{\mathrm{p}}(z,r) - 2\mathrm{i}k_{\mathrm{p}}\frac{\partial\boldsymbol{\xi}_{\mathrm{p}}(z,r)}{\partial z} - \mathrm{i}\frac{\partial k_{\mathrm{p}}}{\partial z}\boldsymbol{\xi}_{\mathrm{p}}(z,r) + \frac{\omega^2_{\mathrm{p}}}{c^2}\left[\mathrm{i}\mathrm{Im}\left[\chi^{(1)}_{\mathrm{p}_G}(z,\omega)\right] + \chi^{(\mathrm{NL})}_{\mathrm{p}_G}(z,\omega)\right]\boldsymbol{\xi}_{\mathrm{p}}(z,r) = 0, \tag{4.5.7}$$

with ∇^2_{T} are defined in (4.2.5) for rectangular coordinate and in (4.2.6) for cylindrical coordinates, and

$$\chi^{(\mathrm{NL})}_{\mathrm{p}_G}(z,\omega) = \chi^{(3)}_{\mathrm{p}_{G1}}(z,\omega)\left|\xi_{\mathrm{p}_f}(z,\omega)\right|^2 + \chi^{(3)}_{\mathrm{p}_{G2}}(z,\omega)\left|\xi_{\mathrm{s}_f}(z,\omega)\right|^2. \tag{4.5.8}$$

It is assumed that the variation of the dielectric of the medium which is created by the signal field doesn't alter the function type. That is, the beam will remain Gaussian, so $\boldsymbol{\xi}_{\mathrm{p}}(z,r)$ can be written as [90]:

$$\boldsymbol{\xi}_{\mathrm{p}}(z,r) = \xi_0 e^{-\mathrm{i}\left(Q_r(z)\frac{r^2}{2}+T(z)\right)}. \tag{4.5.9}$$

The size of the beam and the curvature of the phase front are governed by the complex beam parameter Q_r. The phase and amplitude of the beam are governed by the complex parameter T [90]. If Eq. (4.5.9) is substitute into (4.5.7), it can found by equating equal powers of z and r so that the beam parameters are governed by the following two equations

$$
\begin{aligned}
&Q_r^2(z) + k_{\mathrm{p}}\frac{dQ_r(z)}{dz} = 0, \qquad\qquad (4.5.10)\\
&-2\mathrm{i}Q_r(z) - 2k_{\mathrm{p}}\frac{dT(z)}{dz} - \mathrm{i}\frac{dk_{\mathrm{p}}(z)}{dz} + \frac{\omega_{\mathrm{p}}^2}{c^2}\left(\mathrm{i}\mathrm{Im}\left[\chi_{\mathrm{p}_G}^{(1)}(z,\omega)\right] + \chi_{\mathrm{p}_G}^{(\mathrm{NL})}(z,\omega)\right) = 0.
\end{aligned}
$$

Thus, the wave equation is reduced to two ordinary differential equations [90]. The assumption (4.5.9) requires that only the linear and quadratic terms in z of Eqs. (4.4.10), (4.4.11) and (4.4.12) are kept, while the higher order terms are neglected. Now, Eqs. (4.4.10) and (4.5.8), which are defined by (4.4.11) and (4.4.12) are substituted into (4.5.10)

$$
\begin{aligned}
&Q_r^2(z) + k_{\mathrm{p}}\frac{dQ_r(z)}{dz} = 0, \qquad\qquad (4.5.11)\\
&-2\mathrm{i}Q_r(z) - 2k_{\mathrm{p}}\frac{dT(z)}{dz} - \mathrm{i}\frac{dk_{\mathrm{p}}(z)}{dz} + \mathrm{i}\frac{\omega_{\mathrm{p}}^2}{c^2}\frac{(\varrho_{11}-\varrho_{44})\eta_{\mathrm{p}}}{|\Omega_{\mathrm{s}_0}|^2}\mathrm{Im}\left[\mathrm{i}\gamma_{\mathrm{ps}_-}\left[\mathfrak{D}_0 + (\mathfrak{D}_0+\mathfrak{D}_2)\varsigma_{\mathrm{s}}^2(z)\right]\right]\\
&+\frac{\omega_{\mathrm{p}}^2}{c^2}\frac{\mathrm{i}\eta_{\mathrm{p}_1}(\varrho_{11}-\varrho_{44})|\Omega_{\mathrm{p}_0}|^2\wp_{\mathrm{p}}\left[1+\varsigma_{\mathrm{s}}^2(z)\right]}{|\Omega_{\mathrm{s}_0}|^2\aleph_+\left[1+\varsigma_{\mathrm{p}}^2(z)\right]}\left[\mathfrak{D}_0 + \mathfrak{D}_2\varsigma_{\mathrm{s}}^2(z) - \frac{\gamma_{\mathrm{ps}_-}}{|\Omega_{\mathrm{s}_0}|^2}\left(\mathfrak{D}_0^2 + (\mathfrak{D}_0+2\mathfrak{D}_2)\mathfrak{D}_0\varsigma_{\mathrm{s}}^2(z)\right)\right]\\
&+\frac{\omega_{\mathrm{p}}^2}{c^2}(\varrho_{44}-\varrho_{33})\frac{\mathrm{i}\eta_{sp}}{\aleph_+}\left[\mathfrak{D}_0 + \mathfrak{D}_2\varsigma_{\mathrm{s}}^2(z)\right] = 0.
\end{aligned}
$$

To simplify farther the second equation of (4.5.11), we assume that the fundamental Gaussian-signal and probe fields are identical in their confocal lengths, then (4.5.11) reduces to

$$
\begin{aligned}
&Q_r^2(z) + k_{\mathrm{p}}\frac{dQ_r(z)}{dz} = 0,\\
&-2\mathrm{i}Q_r(z) - 2k_{\mathrm{p}}\frac{dT(z)}{dz} - \mathrm{i}\frac{dk_{\mathrm{p}}(z)}{dz} + \mathrm{i}\frac{\omega_{\mathrm{p}}^2}{c^2}\frac{(\varrho_{11}-\varrho_{44})\eta_{\mathrm{p}}}{|\Omega_{\mathrm{s}_0}|^2}\mathrm{Im}\left[\mathrm{i}\gamma_{\mathrm{ps}_-}\left[\mathfrak{D}_0 + (\mathfrak{D}_0+\mathfrak{D}_2)\varsigma_{\mathrm{s}}^2(z)\right]\right]\\
&+\frac{\omega_{\mathrm{p}}^2}{c^2}\frac{\mathrm{i}\eta_{\mathrm{p}_1}(\varrho_{11}-\varrho_{44})|\Omega_{\mathrm{p}_0}|^2\wp_{\mathrm{p}}}{|\Omega_{\mathrm{s}_0}|^2\aleph_+}\left[\mathfrak{D}_0 + \mathfrak{D}_2\varsigma_{\mathrm{s}}^2(z) - \frac{\gamma_{\mathrm{ps}_-}}{|\Omega_{\mathrm{s}_0}|^2}\left(\mathfrak{D}_0^2 + (\mathfrak{D}_0+2\mathfrak{D}_2)\mathfrak{D}_0\varsigma_{\mathrm{s}}^2(z)\right)\right]\\
&+\frac{\omega_{\mathrm{p}}^2}{c^2}(\varrho_{44}-\varrho_{33})\frac{\mathrm{i}\eta_{sp}}{\aleph_+}\left[\mathfrak{D}_0 + \mathfrak{D}_2\varsigma_{\mathrm{s}}^2(z)\right] = 0. \qquad\qquad (4.5.12)
\end{aligned}
$$

By substituting the $\varsigma_{\mathrm{s}}^2(z)$ defined by (4.3.9) and k_{p} presented by (4.5.4) we get

$$
Q_r^2(z) + \frac{\omega_{\mathrm{p}}}{c}\left[1 + \frac{\eta_{\mathrm{p}}}{2|\Omega_{\mathrm{s}_0}|^2}(\varrho_{11}-\varrho_{44})\mathrm{Re}\left[\mathrm{i}\gamma_{\mathrm{ps}_-}\left(\mathfrak{D}_0 + \frac{4z^2}{b_{\mathrm{s}}^2}(\mathfrak{D}_0+\mathfrak{D}_2)\right)\right]\right]\frac{dQ_r(z)}{dz} = 0, \qquad (4.5.13)
$$

and

$$
\begin{aligned}
&-2\mathrm{i}Q_r(z)-2\frac{\omega_\mathrm{p}}{c}\left[1+\frac{\eta_\mathrm{p}}{2|\Omega_{\mathrm{s}_0}|^2}(\varrho_{11}-\varrho_{44})\mathrm{Re}\left[\mathrm{i}\gamma_{\mathrm{ps}_-}\left(\mathfrak{D}_0+\frac{4z^2}{b_\mathrm{s}^2}\left(\mathfrak{D}_0+\mathfrak{D}_2\right)\right)\right]\right]\frac{dT(z)}{dz}\\
&-\mathrm{i}\frac{\omega_\mathrm{p}}{c|\Omega_{\mathrm{s}_0}|^2}\eta_\mathrm{p}(\varrho_{11}-\varrho_{44})\frac{4z}{b_\mathrm{s}^2}\mathrm{Re}\left[\mathrm{i}\gamma_{\mathrm{ps}_-}\left(\mathfrak{D}_0+\mathfrak{D}_2\right)\right]\\
&+\mathrm{i}\frac{\omega_\mathrm{p}^2}{c^2}\frac{(\varrho_{11}-\varrho_{44})\eta_\mathrm{p}}{|\Omega_{\mathrm{s}_0}|^2}\mathrm{Im}\left[\mathrm{i}\gamma_{\mathrm{ps}_-}\left[\mathfrak{D}_0+\left(\mathfrak{D}_0+\mathfrak{D}_2\right)\frac{4z^2}{b_\mathrm{s}^2}\right]\right]\\
&+\frac{\omega_\mathrm{p}^2}{c^2}\frac{\mathrm{i}\eta_{\mathrm{p}_1}(\varrho_{11}-\varrho_{44})|\Omega_{\mathrm{p}_0}|^2\wp_\mathrm{p}}{|\Omega_{\mathrm{s}_0}|^2\aleph_+}\left[\mathfrak{D}_0+\mathfrak{D}_2\frac{4z^2}{b_\mathrm{s}^2}-\frac{\gamma_{\mathrm{ps}_-}}{|\Omega_{\mathrm{s}_0}|^2}\left(\mathfrak{D}_0^2+\left(\mathfrak{D}_0+2\mathfrak{D}_2\right)\mathfrak{D}_0\frac{4z^2}{b_\mathrm{s}^2}\right)\right]\\
&+\frac{\omega_\mathrm{p}^2}{c^2}(\varrho_{44}-\varrho_{33})\frac{\mathrm{i}\eta_{sp}}{\aleph_+}\left(\mathfrak{D}_0+\mathfrak{D}_2\frac{4z^2}{b_\mathrm{s}^2}(z)\right)=0.
\end{aligned}\tag{4.5.14}
$$

To write (4.5.13) and (4.5.14) in more compact form, the following parameters are introduced

$$
\begin{aligned}
k_{\mathrm{p}_1}&=\frac{\omega_\mathrm{p}}{c}\left(1+\frac{\eta_\mathrm{p}}{2|\Omega_{\mathrm{s}_0}|^2}(\varrho_{11}-\varrho_{44})\mathrm{Re}\left[\mathrm{i}\gamma_{\mathrm{ps}_-}\mathfrak{D}_0\right]\right),\\
k_{\mathrm{p}_2}&=\frac{\omega_\mathrm{p}\eta_\mathrm{p}}{2|\Omega_{\mathrm{s}_0}|^2c}(\varrho_{11}-\varrho_{44})\mathrm{Re}\left[\mathrm{i}\gamma_{\mathrm{ps}_-}\left(\mathfrak{D}_0+\mathfrak{D}_2\right)\right],
\end{aligned}\tag{4.5.15}
$$

$$
\begin{aligned}
\alpha_{\mathrm{p}_1}&=\frac{\omega_\mathrm{p}^2}{c^2}\frac{(\varrho_{11}-\varrho_{44})\eta_\mathrm{p}}{|\Omega_{\mathrm{s}_0}|^2}\mathrm{Im}\left[\mathrm{i}\gamma_{\mathrm{ps}_-}\mathfrak{D}_0\right],\\
\alpha_{\mathrm{p}_2}&=\frac{\omega_\mathrm{p}^2}{c^2}\frac{(\varrho_{11}-\varrho_{44})\eta_\mathrm{p}}{|\Omega_{\mathrm{s}_0}|^2}\mathrm{Im}\left[\mathrm{i}\gamma_{\mathrm{ps}_-}\left(\mathfrak{D}_0+\mathfrak{D}_2\right)\right],
\end{aligned}\tag{4.5.16}
$$

$$
\begin{aligned}
\mathfrak{m}_1&=\frac{\omega_\mathrm{p}^2}{c^2}\frac{\mathrm{i}\eta_{\mathrm{p}_1}(\varrho_{11}-\varrho_{44})|\Omega_{\mathrm{p}_0}|^2\wp_\mathrm{p}}{|\Omega_{\mathrm{s}_0}|^2\aleph_+}\mathfrak{D}_0\left(1-\frac{\gamma_{\mathrm{ps}_-}}{|\Omega_{\mathrm{s}_0}|^2}\mathfrak{D}_0\right),\\
\mathfrak{m}_2&=\frac{\omega_\mathrm{p}^2}{c^2}\frac{\mathrm{i}\eta_{\mathrm{p}_1}(\varrho_{11}-\varrho_{44})|\Omega_{\mathrm{p}_0}|^2\wp_\mathrm{p}}{|\Omega_{\mathrm{s}_0}|^2\aleph_+}\left(\mathfrak{D}_2-\frac{\gamma_{\mathrm{ps}_-}}{|\Omega_{\mathrm{s}_0}|^2}(\mathfrak{D}_0+2\mathfrak{D}_2)\mathfrak{D}_0\right),
\end{aligned}\tag{4.5.17}
$$

$$
\begin{aligned}
\mathfrak{n}_1&=\frac{\omega_\mathrm{p}^2}{c^2}(\varrho_{44}-\varrho_{33})\frac{\mathrm{i}\eta_{sp}}{\aleph_+}\mathfrak{D}_0,\\
\mathfrak{n}_2&=\frac{\omega_\mathrm{p}^2}{c^2}(\varrho_{44}-\varrho_{33})\frac{\mathrm{i}\eta_{sp}}{\aleph_+}\mathfrak{D}_2.
\end{aligned}\tag{4.5.18}
$$

The second term between the brackets for both $\mathfrak{m}_1$ and $\mathfrak{m}_2$ is negligible compared to the first. The imaginary parts of $\mathfrak{m}_1$, $\mathfrak{m}_2$, $\mathfrak{n}_1$, and $\mathfrak{n}_2$ are represented by $\mathfrak{m}_{1i}$, $\mathfrak{m}_{2i}$, $\mathfrak{n}_{1i}$, and $\mathfrak{n}_{2i}$, and the real parts are represented by $\mathfrak{m}_{1r}$, $\mathfrak{m}_{2r}$,$\mathfrak{n}_{1r}$, and $\mathfrak{n}_{2r}$ respectively.

In term of the above parameters Eqs. (4.5.13) and (4.5.14) become

$$\begin{aligned}
&Q_r^2(z) + \left[k_{\mathrm{p}_1} + k_{\mathrm{p}_2}\frac{4z^2}{b_{\mathrm{s}}^2}\right]\frac{dQ_r(z)}{dz} = 0, \qquad (4.5.19)\\
&-2\mathrm{i}Q_r(z) - 2\left[k_{\mathrm{p}_1} + k_{\mathrm{p}_2}\frac{4z^2}{b_{\mathrm{s}}^2}\right]\frac{dT(z)}{dz} + \left[\mathrm{i}\left(\alpha_{\mathrm{p}_2} + \mathfrak{m}_{2i} + \mathfrak{n}_{2i}\right) + \mathfrak{m}_{2r} + \mathfrak{n}_{2r}\right]\frac{4z^2}{b_{\mathrm{s}}^2}\\
&-\mathrm{i}k_{\mathrm{p}_2}\frac{8z}{b_{\mathrm{s}}^2} + \left[\mathrm{i}\left(\alpha_{\mathrm{p}_1} + \mathfrak{m}_{1i} + \mathfrak{n}_{1i}\right) + \mathfrak{m}_{1r} + \mathfrak{n}_{1r}\right] = 0.
\end{aligned}$$

Mathematica software is used to solve Eq. (4.5.19), the following is obtained:

$$Q_r(z) = \frac{2\sqrt{k_{\mathrm{p}_1}k_{\mathrm{p}_2}}}{b_{\mathrm{s}}\tan^{-1}\left[\frac{2z}{b_{\mathrm{s}}}\sqrt{\frac{k_{\mathrm{p}_2}}{k_{\mathrm{p}_1}}}\right] - 2\sqrt{k_{\mathrm{p}_1}k_{\mathrm{p}_2}}C_1}, \qquad (4.5.20)$$

and

$$\begin{aligned}
T(z) =& C_2 - \mathrm{i}\ln\left[b_{\mathrm{s}}\tan^{-1}\left[\frac{2z}{b_{\mathrm{s}}}\sqrt{\frac{k_{\mathrm{p}_2}}{k_{\mathrm{p}_1}}}\right] - 2\sqrt{k_{\mathrm{p}_2}k_{\mathrm{p}_1}}C_1\right]\\
&+ \frac{\mathrm{i}b_{\mathrm{s}}\tan^{-1}\left[\frac{2z}{b_{\mathrm{s}}}\sqrt{\frac{k_{\mathrm{p}_2}}{k_{\mathrm{p}_1}}}\right]}{4\sqrt{k_{\mathrm{p}_1}k_{\mathrm{p}_2}}}\Big[\mathfrak{m}_{1i} + \mathfrak{n}_{1i} + \alpha_{\mathrm{p}_1} - \mathrm{i}\left(\mathfrak{m}_{1r} + \mathfrak{n}_{1r}\right)\\
&- \frac{k_{\mathrm{p}_1}}{k_{\mathrm{p}_2}}\left(\mathfrak{m}_{2i} + \mathfrak{n}_{2i} + \alpha_{\mathrm{p}_2} - \mathrm{i}(\mathfrak{m}_{2r} + \mathfrak{n}_{2r})\right)\Big]\\
&+ \frac{\mathrm{iz}}{2k_{\mathrm{p}_2}}\left(\mathfrak{m}_{2i} + \mathfrak{n}_{2i} + \alpha_{\mathrm{p}_2} - \mathrm{i}\left(\mathfrak{m}_{2r} + \mathfrak{n}_{2r}\right)\right) - \frac{\mathrm{i}}{2}\ln\left[b_{\mathrm{s}}^2k_{\mathrm{p}_1} + 4k_{\mathrm{p}_2}z^2\right]. \qquad (4.5.21)
\end{aligned}$$

The constants C_1 and C_2 in (4.5.21) and ξ_0 in (4.5.9) are determined from the boundary condition. At $z = 0$ the fundamental input-envelope wave function (4.3.1) must equal to the modulated-envelope wave function (4.5.9), then we get

$$\xi_0 = \xi_{\mathrm{p}_0}\,, C_1 = \frac{\text{-i}w_{0_{\mathrm{p}}}^2}{2}\,, \text{and } C_2 = \frac{\mathrm{i}}{2}\left(\ln\left[b_{\mathrm{s}}^2k_{\mathrm{p}_1}\right] + 2\ln\left[\mathrm{i}w_{0_{\mathrm{p}}}^2\sqrt{k_{\mathrm{p}_1}k_{\mathrm{p}_2}}\right]\right). \qquad (4.5.22)$$

Equations (4.5.20) and (4.5.21) become after substituting the determined constants in (4.5.22)

$$Q_r(z) = \frac{2}{\frac{b_{\mathrm{s}}}{\sqrt{k_{\mathrm{p}_1}k_{\mathrm{p}_2}}}\tan^{-1}\left[\frac{2z}{b_{\mathrm{s}}}\sqrt{\frac{k_{\mathrm{p}_2}}{k_{\mathrm{p}_1}}}\right] + \mathrm{i}w_{0_{\mathrm{p}}}^2}, \qquad (4.5.23)$$

and

$$T(z) = \frac{\mathrm{i}}{2}\left(\ln\left[b_{\mathrm{s}}^2 k_{\mathrm{p}_1}\right] + 2\ln\left[\mathrm{i}w_{0_{\mathrm{p}}}^2\sqrt{k_{\mathrm{p}_1}k_{\mathrm{p}_2}}\right]\right) - \mathrm{i}\ln\left[b_{\mathrm{s}}\tan^{-1}\left[\frac{2z}{b_{\mathrm{s}}}\sqrt{\frac{k_{\mathrm{p}_2}}{k_{\mathrm{p}_1}}}\right] + \mathrm{i}w_{0_{\mathrm{p}}}^2\sqrt{k_{\mathrm{p}_2}k_{\mathrm{p}_1}}\right]$$
$$+ \frac{\mathrm{i}b_{\mathrm{s}}\tan^{-1}\left[\frac{2z}{b_{\mathrm{s}}}\sqrt{\frac{k_{\mathrm{p}_2}}{k_{\mathrm{p}_1}}}\right]}{4\sqrt{k_{\mathrm{p}_1}k_{\mathrm{p}_2}}}\left(\mathfrak{m}_{1i} + \mathfrak{n}_{1i} + \alpha_{\mathrm{p}_1} - \frac{k_{\mathrm{p}_1}}{k_{\mathrm{p}_2}}(\mathfrak{m}_{2i} + \mathfrak{n}_{2i} + \alpha_{\mathrm{p}_2})\right) + \frac{\mathrm{i}z}{2k_{\mathrm{p}_2}}\left(\mathfrak{m}_{2i} + \mathfrak{n}_{2i} + \alpha_{\mathrm{p}_2}\right)$$
$$+ \frac{b_{\mathrm{s}}\tan^{-1}\left[\frac{2z}{b_{\mathrm{s}}}\sqrt{\frac{k_{\mathrm{p}_2}}{k_{\mathrm{p}_1}}}\right]}{4\sqrt{k_{\mathrm{p}_1}k_{\mathrm{p}_2}}}\left(\mathfrak{m}_{1r} + \mathfrak{n}_{1r} - \frac{k_{\mathrm{p}_1}}{k_{\mathrm{p}_2}}(\mathfrak{m}_{2r} + \mathfrak{n}_{2r})\right) + \frac{z}{2k_{\mathrm{p}_2}}\left(\mathfrak{m}_{2r} + \mathfrak{n}_{2r}\right)$$
$$- \frac{\mathrm{i}}{2}\ln\left[b_{\mathrm{s}}^2 k_{\mathrm{p}_1} + 4k_{\mathrm{p}_2}z^2\right]. \tag{4.5.24}$$

By defining

$$\mathfrak{p}(z) = \frac{\mathrm{i}b_{\mathrm{s}}\tan^{-1}\left[\frac{2z}{b_{\mathrm{s}}}\sqrt{\frac{k_{\mathrm{p}_2}}{k_{\mathrm{p}_1}}}\right]}{4\sqrt{k_{\mathrm{p}_1}k_{\mathrm{p}_2}}}\left(\mathfrak{m}_{1i} + \mathfrak{n}_{1i} + \alpha_{\mathrm{p}_1} - \frac{k_{\mathrm{p}_1}}{k_{\mathrm{p}_2}}(\mathfrak{m}_{2i} + \mathfrak{n}_{2i} + \alpha_{\mathrm{p}_2})\right) + \frac{\mathrm{i}z}{2k_{\mathrm{p}_2}}\left(\mathfrak{m}_{2i} + \mathfrak{n}_{2i} + \alpha_{\mathrm{p}_2}\right)$$
$$+ \frac{b_{\mathrm{s}}\tan^{-1}\left[\frac{2z}{b_{\mathrm{s}}}\sqrt{\frac{k_{\mathrm{p}_2}}{k_{\mathrm{p}_1}}}\right]}{4\sqrt{k_{\mathrm{p}_1}k_{\mathrm{p}_2}}}\left(\mathfrak{m}_{1r} + \mathfrak{n}_{1r} - \frac{k_{\mathrm{p}_1}}{k_{\mathrm{p}_2}}(\mathfrak{m}_{2r} + \mathfrak{n}_{2r})\right) + \frac{z}{2k_{\mathrm{p}_2}}\left(\mathfrak{m}_{2r} + \mathfrak{n}_{2r}\right), \tag{4.5.25}$$

and using some mathematical rules, the modulated-envelope wave function (4.5.9) can be written in the final form as

$$\boldsymbol{\xi}_{\mathrm{p}}(z,r) = \frac{\xi_{0_{\mathrm{p}}}}{\sqrt{1 + \frac{4k_{\mathrm{p}_2}}{b_{\mathrm{s}}^2 k_{\mathrm{p}_1}}z^2}}\frac{e^{-\mathrm{i}\left(Q_r(z)\frac{r^2}{2} - \mathfrak{p}(z) - \tan^{-1}\left[\frac{b_{\mathrm{s}}}{w_{0_{\mathrm{P}}}^2\sqrt{k_{\mathrm{p}_1}k_{\mathrm{p}_2}}}\tan^{-1}\left[\frac{2z}{b_{\mathrm{s}}}\sqrt{\frac{k_{\mathrm{p}_2}}{k_{\mathrm{p}_1}}}\right]\right]\right)}}{\sqrt{1 + \left(\frac{b_{\mathrm{s}}}{w_{0_{\mathrm{P}}}^2\sqrt{k_{\mathrm{p}_1}k_{\mathrm{p}_2}}}\tan^{-1}\left[\frac{2z}{b_{\mathrm{s}}}\sqrt{\frac{k_{\mathrm{p}_2}}{k_{\mathrm{p}_1}}}\right]\right)^2}}, \tag{4.5.26}$$

with Q_r represented by (4.5.23) and $\mathfrak{p}$ by (4.5.25). The minus sign appears in the third term of the exponent is added to make sure that the phase of the modulated wave in absence of absorption and nonlinear interaction is in the same quadrant as the input-fundamental wave. Figure 4.2 shows how the phase and the amplitude of the envelope-wave function are modulated by the absorption and the nonlinear interaction as the beam propagates through the medium.

Now the wave equation describes the propagation of continuous Gaussian probe field in z-direction through the nonlinear-optical medium can be written as

$$\boldsymbol{E}_{\rm p}(z,r,t)=\frac{\xi_{0_{\rm p}}}{\sqrt{1+\frac{4k_{\rm p2}}{b_{\rm s}^2k_{\rm p1}}z^2}}\frac{e^{-{\rm i}\left(Q_r(z)\frac{r^2}{2}+\int k_{\rm p}(z)dz-\mathfrak{p}(z)-\tan^{-1}\left[\frac{b_{\rm s}}{w_{0_{\rm P}}^2\sqrt{k_{\rm p1}k_{\rm p2}}}\tan^{-1}\left[\frac{2z}{b_{\rm s}}\sqrt{\frac{k_{\rm p2}}{k_{\rm p1}}}\right]\right]-\omega_{\rm p}t\right)}}{\sqrt{1+\left(\frac{b_{\rm s}}{w_{0_{\rm P}}^2\sqrt{k_{\rm p1}k_{\rm p2}}}\tan^{-1}\left[\frac{2z}{b_{\rm s}}\sqrt{\frac{k_{\rm p2}}{k_{\rm p1}}}\right]\right)^2}}\hat{\varepsilon}_{\rm p}. \tag{4.5.27}$$

Equation (4.5.27) governs the propagation of the probe field through the nonlinear medium. It carries all the information about how the probe-field amplitude, phase, size of the beam and the curvature of the phase front are changing with respect to the perpendicular and transverse displacements. Therefore, Eq. (4.5.27) is used in the coming section to examine the modification of the group velocity and the phase in the direction of propagation as field propagates through the medium.

4.6 Phase Function and Group Velocity

In this section, we study the displacement evolution of the group velocity and the phase of a Gaussian probe field propagating through a the nonlinear medium. We show the detailed calculations leading to closed-form expressions for the group velocity and phase. These expressions are derived for the probe field but can be generalized to the signal field case.

The phase function of the probe field can be defined from the wave equation (4.5.27) [92] as

$$\begin{aligned}\phi_{\rm tot}(r,z)=&{\rm Re}\left[Q_r(z)\frac{r^2}{2}\right]-{\rm Re}\left[\mathfrak{p}(z)\right]-\tan^{-1}\left[\frac{b_{\rm s}}{w_{0_{\rm P}}^2\sqrt{k_{{\rm p}_1}k_{{\rm p}_2}}}\tan^{-1}\left[\frac{2z}{b_{\rm s}}\sqrt{\frac{k_{{\rm p}_2}}{k_{{\rm p}_1}}}\right]\right]\\&+\int k_{\rm p}(z,r)dz.\end{aligned} \tag{4.6.1}$$

The part of the phase function that describe the phase of direction of propagation is

$$\phi_{\rm z}(z)=\int k_{\rm p}(z)dz-{\rm Re}\left[\mathfrak{p}(z)\right]-\tan^{-1}\left[\frac{b_{\rm s}}{w_{0_{\rm P}}^2\sqrt{k_{{\rm p}_1}k_{{\rm p}_2}}}\tan^{-1}\left[\frac{2z}{b_{\rm s}}\sqrt{\frac{k_{{\rm p}_2}}{k_{{\rm p}_1}}}\right]\right], \tag{4.6.2}$$

while the part of the phase function that describe the phase front curvature is

$$\phi_{\rm r}(r,z)={\rm Re}\left[Q_r(z)\frac{r^2}{2}\right]. \tag{4.6.3}$$

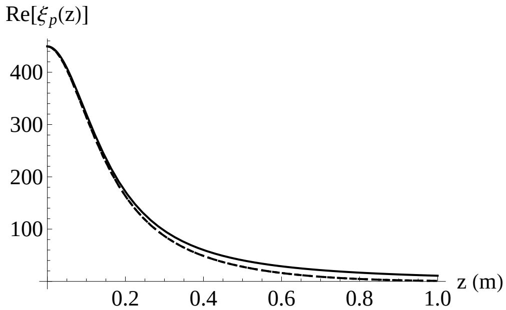

(a)

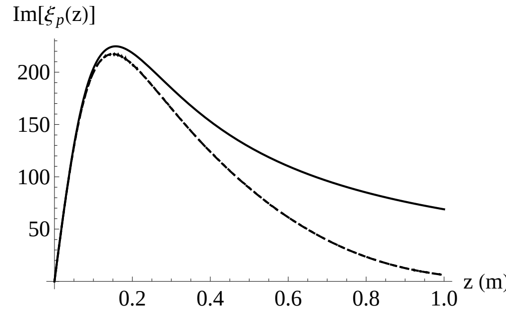

(b)

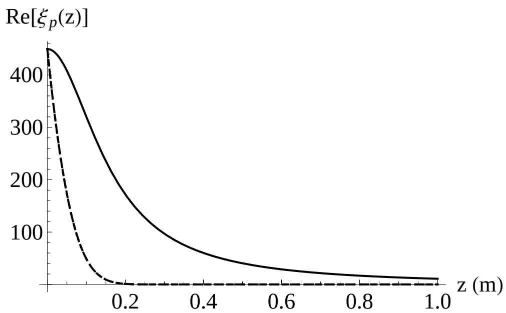

(c)

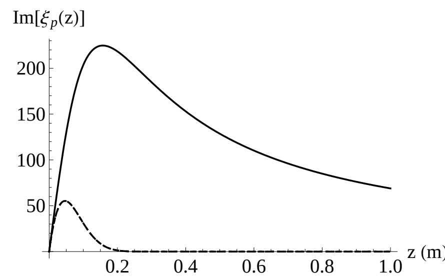

(d)

Figure 4.2: Real and imaginary parts of the Gaussian-envelope wave function as function of the propagation distance z for two different values of γ_3; (a),(b) $\gamma_3 = 0.01$ kHz, and (c),(d) $\gamma_3 = 1$ kHz. Other parameters are $\delta_\mathrm{p} = \delta_\mathrm{s} = 9$ MHz, $\gamma_4 = 18$ MHz, $\Omega_\mathrm{c} = \gamma_4$, $\Omega_\mathrm{s} = \Omega_\mathrm{p} = 0.1\gamma_4$, $\gamma_2 = 40$ kHz, $\delta_\mathrm{c} = 0$, $\varrho_{11} = \varrho_{33} = 0.5$, and $\mathcal{N} = 1 \times 10^{14}$ cm^{-3}. Using ^{87}Rb constants: $|\boldsymbol{d}_{14}| = |\boldsymbol{d}_{34}| = 1.269 \times 10^{-29}$ C.m, and $\omega_0 = 2\pi \cdot 377.11$ THz. The dotted line corresponds to the analytical solution of Eq. (4.5.26), whereas the dashed line corresponds to the numerical solution of Eq. (4.5.14) and the solid line is the fundamental input wave function in the absence of absorption and nonlinear interaction described by Eq. (4.3.1).

4.6.1 Group Velocity of Gaussian Beam

To determine the group velocity along the direction of the propagation z-axis, we set $r = 0$, and use (4.6.2), where the group velocity is defined by [92],

$$v_{g_{\mathrm{pG}}} = \frac{1}{\frac{\partial}{\partial z}\left(\frac{\partial \phi_\mathrm{z}}{\partial \omega}\right)\Big|_{\omega_0}}, \tag{4.6.4}$$

where ω_0 is the central frequency of the probe field, when it is detuned from the $|1\rangle \rightarrow |4\rangle$ transition by δ_p equal to the signal-field detuning from $|3\rangle \rightarrow |4\rangle$ transition.

The denominator of Eq. (4.6.4) is equal to

$$\begin{aligned}\frac{\partial}{\partial z}\left(\left.\frac{\partial \phi_\mathrm{z}}{\partial \omega}\right|_{\omega_0}\right) =& \frac{\partial}{\partial z}\left(\left.\frac{\partial \int k_\mathrm{p}(z)dz}{\partial \omega}\right|_{\omega_0}\right) - \frac{\partial}{\partial z}\left(\left.\frac{\partial \mathrm{Re}\left[\mathfrak{p}(z)\right]}{\partial \omega}\right|_{\omega_0}\right) \\ & - \frac{\partial}{\partial z}\left(\left.\frac{\partial \tan^{-1}\left[\frac{b_\mathrm{s}}{w_{0\mathrm{P}}^2\sqrt{k_{\mathrm{P}1}k_{\mathrm{P}2}}}\tan^{-1}\left[\frac{2z}{b_\mathrm{s}}\sqrt{\frac{k_{\mathrm{P}2}}{k_{\mathrm{P}1}}}\right]\right]}{\partial \omega}\right|_{\omega_0}\right),\end{aligned} \tag{4.6.5}$$

which can be written as

$$\begin{aligned}\frac{\partial}{\partial z}\left(\left.\frac{\partial \phi_\mathrm{z}}{\partial \omega}\right|_{\omega_0}\right) =& \left(\left.\frac{\partial k_\mathrm{p}(z)}{\partial \omega}\right|_{\omega_0}\right) - \frac{\partial}{\partial z}\left(\left.\frac{\partial \mathrm{Re}\left[\mathfrak{p}(z)\right]}{\partial \omega}\right|_{\omega_0}\right) \\ & - \frac{\partial}{\partial z}\left(\left.\frac{\partial \tan^{-1}\left[\frac{b_\mathrm{s}}{w_{0\mathrm{P}}^2\sqrt{k_{\mathrm{P}1}k_{\mathrm{P}2}}}\tan^{-1}\left[\frac{2z}{b_\mathrm{s}}\sqrt{\frac{k_{\mathrm{P}2}}{k_{\mathrm{P}1}}}\right]\right]}{\partial \omega}\right|_{\omega_0}\right).\end{aligned} \tag{4.6.6}$$

To simplify the calculation of the group velocity, each term in Eq. (4.6.6) is found separately. To begin

$$\left.\frac{\partial k_\mathrm{p}(z,r)}{\partial \omega}\right|_{\omega_0} = \left.\frac{\partial k_{\mathrm{p}_1}(z,r)}{\partial \omega}\right|_{\omega_0} + \left.\frac{\partial k_{\mathrm{p}_2}(z,r)}{\partial \omega}\right|_{\omega_0} \frac{4z^2}{b_s^2}. \tag{4.6.7}$$

This term is due to the linear process, and can be approximated to

$$\begin{aligned}\left.\frac{\partial k_\mathrm{p}(z,r)}{\partial \omega}\right|_{\omega_0} \approx & \frac{\omega_\mathrm{p}\eta_\mathrm{p}}{2|\Omega_{\mathrm{s}_0}|^2 c}(\varrho_{11}-\varrho_{44}) \left.\frac{\partial \mathrm{Re}\left[\mathrm{i}\gamma_{\mathrm{ps}_-}\left[\mathfrak{D}_0 + (\mathfrak{D}_0+\mathfrak{D}_2)\frac{4z^2}{b_s^2}\right]\right]}{\partial \delta_\mathrm{p}}\right|_{\delta_\mathrm{p}=\delta_\mathrm{s}} \\ & + \frac{\eta_\mathrm{p}}{2|\Omega_{\mathrm{s}_0}|^2 c}(\varrho_{11}-\varrho_{44})\,\mathrm{Re}\left.\left[\mathrm{i}\gamma_{\mathrm{ps}_-}\left[\mathfrak{D}_0 + (\mathfrak{D}_0+\mathfrak{D}_2)\frac{4z^2}{b_s^2}\right]\right]\right|_{\delta_\mathrm{p}=\delta_\mathrm{s}}.\end{aligned} \tag{4.6.8}$$

Only the first terms of $\mathfrak{D}_0$ and of $\mathfrak{D}_2+\mathfrak{D}_0$ (4.4.8) in the functions k_{p_1} and k_{p_2} (4.5.15) are kept, while neglecting the higher-order terms, because their effects are negligible compared to the first terms. Then, k_{p_1} and k_{p_2} can be approximated as

$$k_{\mathrm{p}_1} \approx \frac{\omega_\mathrm{p}}{c} + k_{\mathrm{p}_2} \tag{4.6.9}$$

and

$$k_{\mathrm{p}_2} \approx \frac{\omega_\mathrm{p}}{c}\frac{\eta_\mathrm{p}}{2|\Omega_{\mathrm{s}_0}|^2}(\varrho_{11}-\varrho_{44})\mathrm{Re}\left[\mathrm{i}\gamma_{\mathrm{ps}_-}\right]. \tag{4.6.10}$$

Then Eq. (4.6.8) using the above approximation of k_{p_1} and k_{p_2} can be written as

$$
\begin{aligned}
\left.\frac{\partial k_{\mathrm{p}}(z)}{\partial \omega}\right|_{\omega_0} &\approx \frac{\eta_{\mathrm{p}}}{2|\Omega_{\mathrm{s}0}|^2 c}(\varrho_{11}-\varrho_{44})\left(\omega_{\mathrm{p}}\left.\frac{\partial \mathrm{Re}\left[\mathrm{i}\gamma_{\mathrm{ps}_-}\right]}{\partial \delta_{\mathrm{p}}}\right|_{\delta_{\mathrm{p}}=\delta_{\mathrm{s}}} + \mathrm{Re}\left[\mathrm{i}\gamma_{\mathrm{ps}_-}\right]\big|_{\delta_{\mathrm{p}}=\delta_{\mathrm{s}}}\right)\left[1+\frac{4z^2}{b_s^2}\right] \\
&\approx \frac{\eta_{\mathrm{p}}}{|\Omega_{\mathrm{s}0}|^2 c}(\varrho_{11}-\varrho_{44})\left(\omega_{\mathrm{p}}\left.\frac{\partial \delta_{\mathrm{ps}}}{\partial \delta_{\mathrm{p}}}\right|_{\delta_{\mathrm{p}}=\delta_{\mathrm{s}}} + \delta_{\mathrm{ps}}\big|_{\delta_{\mathrm{p}}=\delta_{\mathrm{s}}}\right)\left[1+\frac{4z^2}{b_s^2}\right] \\
&\approx \frac{\omega_0\eta_{\mathrm{p}}}{|\Omega_{\mathrm{s}0}|^2 c}(\varrho_{11}-\varrho_{44})\left[1+\frac{4z^2}{b_s^2}\right]. \qquad (4.6.11)
\end{aligned}
$$

The second term in Eq. (4.6.5) is represented by

$$
\begin{aligned}
\left.\left(\frac{\partial \mathrm{Re}\left[\mathfrak{p}(z)\right]}{\partial \omega}\right)\right|_{\omega_0} &= \left.\frac{\partial}{\partial \omega}\left[\frac{b_{\mathrm{s}}\tan^{-1}\left[\frac{2z}{b_{\mathrm{s}}}\sqrt{\frac{k_{\mathrm{p}_2}}{k_{\mathrm{p}_1}}}\right]}{4\sqrt{k_{\mathrm{p}_1}k_{\mathrm{p}_2}}}\left(\mathfrak{m}_{1r}+\mathfrak{n}_{1r}-\frac{k_{\mathrm{p}_1}}{k_{\mathrm{p}_2}}(\mathfrak{m}_{2r}+\mathfrak{n}_{2r})\right)\right]\right|_{\omega_0} \qquad (4.6.12) \\
&\quad + \left.\frac{\partial}{\partial \omega}\left[\frac{\mathrm{z}}{2k_{\mathrm{p}_2}}\left(\mathfrak{m}_{2r}+\mathfrak{n}_{2r}\right)\right]\right|_{\omega_0}.
\end{aligned}
$$

The terms $\mathfrak{m}_{1r}$ and $\mathfrak{m}_{2r}$ are due to probe-field self-action, that is, the action of the probe field on itself. The terms $\mathfrak{n}_{1r}$ and $\mathfrak{n}_{2r}$ are a result of the action of the signal field on the probe field. For equal probe and signal-field strengths, $\mathfrak{m}_{1r}$ is equal to $\mathfrak{n}_{1r}$ and $\mathfrak{m}_{2r}$ is equal to $\mathfrak{n}_{2r}$ but they are opposite in sign, so their sum vanishes. Consequently, Eq. (4.6.12) also vanishes. For non-equal value of probe and signal-field strengths, the contribution of (4.6.12) to the group velocity is negligible compared to the linear term evaluated in (4.6.11). Hence, this term is neglected.

Using the approximation of k_{p_1} and k_{p_2} in (4.6.10) and (4.6.10) respectively, the following can written as

$$
k_{\mathrm{p}_1}k_{\mathrm{p}_2} \approx \frac{\omega_{\mathrm{p}}}{c}k_{\mathrm{p}_2} \qquad (4.6.13)
$$

and

$$
\frac{k_{\mathrm{p}_2}}{k_{\mathrm{p}_1}} \approx \frac{c}{\omega_{\mathrm{p}}}k_{\mathrm{p}_2},\ \frac{k_{\mathrm{p}_1}}{k_{\mathrm{p}_2}} \approx \frac{\omega_{\mathrm{p}}}{ck_{\mathrm{p}_2}}. \qquad (4.6.14)
$$

it is convenient to call the third term of Eq. (4.6.6 as

$$
\mathscr{I}_3 = \left.\frac{\partial\left(\tan^{-1}\left[\frac{b_{\mathrm{s}}}{w_{0\mathrm{P}}^2\sqrt{k_{\mathrm{p}_1}k_{\mathrm{p}_2}}}\tan^{-1}\left[\frac{2z}{b_{\mathrm{s}}}\sqrt{\frac{k_{\mathrm{p}_2}}{k_{\mathrm{p}_1}}}\right]\right]\right)}{\partial \omega}\right|_{\omega_0} \qquad (4.6.15)
$$

Then $\mathscr{I}_3$ can be written as

$$\mathscr{I}_3 \approx \left.\frac{\partial\left(\tan^{-1}\left[\frac{b_\mathrm{s}}{w_{0\mathrm{P}}^2\sqrt{k_{\mathrm{p}1}k_{\mathrm{p}2}}}\frac{2z}{b_\mathrm{s}}\sqrt{\frac{k_{\mathrm{p}2}}{k_{\mathrm{p}1}}}\right]\right)}{\partial\omega}\right|_{\omega_0}$$

$$\approx \left.\frac{\partial\left(\tan^{-1}\left[\frac{2z}{w_{0\mathrm{P}}^2 k_{\mathrm{p}1}}\right]\right)}{\partial\omega}\right|_{\omega_0},$$

where the approximation of $\tan^{-1}\theta \approx \theta$, for $\theta \ll 1$ is used to obtain the last line of Eq. (4.6.16). The above equation is the derivative of the Gouy-phase shift with respect the frequency

$$\frac{\partial\Theta_\mathrm{p}(z)}{\partial\omega} = \left.\frac{\partial\left(\tan^{-1}\left[\frac{2z}{k_{\mathrm{p}1}w_{0\mathrm{P}}^2}\right]\right)}{\partial\omega}\right|_{\omega_0} \approx -\left.\frac{2z\frac{\partial k_{\mathrm{p}1}}{\partial\omega}}{w_{0\mathrm{P}}^2\left(1+\frac{4z^2}{k_{\mathrm{p}1}^2 w_{0\mathrm{P}}^4}\right)k_{\mathrm{p}_1}^2}\right|_{\omega_0}. \tag{4.6.16}$$

The derivative of k_{p_1} is just the first term of (4.6.11):

$$\frac{\partial\Theta_\mathrm{p}(z)}{\partial\omega} \approx -\frac{2\omega_0\eta_\mathrm{p}}{w_{0\mathrm{P}}^2|\Omega_{\mathrm{s}0}|^2 k_{\mathrm{p}_1}^2 c}(\varrho_{11}-\varrho_{44})\frac{z}{\left(1+\frac{4z^2}{k_{\mathrm{p}1}^2 w_{0\mathrm{P}}^4}\right)}. \tag{4.6.17}$$

Then, the derivative with respect to z is calculated as

$$\frac{\partial}{\partial z}\left.\frac{\partial\Theta_\mathrm{p}(z)}{\partial\omega}\right|_{\omega_0} \approx -\frac{2\omega_0\eta_\mathrm{p}}{w_{0\mathrm{P}}^2|\Omega_{\mathrm{s}0}|^2 k_{\mathrm{p}_1}^2 c}\frac{(\varrho_{11}-\varrho_{44})}{\left(1+\frac{4z^2}{k_{\mathrm{p}1}^2 w_{0\mathrm{P}}^4}\right)}\left(\frac{8z}{k_{\mathrm{p}_1}^2 w_{0\mathrm{P}}^4\left(1+\frac{4z^2}{k_{\mathrm{p}1}^2 w_{0\mathrm{P}}^4}\right)}-1\right) \tag{4.6.18}$$

Referring to Fig. 4.3, the third term of Eq. (4.6.18) can be neglected, when compared to the first term (4.6.11). Therefore, the only term contribute to the group velocity is (4.6.11). The group velocity for probe field is

$$v_{g_\mathrm{p}} \approx \frac{v_{g_{\mathrm{p}0}}}{1+\frac{4z^2}{b_s^2}}, \tag{4.6.19}$$

with

$$v_{g_{\mathrm{p}0}} = \frac{|\Omega_{\mathrm{s}0}|^2 c}{\omega_0\eta_\mathrm{p}\left(\varrho_{11}-\varrho_{44}\right)}, \tag{4.6.20}$$

is the group velocity when $z=0$.

Comparing Eq. (4.6.19) to the group velocity which has been obtained for the case of infinite-plane signal wave, represented by Eq. (3.4.71), and certainly for valid (3.4.55), it is evident that Eq. (4.6.19) is equal to Eq. (3.4.71) for $z = 0$, thus $v_{g_{\mathrm{p}0}}$ is equal to the group velocity of probe field when using infinite-plane signal field. Thus, using Gaussian signal field adds an extra term to the denominator of the group velocity of the probe field, leads to further reduction in the group velocity, as long as $z > 0$.

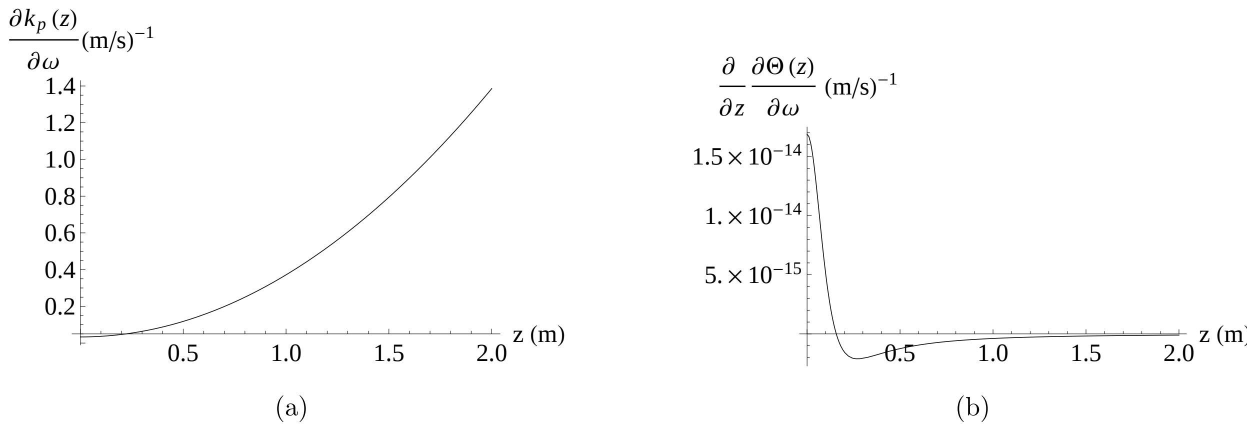

Figure 4.3: (a) $\frac{\partial k_{\mathrm{p}}(z)}{\partial \omega}$. (b) $\frac{\partial}{\partial z} \frac{\partial\left(\tan^{-1}\left[\frac{2zc}{\omega_{\mathrm{p}} w_{0_{\mathrm{P}}}^2}\right]\right)}{\partial \omega}$ as a function of the propagation distance z, for $\gamma_3 = 0.1$ kHz, $\delta_{\mathrm{p}} = \delta_{\mathrm{s}} = 9$ MHz, $\gamma_4 = 18$ MHz, $\Omega_{\mathrm{c}} = \gamma_4$, $\Omega_{\mathrm{s}} = \Omega_{\mathrm{p}} = 0.1\gamma_4$, $\gamma_2 = 40$ kHz, $\delta_{\mathrm{c}} = 0$, $\varrho_{11} = \varrho_{33} = 0.5$, and the beam waist $w_{0_{\mathrm{p}}} = w_{0_{\mathrm{p}}} = 500\ \mu$m. We use the ^{87}Rb constants: $|\boldsymbol{d}_{14}| = |\boldsymbol{d}_{34}| = 1.269 \times 10^{-29}$ C.m, and $\omega_0 = 2\pi \cdot 377.11$ THz.

The extra term in the group velocity's denominator has an influential effect when its value satisfies the following relation

$$\frac{4z^2}{b_s^2} \geq 1. \tag{4.6.21}$$

The lowest limit of Eq. (4.6.21) corresponds to half of the group velocity of the probe field when the signal field is an infinite-plane wave. Graphically, it corresponds to half the intercept point, with $v_{g_{\mathrm{p}}}$-axis as shown in Fig. 4.4. The group velocity of the probe field reaches half of its initial value when $z = z_{R_{\mathrm{s}}}$.

In Figure 4.4, the group velocity of the probe field is plotted using three different values of the signal-field beam waist $w_{0_{\mathrm{s}}}$. The signal-field beam waist controls how fast the group velocity decays as the beam propagates through the medium. Using the values of Fig. 4.4, the group velocity reaches half its initial value by propagating 3.95 cm for $w_{0_\mathrm{s}} = 100\ \mu$m, 1m for $w_{0_\mathrm{s}} = 500\ \mu$m, and 3.95m for $w_{0_\mathrm{s}} = 1000\ \mu$m. A lower value of signal-field beam waist, a faster decay of the group velocity. However, a lower value of signal-field beam waist also mean faster decay of the beam intensity.

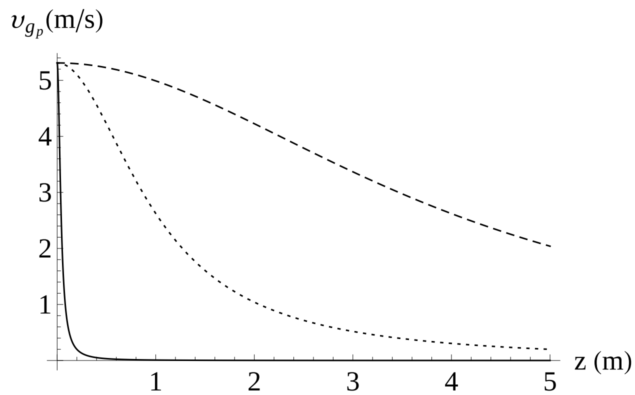

Figure 4.4: Group velocity of the probe field versus the propagation distance z, using three-different values of the signal-field beam waist: $w_{0_\mathrm{s}} = 100\ \mu$m (solid line), $w_{0_\mathrm{s}} = 500\ \mu$m (dotted line) and $w_{0_\mathrm{s}} = 1000\ \mu$m (dashed line). Other parameters are $\gamma_3 = 0.1$ kHz, $\delta_\mathrm{p} = \delta_\mathrm{s} = 9$ MHz, $\gamma_4 = 18$ MHz, $\Omega_\mathrm{c} = \gamma_4$, $\Omega_\mathrm{s} = \Omega_\mathrm{p} = 0.1\gamma_4$, $\gamma_2 = 40$ kHz, $\delta_\mathrm{c} = 0$, $\varrho_{11} = \varrho_{33} = 0.5$. We use the ^{87}Rb constants: $|\boldsymbol{d}_{14}| = |\boldsymbol{d}_{34}| = 1.269 \times 10^{-29}$ C.m, and $\omega_0 = 2\pi \cdot 377.11$ THz.

4.6.2 Phase shift of Gaussian Beam

The phase shift of the probe field in the direction of propagation is given by Eq. (4.6.2. The phase shift of the propagating-Gaussian probe beam due to the nonlinear self-action is

$$\phi_{\mathrm{SPM_{PG}}} = -\frac{b_\mathrm{s}\tan^{-1}\left[\frac{2z}{b_\mathrm{s}}\sqrt{\frac{k_{\mathrm{p}2}}{k_{\mathrm{p}1}}}\right]}{4\sqrt{k_{\mathrm{p}_1}k_{\mathrm{p}_2}}}\left(\mathfrak{m}_{1r} - \frac{k_{\mathrm{p}_1}}{k_{\mathrm{p}_2}}\mathfrak{m}_{2r}\right) + \frac{z}{2k_{\mathrm{p}_2}}\mathfrak{m}_{2r} \tag{4.6.22}$$

Using the approximation of $\tan^{-1}\theta \approx \theta$, for $\theta \ll 1$, the following is obtained

$$\begin{aligned}\phi_{\mathrm{SPM_{PG}}} &\approx -\frac{z}{2k_{\mathrm{p}_1}}\left(\mathfrak{m}_{1r} - \frac{k_{\mathrm{p}_1}}{k_{\mathrm{p}_2}}\mathfrak{m}_{2r}\right) + \frac{z}{2k_{\mathrm{p}_2}}\mathfrak{m}_{2r} \\ &\approx -\frac{z}{2k_{\mathrm{p}_1}}\mathfrak{m}_{1r}.\end{aligned} \tag{4.6.23}$$

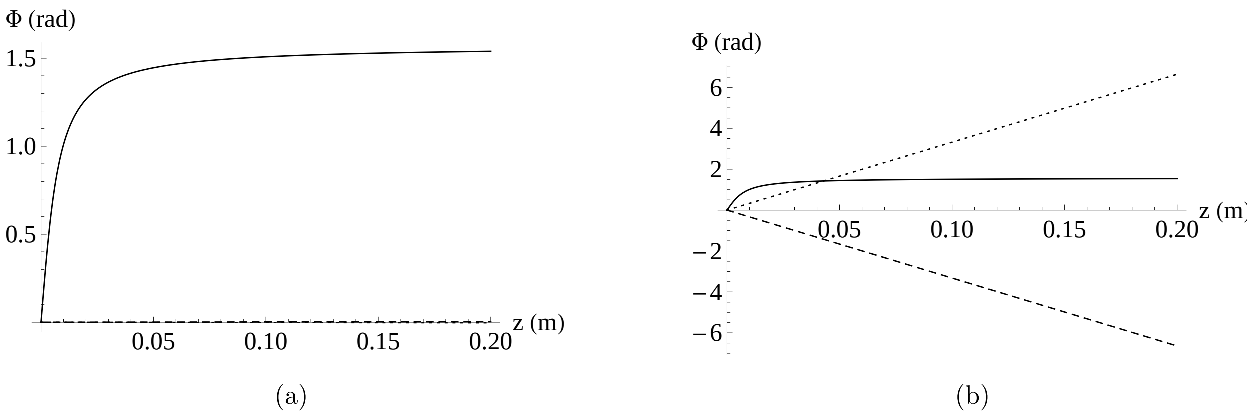

Figure 4.5: Phase shift of the Gaussian-probe beam versus the propagation distance z, $\phi_{\mathrm{XPM}_{\mathrm{PG}}}$ (dashed line), $\phi_{\mathrm{SPM}_{\mathrm{PG}}}$ (dotted line) and the Gouy-phase shift Θ is represented by (solid line), for two different values of the coupling-field detunings: (a) $\delta_{\mathrm{c}} = 0$, and (b) $\delta_{\mathrm{c}} = 0.1$ MHz. Other parameters are $\gamma_3 = 0.1$ kHz, $\delta_{\mathrm{p}} = \delta_{\mathrm{s}} = 9$ MHz, $\gamma_4 = 18$ MHz, $\Omega_{\mathrm{c}} = \gamma_4$, $\Omega_{\mathrm{s}} = \Omega_{\mathrm{p}} = 0.1\gamma_4$, $\gamma_2 = 40$ kHz, $\varrho_{11} = \varrho_{33} = 0.5$, and the beam waist $w_{0_{\mathrm{s}}} = 100$ μm. We use ^{87}Rb constants: $|\boldsymbol{d}_{14}| = |\boldsymbol{d}_{34}| = 1.269 \times 10^{-29}$ C.m, and $\omega_0 = 377.11$ THz.

The nonlinear-phase shift of the propagating-Gaussian probe beam due to the action of the signal field is

$$\begin{aligned}\phi_{\mathrm{XPM}_{\mathrm{PG}}} &= \frac{b_{\mathrm{s}}\tan^{-1}\left[\frac{2z}{b_{\mathrm{s}}}\sqrt{\frac{k_{\mathrm{p}2}}{k_{\mathrm{p}1}}}\right]}{4\sqrt{k_{\mathrm{p}_1}k_{\mathrm{p}_2}}}\left(\mathfrak{n}_{1r} - \frac{k_{\mathrm{p}_1}}{k_{\mathrm{p}_2}}\mathfrak{n}_{2r}\right) + \frac{z}{2k_{\mathrm{p}_2}}\mathfrak{n}_{2r}, \\ &\approx -\frac{z}{2k_{\mathrm{p}_1}}\mathfrak{n}_{1r}. \end{aligned} \tag{4.6.24}$$

The second line of (4.6.24) is achieved by following the same mathematical steps for (4.6.23).

The relation $k_{\mathrm{p}_1} \gg k_{\mathrm{p}_2}$ is always true for the $\pitchfork$ atom-field optical system; then the phase shift can always be approximated to (4.6.24) and (4.6.23). Therefore, the nonlinear-phase shift equation is similar to using infinite-plane signal and probe fields. Using a Gaussian-probe and signal beams doesn't modify the nonlinear interaction.

In Fig. 4.5, the nonlinear phase shift is plotted for two cases. First, when the signal field is in resonance with $|3\rangle \leftrightarrow |-\rangle$ transition, while the second for the signal field is out of resonance of $|3\rangle \leftrightarrow |\pm\rangle$ transitions. As expected, the phase shift is close to zero for the first case, but is extremely large for the second (see Sec. 3.5.2 for details of how the coupling-field detunings modifies the nonlinear phase shift).

4.7 Summary

The wave equation describes the propagation of the Gaussian probe field mode through ⫛ atom-field configuration in which the signal field is also Gaussian have been solved. The solution is based on treating the medium as inhomogeneous. The inhomogeneity of the system is a consequence of the variation in the dielectric, due to the propagation of the signal field within medium. It also assumed that the propagation of the Gaussian probe beam has slow spatial variations of the gain and index of refraction [90]. The variations are sufficiently slow in the vicinity of the beam so that the optical susceptibility can be expanded keeping only the linear and quadratic terms.

Creating an effective inhomogeneity in the medium modifies the group velocity of the probe field, but not the nonlinear phase shift. The group velocity of the probe field reduces as the beam propagates through the medium. The reduction in the group velocity is controlled by the signal-field beam waist.

Chapter 5

The Potential of Atom-Field Tripod Scheme in the Scope of Nonlinear Interaction.

5.1 Introduction

The intensive theoretical analysis and predicted equations presented in the previous chapters make us eligible to compare our proposal for operating atom-field tripod scheme in new region of frequency detuning with other schemes under the same conditions. It also permit us to exhibit how the tripod scheme capable of inducing a high nonlinear interaction between the probe and the signal fields at the level of one photon using experimentally feasible data. In our calculation, we always satisfy the substantial requirements to resolve EIT experimentally, which insure minimizing the absorption, by eliminating homogeneous broadening and confining the probe and signal bandwidth within the EIT window, and saturate the transition.

5.2 Tripod Scheme Operated at the Second DEIT Window in Comparison to N-Scheme

To demonstrate the potential of the tripod scheme operated in the new region of frequency detuning where $\delta_{\mathrm{p}} = \delta_{\mathrm{s}} \neq \delta_{\mathrm{c}}$, we compare the XPM phase shift that can be achieved by the probe field using our scheme with XPM phase shift obtained by other schemes operated using the same optical system and under the same conditions. The best nonlinearity enhancement has been obtained so far by implementing N-scheme [9]. The N-scheme offers non-zero XPM at the center of the transparency where the absorption vanishes, while all other proposed schemes has zero XPM at the center of EIT window [57–60]. Therefore, we compare our scheme with N-scheme. For $\Omega_s = 2$ MHz, $\Omega_c = 2\gamma_4$ MHz, and $\gamma_4 = 18$ MHz, our scheme produces XPM nonlinearity $\mathrm{Re}[\chi_p^{(3)}] = 5.7\times10^{-6}$ m$\cdot$V^{-2} and the probe field phase shifted 90° by propagating distance $z = 24$ μm, while using N-scheme we obtain $\mathrm{Re}[\chi_p^{(3)}] = 4.9\times10^{-6}$ m$\cdot$V^{-2} and the probe field phase shifted 71° by propagating the same distance. Appendix A.1 elucidates the calculation details.

Our scheme produces the same order of magnitude of the optical nonlinearity achieved by N-scheme. However, the tripod scheme has advantage over the N-scheme that both probe and signal field are part of EIT system, such that both field can achieve a high phase shift and their group velocity can be lowered simultaneously. Whereas in N-scheme the interaction between the probe and the signal fields is limited by temporal walk-off, which result of different group velocities of the probe and signal pulses. The probe pulse propagates with slow group velocity due to EIT, while the signal-field group velocity is close to speed of light in vacuum. Operating the tripod scheme in the new region combines the advantage of the N-scheme by obtaining high nonlinearity and the advantage of the DEIT schemes by matching and lowering the group velocity of the interacting probe and signal fields.

5.3 Cross Phase Modulation at the Level of One Photon

Our next step is to show the possibility for the probe and signal beams to acquire high phase shift resolvable experimentally at the level of one photon. Refer to Appendix A.2 for more details of the calculation steps. Using our proposed scheme, it is easy to achieve high nonlinear interaction capable of realizing a π- phase shift between the probe and the signal fields, and to slow and match their group velocities. The challenge lies in achieving a π- phase shift and low matched group velocity, in addition to fulfilling three criteria that ensure minimizing the absorption and saturating the transition and lead to the creation of an appropriate environment to attain EIT experimentally:

(i) The ratio $\frac{|\Omega_{p,s}|^2}{\gamma_4\gamma_3}$ must be large, that is $\frac{|\Omega_{p,s}|^2}{\gamma_4\gamma_3} \gg 1$ to obtain the lowest absorption and eliminate homogeneous broadening. The necessity for this condition is discussed in Sec. 3.4.1.

(ii) The DEIT windows must contain the probe and signal field bandwidths to avoid loss and dissipation. This condition is called the adiabatic limit and can be satisfied by making the pulse duration of the probe and the signal fields $\tau_{\mathrm{p,s}} > \frac{1}{\daleth_{2_{\mathrm{p,s}}}}$, with $\daleth_{2_{\mathrm{p,s}}}$ half-width at the half-maximum of the second EIT window.

(iii) The transition must be saturated. Laser pulses with large intensity and/or large interaction times are good choices to fulfill this criterion. Mathematically, this equivalent to satisfying the condition $|\Omega_{\mathrm{p,s}}| \cdot \tau_{\mathrm{p,s}} \gg 1$.

For example, using a probe and signal pulses of duration $\tau_{\mathrm{p}} = \tau_{\mathrm{s}} = 1$ μs and a spot area of radius $w_{0_{\mathrm{s}}} = w_{0_{\mathrm{s}}} = 300$ nm will result in $\frac{\pi}{2}$ phase shift for each of the probe and signal fields and low group velocity reaching $v_{\mathrm{p}} = v_{\mathrm{s}} = 0.0146\ \mathrm{cm} \cdot s^{-1}$ with a delay time of 122 μs, but at the expense of failing the second and third criteria, which could prevent resolving the EIT experimentally.

In our previous and next calculations we consider ^{87}Rb. The parameters for the dipole matrix elements, decay rates [61], and detunings corresponding to our choice of atom and hyper-fine transition are $|\boldsymbol{d}_{14}| = |\boldsymbol{d}_{34}| = 1.269 \times 10^{-29}$ C·m, $\gamma_{14} = \gamma_{24} = \gamma_{34} = 6$ MHz, $\gamma_3 = 10$ kHz, $\gamma_2 = 40$ kHz, $\Omega_{\mathrm{c}} = 2\gamma_4$, $\delta_{\mathrm{s}} = \delta_{\mathrm{p}} = 0.5\Omega_{\mathrm{c}}$ and $\delta_{\mathrm{c}} = 0.15\Omega_{\mathrm{c}}$. The atomic density is assumed to be $\mathcal{N} = 10^{14}\ \mathrm{cm}^{-3}$.

The intensity required to obtain field strength $\Omega_{\mathrm{s}} = \Omega_{\mathrm{p}} = 1.7$ MHz is equal to 245 $\mu\mathrm{W/cm}^2$, which is sufficient to satisfy the first criterion. The width of the DEIT windows are $\daleth_{2_{\mathrm{p}}} = \daleth_{2_{\mathrm{s}}} \approx 0.08$ MHz, which require the probe and signal pulse duration $\tau_{\mathrm{p}} = \tau_{\mathrm{s}} > \frac{1}{0.08}$ μs to fulfill the second criterion. Hence, a pulse duration $\tau_{\mathrm{p}} = \tau_{\mathrm{s}} = 13$ μs is used. For one photon to produce this required intensity the beam must be focused on an area of radius $w_{0_{\mathrm{s}}} = w_{0_{\mathrm{s}}} = 50$ nm. Then each of the probe and signal fields acquires a phase shift

$\phi_{\mathrm{XPM_p}} = \phi_{\mathrm{XPM_s}} = 0.35$ rad by propagating a distance equal to the confocal length of the Gaussian probe and signal beams. The group velocity for both fields is matched and lowered to a value equal to 0.20 cm/s at the entrance of the medium with a pulse delay time equal to 5.35 μs.

In The previous proposed schemes either achieve high phase shift [9, 10, 51] with mismatched group velocity and combined with high absorption, or matched low group velocities [45, 57–61] with negligible nonlinearity at the center of the EIT window. Operating the tripod scheme in the new region of frequency detuning combines the advantages of the previous proposed schemes. Our scheme is capable of inducing a phase shift between the probe signal field reaching 40°, and lowering and matching their group velocities in addition to the fulfillment of the three criteria at the level of one photon. This ensures the propagation of the probe and signal pulses through the medium without absorption by confining their bandwidths within the EIT and eliminating homogeneous broadening.

One possible limit to this scheme is the feasibility of not being able to focus the Gaussian field to an area of radius $w_{0_\mathrm{s}} = w_{0_\mathrm{s}} = 50$ nm. The need for a tightly focused Gaussian beam is to satisfy the requirement that one photon laser pulse interacts with one atom. This is consistent with the conditions previously derived for laser pulse energy by Harris and Luo [93], which demand a sufficient number of photons in the laser pulse to match the number of atoms in the laser path. Relying on our theoretical calculation, a large XPM with matched and lowered group velocities, in addition to fulfilling the three criteria discussed above, is feasible experimentally at the level of a few tens photons using our scheme, if the laser beam is focused to a spot size of a half wavelength $w_{0_\mathrm{s}} = w_{0_\mathrm{s}} = \frac{\lambda_{\mathrm{s,p}}}{2} = 395$ nm [94] (see Appendix A.2). The performance of our scheme could be improved further if we were able to confine the atom in a cavity [95] to make the photon pass through the atom repeatedly, or bottle [96], to increase the interaction between light and atom and ensure one photon is interacting with one atom.

Chapter 6

Doppler-Broadening Effect

6.1 Introduction

At non-zero temperature atoms move randomly due to thermal energy. Thermal atomic motion leads to a spreading of the absorbed frequency due to the Doppler effect, which broadens the optical line profile and is known as Doppler broadening [97].

In this chapter, we solve susceptibility numerically and also derive an approximate analytical expression under certain assumption as a function of temperature. The analytical solution is used to find the widths of transparency windows and also group velocities of the probe field in each of the two DEIT windows. Our approximate analytical technique is based on approximating the Maxwell-Boltzmann velocity distribution for atoms by Lorentzian distributions over the narrow but relevant domain of small atomic velocities [64, 65]. This approximation is valid as large velocities are sufficiently detuned so as not to affect the optics.

This chapter focuses on the absorption and dispersion of the probe field at the DEIT windows in the Doppler broadening medium, which is modified by the presence of the coupling and the signal fields, under certain detunings. The result can be generalized to describe the absorption and dispersion of the signal field at DEIT windows in the Doppler-broadening medium, which is modified by the presence of the coupling and the probe fields, under certain detunings. By comparing (2.5.10) with (2.5.14), it can be seen that ϱ_{14} and ϱ_{34} are symmetric with regard to $\delta_{\mathrm{p}} \leftrightarrow \delta_{\mathrm{s}}$ and $\varrho_{11} \leftrightarrow \varrho_{33}$ exchange, which insure identical dispersive and absorptive properties of the probe and signal fields for $\delta_{\mathrm{p}} = \delta_{\mathrm{s}}$ and $\varrho_{11} = \varrho_{33}$.

This chapter is organized as follows: In Sec. 6.2, Doppler broadening due to temperature is incorporated into the expression for susceptibility. We solve this susceptibility numerically. Doppler-broadened optical susceptibility is solved analytically in Sec. 6.3. Our analytical solution is based on ignoring quadratic dependence of the probe-field Rabi frequency and employing a Lorentzian approximation for a narrow band around the Gaussian Maxwell-Boltzmann distribution. This approximate expression enables an intuition about how to control group velocities' reduction at the second window. In Sec. 6.4, we present the procedure to reduce the group velocity in the second window. Finally, we summarize in Sec. 6.5.

6.2 Numerical solution

In our scheme, the electromagnetic field passes through a gas of atoms at temperature T. Each atom of mass m has a velocity $\boldsymbol{v}$ obeying the Gaussian Maxwell-Boltzmann distribution

$$f(v) = \frac{1}{u\sqrt{\pi}} \exp\left(-\frac{v^2}{u^2}\right),\ u = \sqrt{\frac{2kT}{m}}, \tag{6.2.1}$$

with v the component of velocity $\boldsymbol{v}$ in the direction of the three copropagating signal, probe, and coupling fields.

One effect of moving atoms is detuning of resonant frequencies due to the Doppler shift, which results in a velocity-dependent probe-field susceptibility $\chi_{\mathrm{p}}(v)$. For our Doppler-broadened system, the susceptibility is thus averaged over the entire velocity distribution according to [97]

$$\bar{\chi}_{\mathrm{p}} := \int_{-\infty}^{\infty} \chi_{\mathrm{p}}(v) f(v) \mathrm{d}v. \tag{6.2.2}$$

The velocity-dependent expression for susceptibility is obtained from Eq. (6.3.4) by the replacement

$$\delta_{\mathrm{x}} \mapsto \delta_{\mathrm{x}} + \frac{v\omega_{\mathrm{x}}}{c},\ \mathrm{x} \in \{\mathrm{p,c,s}\}, \tag{6.2.3}$$

for

$$
\omega_{\mathrm{x}} = \begin{cases} \omega_{14} \equiv \omega_0, & \mathrm{x} = \mathrm{p}, \\ \omega_{24}, & \mathrm{x} = \mathrm{c}, \\ \omega_{34}, & \mathrm{x} = \mathrm{s}, \end{cases} \tag{6.2.4}
$$

the atomic frequencies and c the speed of light *in vacuo*.

Our scheme relies on neglecting Doppler effect on two-photon detuning δ_{xy} (2.2.34), which is achieved for the copropagating fields driving approximately equal transition frequencies:

$$
\omega_0 \equiv \omega_{14} \approx \omega_{24} \approx \omega_{34}. \tag{6.2.5}
$$

This choice is commensurate with our case of a ^{87}Rb gas. For this atom, we assign $|1\rangle$, $|2\rangle$ and $|3\rangle$ to the $5S_{1/2}$ level with $F = 1$, $m_F = 0$ and $F = 2$, $m_F = \{-2, 0\}$ respectively. Level $|4\rangle$ corresponds to the $5P_{1/2}$ level with $F = 2$ and $m_F = -1$. Therefore, the quantities $\{\delta_{\mathrm{xy}}\}$ in Eqs. (6.3.4) do not change under Doppler broadening.

Integration of Eq. (6.2.2) corresponds to a convolution of Lorentzian χ_{p} with the Gaussian profile, which is known as the Voigt profile [98]. The Voigt profile can be solved numerically but is hard to solve analytically [17, 45, 97, 99].

6.2.1 General Case

This section discusses the numerical solution of Eq. (6.2.2) for general case of Doppler-broadening effect on optical susceptibility of $\pitchfork$ atom-field system, without the assumption of constant population and without any constrains on the strength of the applied fields.

Figures 6.1 and 6.2 show the imaginary and real parts of the probe-field optical susceptibility for two different temperatures. Comparison of these figures with the nonbroadened-optical susceptibility shown in 2.7 and 2.8, reveals a reduction in the EIT-window width commensurate with past observations [42, 58, 67, 99], and an increase in the absorption of probe field for low applied driving field strength. The real part of optical susceptibility has constant slope at the center of each EIT window. Despite Doppler broadening, both windows are still evident.

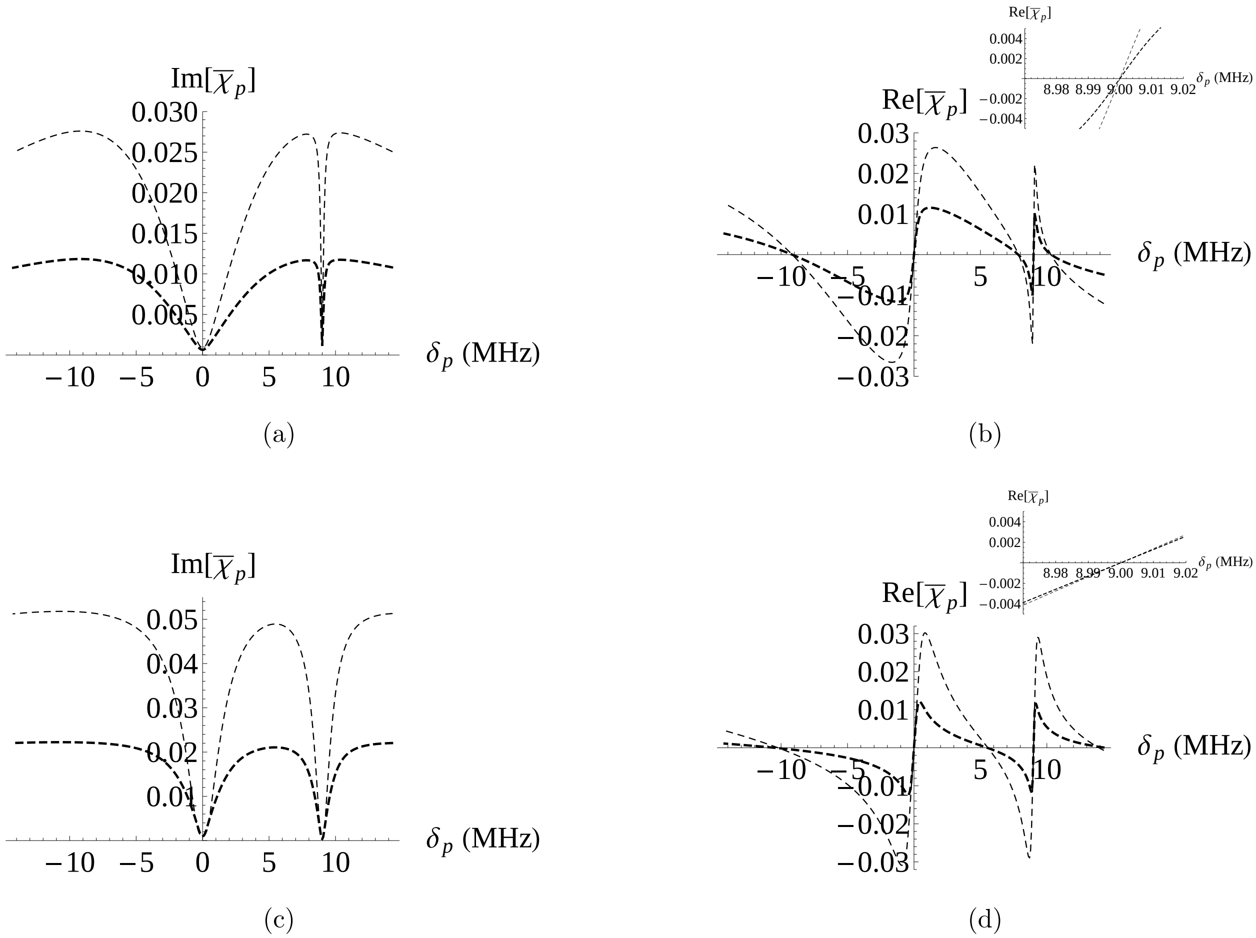

Figure 6.1: Numerically evaluated steady-state Doppler-broadened optical susceptibility $\bar{\chi}_\mathrm{p}$ versus probe-field detuning δ_p at T=50 K (dashed line) and T=300 K (bold-dashed line) for two different values of signal-field Rabi frequencies (a) and (b) $\Omega_\mathrm{s} = 0.1\gamma_4$. (c) and (d) $\Omega_\mathrm{s} = 0.6\gamma_4$. Other parameters are $\gamma_4 = 18$ MHz, $\gamma_3 = 50$ kHz, $\gamma_2 = 40$ kHz, $\Omega_\mathrm{c} = \gamma_4$, $\Omega_\mathrm{p} = 0.1\gamma_4$, $\delta_\mathrm{c} = 0$, $\delta_\mathrm{s} = 0.5\Omega_\mathrm{c}$ and $\mathcal{N} = 1 \times 10^{14}$ cm^{-3}. Using ^{87}Rb constants: $|\boldsymbol{d}_{14}| = |\boldsymbol{d}_{34}| = 1.269 \times 10^{-29}$ C·m, and $\omega_0 = 2\pi \cdot 377.11$ THz.

In Sec. 2.5.1, it was found that the signal-field strength is a crucial parameter that affects the width of the EIT window and the slope of the dispersion curve, when $\delta_\mathrm{p} = \delta_\mathrm{s}$. Therefore, to study the influence of the Doppler effect on the optical properties of the medium in response to the probe field at that window, the temperature is varied for two different values of the signal-field Rabi frequencies, while keeping the coupling-field strength constant. For low value of Ω_s, increasing the temperature leads to an increase in the absorption. Therefore, to reduce the absorption, a higher signal-field strength is required, as shown in Fig 6.1(c). The real part of optical susceptibility has constant slope at the center of the second EIT window. We observe a lower slope for a higher temperature occurs when a low Ω_s is applied, as shown in the inset of Fig. 6.1(b). However, when a high Ω_s is applied, almost the same slope of the dispersion curve is observed at the two different temperatures (see inset, Fig. 6.1(d)).

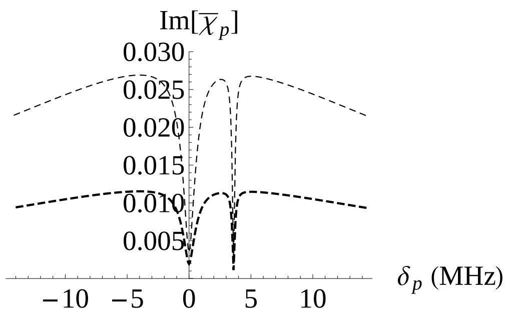

(a)

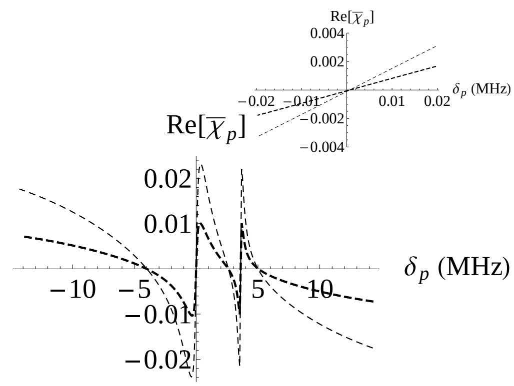

(b)

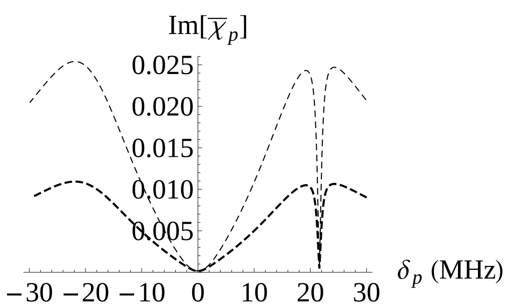

(c)

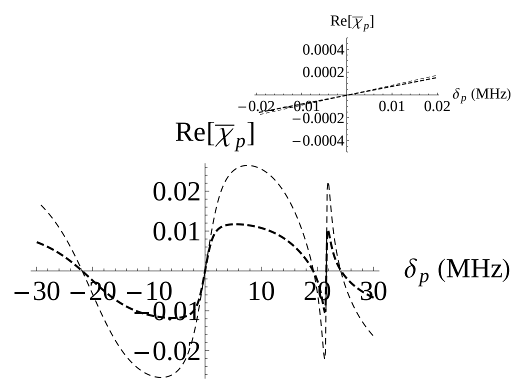

(d)

Figure 6.2: Numerically evaluated steady-state Doppler-broadened optical susceptibility $\bar{\chi}_p$ versus probe-field detuning δ_p at T=50 K (dashed line), and T=300 K (bold-dashed line) for two different values of coupling-field Rabi frequencies (a) and (b) $\Omega_c = 0.4\gamma_4$, $\Omega_s = \Omega_p = 0.1\gamma_4$. (c) and (d) $\Omega_c = 2.4\gamma_4$, $\Omega_s = \Omega_p = 0.2\gamma_4$. Other parameters are $\gamma_4 = 18$ MHz, $\gamma_3 = 50$ kHz, $\gamma_2 = 40$ kHz, and $\delta_c = 0$, $\delta_s = 0.5\Omega_c$ and $\mathcal{N} = 1 \times 10^{14}$ cm^{-3}. Using ^{87}Rb constants: $|\boldsymbol{d}_{14}| = |\boldsymbol{d}_{34}| = 1.269 \times 10^{-29}$ C·m, and $\omega_0 = 2\pi \cdot 377.11$ THz.

Next, the effect of Doppler broadening on the optical susceptibility of the probe field is studied, when $\delta_{\mathrm{p}} = \delta_{\mathrm{c}}$. In Fig. 6.2, the temperatures for two different values of the coupling-field strength are changed, while fixing Ω_{s}. For an applied weak value of Ω_{c}, the absorption increases as the temperature increases. However, for a strong applied coupling field, absorption remains close to zero for the two examined temperatures values, as shown in Figs. 6.2(a) and 6.2(c) respectively. The slope of the dispersion curve around the region, where $\delta_{\mathrm{p}} = \delta_{\mathrm{c}}$, sharply decreases as the temperature increases, when a weak coupling-field strength is applied as shown in the inset of Fig. 6.2(b). The difference between dispersion's slope values at the two different temperatures is negligible when a strong coupling field is applied.

To identify the limit for which the applied-field strengths are considered low, and the limit for which the applied-fields strength are considered high at certain temperature, an analytical solution that relates the the applied-fields strength to the temperature is required. This requirement reflects the necessity of an analytical solution.

6.2.2 Temperature-Dependence Atomic Population

Increasing the temperature adds two more phenomena to the atom-field system which we incorporated into an extended quantum master equation. These two phenomena are thermal dissipation and Doppler broadening. Our examination of thermal dissipation shows that its effect is too weak to influence substantially either the coherence or the population. However, the second phenomenon of Doppler broadening modifies the coherence, as we will see in Secs. 6.3.3, 6.3.4, and 6.3.5 onward for equal populations in levels $|1\rangle$ and $|3\rangle$, is discussed in this subsection in the absence of this equal-population restriction.

Finding an analytical expression for population in Doppler-broadening medium is difficult. Therefore, we perform numerical studies of atomic populations for various temperatures. Now we proceed to analyze the connection between atomic population and coherence.

At high temperature, Doppler broadening reduces coherence [100, 101] and specifically directly reduces the coherences ϱ_{14} and ϱ_{34} that are established by the weak fields. Consequently the populations of the states $|1\rangle$ and $|3\rangle$ change according to the solution of Eq. (2.3.7). As we will see from the approximate analytical expression for optical susceptibility (6.3.42) that increasing Doppler width $W_{\rm L}$ in Eq. (6.3.42) is responsible for reducing coherence.

Reduction of coherence and its consequent effects due to Doppler broadening and to increasing Doppler width are similar to the effects due to adding extra dephasing $\gamma_{\phi 41}$ between $|1\rangle$ and $|4\rangle$ and $\gamma_{\phi 43}$ between $|3\rangle$ and $|4\rangle$ plus increasing the dephasing $\gamma_{\phi 2}$ between $|1\rangle$ and $|2\rangle$. In Fig. 6.3, we present numerically evaluated atomic populations at different probe-field detunings $\delta_{\rm p}$, for Doppler broadening medium at temperature 100 K as shown in Figs. 6.3(a), and 6.3(b), and for free Doppler broadening media at zero temperature accompanied by additional dephasing quantified by $\gamma_{\phi 41}$ and by $\gamma_{\phi 43}$. We choose the dephasing $\gamma_{\phi 41}$ and $\gamma_{\phi 43}$ in Fig. 6.3 to be of the same order of magnitude of $W_{\rm L}$ as shown in Figs. 6.3(c), and 6.3(d). We observe that Figs. 6.3(a), and 6.3(b) are similar to Figs. 6.3(c), and 6.3(d).

6.2.2.1 Signal-Field Rabi Frequency Equal Probe-Field Rabi Frequency ($\Omega_{\rm s} = \Omega_{\rm p}$)

At $\delta_{\rm p} = \delta_{\rm c} = 0$, the population of atoms in state $|3\rangle$ increases as temperature increases, as shown in Fig. 6.3(a) compared to Fig. 2.5(a). Increasing the temperature from 0 to 100 K decreases ϱ_{11} from 1.0 to 0.7 while increasing ϱ_{33} from 0.0 to 0.2. This population changes is due to reduction of the coherence ϱ_{14}. The coherence ϱ_{34} does not have an influence at $\delta_{\rm pc} = 0$. The atom-field system is no longer in the pure dark state $|\psi_{\rm D}\rangle$. Increasing the temperature has the effect of displacing the system from the dark state to different state, where the absorption of the probe field increases. Thus, as the temperature of the system increases, probe-field absorption becomes very high, thereby potentially preventing the first EIT window from being observed.

For $\delta_{\rm p} = \delta_{\rm s}$, the atomic population remains the same at different temperatures; i.e.,

$\varrho_{11} = \varrho_{33} = 0.5$. Therefore, the system remains trapped in the dark state $|\psi'_{\mathrm{D}}\rangle$ [Eq. (2.4.6)]. The population at that detuning is less sensitive to Doppler broadening. This insensitivity can be explained as resulting from higher-order nonlinear interactions between the signal and probe fields resulting from the coupling of ϱ_{14} to ϱ_{34} through the presence of the term ϱ_{13} [72]. This coupling eliminates the effect of Doppler broadening and eliminates the dephasing by W_{L}. Thus, at the second window, the dressed atom-field dark state is stable with respect to the Doppler effect, and this stability enables observing the second window even at higher temperature.

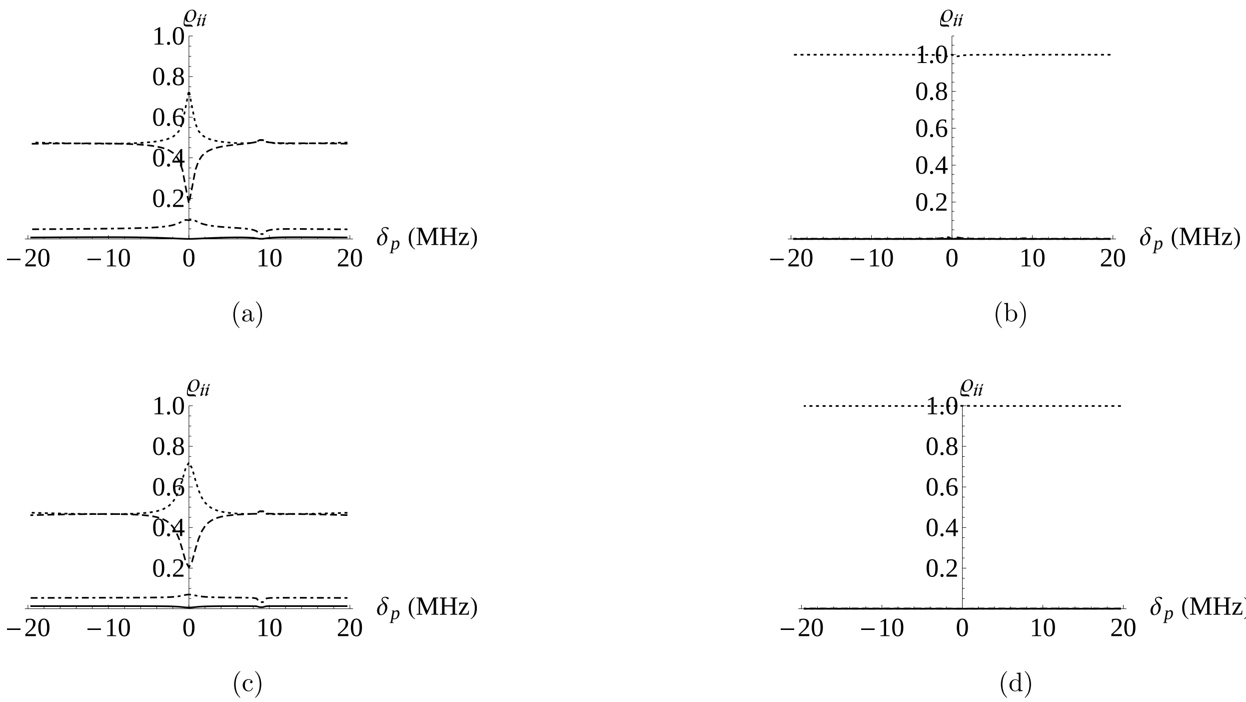

Figure 6.3: Numerically evaluated steady-state populations ϱ_{11} (dotted line), ϱ_{22} (dotted-dashed line), ϱ_{33} (dashed line), and ϱ_{44} (solid line) versus probe-field detuning δ_{p}. (a),(b) at 100 K with $\gamma_{\phi 41} = \gamma_{\phi 43} = 0$ MHz and $\gamma_{\phi 2} = 40$ kHz and (c),(d) at zero temperature and incorporating dephasing $\gamma_{\phi 41} = \gamma_{\phi 43} = 150$ MHz and $\gamma_{\phi 2} = 0.8$ MHz. The plots show (a),(c) $\Omega_{\mathrm{s}} = \Omega_{\mathrm{p}} = 0.3\gamma_4$ and (b),(d) $\Omega_{\mathrm{s}} \gg \Omega_{\mathrm{p}}$, $\Omega_{\mathrm{s}} = 0.3\gamma_4$, $\Omega_{\mathrm{p}} = 0.01\gamma_4$. Other parameters are $\gamma_4 = 18$ MHz, $\gamma_3 = 10$ kHz, and $\Omega_{\mathrm{c}} = \gamma_4$, $\delta_{\mathrm{s}} = 0.5\Omega_{\mathrm{c}}$, $\delta_{\mathrm{c}} = 0$ and $\mathcal{N} = 1 \times 10^{14}$ cm^{-3}. Using ^{87}Rb constants: $|\boldsymbol{d}_{14}| = |\boldsymbol{d}_{34}| = 1.269 \times 10^{-29}$ C·m, and $\omega_0 = 2\pi \cdot 377.11$ THz.

6.2.2.2 Signal-Field Rabi Frequency Greater than Probe-Field Rabi Frequency ($\Omega_\mathrm{s} \gg \Omega_\mathrm{p}$)

The term $\Omega_\mathrm{p}\varrho_{41}(t) - \Omega_\mathrm{p}^*\varrho_{14}(t)$ of Eq. (2.3.7) is neglected because its effect is very small. Therefore, for this case, the coherence ϱ_{14} has negligible effect on the atomic population of state $|1\rangle$. Consequently, the population of $|1\rangle$ is not affected by Doppler broadening at $\delta_\mathrm{p} = \delta_\mathrm{c}$.

Under the additional constraint that $\delta_\mathrm{ps} = 0$, only ϱ_{34} affects the population by reducing ϱ_{33}, and, as ϱ_{33} for the Doppler-free atomic-field system is almost zero, reducing ϱ_{34} thus has no effect on the population of state $|3\rangle$. Hence, the population of each level (2.3.7) at zero temperature will be the same as for the population at any higher temperature. At steady state, the atoms are all trapped in the state $|\psi_\mathrm{D}\rangle$ for $\delta_\mathrm{pc} = 0$ and to $|\psi'_\mathrm{D}\rangle$ for $\delta_\mathrm{ps} = 0$.

6.3 Analytical Solution Based on Lorentzian Function

The lack of an exact analytical solution inhibits finding a simple expression relating the group velocity or width of each EIT window to Doppler broadening. Instead we approximate the Maxwell-Boltzmann distribution by a Lorentzian function over a narrow velocity domain [64, 65] to obtain an approximate analytical expression for the optical susceptibility. This approximation is valid insofar as we are interested in the optical response near the spectral center.

The analytical steady-state density-matrix element ϱ_{14} solution for a stationary atom, to first order in the probe-field Rabi frequency, can be approximated from the exact expression (2.5.10) as

$$\varrho_{14}^{(1)} \approx \mathrm{i}\Omega_\mathrm{p}\frac{(\varrho_{11}-\varrho_{44})\left(\Gamma_{43}+2\mathrm{i}\delta_\mathrm{s}+\frac{|\Omega_\mathrm{c}|^2}{\Gamma_{32}+2\mathrm{i}\delta_\mathrm{sc}}\right)+(\varrho_{44}-\varrho_{33})\frac{|\Omega_\mathrm{s}|^2}{\gamma_3-2\mathrm{i}\delta_\mathrm{ps}}}{\left(\Gamma_{43}+2\mathrm{i}\delta_\mathrm{s}+\frac{|\Omega_\mathrm{c}|^2}{\Gamma_{32}+2\mathrm{i}\delta_\mathrm{sc}}\right)\left(\gamma_4-2\mathrm{i}\delta_\mathrm{p}+\frac{|\Omega_\mathrm{c}|^2}{\gamma_2-2\mathrm{i}\delta_\mathrm{pc}}+\frac{|\Omega_\mathrm{s}|^2}{\gamma_3-2\mathrm{i}\delta_\mathrm{ps}}\right)}, \tag{6.3.1}$$

We verified this expression numerically for weak signal and weaker probe-Rabi frequencies, i.e., for the condition

$$|\Omega_\mathrm{c}|^2 \gg |\Omega_\mathrm{s}|^2 \gg |\Omega_\mathrm{p}|^2. \tag{6.3.2}$$

The coherence decay rates are defined in (2.3.8) and (2.5.9). The dephasing rate between the forbidden transitions is not zero; therefore, $\gamma_2 = \gamma_{\phi 2}$ and $\gamma_3 = \gamma_{\phi 3}$.

The optical susceptibility for an atomic gas in three dimensions with $\mathcal{N}$ the atomic density and $\boldsymbol{d}_{14}$ the dipole moment is defined by (3.4.27) as

$$\chi_{\mathrm{p}} = \eta_{\mathrm{p}} \frac{\varrho_{14}}{\Omega_{\mathrm{p}}}, \tag{6.3.3}$$

with η_{p} defined in Eq. (3.4.28). We can substitute Eq. (6.3.1) into the numerator for $\chi_{\mathrm{p}}^{(1)}$ in Eq. (6.3.3), which is complicated so we express $\chi_{\mathrm{p}}^{(1)}$ as:

$$\chi_{\mathrm{p}}^{(1)} = \frac{\mathrm{i}\eta_{\mathrm{p}}}{2(B_1 + 2\mathrm{i}B_2)} \left(1 - \frac{C_1 + 2\mathrm{i}C_2}{A_1 - 2\mathrm{i}A_2}\right), \tag{6.3.4}$$

with the terms $A_{1,2}$, $B_{1,2}$ and $C_{1,2}$ explained below.

To simplify Eq. (6.3.1), we fix the value $\varrho_{44} = 0$. This is always true because the atoms are trapped to the dark state leaving level $|4\rangle$ unpopulated. The population of the other three levels depends on the Rabi frequency of the driving fields. See Sec. 2.4 for more details of the dark-state analysis and state populations.

The variables in Eq. (6.3.4) are

$$\begin{aligned}
A_1 :=& \Gamma_{43} + \frac{|\Omega_{\mathrm{c}}|^2 \Gamma_{32}}{\Gamma_{32}^2 + 4\delta_{\mathrm{sc}}^2},\ A_2 := \frac{|\Omega_{\mathrm{c}}|^2 \delta_{\mathrm{sc}}}{\Gamma_{32}^2 + 4\delta_{\mathrm{sc}}^2} - \delta_{\mathrm{s}}, \\
B_1 :=& \gamma_4 + \frac{|\Omega_{\mathrm{c}}|^2 \gamma_2}{\gamma_2^2 + 4\delta_{\mathrm{pc}}^2} + \frac{|\Omega_{\mathrm{s}}|^2 \gamma_3}{\gamma_3^2 + 4\delta_{\mathrm{ps}}^2}, \\
B_2 :=& \frac{|\Omega_{\mathrm{c}}|^2 \delta_{\mathrm{pc}}}{\gamma_2^2 + 4\delta_{\mathrm{pc}}^2} + \frac{|\Omega_{\mathrm{s}}|^2 \delta_{\mathrm{ps}}}{\gamma_3^2 + 4\delta_{\mathrm{ps}}^2} - \delta_{\mathrm{p}}, \\
C_1 :=& \frac{|\Omega_{\mathrm{s}}|^2 \gamma_3}{\gamma_3^2 + 4\delta_{\mathrm{ps}}^2}, C_2 := \frac{|\Omega_{\mathrm{s}}|^2 \delta_{\mathrm{ps}}}{\gamma_3^2 + 4\delta_{\mathrm{ps}}^2}.
\end{aligned} \tag{6.3.5}$$

We now have expressions for the steady-state solution (6.3.1) and the corresponding susceptibilities for the probe field (6.3.4).

Expression (6.3.4) is used to calculate and plot the susceptibility, whose imaginary part is shown in Fig. 6.4(a), and whose real part is shown in Fig. 6.4(b). This absorption plot clearly displays the first probe window centered at $\delta_{\mathrm{p}} = \delta_{\mathrm{c}}$ and the second EIT window centered at $\delta_{\mathrm{p}} = \delta_{\mathrm{s}} \neq \delta_{\mathrm{c}}$.

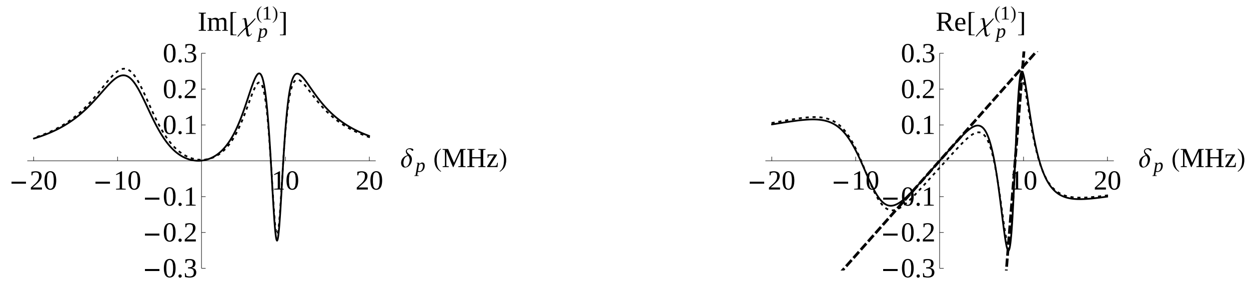

(a) (b)

Figure 6.4: (a) Absorption and (b) dispersion as a function of the probe-field detuning δ_{p}, with numerical (dotted line), analytical (solid line), and approximate linear equation (dashed line), for $\varrho_{11} = \varrho_{33} = 0.5$, $\gamma_4 = 18$ MHz, $\gamma_3 = 10$ kHz, $\gamma_2 = 40$ kHz, $\Omega_{\mathrm{c}} = \gamma_4$, $\Omega_{\mathrm{s}} = 0.3\gamma_4$, $\Omega_{\mathrm{p}} = 0.05\gamma_4$, $\delta_{\mathrm{s}} = 9$ MHz, $\delta_{\mathrm{c}} = 0$, and $\mathcal{N} = 1 \times 10^{14}$ cm^{-3}. Using ^{87}Rb constants: $|\boldsymbol{d}_{14}| = |\boldsymbol{d}_{34}| = 1.269 \times 10^{-29}$ C·m, and $\omega_0 = 2\pi \cdot 377.11$ THz.

6.3.1 Atomic Population for Probe-Field Strength Weaker than Signal-Field Strength

In this section, we derive an analytical expression for atomic populations for the case studied in this chapter. corresponding to $\Omega_{\mathrm{c}} \gg \Omega_{\mathrm{s}} \gg \Omega_{\mathrm{p}}$. The analytical expression can be found by solving Eqs. (2.3.6) and (2.3.7) restricted to the case that $\Omega_{\mathrm{p}} \equiv 0$:

$$\begin{aligned}
\dot{\varrho}_{23}(t) &= \left(-\frac{1}{2}\Gamma_{32} - \mathrm{i}\delta_{\mathrm{sc}}\right)\varrho_{23}(t) - \frac{\mathrm{i}}{2}\Omega_{\mathrm{c}}\varrho_{43}(t),\\
\dot{\varrho}_{24}(t) &= \left(-\frac{1}{2}\Gamma_{42} + \mathrm{i}\delta_{\mathrm{c}}\right)\varrho_{24}(t) - \frac{\mathrm{i}}{2}\left[\Omega_{\mathrm{c}}\left(\varrho_{44}(t) - \varrho_{22}(t)\right) - \Omega_{\mathrm{s}}\varrho_{23}\right],\\
\dot{\varrho}_{43}(t) &= \left(-\frac{1}{2}\Gamma_{43} - \mathrm{i}\delta_{\mathrm{s}}\right)\varrho_{43}(t) + \frac{\mathrm{i}}{2}\left[-\Omega_{\mathrm{c}}^{*}\varrho_{23}(t) + \Omega_{\mathrm{s}}^{*}(\varrho_{44}(t) - \varrho_{33}(t))\right],
\end{aligned} \tag{6.3.6}$$

and

$$\begin{aligned}
\dot{\varrho}_{11}(t) &= \gamma_{41}\varrho_{44}(t),\\
\dot{\varrho}_{22}(t) &= \gamma_{42}\varrho_{44}(t) - \frac{\mathrm{i}}{2}\left[-\Omega_{\mathrm{c}}^{*}\varrho_{24}(t) + \Omega_{\mathrm{c}}\varrho_{42}(t)\right],\\
\dot{\varrho}_{33}(t) &= \gamma_{43}\varrho_{44}(t) - \frac{\mathrm{i}}{2}\left[-\Omega_{\mathrm{s}}^{*}\varrho_{34}(t) + \Omega_{\mathrm{s}}\varrho_{43}(t)\right],\\
1 &\equiv \varrho_{11}(t) + \varrho_{22}(t) + \varrho_{33}(t) + \varrho_{44}(t).
\end{aligned} \tag{6.3.7}$$

As we mentioned earlier the $|1\rangle \leftrightarrow |2\rangle$, $|1\rangle \leftrightarrow |3\rangle$, and $|2\rangle \leftrightarrow |3\rangle$ transitions are dipole-forbidden. Therefore, we restrict $\gamma_{21} = \gamma_{31} = \gamma_{32} = 0$ in the above equation.

With initial population described by $\varrho_{11}(0), \varrho_{22}(0), \varrho_{33}(0)$, and $\varrho_{44}(0)$, the atomic populations for the four atomic bare states in the steady state are

$$\begin{aligned}
\varrho_{11} &= \frac{\gamma_{41} ZY}{\gamma_{41} ZY + \gamma_{43}(X - Y)}, \\
\varrho_{22} &= \frac{\gamma_{41} Z \varrho_{22}(0) + [Z(Y - \gamma_{42}) - X\gamma_{43})(1 - \varrho_{11}(0)]}{\gamma_{41} ZY + \gamma_{43}(X + Y)} + \frac{X\gamma_{41}\varrho_{33}(0)}{\gamma_{41} ZY + \gamma_{43}(X - Y)}, \\
\varrho_{33} &= \frac{Y\left[(Z + \gamma_{43})(1 - \varrho_{11}(0)) + \gamma_{41}\varrho_{33}(0)\right]}{\gamma_{41} ZY + \gamma_{43}(X - Y)}, \\
\varrho_{44} &= \frac{Z(1 - \varrho_{11}(0))Y}{\gamma_{41} ZY + \gamma_{43}(X - Y)},
\end{aligned} \tag{6.3.8}$$

with

$$\begin{aligned}
X &= \frac{|\Omega_{\mathrm{s}}|^2 |\Omega_{\mathrm{c}}|^2}{(\Gamma_{42}^2 + 4\delta_{\mathrm{c}}^2)(\Gamma_{32}^2 + 4\delta_{\mathrm{sc}}^2)} \left[\frac{\left(\Gamma_{43} + \frac{|\Omega_{\mathrm{c}}|^2 \Gamma_{32}}{\Gamma_{32}^2 + 4\delta_{\mathrm{sc}}^2}\right)(4\delta_{\mathrm{s}}\delta_{\mathrm{sc}} + \Gamma_{32}\Gamma_{42})}{\left(\Gamma_{43} + \frac{|\Omega_{\mathrm{c}}|^2 \Gamma_{32}}{\Gamma_{32}^2 + 4\delta_{\mathrm{sc}}^2}\right)^2 + 4\left(\frac{|\Omega_{\mathrm{c}}|^2 \delta_{\mathrm{sc}}}{\Gamma_{32}^2 + 4\delta_{\mathrm{sc}}^2} - \delta_{\mathrm{s}}\right)^2} \right. \\
&\qquad \left. + \frac{\left(\frac{|\Omega_{\mathrm{c}}|^2 \delta_{\mathrm{sc}}}{\Gamma_{32}^2 + 4\delta_{\mathrm{sc}}^2} - \delta_{\mathrm{s}}\right)(4\Gamma_{32}\delta_{\mathrm{c}} - \Gamma_{42}\delta_{\mathrm{sc}})}{\left(\Gamma_{43} + \frac{|\Omega_{\mathrm{c}}|^2 \Gamma_{32}}{\Gamma_{32}^2 + 4\delta_{\mathrm{sc}}^2}\right)^2 + 4\left(\frac{|\Omega_{\mathrm{c}}|^2 \delta_{\mathrm{sc}}}{\Gamma_{32}^2 + 4\delta_{\mathrm{sc}}^2} - \delta_{\mathrm{s}}\right)^2} \right], \\
Y &= \frac{|\Omega_{\mathrm{c}}|^2 \Gamma_{42}}{\Gamma_{42}^2 + 4\delta_{\mathrm{c}}^2},
\end{aligned} \tag{6.3.9}$$

and

$$Z = \frac{|\Omega_{\mathrm{s}}|^2 \left(\Gamma_{43} + \frac{|\Omega_{\mathrm{c}}|^2 \Gamma_{32}}{\Gamma_{32}^2 + 4\delta_{\mathrm{sc}}^2}\right)}{\left(\Gamma_{43} + \frac{|\Omega_{\mathrm{c}}|^2 \Gamma_{32}}{\Gamma_{32}^2 + 4\delta_{\mathrm{sc}}^2}\right)^2 + 4\left(\frac{|\Omega_{\mathrm{c}}|^2 \delta_{\mathrm{sc}}}{\Gamma_{32}^2 + 4\delta_{\mathrm{sc}}^2} - \delta_{\mathrm{s}}\right)^2}. \tag{6.3.10}$$

Equations (6.3.8) tell us that, for all probe-field detunings, almost all the atomic population is in state $|1\rangle$ with almost no population in state $|3\rangle$. This lack of population in $|3\rangle$ eliminates the effect of the nonlinear signal-probe interaction described by the second term of Eq. (6.3.1). As we require population in $|3\rangle$, we introduce an always-on incoherent pump at rate r_{p} to maintain population in $|3\rangle$.

The equations of motion of the density matrix elements with the incoherent pumping will change according to (2.5.12) and (2.5.13) . Then the atomic-population equations in the presence of the incoherent pumping are modified as

$$
\begin{aligned}
\varrho_{11} &= \frac{ZY\left(\gamma_{41}+r_{\mathrm{p}}\right)}{Z\left(-r_{\mathrm{p}}\gamma_{42}+4r_{\mathrm{p}}Y+\gamma_{41}Y\right)+r_{\mathrm{p}}\gamma_{43}\left(Y-X\right)},\\
\varrho_{22} &= \frac{r_{\mathrm{p}}\left(Z\left(Y-\gamma_{42}\right)-\gamma_{43}X\right)}{Z\left(-r_{\mathrm{p}}\gamma_{42}+4r_{\mathrm{p}}Y+\gamma_{41}Y\right)+r_{\mathrm{p}}\gamma_{43}\left(Y-X\right)},\\
\varrho_{33} &= \frac{r_{\mathrm{p}}Y\left(Z+\gamma_{43}\right)}{Z\left(-r_{\mathrm{p}}\gamma_{42}+4r_{\mathrm{p}}Y+\gamma_{41}Y\right)+r_{\mathrm{p}}\gamma_{43}\left(Y-X\right)},\\
\varrho_{44} &= \frac{r_{\mathrm{p}}ZY}{Z\left(-r_{\mathrm{p}}\gamma_{42}+4rY+\gamma_{41}Y\right)+r_{\mathrm{p}}\gamma_{43}\left(Y-X\right)},
\end{aligned}
\tag{6.3.11}
$$

with X, Y, and Z defined in Eq. (6.3.9) with replacement (2.5.12) and (2.5.13).

The modified atomic population in the presence of incoherent pumping for the case $\Omega_{\mathrm{s}} \gg \Omega_{\mathrm{p}}$ is shown in Fig. 6.5(a). The existence of incoherent pumping makes the population constant for all probe-field detunings. The value of the pumping rate r_{p} controls the population in each state. We use $r_{\mathrm{p}} = 1$ MHz to populate states $|1\rangle$ and $|3\rangle$ with $\varrho_{11} = \varrho_{33} = 0.44$. At high temperature, when the Doppler effect plays a critical role in repopulating the states, $|3\rangle$ can be repopulated to a value of one-half by using pump rate r_{p} as low as 10 kHz as shown in Fig. 6.5(b).

In this section, we have presented an incoherent pumping procedure that maintains equal population between $|1\rangle$ and $|3\rangle$ for a weak probe field. In the upcoming Sec. 6.3.3, we do not treat pumping; instead, we assume equal population between $|1\rangle$ and $|3\rangle$. As we use an incoherent pump, we should be concerned that coherence is affected, but we see here that dephasing due to incoherent pumping is negligible for reasonable parameters. Specifically, the extra dephasing of system from incoherent pumping is of the same order as $\gamma_{\phi 3}$ for Doppler-broadened media [61].

6.3.2 Stationary-Atom Linewidth and Group Velocity

The linewidth of each transparency window $\imath \in \{1, 2\}$ is given by the half-width at half-maximum (HWHM) $\daleth_\imath$. In this section, we show the calculations leading to closed-form expressions for the heights, or maxima, of the two absorption windows and also the nadirs, or minima, of these absorption windows, for the case where condition (6.3.2) is valid. These expressions are derived first for the stationary atom and then generalized to the Doppler-broadened case.

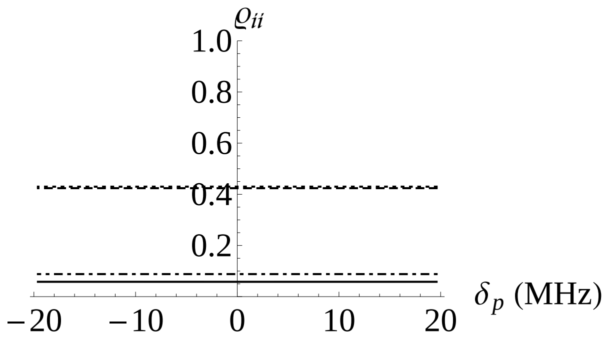

(a)

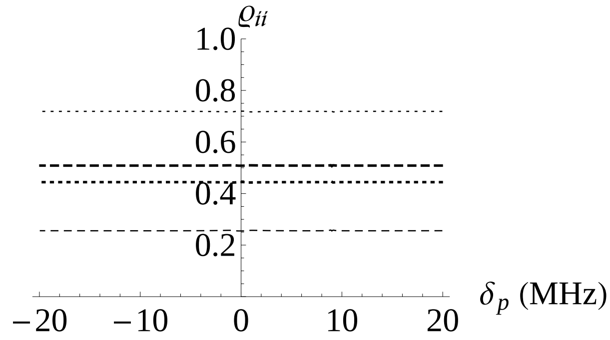

(b)

Figure 6.5: Steady-state populations ϱ_{11} (dotted line), ϱ_{22} (dotted-dashed line), ϱ_{33} (dashed line), and ϱ_{44} (solid line) versus probe-field detuning $\delta_{\rm p}$ for $\Omega_{\rm s} \gg \Omega_{\rm p}$ in the presence of incoherent pumping with constant rate $r_{\rm p}$ evaluated numerically by solving the master equation. The solutions correspond to (a) low temperature for $r_{\rm p} = 1$ MHz and (b) for two temperatures 100 K and 400 K (bold line) with $r_{\rm p} = 0.01$ MHz. Other parameters are $\Omega_{\rm s} = 0.3\gamma_4$, $\Omega_{\rm p} = 0.01\gamma_4$, $\gamma_{41} = \gamma_{42} = 6$ MHz, $\gamma_{43} = 12$ MHz $\gamma_3 = 10$ kHz, $\gamma_2 = 40$ kHz, $\Omega_{\rm c} = \gamma_4$, $\delta_{\rm s} = 13.5$ MHz, $\delta_{\rm c} = 0$, and $\mathcal{N} = 1 \times 10^{14}$ cm^{-3}. Using ^{87}Rb constants: $|\boldsymbol{d}_{14}| = |\boldsymbol{d}_{34}| = 1.269 \times 10^{-29}$ C·m, and $\omega_0 = 2\pi \cdot 377.11$ THz.

Identifying the maximum height, $h_{\max_\imath}$ and minimum height, $h_{\min_\imath}$ of the $\imath^{\rm th}$ window is subtle because the two Lorentzian transparency windows are cut asymmetrically into the overall Lorentzian absorption peak corresponding to zero-coupling field. First, we consider the $i = 1$ case.

The maximum is calculated by setting $\Omega_{\rm c} = 0 = \Omega_{\rm s}$ and evaluating Eq. (6.3.4) at $\delta_{\rm p} = \delta_{\rm c} = 0$

$$h_{\max_1} = \eta_{\rm p} \frac{\varrho_{11} - \varrho_{44}}{\gamma_4}. \tag{6.3.12}$$

The minimum $h_{\min_1}$ is determined following the same procedure discussed in Sec. 3.4.1, by setting $\Omega_\mathrm{s} = 0$ but $\Omega_\mathrm{c} \neq 0$ and evaluating Eq. (6.3.4) at $\delta_\mathrm{p} = \delta_\mathrm{c} = 0$. We obtain

$$h_{\mathrm{min}_1} = \frac{\eta_\mathrm{p} \left(\varrho_{11} - \varrho_{44}\right) \gamma_2}{\gamma_4 \gamma_2 + \left|\Omega_\mathrm{c}\right|^2} \xrightarrow{\gamma_2 \to 0} 0, \tag{6.3.13}$$

with zero absorption attained for $\gamma_2 = 0$. If $\gamma_2 \neq 0$ but condition (3.4.47) holds,

$$h_{\mathrm{min}_1} \to \frac{\eta_\mathrm{p} \left(\varrho_{11} - \varrho_{44}\right) \gamma_2}{\left|\Omega_\mathrm{c}\right|^2}, \tag{6.3.14}$$

and minimum absorption is reached.

The maximum and minimum of the first transparency window are used to calculate the half-maximum

$$\varkappa_1 := \frac{h_{\mathrm{max}_1} + h_{\mathrm{min}_1}}{2} = \frac{\eta_\mathrm{p} \left(\varrho_{11} - \varrho_{44}\right) \left(2\gamma_4\gamma_2 + \left|\Omega_\mathrm{c}\right|^2\right)}{2\gamma_4 \left(\gamma_4\gamma_2 + \left|\Omega_\mathrm{c}\right|^2\right)}. \tag{6.3.15}$$

Applying condition (2.5.1) yields

$$\varkappa_1 = \frac{\eta_\mathrm{p} \left(\varrho_{11} - \varrho_{44}\right)}{2\gamma_4}. \tag{6.3.16}$$

For the $i = 2$ case, we have a Lorentzian transparency window cut into the absorption curve corresponding to the two conditions $\Omega_\mathrm{s} = 0$ and $\Omega_\mathrm{c} \neq 0$ holding. For our case of DDEIT, we set $\Omega_\mathrm{c} = 2\delta_\mathrm{s}$, which establishes the second transparency window centered at $\delta_\mathrm{p} = \delta_\mathrm{s}$, which is the point that the maximum peak height h_{max_2} occurs. Therefore, h_{max_2} can be determined by calculating the $\Omega_\mathrm{s} = 0$ absorption curve value at $\delta_\mathrm{p} = \delta_\mathrm{s}$:

$$h_{\mathrm{max}_2} = \eta_\mathrm{p} \frac{\left(\varrho_{11} - \varrho_{44}\right) \left(\gamma_4 + \frac{\Omega_\mathrm{c}^2 \gamma_2}{4\delta_\mathrm{sc}^2}\right)}{\gamma_4^2 + 4\left(\frac{\Omega_\mathrm{c}^2}{4\delta_\mathrm{sc}^2} - \delta_\mathrm{s}\right)^2}. \tag{6.3.17}$$

Under the approximation that

$$\gamma_4 \gg \frac{\left|\Omega_\mathrm{c}\right|^2}{2\delta_\mathrm{sc}^2} \frac{\gamma_2}{2}, \tag{6.3.18}$$

we obtain

$$h_{\mathrm{max}_2} = \eta_\mathrm{p} \frac{\varrho_{11} - \varrho_{44}}{\gamma_4}. \tag{6.3.19}$$

Thus, $h_{\mathrm{max}_1} \approx h_{\mathrm{max}_2}$.

In order to calculate the minimum of the second transparency window, we set $\Omega_{\mathrm{s}} \neq 0$ and $\Omega_{\mathrm{c}} \neq 0$ and evaluate $\mathrm{Im}\chi_{\mathrm{p}}^{(1)}$ from Eq. (6.3.4) at $\delta_{\mathrm{p}} = \delta_{\mathrm{s}}$ to obtain the minimum

$$h_{\min_2} = \eta_{\mathrm{p}} \left(\frac{(\varrho_{11} - \varrho_{44})\,\gamma_3}{\gamma_4\gamma_3 + |\Omega_{\mathrm{s}}|^2} + \frac{(\varrho_{44} - \varrho_{33})\,|\Omega_{\mathrm{s}}|^2}{\Gamma_{43}\left(\gamma_4\gamma_3 + |\Omega_{\mathrm{s}}|^2\right)} \right). \tag{6.3.20}$$

The first term in the right-hand side of Eq. (6.3.20) represents the absorption minimum, whereas the second term represents the maximum gain (negative absorption).

If we wish to reduce absorption, decay from level $|3\rangle$ must be minimized, i.e., $\gamma_3 \to 0$. For the case $\gamma_3 \neq 0$, condition (2.5.2) must be satisfied to minimize the absorption. As $\Gamma_{43} \approx \gamma_4$, Eq. (6.3.20) is simplified to

$$h_{\min_2} = \eta_{\mathrm{p}} \left(\frac{(\varrho_{11} - \varrho_{44})\,\gamma_3}{|\Omega_{\mathrm{s}}|^2} + \frac{\varrho_{44} - \varrho_{33}}{\gamma_4} \right). \tag{6.3.21}$$

As $\varrho_{44} = 0$ is assumed, gain exists only when

$$\frac{|\varrho_{44} - \varrho_{33}|}{\gamma_4} \gg \frac{|\varrho_{11} - \varrho_{44}|\,\gamma_3}{|\Omega_{\mathrm{s}}|^2}, \tag{6.3.22}$$

or, equivalently, if

$$\frac{|\varrho_{44} - \varrho_{33}|}{|\varrho_{11} - \varrho_{44}|} \gg \frac{\gamma_3\gamma_4}{|\Omega_{\mathrm{s}}|^2}. \tag{6.3.23}$$

In our case

$$\frac{|\varrho_{44} - \varrho_{33}|}{|\varrho_{11} - \varrho_{44}|} \approx 1. \tag{6.3.24}$$

Therefore, we also require condition (2.5.2) in order to achieve gain. The half-maximum is then

$$\varkappa_2 = \eta_{\mathrm{p}} \left[\frac{(\varrho_{11} - \varrho_{44})\left(2\gamma_4\gamma_3 + |\Omega_{\mathrm{s}}|^2\right)}{\gamma_4\left(\gamma_4\gamma_3 + |\Omega_{\mathrm{s}}|^2\right)} + \frac{(\varrho_{44} - \varrho_{33})\,|\Omega_{\mathrm{s}}|^2}{\Gamma_{43}\left(\gamma_4\gamma_3 + |\Omega_{\mathrm{s}}|^2\right)} \right]. \tag{6.3.25}$$

For condition (3.4.55) and $\gamma_4 \gg \gamma_3$,

$$\varkappa_2 = \eta_{\mathrm{p}} \frac{(\varrho_{11} - \varrho_{33})}{\gamma_4}. \tag{6.3.26}$$

For $\varrho_{11} \approx \varrho_{33}$, $\varkappa_2$ is located at zero absorption.

By solving

$$\mathrm{Im}[\chi_{\mathrm{p}}^{(1)}] = \varkappa_{\imath}, \tag{6.3.27}$$

for δ_{pc} and δ_{ps} separately, $\daleth_1$ and $\daleth_2$ are determined respectively with $\delta_{\mathrm{pc}} = \daleth_1$ and $\delta_{\mathrm{ps}} = \daleth_2$.

$$\daleth_1 = \frac{|\Omega_{\mathrm{c}}|^2}{\gamma_4 + \sqrt{4\,|\Omega_{\mathrm{c}}|^2 + \gamma_4^2}},\ \daleth_2 = \frac{|\Omega_{\mathrm{s}}|^2}{2\sqrt{\gamma_4^2 + |\Omega_{\mathrm{s}}|^2}}, \tag{6.3.28}$$

respectively. Probe dispersion is shown in Fig. 6.4(b). For detuning δ_{p} chosen at the center of each window, dispersion is zero or close to zero.

For each of windows 1 and 2, group velocity is calculated using (3.4.67)

$$v_{\mathrm{g}} \approx \frac{2c}{n_{\mathrm{g}}},\ n_{\mathrm{g}} = (\omega_{41} - \delta_{\mathrm{p}}) \left.\frac{\partial \mathrm{Re}[\chi_{\mathrm{p}}^{(1)}]}{\partial \delta_{\mathrm{p}}}\right|_{\delta_{\mathrm{cen}}}, \tag{6.3.29}$$

for n_{g} the group index, δ_{cen} the detuning at the center of each window (1 and 2) and ω_{41} the transition frequency between levels $|1\rangle$ and $|4\rangle$. Detuning δ_{cen} equals δ_{c} at the first window and equals δ_{s} at the second window. The partial derivative of the dispersion in the denominator is determined by

$$\left.\frac{\partial \mathrm{Re}[\chi_{\mathrm{p}}^{(1)}]}{\partial \delta_{\mathrm{p}}}\right|_{\delta_{\mathrm{cen}}} = \lim_{\delta_{\mathrm{p}} \to \delta_{\mathrm{cen}}} \frac{\mathrm{Re}[\chi_{\mathrm{p}}^{(1)}(\delta_{\mathrm{p}})] - \mathrm{Re}[\chi_{\mathrm{p}}^{(1)}(\delta_{\mathrm{p}} = \delta_{\mathrm{cen}})]}{\delta_{\mathrm{p}} - \delta_{\mathrm{cen}}}. \tag{6.3.30}$$

Therefore, the partial derivative of the dispersion

$$\left.\frac{\partial \mathrm{Re}[\chi_{\mathrm{p}}^{(1)}]}{\partial \delta_{\mathrm{p}}}\right|_{\delta_{\mathrm{c}}} = \frac{\eta_{\mathrm{p}}\,|\Omega_{\mathrm{c}}|^2}{\left(\gamma_2\gamma_4 + |\Omega_{\mathrm{c}}|^2\right)^2}, \tag{6.3.31}$$

at the center of the first window and

$$\left.\frac{\partial \mathrm{Re}[\chi_{\mathrm{p}}^{(1)}]}{\partial \delta_{\mathrm{p}}}\right|_{\delta_{\mathrm{s}}} = \frac{\eta_{\mathrm{p}}\,|\Omega_{\mathrm{s}}|^2}{(\gamma_3\gamma_4 + |\Omega_{\mathrm{s}}|^2)^2} \tag{6.3.32}$$

at the center of the second window. Equations (6.3.31) and (6.3.32) yield the slope of the tangent line to points $\delta_{\mathrm{p}} = \delta_{\mathrm{cen}}$ as shown in Fig. 6.4(b).

In Fig. 6.4(b), the group velocity is shown to be approximately constant in each of the two EIT windows, which can be seen by the straight-line tangents. The group velocity scales inversely with slope so the ratio of group velocities for each EIT window is the inverse of the ratio of the slopes for each window. From Eqs. (6.3.31) and (6.3.32) and from Fig. 6.4(b), the group velocity at the first window evidently exceeds the group velocity at the second window for the given parameters.

Under conditions (3.4.47) and (3.4.55), the group velocity reduces to

$$v_{g_1} = \frac{2c}{\eta_p}\frac{|\Omega_c|^2}{\omega_{14}}, \tag{6.3.33}$$

at the first window and to

$$v_{g_2} = \frac{2c}{\eta_p}\frac{|\Omega_s|^2}{\omega_{34}} \tag{6.3.34}$$

at the second window. Hence, for stationary atoms, the group velocities in both windows are linearly proportional to the intensities of the respective driving fields.

6.3.3 Lorentzian Line-Shape Approximation

In this section, we determine an analytical approximation to the optical susceptibility for a Doppler-broadened system. Our approximation uses a Lorentzian fit to the Maxwell-Boltzmann velocity distribution over a narrow range of velocity. We use this approximation to show that the first probe-field transparency window is independent of the signal-field Rabi frequency and the second transparency window is nonlinear in the signal-field Rabi frequency. Furthermore, we derive the connection between the transparency window and the Doppler-broadening width, which is directly dependent on the temperature.

The Lorentzian line-shape function [64]

$$L\left(\frac{v\omega_0}{c}\right) = \frac{1}{\sqrt{\pi}}\frac{W_L}{W_L^2 + \left(\frac{v\omega_0}{c}\right)^2}, \tag{6.3.35}$$

is a function of the atomic velocity with W_L is the HWHM of the Lorentzian profile. To see that the Lorentzian (6.3.35) approximates the Gaussian (6.2.1) well over a narrow domain, we first write both functions as Maclaurin series. The Gaussian (6.2.1) is approximated by

$$f\left(\frac{v\omega_0}{c}\right) = \frac{\sqrt{\ln 2}}{\sqrt{\pi}W_G} - \frac{\omega_0^2(\sqrt{\ln 2})^3}{c^2\sqrt{\pi}W_G^3}v^2 + \frac{\omega_0^4(\sqrt{\ln 2})^5}{c^4\sqrt{\pi}W_G^4}v^5 - \cdots, \tag{6.3.36}$$

with

$$W_{\mathrm{G}} := \frac{\omega_0}{c}\sqrt{\frac{2kT\ln 2}{m}}, \tag{6.3.37}$$

the HWHM of the Gaussian profile and

$$L\left(\frac{v\omega_0}{c}\right) = \frac{1}{\sqrt{\pi}W_{\mathrm{L}}} - \frac{\omega_0^2}{c^2\sqrt{\pi}W_{\mathrm{L}}^3}v^2 + \frac{\omega_0^4}{c^4\sqrt{\pi}W_{\mathrm{L}}^5}v^5 - \cdots, \tag{6.3.38}$$

for

$$-1 < \frac{\omega_0 v}{cW_{\mathrm{L}}} < 1. \tag{6.3.39}$$

The two expansions (6.3.36) and (6.3.38) are approximately equal under the conditions that

$$W_{\mathrm{L}} = \frac{1}{\sqrt{\ln 2}}W_{\mathrm{G}}, \tag{6.3.40}$$

for

$$-1 \ll \frac{\omega_0 v}{cW_{\mathrm{G}}}\sqrt{\ln 2} \ll 1. \tag{6.3.41}$$

Combining Eqs. (6.3.37) and (6.3.40) yields the connection between the Lorentzian linewidth and the temperature. These conditions are satisfied near the center of both function profiles as shown in Fig. 6.6, where the higher-order terms of Eqs. (6.3.36) and (6.3.38) have insignificant influence.

Integration of Eq. (6.2.2) using $L(v)$ instead of $f(v)$ has two terms evaluated with the contour integral using the residue theorem. The final optical susceptibility, including the Doppler-broadening effect, is

$$\bar{\chi}_{\mathrm{p}}(\delta_{\mathrm{p}}) = \mathscr{I}_1(\delta_{\mathrm{p}}) + \mathscr{I}_2(\delta_{\mathrm{p}}), \tag{6.3.42}$$

with δ_{p} the detuning (2.2.20). The terms on the right-hand side of Eq. (6.3.42) are

$$\mathscr{I}_1 = \frac{\mathrm{i}\eta_{\mathrm{p}}}{2}\frac{\sqrt{\pi}}{B_1 + 2\mathrm{i}B_2 + W_{\mathrm{L}}}, \tag{6.3.43}$$

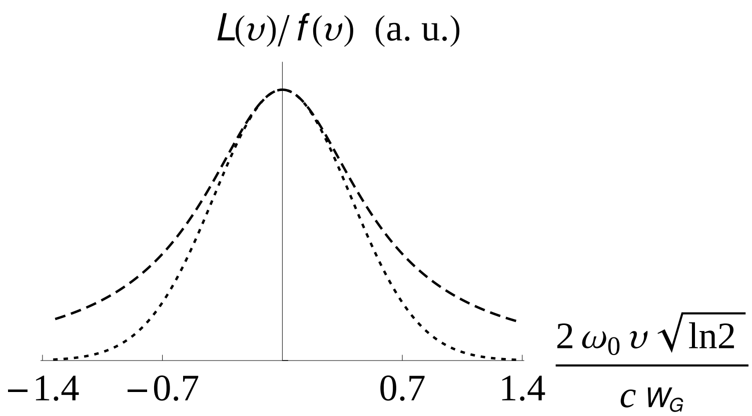

Figure 6.6: Plot of Lorentzian function (dashed line) and Gaussian function (dotted line) versus normalized atomic velocity.

and

$$
\begin{aligned}
\mathscr{I}_2 = &- \frac{\mathrm{i}\eta_{\mathrm{p}}\sqrt{\pi}\,(C_1 + \mathrm{i}C_2)}{2\,(B_1 + W_L + 2\mathrm{i}B_2)\,(A_1 - W_L - 2\mathrm{i}A_2)} \\
&- \frac{\mathrm{i}\eta_{\mathrm{p}}W_{\mathrm{L}}\sqrt{\pi}\,(C_1 + \mathrm{i}C_2)}{(A_1 + B_1 + 2\mathrm{i}(B_2 - A_2))\,(W_L^2 + 4A_2^2 - A_1^2 + 4\mathrm{i}A_1A_2)}.
\end{aligned}
\tag{6.3.44}
$$

The HWHM $\daleth_1$ of the first transparency window, and the group velocity for this window, depend on $\mathscr{I}_1(\delta_{\mathrm{p}})$ but not on $\mathscr{I}_2(\delta_{\mathrm{p}})$ over the domain of δ_{p} pertaining to the first window. In the case of the second transparency window for the probe field, both $\mathscr{I}_1(\delta_{\mathrm{p}})$ and $\mathscr{I}_2(\delta_{\mathrm{p}})$ are non negligible for calculating the HWHM $\daleth_2$ and group velocity.

In Figure 6.7, we plot the imaginary and real parts of the susceptibility $\chi_{\mathrm{p}}^{(1)}$ as a function of the probe-field detuning δ_{p} at various temperature values based on the average susceptibility (6.2.2) for the Maxwell-Boltzmann distribution function $f(v)$ and for the approximation using the Lorentzian function $L(v)$. At low temperatures, for which the broadening is low, there is a discrepancy between the two functions.

At higher temperatures, for which

$$
W_{\mathrm{L}}^2 \gg \gamma_4^2, \tag{6.3.45}
$$

the numerical data agree with the analytical data near the center as seen by comparing the two plots. The plots differ at the tail, which describes far-off-resonant atoms whose contribution is negligible. This numerical result validates the Lorentzian approximation for condition (6.3.45) near the center, which leads to a rather simple form of the inhomogeneously broadened susceptibility.

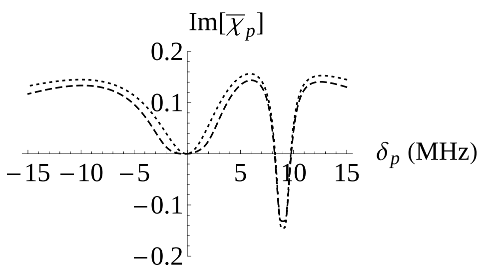

(a)

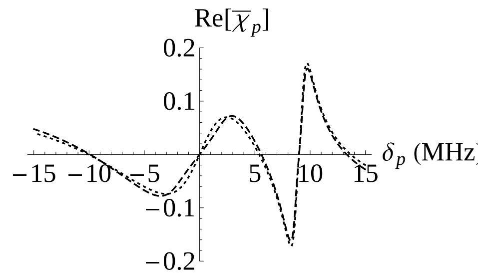

(b)

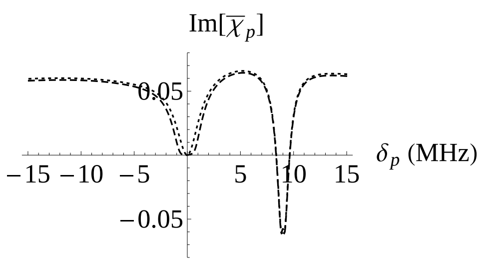

(c)

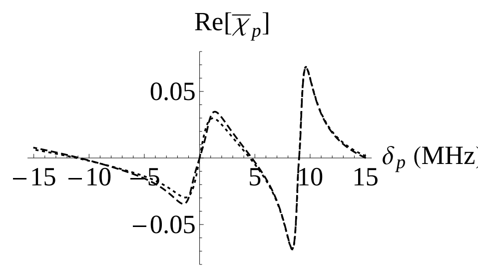

(d)

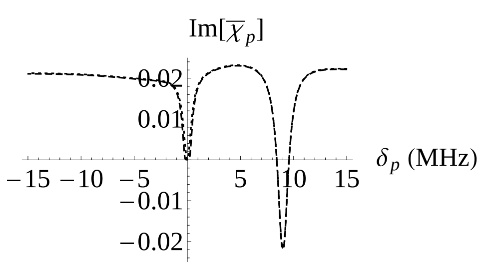

(e)

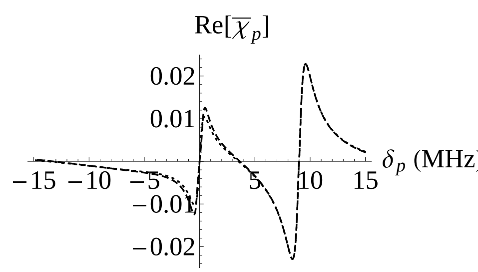

(f)

Figure 6.7: Plots of $\mathrm{Im}[\chi_{\mathrm{p}}^{(1)}]$ and $\mathrm{Re}[\chi_{\mathrm{p}}^{(1)}]$ versus probe-field detuning δ_{p} at different temperatures for $\gamma_4 = 18$ MHz, $\gamma_3 = 10$ kHz, $\gamma_2 = 40$ kHz, $\Omega_{\mathrm{c}} = \gamma_4$, $\Omega_{\mathrm{s}} = 0.35\gamma_4$, $\delta_{\mathrm{s}} = 9$ MHz, $\delta_{\mathrm{c}} = 0$, $\mathcal{N} = 1 \times 10^{14}$ cm^{-3}, and using ^{87}Rb constants: $|\boldsymbol{d}_{14}| = |\boldsymbol{d}_{34}| = 1.269 \times 10^{-29}$ C·m, and $\omega_0 = 2\pi \cdot 377.11$ THz. (a), (c) and (e) are $\mathrm{Im}[\bar{\chi}_{\mathrm{p}}]$ and (b), (d), and (f) are $\mathrm{Re}[\bar{\chi}_{\mathrm{p}}]$. We set T= (1, 10, 100) K for (a),(b), (c),(d) and (e),(f) respectively, which is equivalent to $W_{\mathrm{L}} = (34.8, 110, 348)$ MHz, respectively. The dotted line corresponds to the analytical solution using the Lorentzian line-shape function, whereas the dashed line is the numerical solution using the Maxwell-Boltzmann distribution function.

Analyzing the numerical result reveals that condition (3.4.47) and condition

$$|\Omega_{\rm c}|^2 > \gamma_2 W_{\rm L}, \tag{6.3.46}$$

are required to observe the first transparency window. These conditions (3.4.47) and (6.3.46) eliminate the homogeneous broadening and reduce the effect of inhomogeneous broadening, respectively. At a temperature for which the Doppler broadening satisfies condition (6.3.45), and Eqs. (6.3.42-6.3.44) are a valid approximation, satisfying condition (6.3.46) certainly implies satisfying condition (3.4.47). As shown in Fig. 6.7, the width $\bar{\daleth}_2$ of the second transparency window is not noticeably affected by varying the Doppler width $W_{\rm L}$. The reason for the robustness of $\bar{\daleth}_2$ is that the nonlinear interaction in $\mathscr{I}_2$, but not in $\mathscr{I}_1$, protects the second window from deleterious temperature effects. Therefore, the strong-signal-field condition is not required to overcome Doppler broadening damaging the second transparency window. In other words, condition

$$|\Omega_{\rm s}|^2 > \gamma_3 W_{\rm L}, \tag{6.3.47}$$

is no longer mandatory to observe the second window.

Condition (3.4.55) is still required to eliminate the homogeneous broadening for significant transparency at the second window. Furthermore, the relaxation of condition (6.3.47) leads to further reduction of group velocity in Doppler-broadened media, which was limited by the Doppler width appearing in the right-hand side of condition (6.3.47).

The two terms $\gamma_2 W_{\rm L}$ in Eq. (6.3.46) and $\gamma_3 W_{\rm L}$ in Eq. (6.3.47) quantify the inhomogeneous broadening of the two EIT windows. In other words the Doppler broadening alone is not the whole story; rather the products $\gamma_{2,3} W_{\rm L}$ incorporating the rates γ_2 and γ_3 are the key quantities. In Sec. 6.3.4 we derive the linewidth and the group velocity for which the requisite conditions (3.4.47) and (3.4.55) for eliminating homogeneous broadening, are always satisfied for both windows.

6.3.4 Widths of the Transparency Windows

This section shows first, the calculations leading to closed-form expressions for absorption maxima, minima, and half maxima of the two absorption windows for Doppler-broadened case. Then, discusses the dependence of the transparency-window linewidth on temperatures variation, based on the analytical solution of the optical susceptibility introduce by (6.3.42).

6.3.4.1 Absorption Maxima and Minima

In the case of Doppler-broadened susceptibility, the absorption profile near the center (corresponding to zero velocity) is quite flat. As the two windows occur near the center; the maxima for both windows are the same. The maximum value is calculated for $\Omega_c = \Omega_s = 0$ and for $\delta_p = \delta_c$:

$$h_{\mathrm{Dmax}_{1,2}} = \frac{\eta_p \sqrt{\pi}\left(\varrho_{11} - \varrho_{44}\right)}{\gamma_4 + W_L}. \tag{6.3.48}$$

The minimum value of the first window is calculated for $\Omega_s = 0$ and $\delta_p = \delta_c$:

$$h_{\mathrm{Dmin}_1} = \frac{\eta_p \sqrt{\pi}\left(\varrho_{11} - \varrho_{44}\right)\gamma_2}{\left|\Omega_c\right|^2 + \gamma_2\left(\gamma_4 + W_L\right)} \xrightarrow{\gamma_2 \to 0} 0, \tag{6.3.49}$$

which requires the condition $\left|\Omega_c\right|^2 \gg \gamma_2\left(\gamma_4 + W_L\right)$ to hold in order to reach minimum absorption. For $\gamma_2 \neq 0$, and for $W_L \gg \gamma_4$ this condition can be reduced to $\left|\Omega_c\right|^2 \gg \gamma_2 W_L$. If the intensity of the driving field eliminates the inhomogeneous broadening due to Doppler broadening, it certainly eliminates the homogeneous broadening as well. The half-maximum of the first window is then equal to

$$\bar{\varkappa}_1 = \frac{\eta_p \sqrt{\pi}\left(\varrho_{11} - \varrho_{44}\right)}{2} \frac{2\gamma_2 W_L + \left|\Omega_c\right|^2}{\gamma_2 W_L^2 + \left|\Omega_c\right|^2\left(\gamma_4 + W_L\right)}. \tag{6.3.50}$$

For $i = 2$, the minimum is calculated for $\Omega_c = 0$ and $\delta_p = \delta_s$ with the result

$$h_{\mathrm{Dmin}_2} = \eta_p \sqrt{\pi}\left[\frac{\left(\varrho_{11} - \varrho_{44}\right)\gamma_3}{\gamma_3\left(\gamma_4 + W_L\right) + \left|\Omega_s\right|^2} - \frac{\left(\varrho_{44} - \varrho_{33}\right)\left|\Omega_s\right|^2}{\gamma_3 W_L^2 + \left(W_L - \gamma_4\right)\left|\Omega_s\right|^2} + \frac{2\left(\varrho_{44} - \varrho_{33}\right)\left|\Omega_s\right|^2}{W_L\left(2\gamma_3\gamma_4 + \left|\Omega_s\right|^2\right)}\right]. \tag{6.3.51}$$

The first term in the right-hand side of Eq. (6.3.51) represents the absorption minimum. This term tends to 0 if $\gamma_3 \to 0$.

For the case of nonzero dephasing or relaxation decay from state $|3\rangle$, condition $|\Omega_\mathrm{s}|^2 \gg \gamma_3(\gamma_4 + W_\mathrm{L})$ is required to minimize the absorption. For $W_\mathrm{L} \gg \gamma_4$, this condition can be reduced to (6.3.47). The last two terms of the right-hand side of Eq. (6.3.51) represent the maximum of the gain. After solving some algebraic expressions, Eq. (6.3.51) becomes

$$\begin{aligned} h_{\mathrm{Dmin}_2} =& \eta_\mathrm{p}\sqrt{\pi}\left[\frac{(\varrho_{11} - \varrho_{44})\,\gamma_3}{\gamma_3(\gamma_4 + W_\mathrm{L}) + |\Omega_\mathrm{s}|^2} - \frac{(\varrho_{44} - \varrho_{33})\,|\Omega_\mathrm{s}|^2}{W_\mathrm{L}(2\gamma_3\gamma_4 + |\Omega_\mathrm{s}|^2)}\right. \\ &\left.\times\frac{2\gamma_3 W_\mathrm{L}(\gamma_4 - W_\mathrm{L}) + |\Omega_\mathrm{s}|^2(2\gamma_4 - W_\mathrm{L})}{\gamma_3 W_\mathrm{L}^2 - |\Omega_\mathrm{s}|^2(\gamma_4 - W_\mathrm{L})}\right]. \end{aligned} \tag{6.3.52}$$

Now, we want to examine whether condition (6.3.47), for $\gamma_3 \neq 0$, is required to observe gain of the Doppler broadening susceptibility. If not, then the existence of gain suppresses absorption, and the second transparency window is observed even if condition (6.3.47) fails. We evaluate Eq. (6.3.52) for the condition $W_\mathrm{L} \gg \gamma_4$, in order to simplify the calculation, and evaluate for condition (3.4.55), which is necessary to minimize the absorption as shown earlier

$$h_{\mathrm{Dmin}_2} = \eta_\mathrm{p}\sqrt{\pi}\left[\frac{(\varrho_{11} - \varrho_{44})\,\gamma_3}{\gamma_3 W_\mathrm{L} + |\Omega_\mathrm{s}|^2} - \frac{(\varrho_{44} - \varrho_{33})}{W_\mathrm{L}}\left(1 + \frac{\gamma_3 W_\mathrm{L}}{\gamma_3 W_\mathrm{L} + |\Omega_\mathrm{s}|^2}\right)\right]. \tag{6.3.53}$$

In order for gain to exist,

$$\frac{|\varrho_{44} - \varrho_{33}|}{W_\mathrm{L}}\left(1 + \frac{\gamma_3 W_\mathrm{L}}{\gamma_3 W_\mathrm{L} + |\Omega_\mathrm{s}|^2}\right) \gg \frac{|\varrho_{11} - \varrho_{44}|\,\gamma_3}{\gamma_3 W_\mathrm{L} + |\Omega_\mathrm{s}|^2}, \tag{6.3.54}$$

which can be simplified by rearranging terms and substituting the quantity

$$\frac{|\varrho_{44} - \varrho_{33}|}{|\varrho_{11} - \varrho_{44}|} \approx 1 \tag{6.3.55}$$

to yield

$$\frac{|\Omega_\mathrm{s}|^2 + W_\mathrm{L}}{\gamma_3 W_\mathrm{L}} \gg 0. \tag{6.3.56}$$

Condition (6.3.56) is always valid even if condition (6.3.47) is not satisfied. Note that the derivation of inequality (6.3.56) is based on the validity of condition (3.4.55) for homogeneous broadening. Therefore, condition (3.4.55) is required for the gain to exist in our system, whereas condition (6.3.47) is not.

The half-maximum for the second EIT window, without making any approximation, is

$$\begin{aligned}\bar{\varkappa}_2 = \frac{\eta_\mathrm{p}\sqrt{\pi}}{2} \Bigg[&\frac{(\varrho_{11}-\varrho_{44})\left(2\gamma_3\left(\gamma_4+W_\mathrm{L}\right)+\left|\Omega_\mathrm{s}\right|^2\right)}{\left(\gamma_3\left(\gamma_4+W_\mathrm{L}\right)+\left|\Omega_\mathrm{s}\right|^2\right)\left(\gamma_4+W_\mathrm{L}\right)} \\ &+ \frac{(\varrho_{44}-\varrho_{33})\left|\Omega_\mathrm{s}\right|^2\left[2\gamma_3 W_\mathrm{L}(\gamma_4-W_\mathrm{L})+\left|\Omega_\mathrm{s}\right|^2\left(2\gamma_4-W_\mathrm{L}\right)\right]}{-W_\mathrm{L}(2\gamma_3\gamma_4+\left|\Omega_\mathrm{s}\right|^2)\left[\gamma_3 W_\mathrm{L}^2+\left|\Omega_\mathrm{s}\right|^2\left(\gamma_4-W_\mathrm{L}\right)\right]}\Bigg]. \end{aligned} \tag{6.3.57}$$

Applying condition (3.4.55) simplifies this expression to

$$\bar{\varkappa}_2 = \frac{\eta_\mathrm{p}\sqrt{\pi}}{2}\left[\frac{(\varrho_{11}-\varrho_{44})\left(2\gamma_3 W_\mathrm{L}+\left|\Omega_\mathrm{s}\right|^2\right)}{\left(\gamma_3 W_\mathrm{L}+\left|\Omega_\mathrm{s}\right|^2\right)\left(\gamma_4+W_\mathrm{L}\right)} + \frac{(\varrho_{44}-\varrho_{33})\left[2\gamma_3 W_\mathrm{L}(\gamma_4-W_\mathrm{L})+\left|\Omega_\mathrm{s}\right|^2\left(2\gamma_4-W_\mathrm{L}\right)\right]}{W_\mathrm{L}\left[-\gamma_3 W_\mathrm{L}^2+\left|\Omega_\mathrm{s}\right|^2\left(\gamma_4-W_\mathrm{L}\right)\right]}\right], \tag{6.3.58}$$

For the condition that $W_\mathrm{L} \gg \gamma_4$, Eq. (6.3.58) reduces to

$$\bar{\varkappa}_2 = \frac{\eta_\mathrm{p}\sqrt{\pi}}{2W_\mathrm{L}}\left(\frac{2\gamma_3 W_\mathrm{L}+\left|\Omega_\mathrm{s}\right|^2}{\gamma_3 W_\mathrm{L}+\left|\Omega_\mathrm{s}\right|^2}\right)\left(\varrho_{11}-\varrho_{33}\right). \tag{6.3.59}$$

Thus, the half-maximum of the second EIT window for high Doppler broadening depends on the population difference between states $|1\rangle$ and $|3\rangle$. For equal population, the half maximum is always located at zero where absorption vanishes.

The HWHM of the first and second windows are determined By solving

$$\mathrm{Im}[\bar{\chi}_\mathrm{p}] = \bar{\varkappa}_\imath, \tag{6.3.60}$$

for δ_pc and δ_ps separately, $\bar{\daleth}_1$ and $\bar{\daleth}_2$ are determined respectively with $\delta_\mathrm{pc} = \bar{\daleth}_1$ and $\delta_\mathrm{ps} = \bar{\daleth}_2$.

6.3.4.2 Dependence of the EIT-Window Width on Doppler broadening

The EIT width in a three-level Doppler-broadened Λ system can be maintained by keeping the temperature of the system constant while changing the driving field [63–67]. Here we follow a different approach by studying the dependence of the linewidth on temperature while fixing the intensity of the driving fields. The intensities of the driving fields are chosen such to eliminate the homogeneous broadening.

The HWHM of the first window for the Doppler-broadened system is equal to

$$\bar{\daleth}_1 = \frac{|\Omega_{\mathrm{c}}|^2}{2}\left[\frac{\left(2\gamma_2 W_{\mathrm{L}} + |\Omega_{\mathrm{c}}|^2\right)}{2(\gamma_4 + W_{\mathrm{L}})^2\left(\gamma_2 W_{\mathrm{L}} + |\Omega_{\mathrm{c}}|^2\right) - W_{\mathrm{L}}\left(W_{\mathrm{L}} + 2\gamma_4\right)\left(2\gamma_2 W_{\mathrm{L}} + |\Omega_{\mathrm{c}}|^2\right)}\right]^{1/2}. \tag{6.3.61}$$

The width decreases nonlinearly as the Doppler width W_{L} increases as shown in Fig. 6.8. The condition $|\Omega_{\mathrm{c}}|^2 \gg \gamma_2 W_{\mathrm{L}}$ is valid for all W_{L} values in the figure. For a high-intensity coupling field (6.3.46), the width of the first window reduces to

$$\bar{\daleth}_1 = \frac{|\Omega_{\mathrm{c}}|^2}{2\sqrt{W_{\mathrm{L}}(2\gamma_4 + W_{\mathrm{L}})}}. \tag{6.3.62}$$

The formula for HWHM can be further simplified if $W_{\mathrm{L}} \gg \gamma_4$, thereby yielding

$$\bar{\daleth}_1 = \frac{|\Omega_{\mathrm{c}}|^2}{2W_{\mathrm{L}}}. \tag{6.3.63}$$

This result is consistent with the previous result for a three-level Λ atom, subject to a high-intensity driving field, for which the linewidth is proportional to the intensity of the driving field and inversely proportional to the Doppler width [65]. The HWHM of the second window of the Doppler-broadened system has a more complicated form than for the first window

$$\bar{\daleth}_2 = \frac{|\Omega_{\mathrm{s}}|^2}{2}\sqrt{\frac{(\gamma_4 + W_{\mathrm{L}}) + W_{\mathrm{L}}\left(\bar{\varkappa}_2\left(\gamma_4 + W_{\mathrm{L}}\right) - \frac{1}{2}\right)}{4W_{\mathrm{L}}\gamma_4^2\left(\frac{1}{2} - \bar{\varkappa}_2\left(\gamma_4 + W_{\mathrm{L}}\right)\right) + |\Omega_{\mathrm{s}}|^2\left(\gamma_4 + W_{\mathrm{L}}\right)}}, \tag{6.3.64}$$

where $\bar{\varkappa}_2$ is defined by (6.3.57) is the half-maximum value of $\mathrm{Im}\bar{\chi}_{\mathrm{p}}$ of the second window. The dependence of the HWHM of the second window on Doppler width is shown in Fig. 6.8. The width of the second window slightly decreases as the Doppler width increases.

For large Doppler-broadening, $W_L \gg \gamma_4$, $\bar{\varkappa}_2$ depends on the population difference $\varrho_{11} - \varrho_{33}$. As we set $\varrho_{11} \approx \varrho_{33} \approx 0.5$, $\bar{\varkappa}_2$ is always located at $\mathrm{Im}\bar{\chi}_{\mathrm{p}} \approx 0$, i. e., where absorption vanishes. Consequently, the width of the second window remains approximately constant with respect to Doppler width

$$\bar{\daleth}_2 = \frac{|\Omega_{\mathrm{s}}|^2}{2\sqrt{2}\sqrt{\gamma_4^2 + 2\,|\Omega_{\mathrm{s}}|^2}}. \tag{6.3.65}$$

This independence Doppler broadening width response of the second window is due to the gain described by $\mathrm{Im}\mathscr{I}_2$ of Eq. (6.3.42). Expression (6.3.65) reveals that further reduction of the group velocity can be achieved by reducing the intensity of the signal field without losing the transparency window due to Doppler broadening.

The two EIT windows have the same width at the intercept point between the two curves as shown in Fig. 6.8. For all values of Doppler width the signal field has lower intensity than the coupling field. The inset to Fig. 6.8 shows how the second window would behave as a function of $W_{\rm L}$ if the nonlinear contribution $\mathscr{I}_2$ were suppressed. This inset makes clear how important the optical nonlinearity is for achieving quite different temperature sensitivities of the two transparency windows for the probe field. Mathematically an effect of forcing $\mathscr{I}_2 \equiv 0$ is that the HWHM of the second transparency window is given by a modification of the HWHM of the first window (6.3.61) with the proviso that $\Omega_{\rm c}$ is replaced by $\Omega_{\rm s}$ and γ_2 is replaced by γ_3.

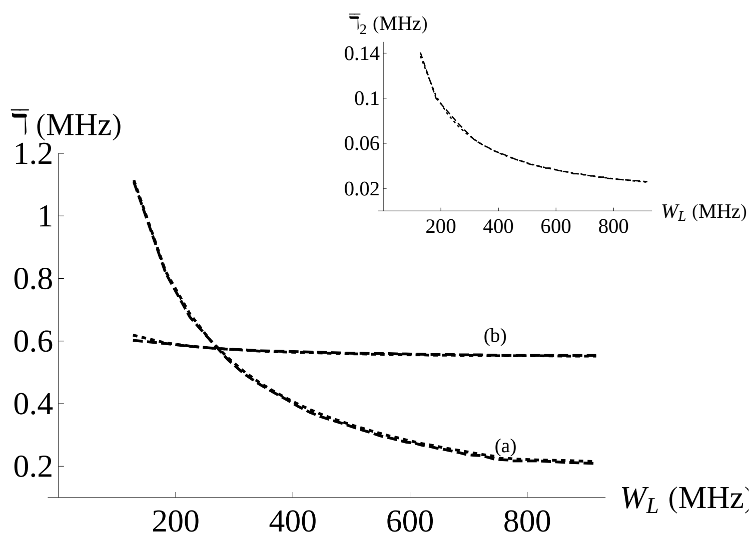

Figure 6.8: Numerical (dashed line) and analytical (dotted line) solutions of the HWHM ($\daleth$) for the (a) first and (b) second EIT transparency windows versus Doppler width $W_{\rm L}$ for $\gamma_4 = 18$ MHz, $\gamma_3 = 10$ kHz, $\gamma_2 = 40$ kHz, $\Omega_{\rm c} = \gamma_4$, $\Omega_{\rm s} = 0.35\gamma_4$, $\delta_{\rm s} = 9$ MHz, and $\delta_{\rm c} = 0$. Inset: Numerical (dashed line) and analytical (dotted line) HWHM of the second EIT window evaluated for the gain term eliminated.

For atoms copropagating with the probe field, the gain term suppresses the narrowing of the width results from Doppler broadening. Generalizing the choice of atomic propagation direction relative to the direction of the three driving fields would of course lead to different results [17]

In summary, Eq. (6.3.64) is the full expression of the HWHM of the second transparency window and accounts for the nonlinear interaction between the probe and the signal fields. Its behavior is depicted in Fig. 6.8 and shows the insensitivity of the second transparency window on temperature, which is represented by width $W_{\rm L}$. Contrariwise the first window is sensitive to $W_{\rm L}$.

6.3.5 Group Velocities at the Transparency Windows

From Sec. 6.3.3, we have approximate analytical expressions for susceptibilities at the two transparency windows. In this section, we determine the derivative of the susceptibility with respect to the detuning $\delta_{\rm p}$ and use these partial derivatives of dispersion (6.3.30) to calculate the group velocities for the probe field in each of the two transparency windows. The response of the partial derivative of dispersion with respect to Doppler-broadening system is shown in Fig. 6.9. In this figure, numerical calculations show constant group velocity at the first window and a sharply increased group velocity at the second window.

The analytical expression for the group velocity of the Doppler-broadened system is evaluated using Eq. (6.3.29) but with the Doppler-broadened susceptibility (6.3.42) replaced the free Doppler-broadened susceptibility $\chi_{\rm p}^{(1)}$ [20]. The partial derivative of $\mathrm{Re}[\bar{\chi}_{\rm p}]$ at the center of the first window is

$$\left.\frac{\partial \mathrm{Re}[\bar{\chi}_{\rm p}]}{\partial \delta_{\rm p}}\right|_{\delta_{\rm c}} = \frac{\eta_{\rm p}\sqrt{\pi}|\Omega_{\rm c}|^2}{\left(\gamma_2 W_{\rm L} + |\Omega_{\rm c}|^2\right)^2}, \tag{6.3.66}$$

and at the center of the second window is

$$\left.\frac{\partial \mathrm{Re}[\bar{\chi}_{\rm p}]}{\partial \delta_{\rm p}}\right|_{\delta_{\rm s}} = \frac{2\eta_{\rm p}\sqrt{\pi}\,|\Omega_{\rm s}|^2\,\gamma_4}{(\gamma_4 - W_{\rm L})\left(\gamma_3 W_{\rm L} + |\Omega_{\rm s}|^2\right)^2} + \frac{4\eta_{\rm p}\sqrt{\pi}\,|\Omega_{\rm s}|^2\,\gamma_4}{W_{\rm L}\,|\Omega_{\rm s}|^4}. \tag{6.3.67}$$

For the first transparency window and for a strong coupling field (6.3.46), the group velocity of the probe field at the center of the first window has the same group velocity as for the Doppler-free case (6.3.33). The negligibility of the Doppler broadening effect is due to the intensity of the coupling field being large, as can be explained from the analytical expression (6.3.66).

Figure 6.9 shows agreement between the analytical expression (6.3.66) and the full numerical result applicable for small W_{L}. This agreement diminishes slightly as W_{L} increases. Therefore, the Lorentzian function can be used to study the Doppler-broadened dispersion response of the Λ configuration comprising the three states $|1\rangle$, $|2\rangle$ and $|4\rangle$ provided that condition (6.3.46) is satisfied.

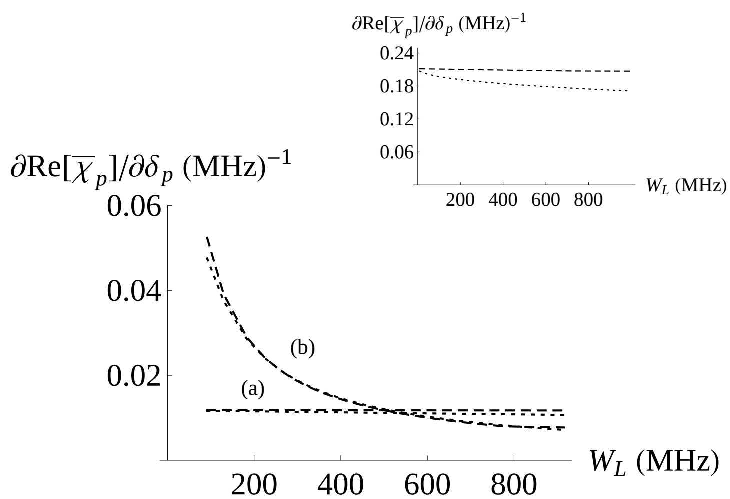

Figure 6.9: Plots of the numerical (dashed line) and analytical (dotted line) results for the partial derivative of dispersion with respect to Doppler width for (a) the first window and (b) the second window for $\gamma_4 = 18$ MHz, $\gamma_3 = 10$ kHz, $\gamma_2 = 40$ kHz, $\Omega_{\mathrm{c}} = 1.5\gamma_4$, $\Omega_{\mathrm{s}} = 0.5\gamma_4$, $\delta_{\mathrm{s}} = 13.5$ MHz, $\delta_{\mathrm{c}} = 0$, and $\mathcal{N} = 1 \times 10^{14}$ cm^{-3}. Using ^{87}Rb constants: $|\boldsymbol{d}_{14}| = |\boldsymbol{d}_{34}| = 1.269 \times 10^{-29}$ C·m, and $\omega_0 = 2\pi \cdot 377.11$ THz. Inset: numerical (dashed line) and analytical (dotted line) results for the partial derivative of dispersion vs Doppler width at the second window for $I_2 \equiv 0$.

Our analytical expression is reliable in practical parameter regimes. This agreement between the analytical Lorentzian approximation and the full numerical result under condition (6.3.46) is presented in Fig. 6.10 for varying coupling-field Rabi frequency.

We establish reliability of our approximation by comparing to an approximate Lorentzian expression derived for a Λ EIT system [20]. In our notation, their result for group index is

$$n_{\mathrm{g}} \propto \frac{\gamma_4 \left|\Omega_{\mathrm{c}}\right|^2}{\left[\gamma_2\left(\gamma_4 + W_{\mathrm{L}}\right) + \left|\Omega_{\mathrm{c}}\right|^2\right]^2}, \tag{6.3.68}$$

with the relation between group index and derivative of dispersion Eq. (6.3.66) given by Eq. (6.3.29). We can neglect γ_4 from (6.3.68) according to the approximation (3.4.47). Although result (6.3.68) is derived for a Λ system and our result Eq. (6.3.66) for a $\pitchfork$ system, both results pertain to an EIT window in a strong-coupling regime, and the two Lorentzian-based approximations agree.

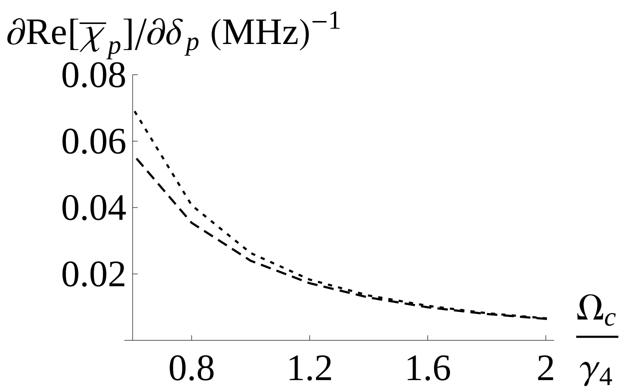

Figure 6.10: Plot of the numerical (dotted line) and analytical (dashed line) results for the partial derivative of dispersion versus coupling field at the first window for Doppler width $W_{\mathrm{L}} = 409$ MHz, $\gamma_4 = 18$ MHz, $\gamma_3 = 10$ kHz, $\gamma_2 = 40$ kHz, $\delta_{\mathrm{c}} = \delta_{\mathrm{p}} = 0$, and $\mathcal{N} = 1 \times 10^{14}$ cm^{-3}. Using ^{87}Rb constants: $|\boldsymbol{d}_{14}| = |\boldsymbol{d}_{34}| = 1.269 \times 10^{-29}$ C·m, and $\omega_0 = 2\pi \cdot 377.11$ THz.

At the second window, the analytical calculation fits the numerical solution for all chosen Doppler widths in the figure. Eliminating $\mathscr{I}_2$ (6.3.44) leads to an equation for group velocity at the center of the second window being similar equation to Eq. (6.3.66) but with Ω_{c} replaced by Ω_{s} and γ_2 replaced by γ_3. Similar dependence on Doppler width is shown in the inset of Fig. 6.9.

To achieve matched group velocity for the probe pulse propagating through the first and through the second window, a non-zero nonlinearity is required. The nonlinearity $\mathscr{I}_2$ is zero only if the condition $\varrho_{44} = \varrho_{33} = 0$ is met. This case for nonlinearity is depicted in the inset of Fig. 6.9. By fixing $\varrho_{44} = \varrho_{33} = 0$ we have the unwanted additional effect of violating condition (3.4.55) and thereby destroying the second window.

The intercept point between the two curves shown in Fig. 6.9 reveals the operating temperature for group velocity matching. At temperatures exceeding the matched group velocity case, the group velocity in the first window is lower than the group velocity for the second window and vice versa for temperatures lower than the condition for matched group velocity.

In summary, we demonstrate three important points in this subsection. First, the Lorentzian approximation is a useful and valid approximation for studying the dispersion response of the probe field as long as the conditions (6.3.46) and (6.3.47) for $\mathscr{I}_2 \equiv 0$ (6.3.44) hold. Second, the second term of Eq. (6.3.42) modifies the optical dispersion at the second window, which leads to a capacity for group velocity control through manipulating the temperature. Finally, due to nonlinearity, a signal-field intensity less than the coupling-field intensity does not necessarily imply that the probe field has lower group velocity at the second EIT window than at the first window.

6.4 Group-Velocity Reduction

In the previous sections 6.3.4 and 6.3.5, we have studied the behavior of the width and the group velocity for both EIT windows of the probe field in Doppler broadening media. We have shown that a high intensity coupling field is required to overcome inhomogeneous broadening, which represents an obstacle for group velocity reduction. The width of the second EIT window is independent of temperature, which means that the enhanced group-velocity reduction is superior to the case that would hold if the width did depend on temperature as temperature dependence could only worsen this effect.

In this section, we derive two expressions that relate the signal-field Rabi frequency Ω_s to the coupling-field Rabi Ω_c and Doppler width W_L. Satisfying the first expression guarantees that the probe field has the same group velocity in each transparency window. Satisfying the second expression guarantees the same HWHM for the two EIT windows.

The relation between Ω_s and Ω_c can be satisfied for a wide range of temperatures bounded above and below by the requirements for the analytical approximations to be valid according to Eqs. (6.3.45) and (6.3.46). We then use these two expressions to divide the signal-field intensity to three regimes: a low-strength regime where the group velocity and EIT width are lower than the first window, a high-strength regime where both group velocity and width of EIT window are greater than for the first window, and a middle regime where the group velocity is lower and the width is higher than for the first window.

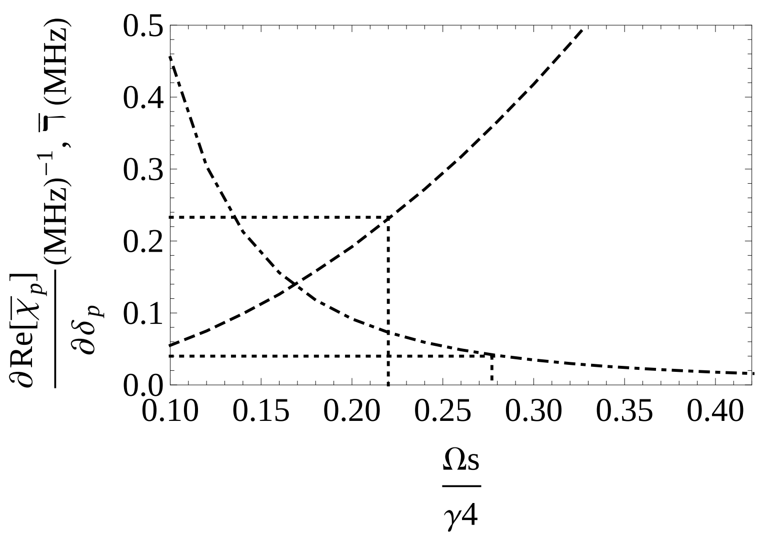

Figure 6.11: Plot of the partial derivative of dispersion (dotted-dashed line) and HWHM (dashed line) for the second EIT window and HWHM (upper horizontal-dotted line) and partial derivative of dispersion (lower horizontal-dotted line) for the first EIT window versus normalized signal-field Rabi frequency with $\Omega_\mathrm{c} = \gamma_4$, $W_\mathrm{L} = 700$ MHz, $\gamma_4 = 18$ MHz, $\gamma_3 = 10$ kHz, and $\gamma_2 = 40$ kHz, and $\mathcal{N} = 1 \times 10^{14}$ cm^{-3}. Using ^{87}Rb constants: $|\boldsymbol{d}_{14}| = |\boldsymbol{d}_{34}| = 1.269 \times 10^{-29}$ C·m, and $\omega_0 = 2\pi \cdot 377.11$ THz.

In Fig. 6.11, we plot the HWHM and partial derivative of dispersion for the second EIT window using Eqs. (6.3.65) and (6.3.67), respectively. We also plot the HWHM and partial derivative of dispersion for the first EIT window. Intercepts between lines show which signal-field Rabi frequencies yield matched HWHM or group-velocity conditions. Matched HWHM occurs at $\Omega_{\mathrm{s_l}}$ and matched-group velocity occurs at $\Omega_{\mathrm{s_h}}$ with $\Omega_{\mathrm{s_l}}$ lower than $\Omega_{\mathrm{s_h}}$, and l and h refer to lower and higher values, respectively. We can choose values of Ω_{s} to control which of the two windows has higher HWHM and group velocity.

We exploit our analytical expressions for the HWHM and the group velocity at the center of each window to find the lower and higher boundary values of the signal field. Equating Eqs. (6.3.63) and (6.3.65) for real values of Ω_{c} and Ω_{s} gives us the lower boundary value of Ω_{s}:

$$\Omega_{\mathrm{s_l}} = 2^{\frac{3}{4}}\Omega_{\mathrm{c}}\sqrt{\frac{\gamma_4}{W_{\mathrm{L}}}}. \tag{6.4.1}$$

Similarly equating Eqs. (6.3.66) and (6.3.67) gives us the higher boundary value of Ω_{s}:

$$\Omega_{\mathrm{s_h}} = \frac{2}{3}\sqrt{\frac{9}{2}\gamma_3 W_{\mathrm{L}} + \frac{\gamma_4\Omega_{\mathrm{c}}^2}{3W_{\mathrm{L}}}\left(19 + \frac{2\gamma_4\Omega_{\mathrm{c}}^2}{W_{\mathrm{L}}^2\gamma_3}\right)}. \tag{6.4.2}$$

Equations (6.4.1) and (6.4.2) reveal which signal-field strength should be selected to achieve either matched width or matched-group velocity, respectively.

At certain Doppler width, the boundary values of Ω_{s} in Eqs. (6.4.1) and (6.4.2) can be tuned by varying the coupling-field strength Ω_{c}. Both the matched group velocity and the matched HWHM have lower value as Ω_{c} is reduced.

In summary, our four-level atom optical system can be operated at the second window in three different regimes depending on the signal-field strength. In the low-strength regime, the second window has very low group velocity compared to the first window but also has a lower EIT width. However, we can operate in this regime for lower group velocity as long as the width is resolvable experimentally. Alternatively, in the high-strength regime, the second window has a higher group velocity than for the first window. which makes this high-strength regime less desirable for low group-velocity experiments.

6.5 Summary

We have achieved our objective of showing that the second DDEIT window has advantages over the first window with respect to obtaining an enhanced reduction of group velocity. The presence of a nonlinear interaction between the probe and signal fields in optical susceptibility plays a crucial role in enabling temperature-controlled modification of the optical response. At the second window this term signifies the ability to reduce the narrowing of width and thereby yields increases of the group velocity as the Doppler width increases. The modified optical response due to nonlinear interaction permits observing the second window for low intensity signal field and suggest greater reduction in the group velocities at the second EIT window.

By identifying the signal-field boundary values $\Omega_{\mathrm{s_l}}$ and $\Omega_{\mathrm{s_h}}$, we are able to identify the regime of the signal-field strength values that could result in slower group velocity than for the first window. The low-strength regime is the best for realizing low group velocity, but the EIT window could be difficult to resolve. The middle-strength regime is more robust in that the second EIT window is expected to be resolvable and the group velocity is expected to be low. The high-strength regime is less interesting as the group velocity is relatively high.

Our approximate analytical calculation succeeds in describing the optical response of the Doppler-broadened four-level optical system and helps in analyzing the system in the presence or absence of the nonlinear interaction. These analytical calculations also provide us with intuition of how the width or group velocities change in a Doppler-broadened system. Importantly our analytical expression helps us to study the relation between the coupling and signal fields and to achieve matching of either widths or the group velocities of the two window. These conditions are not intuitively clear otherwise, and hence would be difficult to discern using only numerical calculations.

Chapter 7

Conclusion

The goal of this study has been attained by showing that $\pitchfork$-atomic configurations have interesting characteristics that have not been resolved before, especially DDEIT, wherein both fields can pass through the medium without absorption, and with a lower group velocity than the speed of light, at two different EIT windows. This system creates DEIT windows for the double fields. For identical probe and signal-Rabi frequencies, the optical properties of both fields at the first and second windows are identical. Therefore, their group velocities can be matched in either the first or second pair of transparency windows.

The second EIT window in both probe and signal fields is predicted theoretically for the first time in this work. A theoretical study for this window has been introduced, using a density-matrix approach, where the observation of this window is explained in terms of the coherence between atomic levels in both the bare and semiclassical dressed bases. The new EIT window shows rich characteristics when compared to the first window; as well as lower constant group velocity, and higher nonlinear-optical susceptibility for both fields, used to achieve large-phase modulation. This investigation has demonstrated that the SPM and XPM of both probe and signal fields vanish at the center of two transparency windows. However, the SPM and XPM around the region of the second window exceed their values around the region of the first window. The values of SPM and XPM at the region of the second window are higher than their values in the region of the first window, by a factor of 1000. Our results revealed that the nonlinear index of refraction of the probe field can be enhanced if the signal field does not resonate either with $|3\rangle \leftrightarrow |-\rangle$ or $|3\rangle \leftrightarrow |+\rangle$ transitions. Similarly, to get a non-zero value of the SPM and XPM of the signal field, the probe field must not be in resonance with $|3\rangle \leftrightarrow |-\rangle$ or with $|3\rangle \leftrightarrow |+\rangle$ transitions.

Another new concept presented in this study is Raman amplification under EIT condition. This new prediction makes it possible to amplify either one of the weak fields, by scattering the second in the absence of population inversion between the states that define the Raman transition, which is a key requirement for Raman gain. The overall gain occurs in the second window, due to a nonlinear process in which the higher-order terms of probe and signal fields becomes significant, and cannot be ignored. The gain is achieved without population inversion at the operating transition, but needs condition (2.5.11) to be satisfied in order to amplify the probe field, and condition (2.5.15) must be satisfied to amplify the signal field. Amplification cannot be detected in the probe and signal-field outputs simultaneously, because the gain that appears in the probe field is accompanied by the absorption of the signal field, and vice versa.

Furthermore, a solution for the wave equation is presented, and describes the propagation of a Gaussian probe field, through the $\pitchfork$ atom-field configuration, in which the signal field is also Gaussian. The solution is based on the assumption that the medium is inhomogeneous, a consequence of the variation optical susceptibility, due to the propagation of the signal field within the medium. It was also assumed that the propagation of the Gaussian probe beam had slow spatial variations in the gain and index of refraction. The variations are sufficiently slow in the vicinity of the beam that the optical susceptibility can be expanded, keeping only the linear and quadratic terms. The solution has assisted in predicting the changes that occur in the amplitude and phase of the wave during its propagation within the medium. We also show that generating inhomogeneity within the medium modifies the group velocity of the probe field, but not the nonlinear phase shift. The group velocity of the probe field reduces as the beam propagates through the medium. The reduction of the group velocity is controlled by the signal-field beam waist.

Additionally, this examination has studied the properties of the second transparency window at high temperatures under the Doppler-broadening effect, but was limited to the condition that the probe field is weaker than the signal field. The results demonstrated that the second EIT window has advantages over the first window, regarding obtaining an enhanced reduction of group velocity. The presence of a nonlinear interaction between the probe and signal fields in optical susceptibility plays a crucial role in enabling temperature-controlled modification of the optical response. The modified optical response, due to nonlinear interaction, permits observation of the second window for the low intensity signal field, and promises more group-velocity reduction in the second EIT window. It was found that the nonlinear interaction between the probe and signal fields keep the width of the second window constant for high Doppler widths. This result permits further lowering of the intensity of the signal field, without losing the EIT transparency window, and gets lower probe-field group velocity at the second window than at the first window.

It was also found that in the presence of nonlinear interaction, that the lower strength of the signal field (which controls the width and group velocity of the second window) compared to the coupling-field strength (which controls the width and group velocity of the first window) does not mean that the second window always has a lower group velocity or a lower EIT window width than the first, for all applied temperatures. By determining the signal-field boundary values $\Omega_{\mathrm{s_l}}$ and $\Omega_{\mathrm{s_h}}$, it was possible to identify the regime of the signal-field strength values that could result in slower group velocity than the first window. The low strength regime is best for realizing low-group velocity, but the EIT window could be difficult to resolve. The middle-strength regime is more robust, in that the second EIT window is expected to be resolvable, and the group velocity is expected to be low. The high-strength regime is less interesting, as the group velocity is relatively high.

Operating the tripod scheme in the new region of frequency detuning merges the advantage of the N-scheme by inducing high nonlinearity at the center of the EIT window and the advantage of DEIT schemes by lowering and matching the group velocities of the interacting fields within the EIT window. Relying on our theoretical calculation, a large XPM sufficient to produce a π-phase shift with matched and lowered group velocities is feasible experimentally at the level of a few tens photons using our scheme. At the level of a photon and by satisfying all conditions required to resolve the EIT experimentally, our scheme is capable of inducing a phase shift between the probe and the signal field reaching 40°, with the probe and signal bandwidth confined within the EIT window to ensure the propagation of the probe and signal pulses through the medium without absorption.

Appendix A

Optical Parameters Calculation

In this section, we show the detail calculation of the optical parameters including the group velocity, HWHM of the EIT windows and XPM phase shift using our proposed scheme. In our calculation we specifically consider ^{87}Rb and assign $|1\rangle$, $|2\rangle$ and $|3\rangle$ to the $5S_{1/2}$ with $F = 1$, $m_F = 0$, $F = 2$ and $m_F = \{-2, 0\}$ respectively. Level $|4\rangle$ corresponds to level $5P_{1/2}$ with $F = 2$ and $m_F = -1$. The parameters for the dipole matrix elements, decay rates [61], and detuning correspond to our choice of atom and hyper-fine transition are $|\boldsymbol{d}_{14}| = |\boldsymbol{d}_{34}| = 1.269 \times 10^{-29}$ C·m, $\omega_0 = 2\pi \cdot 377.11$ THz, $\gamma_{14} = \gamma_{24} = \gamma_{34} = 6$ MHz, $\gamma_3 = 10$ kHz, $\gamma_2 = 40$ kHz, $\Omega_\mathrm{c} = 2\gamma_4$, $\delta_\mathrm{s} = \delta_\mathrm{p} = 0.5\Omega_\mathrm{c}$ and $\delta_\mathrm{c} = 0.045\Omega_\mathrm{c}$.

A.1 Tripod Cross Phase Modulation in Comparison to N-Scheme

The XPM phase shift of the probe field using our scheme is calculated from the second term of Eq.(3.5.33)

$$\phi_{\mathrm{XPM_p}}(\omega) = \frac{\omega}{c} \frac{\mathrm{Re}\left[\chi^{(3)}_{\mathrm{p}\ 2}(\omega)\right] \left|\xi_{\mathrm{s}_f}\right|^2}{2n_\mathrm{p}(\omega)} z, \tag{A.1.1}$$

with $n_\mathrm{p}(\omega) \approx 1$at the center of the second EIT window and $\mathrm{Re}\left[\chi^{(3)}_{\mathrm{p}_2}(\omega)\right]$ defined by Eq. (3.5.38). In term of the Rabi frequency and using (2.2.11)

$$\left|\xi_{\mathrm{s}_f}\right|^2 = \frac{|\Omega_\mathrm{s}|^2 \hbar^2}{|d_{34}|^2}. \tag{A.1.2}$$

For $\Omega_\mathrm{s} = 2$ MHz, which is necessary to obtain the HWHM of the EIT resolvable experimentally $\daleth_{2_{\mathrm{p,s}}} = 0.12$ MHz, and for atomic density $\mathcal{N} = 10^{12}$ cm^{-3}, the real part of the nonlinear optical susceptibility, $\mathrm{Re}\left[\chi^{(3)}_{\mathrm{p}_2}(\omega)\right] = 5.7 \times 10^{-6}$ m $\cdot$ V^{-2} and the XPM phase shift, $\phi_{\mathrm{XPM_p}}(\omega) = 1.58$ rad.

For the N-scheme the real part of the nonlinear optical susceptibility, $\mathrm{Re}\left[\chi^{(3)}_{\mathrm{p}_N}\right]$, using our notation is defined by [9]

$$\mathrm{Re}\left[\chi^{(3)}_{\mathrm{p}_N}\right] = \frac{\eta_{\mathrm{sp}}\delta_{\mathrm{s}}\left|\Omega_{\mathrm{s}}\right|^2}{3\left|\Omega_{\mathrm{c}}\right|^2\left(\delta_{\mathrm{s}}^2+\gamma_4^2\right)}, \tag{A.1.3}$$

and the XPM phase shift are calculated using a similar equation to (A.1.1) with $\mathrm{Re}\left[\chi^{(3)}_{\mathrm{p}_2}(\omega)\right]$ exchanged with $\mathrm{Re}\left[\chi^{(3)}_{\mathrm{p}_N}(\omega)\right]$. The $\mathrm{Re}\left[\chi^{(3)}_{\mathrm{p}_N}(\omega)\right]$ and the XPM phase shift $\phi_{\mathrm{XPM}_{\mathrm{p_N}}}(\omega)$ obtained using $\Omega_{\mathrm{s}} = 2$ MHz and atomic density $\mathcal{N} = 10^{12}$ cm^{-3} are 4.9×10^{-6} m $\cdot$ V^{-2} and 1.24 rad respectively. The above calculation shows that the tripod scheme operated in the new frequency region and the N-scheme produce the same order of magnitude of optical nonlinearity.

A.2 Cross Phase Modulation at the Level of One Photon

In the first part of this section, we show by calculation using experimentally feasible data that the tripod scheme operated in the new frequency region exhibits high nonlinearity that is able to produce phase shifts in the probe and signal fields equal to $\frac{\pi}{2}$ at the level of tens of photons. During our calculation the fulfillment of the three criteria discussed in Sec. 1.5 are taken into account.

The energy of the single probe and signal photon in ^{87}Rb at 795 nm wavelength and angular frequency $\omega_0 = 2\pi\cdot 377.11$ THz can be obtained by

$$\begin{aligned} E &= \hbar\omega_0 \\ &\approx 25\times10^{-20}\mathrm{J}. \end{aligned} \tag{A.2.1}$$

Then the intensity of the probe and the signal light pulses, each with 65 photons and 10 μs duration and focused to spot size $w_{0_{\mathrm{s}}} = w_{0_{\mathrm{p}}} = \frac{\lambda_{\mathrm{p,s}}}{2} = 395$ nm [94] are

$$\begin{aligned} I = I_{\mathrm{p,s}} &= \frac{65E}{\tau_{\mathrm{p,s}}\pi w_{0_{\mathrm{p,s}}}^2} \\ &\approx 330\ \mu\mathrm{W}\cdot\mathrm{cm}^{-2}, \end{aligned} \tag{A.2.2}$$

which is equivalent to the Rabi frequency

$$\Omega_{\rm p} = \Omega_{\rm s} = \sqrt{\frac{I\gamma^2}{2I_{\rm sat}}}, \qquad (A.2.3)$$
$$\approx 1.9 \text{ MHz}$$

where $I_{\rm sat}$ is the saturation intensity for ^{87}Rb atom, which is equal to 1.6 mWcm^{-2} [23], and

$$\gamma_{14} = \gamma_{24} = \gamma_{34} = \gamma = 6 \text{ MHz}, \qquad (A.2.4)$$

then the group velocity of the signal and probe field in sample of $\mathcal{N} = 10^{14}$ cm^{-3} and after propagating a distance $z = z_{R_{\rm s,p}} \approx 0.67$ μm are

$$v_{g_{\rm p}} = \frac{|\Omega_{\rm s}|^2 c}{\omega_0 \eta_{\rm p} \left(\varrho_{11} - \varrho_{44}\right) \left[1 + \left(\frac{z}{z_{R_{\rm p}}}\right)^2\right]} = 2.75 \text{ cm} \cdot \text{s}^{-1}, \qquad (A.2.5)$$

$$v_{g_{\rm s}} = \frac{|\Omega_{\rm p}|^2 c}{\omega_0 \eta_{\rm s} \left(\varrho_{33} - \varrho_{44}\right) \left[1 + \left(\frac{z}{z_{R_{\rm s}}}\right)^2\right]} = 2.75 \text{ cm} \cdot \text{s}^{-1}, \qquad (A.2.6)$$

and the EIT window widths are

$$\daleth_{2_{\rm p}} = \frac{|\Omega_{\rm s}|^2}{2\sqrt{\gamma_4^2 + |\Omega_{{\rm s}_0}|^2}} = 0.1 \text{ MHz}, \qquad (A.2.7)$$

$$\daleth_{2_{\rm s}} = \frac{|\Omega_{\rm p}|^2}{2\sqrt{\gamma_4^2 + |\Omega_{{\rm p}_0}|^2}} = 0.1 \text{ MHz}. \qquad (A.2.8)$$

The probe and the signal XPM phase shift are calculated using Eq. (3.5.36) and Eq. (3.5.49) respectively:

$$\phi_{{\rm XPM}_{\rm p}} = \phi_{{\rm XPM}_{\rm s}} = 1.56 \text{ rad}. \qquad (A.2.9)$$

Now, we check the fulfillment of the three criteria discussed in Sec. 1.5 by calculating the ratio $\frac{|\Omega_{\rm p,s}|^2}{\gamma_4\gamma_3} = 20$, the product of $|\Omega_{\rm p,s}| \cdot \tau_{\rm p,s} = 19$, and by comparing the value of $\tau_{\rm p,s}$ with the value of $\frac{1}{\daleth_{2_{\rm p,s}}}$. The resultant values ensure that the Rabi frequencies are sufficient to eliminate the homogeneous broadening and to saturate the transition, and the EIT windows contain the probe and signal bandwidths.

Our next step is to show the possibility for achieving a high phase shift at the level of one photon. The intensity of the probe and signal light pulses, each with one photon and 13 μs duration and focused to spot size $w_{0_{\mathrm{s}}} = w_{0_{\mathrm{p}}} = \frac{\lambda_{\mathrm{p,s}}}{2} = 50$ nm, is

$$\begin{aligned} I &= \frac{E}{\tau_{\mathrm{p,s}} \pi w_{0_{\mathrm{p,s}}}^2} \\ &\approx 245\ \mu\mathrm{W} \cdot \mathrm{cm}^{-2}. \end{aligned} \tag{A.2.10}$$

Using (A.2.3) the Rabi frequency is $\Omega_{\mathrm{p}} = \Omega_{\mathrm{s}} = 1.7$ MHz. The group velocity of the signal and probe field in a sample of $\mathcal{N} = 10^{15}$ cm^{-3} and after propagating a distance $z = 2z_{R_{\mathrm{s,p}}} \approx 0.033$ μm are

$$v_{g_{\mathrm{p}}} = \frac{|\Omega_{\mathrm{s}}|^2 c}{\omega_0 \eta_{\mathrm{p}} \left(\varrho_{11} - \varrho_{44}\right) \left[1 + \left(\frac{z}{z_{R_{\mathrm{p}}}}\right)^2\right]} = 0.08\ \mathrm{cm} \cdot \mathrm{s}^{-1}, \tag{A.2.11}$$

$$v_{g_{\mathrm{s}}} = \frac{|\Omega_{\mathrm{p}}|^2 c}{\omega_0 \eta_{\mathrm{s}} \left(\varrho_{33} - \varrho_{44}\right) \left[1 + \left(\frac{z}{z_{R_{\mathrm{s}}}}\right)^2\right]} = 0.08\ \mathrm{cm} \cdot \mathrm{s}^{-1}, \tag{A.2.12}$$

and the EIT window widths are

$$\daleth_{2_{\mathrm{p}}} = \frac{|\Omega_{\mathrm{s}}|^2}{2\sqrt{\gamma_4^2 + |\Omega_{\mathrm{s}_0}|^2}} = 0.076\ \mathrm{MHz}, \tag{A.2.13}$$

$$\daleth_{2_{\mathrm{s}}} = \frac{|\Omega_{\mathrm{p}}|^2}{2\sqrt{\gamma_4^2 + |\Omega_{\mathrm{p}_0}|^2}} = 0.076\ \mathrm{MHz}. \tag{A.2.14}$$

The probe and the signal XPM phase shift are calculated using Eq. (3.5.36) and Eq. (3.5.49) respectively:

$$\phi_{\mathrm{XPM_p}} = \phi_{\mathrm{XPM_s}} = 0.35\ \ \mathrm{rad} \tag{A.2.15}$$

The ratio of $\frac{|\Omega_{\mathrm{p,s}}|^2}{\gamma_4 \gamma_3} = 15$, and the product of $|\Omega_{\mathrm{p,s}}| \cdot \tau_{\mathrm{p,s}} = 21.5$, which ensures that the Rabi frequencies are sufficient to eliminate homogeneous broadening and to saturate the transition. By comparing the value of $\tau_{\mathrm{p,s}}$ with the value of $\frac{1}{\daleth_{2_{\mathrm{p,s}}}}$, the signal and probe bandwidth are confined within the EIT window.

Appendix B

Diagonal and Off-Diagonal Elements of the Density Matrix

The content of this section is based on [102]. In order to use the density matrix elements to describe the dynamics of the quantum system, we must first understand what is the physical meaning of each matrix elements. Let us start with the diagonal elements $\varrho_{\phi\phi}$

$$\begin{aligned}\varrho_{\phi\phi} =& \langle\phi|\varrho|\phi\rangle \\ =& \sum_{\Psi} \mathscr{P}_{\Psi} \langle\phi\,|\Psi\rangle\,\langle\Psi\,|\phi\rangle \\ =& \sum_{\Psi} \mathscr{P}_{\Psi} |\langle\phi\,|\Psi\rangle\,|^2,\end{aligned} \tag{B.1}$$

the second step in (B.1) follows from (2.3.4). The state vector $|\Psi\rangle$ in term of its basis $\{|\phi\rangle\}$ can be expressed as

$$|\Psi\rangle = \sum_{\phi} c_{\phi}\,|\phi\rangle\,. \tag{B.2}$$

Therefore, the term $|\langle\phi\,|\Psi\rangle\,|^2$ in the last line of Eq. (B.1) is just $|c_{\phi}|^2$, which is the probability of being in state $|\phi\rangle$. Thus, Eq. (B.1) gives us the probability of being in base state $|\phi\rangle$ for quantum system being in mixture or pure vector state. For this reason, $\varrho_{\phi\phi}$ is called the population of the state $|\phi\rangle$.

For the case of the off-diagonal elements of density matrix

$$\begin{aligned}\rho_{\phi\varphi} =& \langle\phi|\rho|\varphi\rangle \\ =& \sum_{\Psi} \mathscr{P}_{\Psi} \langle\phi\,|\Psi\rangle\,\langle\Psi\,|\varphi\rangle \\ =& \sum_{\Psi} \mathscr{P}_{\Psi} c_{\phi} c^*_{\varphi},\end{aligned} \tag{B.3}$$

the term $c_{\phi}c^*_{\varphi}$ is cross term express the interference between states $|\phi\rangle$ and $|\varphi\rangle$ when the state $|\Psi\rangle$ is coherent linear superposition of these states. According to Eq. (B.3) $\rho_{\phi\varphi}$ is the average of these cross term, taken over all the possible states of the statistical mixture. If $\rho_{\phi\varphi}$ is zero, this means that the statistical average has canceled out any interference effect between $|\phi\rangle$ and $|\varphi\rangle$. On the other hand, if $\rho_{\phi\varphi}$ is different from zero, a certain coherence effect between these states are occurs. For this reason the off-diagonal elements of $\rho_{\phi\varphi}$ are called coherences.

Appendix C

Polarization and Optical Susceptibility

The polarization generated in the atomic medium by the applied fields is of primary interest, since it acts as a source term in Maxwells equations, and determines the electromagnetic field dynamics. By knowing the induced polarization established by an applied field we can determine a crucial parameter describe the response of the media to the applied field: the optical susceptibility $\boldsymbol{\chi}$. Therefore, in this part we review the basic physical concepts of induced polarization due to an applied field, where we discusses the macroscopic polarization using different optical representations: time-domain, frequency-domain, and the hybrid of the time and frequency domain. The content of this section summarizes chapter 2 of [2].

C.1 Macroscopic Polarization

The polarization of the medium under the influence of an applied electric field is described in terms of a power series in the field

$$\boldsymbol{P}(t) = \boldsymbol{P}^{(1)}(t) + \boldsymbol{P}^{(2)}(t) + \cdots + \boldsymbol{P}^{(m)}(t) + \cdots , \tag{C.1.1}$$

where $\boldsymbol{P}^{(1)}(t)$ is linear in the applied field defined by

$$\boldsymbol{P}^{(1)}(t) = \epsilon_0 \int_{-\infty}^{\infty} \boldsymbol{\chi}^{(1)}(\tau)\boldsymbol{E}(t-\tau)d\tau. \tag{C.1.2}$$

Here, $\boldsymbol{\chi}^{(1)}(\tau)$ is a second rank tensor known as the linear optical susceptibility. It is a real function of the variable τ because it relates two real function polarization and electric fields, and vanishes for $\tau < 0$ to ensure that $\boldsymbol{P}^{(1)}(t)$ depends only on values of the field for time before t [2].

The second term of Eq. (C.1.1) is quadratic in the applied field. It is expressed in the form [2]

$$\boldsymbol{P}^{(2)}(t) = \epsilon_0 \int_{-\infty}^{\infty} d\tau_1 \int_{-\infty}^{\infty} d\tau_2 \; \boldsymbol{\chi}^{(2)}(\tau_1, \tau_2) : \boldsymbol{E}(t-\tau_1)\boldsymbol{E}(t-\tau_2), \tag{C.1.3}$$

where $\boldsymbol{\chi}^{(2)}(\tau_1, \tau_2)$ is a third-rank tensor that determines the quadratic polarization in the medium. The causality requirement dictates that $\boldsymbol{\chi}^{(2)}(\tau_1, \tau_2) = 0$ when, either τ_1 or τ_2 is negative [2].

Similarly, the mth-order polarization $\boldsymbol{P}^{(m)}(t)$ is determined by [2]

$$\boldsymbol{P}^{(m)}(t) = \epsilon_0 \int_{-\infty}^{\infty} d\tau_1 \cdots \int_{-\infty}^{\infty} d\tau_m \; \boldsymbol{\chi}^{(m)}(\tau_1, \cdots, \tau_m) | \boldsymbol{E}(t-\tau_1) \cdots \boldsymbol{E}(t-\tau_m). \tag{C.1.4}$$

The mth-order optical susceptibility $\boldsymbol{\chi}^{(m)}(\tau_1, \cdots, \tau_m)$ tensor is of rank $m+1$, and is real function of the m time variable $\tau_1, \cdots, \tau_m$. It vanishes when any of τ_m is negative.

Another representation of optical polarization is provided by frequency-domain. Both the time-domain and frequency-domain representations provide useful descriptions of the linear and nonlinear-optical properties, and the choice of which is most appropriate largely depends on the type of applied field. For example, the frequency-domain more appropriate when considering a monochromatic field, such as that obtained from continuous-wave single-mode lasers [2]. On the other hand, time-domain representation is more appropriate when considering short-pulse lasers that are shorter in duration than the fundamental ultrafast relaxation process of the nonlinear medium [2].

Defining the Fourier time transform and its inverse of function F to be

$$\boldsymbol{F}(\omega) = \frac{1}{2\pi} \int_{-\infty}^{\infty} \boldsymbol{F}(t) e^{\mathrm{i}\omega t} dt, \qquad \boldsymbol{F}(t) = \int_{-\infty}^{\infty} \boldsymbol{F}(\omega) e^{-\mathrm{i}\omega t} d\omega. \tag{C.1.5}$$

After the applied field is defined by its Fourier transform, equations (C.1.2), (C.1.3) and (C.1.4) become transform(C.1.5)

$$\begin{aligned}
\boldsymbol{P}^{(1)}(t) &= \epsilon_0 \int_{-\infty}^{\infty} \boldsymbol{\chi}^{(1)}(\omega_k; \omega) \boldsymbol{E}(\omega) e^{-\mathrm{i}\omega_k t} d\omega, && \text{(C.1.6)} \\
\boldsymbol{P}^{(2)}(t) &= \epsilon_0 \int_{-\infty}^{\infty} d\omega_1 \int_{-\infty}^{\infty} d\omega_2 \; \boldsymbol{\chi}^{(2)}(\omega_k; \omega_1, \omega_2) : \boldsymbol{E}(\omega_1)\boldsymbol{E}(\omega_2) e^{-\mathrm{i}\omega_k t}, \;\; \omega_k = \omega_1 + \omega_2, \\
\boldsymbol{P}^{(m)}(t) &= \epsilon_0 \int_{-\infty}^{\infty} d\omega_1 \cdots \int_{-\infty}^{\infty} d\omega_m \; \boldsymbol{\chi}^{(m)}(\omega_k; \omega_1, \cdots, \omega_m) | \boldsymbol{E}(\omega_1) \cdots \boldsymbol{E}(\omega_m) e^{-\mathrm{i}\omega_k t},
\end{aligned}$$

with

$$\omega_k = \omega_1 + \cdots + \omega_m,$$

for $\boldsymbol{P}^{(m)}(t)$, and

$$\begin{aligned}
\boldsymbol{\chi}^{(1)}(\omega) &= \int_{-\infty}^{\infty} \boldsymbol{\chi}^{(1)}(\tau) e^{\mathrm{i}\omega\tau} d\tau, \qquad \text{(C.1.7)}\\
\boldsymbol{\chi}^{(2)}(\omega_k;\omega_1,\omega_2) &= \int_{-\infty}^{\infty} d\tau_1 \int_{-\infty}^{\infty} d\tau_2\ \boldsymbol{\chi}^{(2)}(\tau_1,\tau_2) e^{\mathrm{i}(\omega_1\tau_1+\omega_2\tau_2)},\\
\boldsymbol{\chi}^{(m)}(\omega_k;\omega_1,\cdots,\omega_m) &= \int_{-\infty}^{\infty} d\tau_1 \cdots \int_{-\infty}^{\infty} d\tau_m\ \boldsymbol{\chi}^{(m)}(\tau_1,\cdots,\tau_m) e^{\mathrm{i}(\omega_1\tau_1+\cdots+\omega_m\tau_m)},
\end{aligned}$$

as the optical susceptibilities in the frequency domain. By substituting Eq. (C.1.6) into (C.1.5), we relate the polarization to the electric field in the frequency domain, and the polarization is determined by the values of the susceptibility tensor at the various frequencies involved

$$\begin{aligned}
&\boldsymbol{P}^{(1)}(\omega) = \epsilon_0 \int_{-\infty}^{\infty} \boldsymbol{\chi}^{(1)}(\omega_k;\omega)\boldsymbol{E}(\omega)\delta(\omega-\omega_k)d\omega,\ \omega_k = \omega \qquad \text{(C.1.8)}\\
&\boldsymbol{P}^{(2)}(\omega) = \epsilon_0 \int_{-\infty}^{\infty} d\omega_1 \int_{-\infty}^{\infty} d\omega_2\ \boldsymbol{\chi}^{(2)}(\omega_k;\omega_1,\omega_2) : \boldsymbol{E}(\omega_1)\boldsymbol{E}(\omega_2)\delta(\omega-\omega_k),\ \omega_k = \omega_1+\omega_2,\\
&\boldsymbol{P}^{(m)}(\omega) = \epsilon_0 \int_{-\infty}^{\infty} d\omega_1 \cdots \int_{-\infty}^{\infty} d\omega_m\ \boldsymbol{\chi}^{(m)}(\omega_k;\omega_1,\cdots,\omega_m) | \boldsymbol{E}(\omega_1)\cdots\boldsymbol{E}(\omega_m)\delta(\omega-\omega_k),\\
&\omega_k = \omega_1 + \cdots + \omega_m
\end{aligned}$$

where the Dirac delta-function is defined by

$$\delta(\omega-\omega_k) = \frac{1}{2\pi}\int_{-\infty}^{\infty} e^{-\mathrm{i}(\omega-\omega_k)t} dt, \qquad \text{(C.1.9)}$$

with $\delta(\omega-\omega_k) = 0$ for $\omega \neq \omega_k$, $\delta(\omega-\omega_k) \to \infty$ for $\omega = \omega_k$, such that $\int_{-\infty}^{\infty} \delta(\omega-\omega_k-a) f(\omega-\omega_k) d(\omega-\omega_k) = f(a)$

C.1.1 Monochromatic Applied Field

Consider an applied field consisting of a superposition of monochromatic fields, such as

$$\boldsymbol{E}(t) = \sum_l \frac{\boldsymbol{\xi}_l e^{\mathrm{i}(\omega_l t)} + \boldsymbol{\xi}_l^* e^{-\mathrm{i}(\omega_l t)}}{2}. \qquad \text{(C.1.10)}$$

Its Fourier transform is given by

$$\boldsymbol{E}(\omega) = \sum_l \frac{\boldsymbol{\xi}_l \delta(\omega + \omega_l) + \boldsymbol{\xi}_l^* \delta(\omega - \omega_l)}{2}. \tag{C.1.11}$$

We can write the mth-order polarization in the form

$$\boldsymbol{P}^{(m)}(z,t) = \sum_l \boldsymbol{P}_l^{(m)}(z,t) = \sum_l \frac{\boldsymbol{p}_l^{(m)} e^{\mathrm{i}(\omega_l t)} + \left(\boldsymbol{p}_l^{(m)}\right)^* e^{-\mathrm{i}(\omega_l t)}}{2}, \tag{C.1.12}$$

with $\boldsymbol{p}_l^{(m)}$ as the polarization complex envelope function. By substituting (C.1.11) into (C.1.8) we can obtain an expression for $\boldsymbol{p}_l^{(m)}$. The Cartesian μ-component is given by [2]

$$\begin{aligned}\left(p_{\omega_k}^{(m)}\right)_\mu = 2\epsilon_0 \sum_{\alpha_1\cdots\alpha_m} & \chi^{(m)}_{\mu\alpha_1\cdots\alpha_m}(\omega_k;\omega_1,\omega_2,\cdots,\omega_m)\frac{1}{2}\xi_{1\alpha_1}\frac{1}{2}\xi_{2\alpha_2}\cdots\frac{1}{2}\xi_{l\alpha_m} \\ & +\chi^{(m)}_{\mu\alpha_1\cdots\alpha_m}(\omega_k;\omega_2,\omega_1,\cdots,\omega_m)\frac{1}{2}\xi_{1\alpha_1}\frac{1}{2}\xi_{2\alpha_2}\cdots\frac{1}{2}\xi_{l\alpha_m} \\ & + \text{further distinguishable terms,}\end{aligned} \tag{C.1.13}$$

where the repeated cartesian-coordinates $\alpha_1, \cdots, \alpha_m$ are summed over x, y and z. Here, we consider a specific frequency $\omega_k \geq 0$, and that $\omega_1, \omega_2, \cdots, \omega_m$ denotes any of the frequency modes of the applied electric field of (2.2.5), which together satisfy $\omega_k = \omega_1 + \omega_2 + \cdots + \omega_l$. The factors $\frac{1}{2}$s appear in the left-hand side of (C.1.13) is because we chose to include $\frac{1}{2}$ in the definition (C.1.11), while the factor 2 in the same side of equation arises from the $\frac{1}{2}$ in the definition (C.1.13). In general, it is rather tiresome to keep track of the various numerical factors, and this is a source of error. For this reason it is convenient to define the electric field and polarization without $\frac{1}{2}$.

In contract notation, Eq. (C.1.13) can be written as

$$\left(p_{\omega_k}^{(m)}\right)_\mu = \epsilon_0 \sum_{\alpha_1\cdots\alpha_m} \sum_l K\left(\omega_k;\omega_1,\omega_2,\cdots,\omega_l\right) \chi^{(m)}_{\mu\alpha_1\cdots\alpha_m}\left(\omega_k;\omega_1,\omega_2,\cdots,\omega_l\right)\left(\xi_{1\alpha_1}\xi_{2\alpha_2}\cdots\xi_{l\alpha_m}\right). \tag{C.1.14}$$

The second summation is over all distinct sets of $\omega_1, \omega_2, \cdots, \omega_l$ which satisfy $\omega_k = \omega_1 + \omega_2 + \cdots + \omega_l$. K is a numerical factor, defined by

$$K(\omega_k;\omega_1+\omega_2+\cdots+\omega_l) = 2^{o+p-m}q, \tag{C.1.15}$$

where q is the number of distinct permutations of $\omega_1, \omega_2, \cdots, \omega_l$, m is the order of nonlinearity, and p are the sets of dc fields ($p = 0$ if there is no dc field, $o = 1$ for $\omega_k \neq 0$, otherwise $o = 0$). Thus, $K = 2^{1-m}m!$ is for different $\omega_1, \omega_2, \cdots, \omega_l$ values, with none equal to zero. In vector notation Eq. (C.1.14) are written as

$$\boldsymbol{p}_{\omega_k}^{(m)} = \epsilon_0 \sum_l K(\omega_k; \omega_1, \omega_2, \cdots, \omega_l) \boldsymbol{\chi}^{(m)}(\omega_k; \omega_1, \omega_2, \cdots, \omega_l) \boldsymbol{\xi}_1 \boldsymbol{\xi}_2 \cdots \boldsymbol{\xi}_l. \tag{C.1.16}$$

This equation represent more general case, in which the optical susceptibility becomes complex, relates the complex amplitude of the applied field to complex amplitude of the polarization. This case is used to study dissipative and dispersive material.

C.1.2 Quasi-Monochromatic Applied Field

Another widely used approach describing the optical response is a hybrid of the time and frequency domain representations, known as the quasi-monochromatic description [2]. It is an appropriate description when considering quasi-monochromatic applied fields, such as from a pulsed or modulated laser source.

An applied field consisting of the superposition of a quasi-monochromatic field can also be defined by Eq. (2.2.5). In its frequency domain, each wave occupies a spectral band width centered at ω_l. The slowly-varying envelope of its amplitude function contains both amplitude and phase information. In a similar way, the polarization can be defined as

$$\boldsymbol{P}^{(m)}(z,t) = \sum_l \boldsymbol{P}_l^{(m)}(z,t) = \sum_l \frac{\boldsymbol{p}_l^{(m)}(t) e^{\mathrm{i}(\omega_l t)} + \left(\boldsymbol{p}_l^{(m)}\right)^* (t) e^{-\mathrm{i}(\omega_l t)}}{2}. \tag{C.1.17}$$

After substituting Eq. (2.2.5) into (C.1.4) and choosing the particular component at ω_k, the mth-order polarization in the time domain becomes

$$\begin{aligned} \boldsymbol{p}_{\omega_k}^{(m)}(t) =& \epsilon_0 K(\omega_k; \omega_1, \omega_2, \cdots, \omega_l) \int_{-\infty}^{\infty} d\tau_1 \cdots \int_{-\infty}^{\infty} d\tau_m \; \boldsymbol{\chi}^{(m)}(t-\tau_1, \cdots, t-\tau_m) | \boldsymbol{\xi}_1(\tau_1) \\ & \cdots \boldsymbol{\xi}_l(\tau_m) \exp\left(\mathrm{i} \sum_{l=1}^{m} \omega_l \tau_l\right). \end{aligned} \tag{C.1.18}$$

It is convenient to introduce a tensor $\mathbf{\Phi}^{(m)}$ of rank $m+1$, defined as

$$\mathbf{\Phi}^{(m)}_{\omega_k;\omega_1,\cdots,\omega_m}(\tau_1,\cdots,\tau_m) = \boldsymbol{\chi}^{(m)}(\tau_1,\cdots,\tau_m)\mathrm{exp}\left(\mathrm{i}\sum_{l=1}^{m}\omega_l\tau_l\right), \tag{C.1.19}$$

and related to the frequency domain optical susceptibility

$$\boldsymbol{\chi}^{(m)}(\omega_k;\omega_1,\cdots,\omega_m) = \int_{-\infty}^{\infty} d\tau_1 \cdots \int_{-\infty}^{\infty} d\tau_m \mathbf{\Phi}^{(m)}_{\omega_k;\omega_1,\cdots,\omega_m}(\tau_1,\cdots tau_m). \tag{C.1.20}$$

Then (C.1.18) can be written as

$$\begin{aligned}\boldsymbol{p}^{(m)}_{\omega_k}(t) = \epsilon_0 K(\omega_k;\omega_1,\omega_2,\cdots,\omega_l)\int_{-\infty}^{\infty} d\tau_1 \cdots \int_{-\infty}^{\infty} d\tau_m \ \mathbf{\Phi}^{(m)}_{\omega_k;\omega_1,\cdots,\omega_m}(t-\tau_1,\cdots,t-\tau_m)|\boldsymbol{\xi}_1(\tau_1) \\ \cdots \boldsymbol{\xi}_l(\tau_m).\end{aligned} \tag{C.1.21}$$

The adiabatic limit is when the amplitude fluctuations of the applied field are much slower than the relaxation time for the polarization induced in the medium, and the response depends only on the instantaneous values of the field envelopes [2]. This can be expressed as [2]

$$\mathbf{\Phi}^{(m)}_{\omega_k}(t-\tau_1,\cdots,t-\tau_m) \to \boldsymbol{S}^{(m)}\delta(t-\tau_1)\cdot\delta(t-\tau_m) \tag{C.1.22}$$

where $\boldsymbol{S}^{(m)}$ is a time-independent tensor of rank $m+1$. Then Eq. (C.1.21) becomes

$$\boldsymbol{p}^{(m)}_{\omega_k}(t) = \epsilon_0 K(\omega_k;\omega_1,\omega_2,\cdots,\omega_l)\boldsymbol{S}^{(m)}\boldsymbol{\xi}_1(t)\boldsymbol{\xi}_2\cdots\boldsymbol{\xi}_l(t). \tag{C.1.23}$$

Equation C.1.23 is also valid for continuous waves (time-independent envelopes). Comparing with (C.1.16), we see that $\boldsymbol{S}^{(m)} = \boldsymbol{\chi}^{(m)}(\omega_k;\omega_1,\omega_2,\cdots,\omega_l)$, and we can obtain the adiabatic limit for (C.1.21)

$$\boldsymbol{p}^{(m)}_{\omega_k}(t) = \epsilon_0 K(\omega_k;\omega_1,\omega_2,\cdots,\omega_l)\boldsymbol{\chi}^{(m)}(\omega_k;\omega_1,\omega_2,\cdots,\omega_l)\boldsymbol{\xi}_1(t)\boldsymbol{\xi}_2\cdots\boldsymbol{\xi}_l(t). \tag{C.1.24}$$

As with (C.1.16), the optical susceptibility becomes a complex quantity related to the complex amplitudes of applied electric fields and polarization.

Appendix D

Gaussian-Beam Fundamental Mode In Compact Form

Equations (4.2.12) and (4.2.17) represent the Gaussian-beam fundamental mode equation, while the first form of equation is intuitive and more descriptive to Gaussian beam, the second form of equation is compact and easier to handle by theoretical analysis. In this part we prove that both are equivalent by deriving the Gaussian beam equation introduced by (4.2.17) from the one given by (4.2.12) as

$$\xi_l(r) = \xi_0 \frac{w_0}{w_l(z)} e^{-r^2\left(\frac{1}{w_l^2(z)} + \frac{\mathrm{i}k_l}{2R_l(z)}\right)} e^{\mathrm{i}\Theta_l(z)}. \tag{D.1}$$

The wave radius can be written in term of ς as

$$w_l^2(z) = w_0^2\left(1+\varsigma^2\right) = w_0^2(1+\mathrm{i}\varsigma)(1-\mathrm{i}\varsigma), \tag{D.2}$$

with ς is defined in (4.2.18). By substituting (D.2) into (D.1) we get

$$\xi_l(r) = \xi_0 \frac{1}{\sqrt{(1+\mathrm{i}\varsigma)(1-\mathrm{i}\varsigma)}} e^{-r^2\left(\frac{1}{w_0^2(1+\mathrm{i}\varsigma)(1-\mathrm{i}\varsigma)} + \frac{\mathrm{i}k_l}{2R_l(z)}\right)} e^{\mathrm{i}\Theta_l(z)}. \tag{D.3}$$

By rearranging the terms we obtain

$$\xi_l(r) = \frac{\xi_0}{1-\mathrm{i}\varsigma}\sqrt{\frac{1-\mathrm{i}\varsigma}{1+\mathrm{i}\varsigma}} e^{-\frac{r^2}{w_0^2(1-\mathrm{i}\varsigma)}\left(\frac{1}{(1+\mathrm{i}\varsigma)} + \frac{\mathrm{i}w_0^2(1+\mathrm{i}\varsigma)k_l}{2R_l(z)}\right)} e^{\mathrm{i}\Theta_l(z)}. \tag{D.4}$$

The Gouy-phase shift in term of ς has the form

$$\Theta_l(z) = \tan^{-1}\varsigma. \tag{D.5}$$

The trigonometric function, $\tan^{-1}\varsigma$ can be written in the logarithmic form as

$$\tan^{-1}\varsigma = \frac{\mathrm{i}}{2}\left[\ln(1-\mathrm{i}\varsigma) - \ln(1+\mathrm{i}\varsigma)\right] = \mathrm{i}\ln\left(\sqrt{\frac{1-\mathrm{i}\varsigma}{1+\mathrm{i}\varsigma}}\right). \tag{D.6}$$

Then

$$e^{-\mathrm{i}\Theta_l(z)} = \sqrt{\frac{1+\mathrm{i}\varsigma}{1-\mathrm{i}\varsigma}}, \tag{D.7}$$

and (D.4) becomes

$$\xi_l(r) = \frac{\xi_0}{1 - \mathrm{i}\varsigma} e^{-\frac{r^2}{w_0^2(1-\mathrm{i}\varsigma)}\left(\frac{1}{(1+\mathrm{i}\varsigma)} + \frac{\mathrm{i}w_0^2(1+\mathrm{i}\varsigma)k_l}{2R_l(z)}\right)}. \tag{D.8}$$

The radius of the beam curvature in term of ς can be written as

$$R(z) = z\left(1 + \frac{1}{\varsigma^2}\right). \tag{D.9}$$

Now substitute (D.9) with $k_l = \frac{2\pi}{\lambda_l}$ into (D.8) to obtain

$$\xi_l(r) = \frac{\xi_0}{1 - \mathrm{i}\varsigma} e^{-\frac{r^2}{w_0^2(1-\mathrm{i}\varsigma)}\left(\frac{1}{(1+\mathrm{i}\varsigma)} + \frac{\mathrm{i}\left(\varsigma + \mathrm{i}\varsigma^2\right)}{1+\varsigma^2}\right)}. \tag{D.10}$$

The term between the large bracket is equal to one, therefore, we reach the Gaussian beam in compact form as presented in (4.2.17)

$$\xi_l(r) = \frac{\xi_0}{1 - \mathrm{i}\varsigma} e^{-\frac{r^2}{w_0^2(1-\mathrm{i}\varsigma)}}. \tag{D.11}$$

Bibliography

[1] S. L. McCall and E. L. Hahn. Self-Induced Transparency. *Phys. Rev.*, 183:457–485, Jul 1969. doi: 10.1103/PhysRev.183.457. URL `http://link.aps.org/doi/10.1103/PhysRev.183.457`.

[2] Paul N. Butcher and David Cotter. *Elements of Nonlinear Optics*. Cambridge University press, New York, NY, 1st edition, 1990.

[3] E. A. Manykin and A.M. Afanas'ev. On One Possibility of Making a Medium Transparent By Multi-quantum Resonance. *JETP*, 25(5):828, November 1967. URL `http://www.jetp.ac.ru/cgi-bin/e/index/e/25/5/p828?a=list`.

[4] V. V. Krasnikov, M. S. Pshenichnikov, and V. S. Solomatin. Parametric Bleaching of a Two-Photon Absorbing Medium. *JETP*, 65(5):884, May 1987. URL `http://www.jetp.ac.ru/cgi-bin/e/index/e/65/5/p884?a=list`.

[5] O. A Kocharovskaya and Ya. I. Khanin. Population Trapping and Coherent Bleaching of a Three-Level Medium by a Periodic Train of Ultrashort Pulses. *JETP*, 63(5):945, May 1986. URL `http://www.jetp.ac.ru/cgi-bin/e/index/e/63/5/p945?a=list`.

[6] M. B. Gornyi, B. G. Matisov, and Yu. V. Rozhdestvenskii. Coherent Population Trapping in an Optically Dense Medium. *JETP*, 68(4):728, April 1989. URL `http://www.jetp.ac.ru/cgi-bin/e/index/e/68/4/p728?a=list`.

[7] S. E. Harris, J. E. Field, and A. Imamoğlu. Nonlinear Optical Processes Using Electromagnetically Induced Transparency. *Phys. Rev. Lett.*, 64:1107–1110, Mar 1990. doi: 10.1103/PhysRevLett.64.1107. URL `http://link.aps.org/doi/10.1103/PhysRevLett.64.1107`.

[8] Hai Wang, David Goorskey, and Min Xiao. Enhanced Kerr Nonlinearity via Atomic Coherence in a Three-Level Atomic System. *Phys. Rev. Lett.*, 87:073601, Jul 2001. doi: 10.1103/PhysRevLett.87.073601. URL `http://link.aps.org/doi/10.1103/PhysRevLett.87.073601`.

[9] Hoonsoo Kang and Yifu Zhu. Observation of Large Kerr Nonlinearity at Low Light Intensities. *Phys. Rev. Lett.*, 91:093601, Aug 2003. doi: 10.1103/PhysRevLett.91.093601. URL `http://link.aps.org/doi/10.1103/PhysRevLett.91.093601`.

[10] J. Kou, R. G. Wan, Z. H. Kang, H. H. Wang, L. Jiang, X. J. Zhang, Y. Jiang, and J. Y. Gao. EIT-assisted large cross-Kerr nonlinearity in a four-level inverted-Y atomic system. *J. Opt. Soc. Am. B*, 27 (10):2035–2039, Oct 2010. doi: 10.1364/JOSAB.27.002035. URL `http://josab.osa.org/abstract.cfm?URI=josab-27-10-2035`.

[11] Bor-Wen Shiau, Meng-Chang Wu, Chi-Ching Lin, and Ying-Cheng Chen. Low-Light-Level Cross-Phase Modulation with Double Slow Light Pulses. *Phys. Rev. Lett.*, 106:193006, May 2011. doi: 10.1103/PhysRevLett.106.193006. URL `http://link.aps.org/doi/10.1103/PhysRevLett.106.193006`.

[12] A. Imamoğlu and S. E. Harris. Lasers without inversion: interference of dressed lifetime-broadened states. *Opt. Lett.*, 14(24):1344–1346, Dec 1989. doi: 10.1364/OL.14.001344. URL `http://ol.osa.org/abstract.cfm?URI=ol-14-24-1344`.

[13] S. E. Harris. Lasers Without Inversion: Interference of Lifetime-Broadened Resonances. *Phys. Rev. Lett.*, 62(9):1033–1036, 1989.

[14] Olga Kocharovskaya. Amplification and lasing without inversion. *Phys. Rep.*, 219(3–6):175–190, 1992.

[15] Olga Kocharovskaya. Lasing without inversion: Problems and prospects. *Hyperfine Interactions*, 107: 187–195, 1997.

[16] J. Mompart and R. Corbalan. Lasing without inversion. *J. Opt. B: Quantum Semiclassical*, 2(3): R7–R24, 2000.

[17] Gautam Vemuri and Girish S. Agarwal. Role of inhomogeneous broadening in lasing without inversion in ladder systems. *Phys. Rev. A*, 53:1060–1064, Feb 1996. doi: 10.1103/PhysRevA.53.1060. URL `http://link.aps.org/doi/10.1103/PhysRevA.53.1060`.

[18] L. V. Hau, S. E. Harris, Z. Dutton, and C. H. Behroozi. Light Speed Reduction to 17 Metres Per Second In An Ultracold Atomic Gas. *Nature (Londen)*, 397(6720):594–598, 1999.

[19] S. E. Harris and Lene Vestergaard Hau. Nonlinear optics at low light levels. *Phys. Rev. Lett.*, 82: 4611–4614, Jun 1999. doi: 10.1103/PhysRevLett.82.4611. URL `http://link.aps.org/doi/10.1103/PhysRevLett.82.4611`.

[20] Michael M. Kash, Vladimir A. Sautenkov, Alexander S. Zibrov, L. Hollberg, George R. Welch, Mikhail D. Lukin, Yuri Rostovtsev, Edward S. Fry, and Marlan O. Scully. Ultraslow Group Velocity and Enhanced Nonlinear Optical Effects in a Coherently Driven Hot Atomic Gas. *Phys. Rev.*

Lett., 82:5229–5232, Jun 1999. doi: 10.1103/PhysRevLett.82.5229. URL `http://link.aps.org/doi/10.1103/PhysRevLett.82.5229`.

[21] D. Budker, D. F. Kimball, S. M. Rochester, and V. V. Yashchuk. Nonlinear Magneto-optics and Reduced Group Velocity of Light in Atomic Vapor with Slow Ground State Relaxation. *Phys. Rev. Lett.*, 83:1767–1770, Aug 1999. doi: 10.1103/PhysRevLett.83.1767. URL `http://link.aps.org/doi/10.1103/PhysRevLett.83.1767`.

[22] Anil K. Patnaik, J. Q. Liang, and K. Hakuta. Slow light propagation in a thin optical fiber via electromagnetically induced transparency. *Phys. Rev. A*, 66:063808, Dec 2002. doi: 10.1103/PhysRevA.66.063808. URL `http://link.aps.org/doi/10.1103/PhysRevA.66.063808`.

[23] H. Gao, M. Rosenberry, J. Wang, and H. Batelaan. Experimental studies of light propagation and storage in warm atomic gases. *Journal of Physics B: Atomic, Molecular and Optical Physics*, 38(12):1857, 2005. doi: 10.1088/0953-4075/38/12/003. URL `http://iopscience.iop.org/0953-4075/38/12/003`.

[24] M. Bajcsy, S. Hofferberth, V. Balic, T. Peyronel, M. Hafezi, A. S. Zibrov, V. Vuletic, and M. D. Lukin. Efficient All-Optical Switching Using Slow Light within a Hollow Fiber. *Phys. Rev. Lett.*, 102:203902, May 2009. doi: 10.1103/PhysRevLett.102.203902. URL `http://link.aps.org/doi/10.1103/PhysRevLett.102.203902`.

[25] K. V. R. M. Murali, Z. Dutton, W. D. Oliver, D. S. Crankshaw, and T. P. Orlando. Probing Decoherence with Electromagnetically Induced Transparency in Superconductive Quantum Circuits. *Phys. Rev. Lett.*, 93(8):087003, Aug 2004.

[26] Jaewoo Joo, Jérôme Bourassa, Alexandre Blais, and Barry C. Sanders. Electromagnetically Induced Transparency with Amplification in Superconducting Circuits. *Phys. Rev. Lett.*, 105:073601, Aug 2010. doi: 10.1103/PhysRevLett.105.073601. URL `http://link.aps.org/doi/10.1103/PhysRevLett.105.073601`.

[27] Patrick M. Leung and Barry C. Sanders. Coherent Control of Microwave Pulse Storage in Superconducting Circuits. *Phys. Rev. Lett.*, 109:253603, Dec 2012. doi: 10.1103/PhysRevLett.109.253603. URL `http://link.aps.org/doi/10.1103/PhysRevLett.109.253603`.

[28] Mark C. Phillips, Hailin Wang, I. Rumyantsev, N. H. Kwong, R. Takayama, and R. Binder. Electromagnetically Induced Transparency in Semiconductors via Biexciton Coherence. *Phys. Rev. Lett.*, 91:

183602, Oct 2003. doi: 10.1103/PhysRevLett.91.183602. URL http://link.aps.org/doi/10.1103/PhysRevLett.91.183602.

[29] V. Ahufinger, R. Corbalán, F. Cataliotti, S. Burger, F. Minardi, and C. Fort. Electromagnetically induced transparency in a Bose–Einstein condensate. *Optics Communications*, 211:159–165, Oct 2002. URL http://dx.doi.org/10.1016/S0030-4018(02)01826-6.

[30] A. H. Safavi-Naeini, T. P. Mayer Alegre, J. Chan, M. Eichenfield, M. Winger, Q. Lin, J. T. Hill, D. E. Chang, and O. Painter. Electromagnetically induced transparency and slow light with optomechanics. *Nature*, 472:69–73, April 2011. doi: doi:10.1038/nature09933. URL http://www.nature.com/nature/journal/v472/n7341/full/nature09933.html.

[31] Surya P. Tewari and G. S. Agarwal. Control of Phase Matching and Nonlinear Generation in Dense Media by Resonant Fields. *Phys. Rev. Lett.*, 56:1811–1814, Apr 1986. doi: 10.1103/PhysRevLett.56.1811. URL http://link.aps.org/doi/10.1103/PhysRevLett.56.1811.

[32] Andrew J. Merriam, S. J. Sharpe, M. Shverdin, D. Manuszak, G. Y. Yin, and S. E. Harris. Efficient Nonlinear Frequency Conversion in an All-Resonant Double-Lambda System. *Phys. Rev. Lett.*, 84:5308–5311, Jun 2000. doi: 10.1103/PhysRevLett.84.5308. URL http://link.aps.org/doi/10.1103/PhysRevLett.84.5308.

[33] Yanxu Han, Jintao Xiao, Yonghong Liu, Chunhong Zhang, Hai Wang, Min Xiao, and Kunchi Peng. Interacting dark states with enhanced nonlinearity in an ideal four-level tripod atomic system. *Phys. Rev. A*, 77:023824, Feb 2008. doi: 10.1103/PhysRevA.77.023824. URL http://link.aps.org/doi/10.1103/PhysRevA.77.023824.

[34] Tao Hong, Claire Cramer, Warren Nagourney, and E. N. Fortson. Optical Clocks Based on Ultranarrow Three-Photon Resonances in Alkaline Earth Atoms. *Phys. Rev. Lett.*, 94:050801, Feb 2005. doi: 10.1103/PhysRevLett.94.050801. URL http://link.aps.org/doi/10.1103/PhysRevLett.94.050801.

[35] Robin Santra, Ennio Arimondo, Tetsuya Ido, Chris H. Greene, and Jun Ye. High-Accuracy Optical Clock via Three-Level Coherence in Neutral Bosonic ^{88}Sr. *Phys. Rev. Lett.*, 94:173002, May 2005. doi: 10.1103/PhysRevLett.94.173002. URL http://link.aps.org/doi/10.1103/PhysRevLett.94.173002.

[36] S. E. Harris. Electromagnetically Induced Transparency. *Phys. Today*, 50(7):36–42, 1997.

[37] Marlan O. Scully. Enhancement of the Index of Refraction via Quantum Coherence. *Phys. Rev. Lett.*, 67:1855–1858, Sep 1991. doi: 10.1103/PhysRevLett.67.1855. URL `http://link.aps.org/doi/10.1103/PhysRevLett.67.1855`.

[38] A. S. Zibrov, M. D. Lukin, L. Hollberg, D. E. Nikonov, M. O. Scully, H. G. Robinson, and V. L. Velichansky. Experimental Demonstration of Enhanced Index of Refraction via Quantum Coherence in Rb. *Phys. Rev. Lett.*, 76:3935–3938, May 1996. doi: 10.1103/PhysRevLett.76.3935. URL `http://link.aps.org/doi/10.1103/PhysRevLett.76.3935`.

[39] Michael Fleischhauer, Atac Imamoğlu, and Jonathan P. Marangos. Electromagnetically Induced Transparency: Optics In Coherent Media. *Rev. Mod. Phys.*, 77(2):633–673, Jul 2005. doi: 10.1103/RevModPhys.77.633.

[40] Jonathan P. Marangos and Thomas Halfmann. *Handbook of Optics*, volume IV. McGraw-Hill, New York, NY, 3rd edition, 2010.

[41] Marlan O. Scully and M. Zubairy Suhail. *Quantum Optics*. Cambridge University Press, Cambridge, 1st edition, 1997.

[42] Yong-qing Li and Min Xiao. Electromagnetically induced transparency in a three-level Λ-type system in rubidium atoms. *Phys. Rev. A*, 51:R2703–R2706, Apr 1995. doi: 10.1103/PhysRevA.51.R2703. URL `http://link.aps.org/doi/10.1103/PhysRevA.51.R2703`.

[43] Sadaf Sultana and M. Suhail Zubairy. Effect of finite bandwidth on refractive-index enhancement and lasing without inversion. *Phys. Rev. A*, 49:438–448, Jan 1994. doi: 10.1103/PhysRevA.49.438. URL `http://link.aps.org/doi/10.1103/PhysRevA.49.438`.

[44] Baolong Lü, W. H. Burkett, and Min Xiao. Electromagnetically induced transparency with variable coupling-laser linewidth. *Phys. Rev. A*, 56:976–979, Jul 1997. doi: 10.1103/PhysRevA.56.976. URL `http://link.aps.org/doi/10.1103/PhysRevA.56.976`.

[45] Shujing Li, Xudong Yang, X. Cao, C. Zhang, and H. Xie, C.and Wang. Two electromagnetically induced transparency windows and an enhanced electromagnetically induced transparency signal in a four-level tripod atomic system. *JPhys. B: At. Mol. Opt. Phys.*, 40:3211, Aug 2007.

[46] Paul Mandel and Olga Kocharovskaya. Inversionless amplification of a monochromatic field by a three-level medium. *Phys. Rev. A*, 46:2700–2706, Sep 1992. doi: 10.1103/PhysRevA.46.2700. URL `http://link.aps.org/doi/10.1103/PhysRevA.46.2700`.

[47] A. S. Zibrov, M. D. Lukin, D. E. Nikonov, L. Hollberg, M. O. Scully, V. L. Velichansky, and H. G. Robinson. Experimental Demonstration of Laser Oscillation without Population Inversion via Quantum Interference in Rb. *Phys. Rev. Lett.*, 75:1499–1502, Aug 1995. doi: 10.1103/PhysRevLett.75.1499. URL `http://link.aps.org/doi/10.1103/PhysRevLett.75.1499`.

[48] M. D. Lukin, M. O. Scully, G. R. Welch, E. S. Fry, L. Hollberg, G. G. Padmabandu, H. G. Robinson, and A. S. Zibrov. Lasing without Inversion: the Road to New Short-Wavelength Lasers. *Laser Physics*, 6:436–447, 1996.

[49] G. G. Padmabandu, George R. Welch, Ivan N. Shubin, Edward S. Fry, Dmitri E. Nikonov, Mikhail D. Lukin, and Marlan O. Scully. Laser Oscillation without Population Inversion in a Sodium Atomic Beam. *Phys. Rev. Lett.*, 76:2053–2056, Mar 1996. doi: 10.1103/PhysRevLett.76.2053. URL `http://link.aps.org/doi/10.1103/PhysRevLett.76.2053`.

[50] J. L. Cohen and P. R. Berman. Amplification without inversion:mUnderstanding probability amplitudes, quantum interference, and Feynman rules in a strongly driven system. *Phys. Rev. A*, 55:3900–3917, May 1997. doi: 10.1103/PhysRevA.55.3900. URL `http://link.aps.org/doi/10.1103/PhysRevA.55.3900`.

[51] H. Schmidt and A. Imamoğlu. Giant Kerr nonlinearities obtained by electromagnetically induced transparency. *Opt. Lett.*, 21(23):1936–1938, Dec 1996. doi: 10.1364/OL.21.001936. URL `http://ol.osa.org/abstract.cfm?URI=ol-21-23-1936`.

[52] A. I. Lvovsky, B. C. Sanders, and W. Tittel. Optical Quantum Memory. *Nature Photonics*, 3:706 – 714, Dec 2009.

[53] Matthew S. Bigelow, Nick N. Lepeshkin, and Robert W. Boyd. Superluminal and Slow Light Propagation in a Room-Temperature Solid. *Science*, 301(5630):200–202, 2003. doi: 10.1126/science.1084429. URL `http://www.sciencemag.org/content/301/5630/200.abstract`.

[54] F. Zimmer and M. Fleischhauer. Sagnac Interferometry Based on Ultraslow Polaritons in Cold Atomic Vapors. *Phys. Rev. Lett.*, 92:253201, Jun 2004. doi: 10.1103/PhysRevLett.92.253201. URL `http://link.aps.org/doi/10.1103/PhysRevLett.92.253201`.

[55] Vincent Wong, Robert W. Boyd, C. R. Stroud, Ryan S. Bennink, David L. Aronstein, and Q-Han Park. Absorptionless self-phase-modulation via dark-state electromagnetically induced transparency. *Phys. Rev. A*, 65:013810, Dec 2001. doi: 10.1103/PhysRevA.65.013810. URL http://link.aps.org/doi/10.1103/PhysRevA.65.013810.

[56] Dinh Xuan Khoa, Le Van Doai, Doan Hoai Son, and Nguyen Huy Bang. Enhancement of self-Kerr nonlinearity via electromagnetically induced transparency in a five-level cascade system: an analytical approach. *J. Opt. Soc. Am. B*, 31(6):1330–1334, Jun 2014. doi: 10.1364/JOSAB.31.001330. URL http://josab.osa.org/abstract.cfm?URI=josab-31-6-1330.

[57] S. Rebić, D. Vitali, C. Ottaviani, P. Tombesi, M. Artoni, F. Cataliotti, and R. Corbalán. Polarization phase gate with a tripod atomic system. *Phys. Rev. A*, 70:032317, Sep 2004. doi: 10.1103/PhysRevA.70.032317. URL http://link.aps.org/doi/10.1103/PhysRevA.70.032317.

[58] Amitabh Joshi and Min Xiao. Phase Gate with a Four-Level Inverted-Y System. *Phys. Rev. A*, 72:062319, Dec 2005. doi: 10.1103/PhysRevA.72.062319. URL http://link.aps.org/doi/10.1103/PhysRevA.72.062319.

[59] Zeng-Bin Wang, Karl-Peter Marzlin, and Barry C. Sanders. Large Cross-Phase Modulation Between Slow Copropagating Weak Pulses in ^{87}Rb. *Phys. Rev. Lett.*, 97:063901, Aug 2006. doi: 10.1103/PhysRevLett.97.063901. URL http://link.aps.org/doi/10.1103/PhysRevLett.97.063901.

[60] C. Ottaviani, S. Rebić, D. Vitali, and P. Tombesi. Quantum phase-gate operation based on nonlinear optics: Full quantum analysis. *Phys. Rev. A*, 73:010301, Jan 2006. doi: 10.1103/PhysRevA.73.010301. URL http://link.aps.org/doi/10.1103/PhysRevA.73.010301.

[61] A. MacRae, G. Campbell, and A. I. Lvovsky. Matched slow pulses using double electromagnetically induced transparency. *Opt. Lett*, 33:2659, 2008.

[62] E. Paspalakis and P. L. Knight. Electromagnetically induced transparency and controlled group velocity in a multilevel system. *Phys. Rev. A*, 66:015802, Jul 2002. doi: 10.1103/PhysRevA.66.015802. URL http://link.aps.org/doi/10.1103/PhysRevA.66.015802.

[63] A. V. Taichenachev, A. M. Tumaikin, and V. I. Yudin. Influence of Atomic Motion on the Shape of Two-Photon Resonance in Gas. *JETP Letters*, 72(3):119–122, 2000.

[64] Yuri Rostovtsev, Igor Protsenko, Hwang Lee, and Ali Javan. From laser-induced line narrowing to electromagnetically induced transparency in a Doppler-broadened system. *Journal of Modern Optics*, 49(14-15):2501–2516, 2002. doi: 10.1080/0950034021000011400. URL `http://www.tandfonline.com/doi/abs/10.1080/0950034021000011400`.

[65] Ali Javan, Olga Kocharovskaya, Hwang Lee, and Marlan O. Scully. Narrowing of electromagnetically induced transparency resonance in a Doppler-broadened medium. *Phys. Rev. A*, 66:013805, Jul 2002. doi: 10.1103/PhysRevA.66.013805. URL `http://link.aps.org/doi/10.1103/PhysRevA.66.013805`.

[66] C. Y. Ye and A. S. Zibrov. Width of the electromagnetically induced transparency resonance in atomic vapor. *Phys. Rev. A*, 65:023806, Jan 2002. doi: 10.1103/PhysRevA.65.023806. URL `http://link.aps.org/doi/10.1103/PhysRevA.65.023806`.

[67] E. Figueroa, F. Vewinger, J. Appel, and A. I. Lvovsky. Decoherence of electromagnetically induced transparency in atomic vapor. *Opt. Lett.*, 31:2625–2627, Sep. 2006. doi: 10.1103/PhysRevA.65.023806. URL `http://www.opticsinfobase.org/ol/abstract.cfm?URI=ol-31-17-2625`.

[68] A. A. Abdumalikov, Jr., O. Astafiev, A. M. Zagoskin, Yu. A. Pashkin, Y. Nakamura, and J. S. Tsai. Electromagnetically Induced Transparency on a Single Artificial Atom. *Phys. Rev. Lett.*, 104:193601, May 2010. doi: 10.1103/PhysRevLett.104.193601.

[69] C. Cohen-Tannoudji, Bernard Diu, and Franck Laloë. *Quantum Mechanics*, volume 2. John Wiley and Son, New York, NY, 1st edition, 1977.

[70] Pierre Meystre and Murray Sargent III. *Elements of Quantum Optics*. Springer, New York, NY, 3rd edition, 2009.

[71] David L. Andrews and Mohamed Babiker. *The Angular Momentum of Light*. Cambridge University Press, Cambridge, 1st edition, 2013.

[72] Hessa M. M. Alotaibi and Barry C. Sanders. Double-double electromagnetically induced transparency with amplification. *Phys. Rev. A*, 89:021802, Feb 2014. doi: 10.1103/PhysRevA.89.021802. URL `http://link.aps.org/doi/10.1103/PhysRevA.89.021802`.

[73] M. S. Zubairy, A. B. Matsko, and Marlan O. Scully. Resonant Enhancement of High-Order Optical Nonlinearities Based On Atomic Coherence. *Phys. Rev. A*, 65:043804, Mar 2002. doi: 10.1103/PhysRevA.65.043804. URL `http://link.aps.org/doi/10.1103/PhysRevA.65.043804`.

[74] A. S. Zibrov, M. D. Lukin, D. E. Nikonov, L. W. Hollberg, M. O. Scully, and V. L. Velichansky. Experimental Demonstration of Continuous Wave Amplification without Inversion via Quantum Interference in Rb. *Laser Physics*, 5:553–555, 1994.

[75] Y. R. Shen and N. Bloembergen. Theory of Stimulated Brillouin and Raman Scattering. *Phys. Rev.*, 137:A1787–A1805, Mar 1965. doi: 10.1103/PhysRev.137.A1787. URL `http://link.aps.org/doi/10.1103/PhysRev.137.A1787`.

[76] N. Bloembergen and Y. R. Shen. Quantum-Theoretical Comparison of Nonlinear Susceptibilities in Parametric Media, Lasers, and Raman Lasers. *Phys. Rev.*, 133:A37–A49, Jan 1964. doi: 10.1103/PhysRev.133.A37. URL `http://link.aps.org/doi/10.1103/PhysRev.133.A37`.

[77] Alan C. Newell and Jerome V. Moloney. *Nonlinear Optics*. Addison Wasley, Redwood, CA, 1992.

[78] P. R. Berman and Rainer Salomaa. Comparison between dressed-atom and bare-atom pictures in laser spectroscopy. *Phys. Rev. A*, 25:2667–2692, May 1982. doi: 10.1103/PhysRevA.25.2667. URL `http://link.aps.org/doi/10.1103/PhysRevA.25.2667`.

[79] P. R. Berman. Theory of fluorescence and probe absorption in the presence of a driving field using semiclassical dressed states. *Phys. Rev. A*, 53:2627–2632, Apr 1996. doi: 10.1103/PhysRevA.53.2627. URL `http://link.aps.org/doi/10.1103/PhysRevA.53.2627`.

[80] Frank Vewinger, J. Appel, Eden Figueroa, and A. I. Lvovsky. Adiabatic frequency conversion of quantum optical information in atomic vapor. *Opt. Lett.*, 32(19):2771–2773, Sep 2007.

[81] Robert W. Boyd. *Nonlinear Optics*. Academic Press, Burlington,MA, 3rd edition, 2008.

[82] Chen-Show Wang. Theory of Stimulated Raman Scattering. *Phys. Rev.*, 182:482–494, Jun 1969. doi: 10.1103/PhysRev.182.482. URL `http://link.aps.org/doi/10.1103/PhysRev.182.482`.

[83] Max Maier. Application of Stimulated Raman Scattering. *Appl. Phys.*, 11:209–231, 1976.

[84] P. P. Sorokin, N. S. Shiren, J. R. Lankard, E. C. Hammond, and T. G. Kazyaka. STIMULATED ELECTRONIC RAMAN SCATTERING. *Applied Physics Letters*, 10(2):44–46, 1967. doi: http://dx.doi.org/10.1063/1.1754839. URL `http://scitation.aip.org/content/aip/journal/apl/10/2/10.1063/1.1754839`.

[85] D. Cotter and D. C. Hanna. Stimulated Electronic Raman Scattering in Cs Vapour: a Simple Tunable Laser System for 2.7 to 3.5 μm Region. *Optical and Quantum electronic*, 9:509–518, 1977.

[86] Y. Takubo, M. Tsuchiya, and M. Shimazu. Stimulated Electronic Raman Scattering in In Vapor. *Appl. Phys.*, 24:139–142, 1981.

[87] H Kogelnik and T. Li. Laser beams and resonators. *Appl. Opt.*, 5(10):1552–1566, 1966.

[88] Warren Nagourney. *Quantum Electronics for Atomic Physics and Telecommunication.* Oxford University Press, 2nd edition, 2014.

[89] Keqian Zhang and Dejie Li. *Electromagnetic Theory for Microwaves and Optoelectronics.* Springer, New York,NY, 2nd edition, 2008.

[90] Lee W. Casperson. Gaussian Light Beams in Inhomogeneous Media. *Appl. Opt.*, 12(10):2434–2441, Oct 1973. doi: 10.1364/AO.12.002434. URL `http://ao.osa.org/abstract.cfm?URI=ao-12-10-2434`.

[91] Alex Mahalov. Physics-Based Predictive Modeling of Atmospheric Optical Turbulence Layers: Solution of Paraxial Wave Equation for Inhomogeneous Media in Linear and Quadratic Approximation. In *Imaging and Applied Optics*, page PTu1F.2. Optical Society of America, 2013. doi: 10.1364/PCDVT.2013.PTu1F.2. URL `http://www.osapublishing.org/abstract.cfm?URI=pcDVT-2013-PTu1F.2`.

[92] Z.L. Horváth, J. Vinkó, Zs. Bor, and D. von der Linde. Acceleration of femtosecond pulses to superluminal velocities by Gouy phase shift. *Applied Physics B*, 63(5):481–484, 1996. ISSN 0946-2171. doi: 10.1007/BF01828944. URL `http://dx.doi.org/10.1007/BF01828944`.

[93] S. E. Harris and Zhen-Fei Luo. Preparation energy for electromagnetically induced transparency. *Phys. Rev. A*, 52:R928–R931, Aug 1995. doi: 10.1103/PhysRevA.52.R928. URL `http://link.aps.org/doi/10.1103/PhysRevA.52.R928`.

[94] Rafayel Mirzoyan. Study of the coherent effects in rubidium atomic vapor under bi-chromatic laser radiation. A Thesis in Physics Submitted for the Degree of Doctor of Philosophy, 2013.

[95] Darrick E. Chang, Vladan Vuletić, and Mikhail D. Lukin. Quantum nonlinear optics photon by photon. *Nature Photonics*, 8:685694, August 2014.

[96] Jürgen Volz, Michael Scheucher, Christian Junge, and Arno Rauschenbeutel. Nonlinear phase shift for single fibre-guided photons interacting with a single resonator-enhanced atom. *Nature Photonics*, 8:965970, November 2014.

[97] Julio Gea-Banacloche, Yong-qing Li, Shao-zheng Jin, and Min Xiao. Electromagnetically induced transparency in ladder-type inhomogeneously broadened media: Theory and experiment. *Phys. Rev. A*, 51:576–584, Jan 1995. doi: 10.1103/PhysRevA.51.576. URL `http://link.aps.org/doi/10.1103/PhysRevA.51.576`.

[98] Gianni Pagnini and R. K. Saxena. A note on the Voigt profile function. arXiv:math-phys, 2008.

[99] C. Y. Ye and A. S. Zibrov. Width of the electromagnetically induced transparency resonance in atomic vapor. *Phys. Rev. A*, 65:023806, Jan 2002. doi: 10.1103/PhysRevA.65.023806. URL `http://link.aps.org/doi/10.1103/PhysRevA.65.023806`.

[100] J. R. Ackerhalt, J. H. Eberly, and B. W. Shore. Statistical broadening and population loss in strongly excited three-level systems. *Phys. Rev. A*, 19:248–263, Jan 1979.

[101] A. S. Choe, J. Han, Y. Rhee, J. Lee, P. S. Han, M. A. Kuzmina, and V. A. Mishin. Laser bandwidth and Doppler broadening effects on the population dynamics of three-level atomic gadolinium. *J. Phys. B: At. Mol. Opt. Phys*, 28:2355, 1995.

[102] Fam Le Kien and K. Hakuta. Density Operator and Applications in Nonlinear Optics. University Lecture, 2004.